

---

# Investigations of ultrathin nanocrystalline metal films generated at the liquid-liquid interface

---

A Thesis submitted in partial fulfillment  
of the requirements of the degree of

## Doctor of Philosophy

By  
Ved Varun Agrawal



Chemistry and Physics of Material Unit  
Jawaharlal Nehru Centre for Advanced Scientific Research  
(A Deemed University)  
Bangalore – 560064 (INDIA)  
March 2008



*Dedicated to Mummy and Papa...*



## Declaration

I hereby declare that this thesis entitled “**Investigations of ultrathin nanocrystalline metal films generated at the liquid-liquid interface**” is an authentic record of research work carried by me under the supervision of Prof. G. U. Kulkarni and Prof. C. N. R. Rao, FRS at the Chemistry and Physics of Material Unit, Jawaharlal Nehru Centre for Advanced Scientific Research, Bangalore, India.

In keeping with the general practice of reporting scientific observation, due acknowledgement has been made whenever work described here has been based on the findings of other investigations. Any oversight due to error of judgment is regretted.

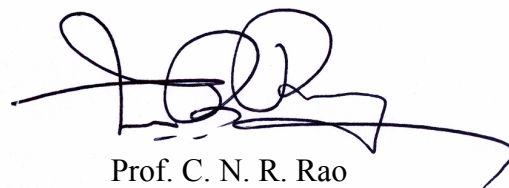
Ved Varun Agrawal



## Certificate

Certified that the work described in this thesis titled “**Investigations of ultrathin nanocrystalline metal films generated at the liquid-liquid interface**” has been carried out under our supervision at the Chemistry and Physics of Material Unit, Jawaharlal Nehru Centre for Advanced Scientific Research, Bangalore, India.

Prof. G. U. Kulkarni

A handwritten signature in black ink, consisting of several loops and a long horizontal stroke extending to the right.

Prof. C. N. R. Rao





## Acknowledgements

Words will fail any day if I try to acknowledge my supervisors Prof. G. U. Kulkarni and Prof. C. N. R. Rao. I can only show my gratitude to what they have blessed me with. Their blessings were showered in the form of knowledge, time and love, which are the priceless assets.

I thank Prof. G. U. Kulkarni for educating me with life lessons. Many times, he taught me the most complex things by giving the simplest of analogies. He actually taught me how to simplify problems, how to break bigger problems into smaller ones and work with one parameter at a time. In one line, he taught me the art of doing research. I thank him for exposing me to the field of instrumentation, (he was like Dronaacharya to me, who taught me various skills).

But all the skills I learnt would have not been manifested if I had missed an opportunity, lacked motivation or had no reason to perform - they all came through Prof. C N R Rao, like Krishna, he lead me to the field of science. Prof. Rao's mere presence is an inspiration and motivation. I especially thank him for giving me opportunities to work in the field of nanoscience, and to open up opportunity to work on synchrotron with Prof Sanyal and on rheology with Prof. Sood.

I express my sincere thanks to various collaborators, Dr. P. Saravanan, Dr. P. J. Thomas, Reji, Prof. A. K. Sood, Prof. B. R. Mehta, Prof. M. K. Sanyal, Indranil, Mrinal, Prof J. Daillant, Dr. C. Blot, S. Kubowicz, Dr. O. Konovalov, Dr. R. Krishnaswamy, S. Majumdar, Dr. R. Ganapathy, Dr. Ujjal, Dr. Moumita, Mahalakhmi and Neenu.

I thank DST (India) and Service pour la Science & la Technologie (France) for financial assistance in carrying out experiment at ESRF synchrotron beamline.

I am thankful to the JNC faculty members and faculty members of Division of Chemical Science, Indian Institute of Science for offering courses that have been highly beneficial in my research activity. In particular, I would like to thank Profs. K. S. Narayan, N. Chandrabhas, S. Balasubramanian, S. Narasimhan, U. Waghmare, S.

Shastry, S. M. Shivaprasad, S. Pati, R. Uday, D. D. Sharma, J. Gopalakrishnan, A. K. Shukla. Drs. A. Govindaraj, A. R. Raju, Kini, Eswaramoorthy, Sundaresan.

I have enjoyed the company and friendship of my lab mates and coworkers and I thank them all for helping me at various phase of reaserch work and for all the useful discussion I had: Reji, Girish, Ramesh, Vijay, Selvi, Bhuvana, Radha, Manoj, Mahalakhmi, Sreejith, Suchetan, Shruthi, Kyle, Drs. John, Gargi, Anupama, Neena, Ujjal, Gautam, Deepak, Moumita, Angappane, Sailaja, Karthick

I particularly thank all those people who helped in moving research work during my PhD, the help of Mrs. Usha with TEM, Srinath, Srinivas and Srinivas Rao with various instruments in Nanolab, Anil with X-ray diffraction, Vasu with Uv-Vis and Basavraj with SEM and EDAX have been valuable to this study.

I thank JNC for scholarship and various facilities that were offered. I would like to thank Prof. M. R. S. Rao and Mr. A. N. Jaychandra for support that came in various forms. I am thankful to the administration, complab members and library staff members. I am thankful to Mrs Shashi, Gowda, Xavier and Victor at Prof. Rao's office. I am also thankful to Jitender Kaur of ETU for helping me in using softwares. I am thankful to Dr. Subba Rao for his kind attention and medical treatements. I am also thankful to Sunil and Murthy for many lab related helps.

All friends, Ujjal, Gautam, Leo, Motin, Biru, Sachin, Sudhee, Kapoor, Ram, Manoj, Shailesh, Dash, Chandu, Bhat, Vijay, Kalyani, Vegadesh, Subbu, Leela, Rakesh, Anil, Migfar, Saikrishna, Dinesh, Datta, Kalyan, Gurunath, Sameer, Suthirth, Gopal, Drutiman, Manu, Vivek, Pavan, Sairam, Hemadri, Raju, Kalyan, Madhu, Pranab, Ayan, Kabra, Ksiva, Pattu, Neenu, Gomathi, Asish, Amit, Hazra, Sukhendu, Partho, Achute, Kripa, Himanshu, Sweta, Juhi, Rudra, Ambika and others, for sharing their time and love.

I thank Mrs. Indumati Rao and Mrs. Indira Kulkarni for their warmth and hospitality.

***Above all, to my mother and father for being universe to me and it is their love, encouragement and sacrifice that made me come so far.***

## Preface

The thesis presents the results of investigations on the preparation, characterization and organization of metal nanocrystals at the liquid-liquid interface, and exploring the formation of their mesoscopic assemblies. Section 1 contains a brief overview of nanocrystals and their mesoscopic organization. Section 2 contains the scope of investigations as well as the results and discussion. Section 3 covers other studies undertaken by the candidate.

The Liquid-liquid interface serves as an excellent nanoreactor where the interaction among the reacting species from the two immiscible layers is confined due to the interface. Synthesis of nanocrystalline films of Au, Ag, Pd and Cu metals and their alloys using the liquid-liquid interface has been carried out by this elegant, yet simple technique. Control parameters such as type of solvent, solution concentration, temperature, viscosity and mechanical vibrations-all influence the nanocrystal formation. Thus, it has been possible to achieve good control over the particle size and the extent of packing in mesoscopic assemblies. Nanocrystalline Au films so prepared have been investigated for their optical and electrical properties. The course of growth of Au nanocrystalline films at the interface has been studied using small angle X-ray scattering. Rheological properties of Ag films at the interface have also been examined. Besides monometallic films, nanocrystalline alloy films of Au-Ag, Au-Cu and Au-Ag-Cu have been prepared by suitably mixing metal precursors in the top organic phase. By adding surfactants to either of the layers, the formation of dendritic structures and fractal assemblies has been observed. The nanocrystalline films of Au have been chemically modified by adsorbing thiols of various types, such as alkane thiols of different chain lengths as well as conjugated dithiols. The modified films have been examined for their structural, optical and electrical properties. This aspect of the study has enabled to understand the dependence of the surface plasmon band and other characteristics on the interparticle separation. Apart from above studies, a small electrode system was designed and fabricated to study single molecular properties using two identical palladium nanocrystals, and scanning tunneling microscopy to study molecular properties.



# Contents

<b>Declaration .....</b>	<b>iii</b>
<b>Certificate .....</b>	<b>v</b>
<b>Acknowledgements .....</b>	<b>vii</b>
<b>Preface .....</b>	<b>ix</b>
<b>Contents .....</b>	<b>xi</b>
<b>1 Nanomaterials: A Brief Overview .....</b>	<b>1</b>
1.1 Metal nanocrystals and arrays.....	4
1.2 Individual nanocrystals .....	6
1.2.1 Synthesis of nanocrystal sols.....	6
1.2.2 Properties of individual nanocrystals .....	14
1.3 Array of nanocrystals .....	34
1.3.1 1D array.....	35
1.3.2 2D array.....	37
1.3.3 3D array.....	48
1.3.4 Structural properties of 1D, 2D and 3D array .....	52
1.3.5 Electrical properties of an array .....	53
1.3.6 Optical properties of an array .....	56
1.4 Concluding remarks .....	60
<b>2 Ultra-Thin Nanocrystalline Films of Metals Generated at the Liquid-Liquid Interface.....</b>	<b>63</b>
2.1 Summary.....	63
2.2 Introduction.....	65
2.3 Scope of the Present Investigations.....	70
2.3.1 Nanocrystalline films of Au and other metals and their characterizations .....	70
2.3.2 Nanocrystalline films of Au-Ag, Au-Cu and Au-Ag-Cu alloys .....	71
2.3.3 Rheological study of nanocrystalline Ag film.....	71
2.3.4 Evolution of Au nanocrystalline film studied using SAXS.....	71
2.3.5 Nanocrystalline films adsorbed with alkanethiols of varying chain lengths .....	72
2.3.6 Effect of surfactants on interfacial reaction.....	73

<b>2.4</b>	<b>Experimental.....</b>	<b>73</b>
2.4.1	Materials and synthesis.....	73
2.4.2	Characterization Techniques and methods.....	77
<b>2.5</b>	<b>Results and Discussion.....</b>	<b>83</b>
2.5.1	Nanocrystalline films of Au and other metals and their characterizations.....	83
2.5.2	Nanocrystalline films of Au-Ag, Au-Cu and Au-Ag-Cu alloys.....	105
2.5.3	Rheological study of nanocrystalline Ag film.....	112
2.5.4	Evolution of Au nanocrystalline films studied using SAXS.....	119
2.5.5	Nanocrystalline films adsorbed with alkanethiols of varying chain lengths.....	124
2.5.6	Effect of surfactants on interfacial reaction.....	137
<b>2.6</b>	<b>Conclusions.....</b>	<b>146</b>
<b>3</b>	<b>A Single Molecule Switch Based on Two Pd Nanocrystals Linked by a Conjugated Dithiol.....</b>	<b>151</b>
3.1	Summary.....	151
3.2	Introduction.....	151
3.3	Scope of the present investigations.....	152
3.4	Experimental details.....	152
3.5	Results and Discussion.....	154
3.6	Conclusions.....	157
	<b>References.....</b>	<b>159</b>
	<b>Index.....</b>	<b>169</b>

## 1 Nanomaterials: A Brief Overview

The term nano in SI units means  $10^{-9}$ , or in other words, one billionth. It is derived from the Greek word for dwarf. Materials, structures and devices that have dimensions in the nano scale range are encompassed with in nanosciences. Materials that have at least one dimension less than 100 nm may be considered to be nano-dimensional Figure 1.1.

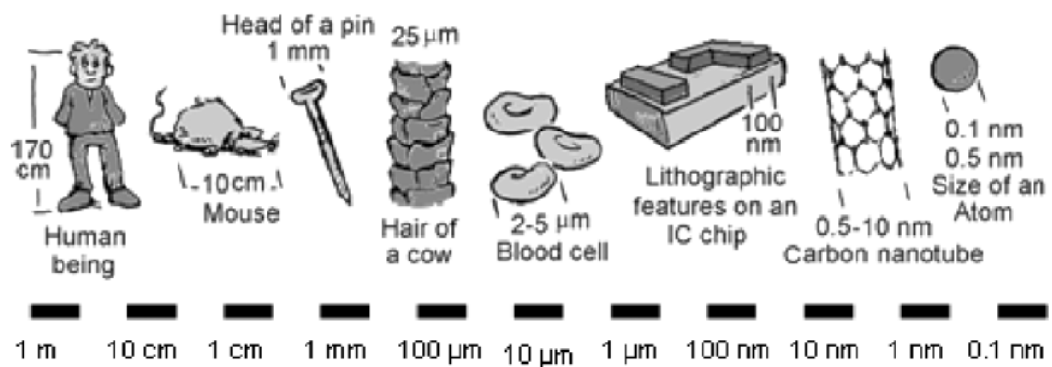


Figure 1.1 Examples of objects with different dimensions [1].

The dawn of the journey into the nano world can be traced back to 1959, when Caltech physicist Richard Feynman painted a vision of the future of science. In a talk titled, “There’s Plenty of Room at the Bottom,” Feynman hypothesized that atoms and molecules could be manipulated like building blocks. The first “proof-of-principle” that atoms could be precisely positioned by a manmade tool (living cells have, of course, been positioning atoms since time immemorial) took place in 1989 when scientists at IBM manipulated 35 xenon atoms to form the letters IBM. In the last few years, exploration within the field of nanotechnology has ramped up substantially.

Nanoscience and nanotechnology primarily deal with the synthesis, characterization, exploration, and exploitation of nanostructured materials. These materials are characterized by at least one dimension in the nanometer range. Nanostructures constitute a bridge between molecules and infinite bulk systems.

Individual nanostructures include clusters, quantum dots, nanocrystals, nanowires, and nanotubes, while collections of nanostructures involve arrays, assemblies, and superlattices of the individual nanostructures [2, 3]. The physical and chemical properties of nanomaterials can differ significantly from those of atomic-molecular or bulk materials of the same composition. These differences between nanomaterials and the molecular and condensed-phase materials pertain to the spatial structures and shapes, phase changes, energetics, electronic structure, chemical reactivity, and catalytic properties of large, finite systems, and their assemblies. The uniqueness of the structural characteristics, energetics, response, dynamics, and chemistry of nanostructures constitutes the basis of nanoscience. Some of the important issues in nanoscience relate to size effects, shape phenomena, quantum confinement, and response to external electric and optical excitations of individual and coupled finite systems.

The themes underlying nanoscience and nanotechnology are twofold: one is the bottom-up approach, that is, the miniaturization of the components, and the other is the approach of the self-assembly of molecular components, where each nanostructured component becomes part of a suprastructure. The latter approach is akin to that of Jean- Marie Lehn [4].

The nano world is full of surprises and potential. In this realm, the disciplinary boundaries between chemistry, molecular biology, materials science, and condensed matter physics dissolve as scientists struggle to understand new and sometimes unexpected properties. Significant progress in synthesizing and understanding the “building blocks” of nanotechnology has been made in past few years. In this thesis, I summarize our contribution to the same and other interesting properties studied. In the coming years, the ability to utilize these building blocks for practical purposes will greatly increase. Suitable control of the properties and response of nanostructures can lead to new devices and technologies.

Nanoparticles constitute a major class of nanomaterials. Nanoparticles are the chief and simplest form of building blocks. They have diameters ranging from one to a few hundred nanometers in all three dimensions.



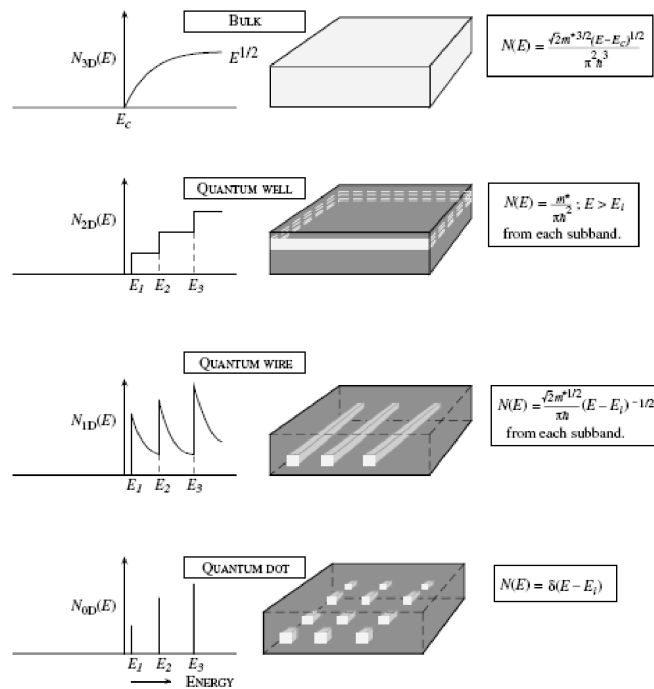


Figure 1.2 A schematic of how the density of states (DOS) change as a function of dimensionality.

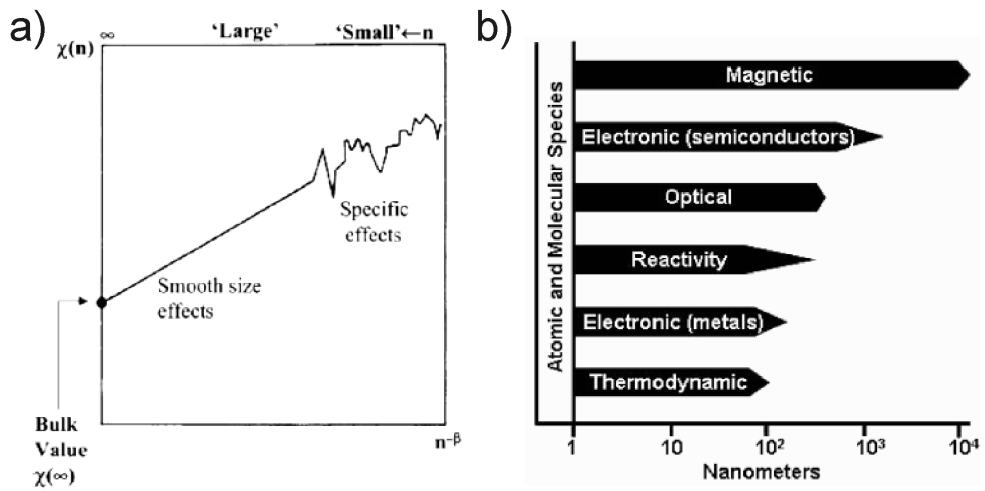


Figure 1.3 (a) The size dependence of a property  $\chi(n)$  on the number of atoms ( $n$ ) in a nanoparticle. The data are plotted against  $n^{-\beta}$  where  $\beta \geq 0$ . Small nanoparticles reveal specific size effects, while larger particles are expected to exhibit a smooth size dependence, converging to the bulk value [5]. (b) Schematic illustration of the size-dependence of various nanocrystal properties. The property specific regimes are indicated [2].

The size-dependent properties of nanocrystals include electronic, optical, magnetic, and chemical characteristics. Figure 1.2 shows a schematic of the density of states in 3D, 2D, 1D, and 0D systems. The change in properties of

material as a function of size is shown schematically in Figure 1.3. Nanoparticles can be amorphous or crystalline. Being small in size, crystalline nanoparticles can be of single domain. Nanoparticles of metals, chalcogenides, nitrides, and oxides are often composed of a single crystal. Crystalline nanoparticles are referred to as nanocrystals (NCs).

## 1.1 Metal nanocrystals and arrays

Nanoparticles are not new and their history can be traced back to the Roman period. Colloidal metals were used to dye glass articles and fabrics and as a therapeutic aid in the treatment of arthritis. The Purple of Cassius, formed on reacting stannic acid with chloroauric acid, was a popular purple dye in the olden days. It is actually made up of tin oxide and Gold (Au) nanocrystals [6]. The Romans were adept at impregnating glass with metal particles to achieve dramatic color effects. The Lycurgus cup, a glass cup of 4th century AD, appears red in transmitted light and green in reflected light. This effect, which can be seen in the cup preserved in the British museum in London, is due to Au and Silver (Ag) nanocrystals present in the walls of the cup. Maya blue, a blue dye employed by the Mayas around 7th century AD has been shown recently to consist of metal and oxide nanocrystals in addition to indigo and silica [7]. Clearly, the ability to synthesize nanocrystals preceded the understanding of nanoscale phenomena. Systematic studies of nanocrystals began to appear as early as the seventeenth century. Antonio Neri, a Florentine glassmaker and priest, describes the synthesis of colloidal Au in his 1612 treatise *L'Arte Vetraria*. John Kunckel, revised and translated Neri's work into German in 1689. Kunckel is often credited with the discovery that glass can be colored red by addition of Au.

Despite the early advances, studies of nanoscale particles did not gather momentum in later years. Thus, for most part of the 20th century, colloid science was the domain of a few specialized groups and did not receive sufficient importance. As early as 1857, Michael Faraday [8, 9] carried out ground-breaking work on colloidal metals. He called them divided metals. Faraday established the very basis for the area, noting that colloidal metal sols were thermodynamically unstable, and that the individual particles must be stabilized kinetically against aggregation. Remarkably, Faraday also identified the essence of the nature of

colloidal, nanoscale particles of metals. In the case of Au, he stated, “Au is reduced to exceedingly fine particles which on becoming diffused, produce a beautiful fluid . . . the various preparations of Au whether ruby, green, violet, or blue . . . consist of that substance in a metallic divided state.” Einstein [10] related the Brownian motion executed by the nanocrystals to their diffusion coefficient. Mie and Gans [11-13] proposed a theoretical basis for the optical properties of the nanoscale particles, which continues to be widely used till date. Frölich and Kubo proposed theories that predicted that the electronic structure of colloidal metals would differ from their respective bulk.

The growth of nanoscience and nanotechnology in the last decade has been tremendous because of the success in the synthesis of nanomaterials in conjunction with the advent of tools for characterization and manipulation. The synthesis of nanomaterials spans inorganic, organic, and biological systems. The subsequent assembling of the individual nanostructures into ordered arrays is often imperative. Notable examples of the synthesis of novel nanobuilding units are:

- Nanocrystals of metals, semiconductors and magnetic materials, employing colloid chemistry methods
- The use of physical and chemical methods for the synthesis of nanoparticles of ceramic materials
- Surface deposition of clusters and nanocrystals on graphite and other metallic or semiconducting surfaces to obtain novel three- or two-dimensional nanosystems
- Single- and multi-walled carbon nanotubes as well as nanotubes of inorganic materials, such as metal oxides, chalcogenides, and nitrides
- Nanowires of metals, semiconductors, oxides, nitrides, sulfides, and other materials [14]
- New polymeric structures involving dendrimers and block copolymers
- Nanobiological structures (e.g., bacterial and plant photosynthetic reaction centers and segments of DNA). Mutagenesis of the protein

structure, as well as chemical modifications of the DNA double strand, enables the control of the response of these systems.

The synthesis of nanomaterials includes control of size, shape, and structure. Assembling the nanostructures into ordered arrays often becomes necessary for rendering them functional and operational. In the last decade, nanoparticles (powder) of ceramic materials have been produced in large scales by employing both physical and chemical methods. There has been considerable progress in the preparation of nanocrystals of metals, semiconductors, and magnetic materials by employing colloid chemical methods.

## 1.2 Individual nanocrystals

It is useful to categorize sizes of nanocrystals into different regimes specific to the different properties, beyond which size dependence would not be relevant. The schematic in Figure 1.3 illustrates this aspect. All the regimes begin essentially with small clusters ( $\geq 1$  nm), but the upper limits are different. There are phenomenological approaches to the problem of size dependence [15]. Jortner suggests that a cluster property,  $G$ , can be represented by a universal scaling law involving  $N$  or  $R$ . Thus,

$$\begin{aligned} G(R) &= G(\infty) + aR^{-\alpha_1} \\ G(N) &= G(\infty) + aN^{-\beta_1} \end{aligned} \quad (1.1)$$

Here,  $N$  and  $R$  represent nuclearity and radius, respectively. The values of the exponents  $\alpha_1$  and  $\beta_1$  are normally 1 and  $1/3$ , respectively. The scaling law describes the experimental observations on ionization energy and charging energy reasonably well. When the size of clusters becomes extremely small (say less than 10–12 metal atoms), the clusters act like molecules with different energy level manifolds.

### 1.2.1 Synthesis of nanocrystal sols

Atoms are the most basic units of matter. They can be combined to form more complex structures such as molecules, crystals, and compounds. Fabrication, or the making, of nanomaterials falls into one of two categories: top-down or bottom-up.

Top-down methods rely on continuous breakup of bulk matter, while bottom-up methods build up nanomaterials from their constituent atoms. The top-down and bottom-up approaches can also be considered as physical and chemical methods, respectively. Varieties of hybrid methods have since come into being.

Many of the physical methods involve the evaporation of a solid material to form a supersaturated vapor from which homogenous nucleation of nanoparticles occurs. In these methods, the size of the particles is controlled by temporarily inactivating the source of evaporation, or by slowing the rate by introducing gas molecules to collide with the particles. The growth generally occurs rapidly, from milliseconds to seconds, requiring a precise control over experimental parameters. Several specialized techniques have been developed in the last few decades and they can be classified on the basis of the energy source and whether they make use of solid or liquid (vapor) precursors [16].

Chemical methods have emerged to be indispensable for synthesizing nanocrystals of various types of materials. These methods are generally carried out under mild conditions and are relatively straightforward. Nanodimensional materials in the form of embedded solids, liquids, and foams have also been prepared by chemical means and such materials have been in use for some time.

Nanocrystals of metals such as Au, Ag, Cu and Pt have been prepared by a variety of methods including thermal decomposition or controlled reduction of metal salts in constrained environments such as micelles and at the air-water interface [17, 18]. In particular tiny nanocrystals containing the magic number of 55 Au atoms have been obtained starting with Au(PPh<sub>3</sub>)Cl [19]. The use of the AOT-water-isooctane reverse micelles has proven to be a useful method to synthesize metal nanocrystals of controlled dimensions [20]. Duff et al. elucidated the role of partially hydrolyzed tetrakis(hydroxymethyl)phosphonium chloride (THPC) as a reducing agent in the preparation of Au nanocrystals [21, 22]. Cu nanocrystals in the form of hydrosols are prepared using hydrazine as a reducing agent [23]. High quality Ag nanocrystals have been prepared by thermal decomposition of fatty acids of Ag [24]. A popular method due to Brust et al. [25] involves the use of tetraoctylammonium bromide as a phase transfer agent to transfer Au<sup>3+</sup> ions from the aqueous medium to the organic medium prior to

reduction. Capping agents such as long-chain alkane thiols are usually added to stabilize the organosol. Previously in our lab it was found that metal nanocrystals are readily transferred from the aqueous to the organic layer, by first cleansing the nanocrystals and then capping them with long chain thiols. Au, Ag, Pt and Pd nanocrystals of diameters in the range of 2 - 8 nm could be transferred from the aqueous to the organic medium by this method [26].

There are several reviews in the literature focusing on the synthesis of nanocrystals. Any chemical reaction resulting in a sol consists of three steps - seeding, particle growth, and growth termination by capping. An important process that occurs during the growth of a colloid is Ostwald ripening. Ostwald ripening is a growth mechanism whereby smaller particles dissolve releasing monomers or ions for consumption by larger particles, the driving force being the lower solubility of larger particles. Ostwald ripening limits the ultimate size distribution obtainable to about 15% of the particle diameter when the growth occurs under equilibrium conditions. However, by employing high concentrations of the monomers and capping agents, growth can be forced to occur in a transient regime. The seeding, nucleation, and termination steps are often not separable and one, therefore, starts with a mixture of the nanocrystal constituents, capping agents, and the solvent. The relative rates of the steps can be altered by changing parameters such as concentrations and temperature.

This is a popular trick employed to obtain nanocrystals of different dimensions from the same reaction mixture. One of the important factors that determine the quality of a synthetic procedure is the monodispersity of the nanocrystals obtained. It is desirable to have nanocrystals of nearly the same size, in order to be able to relate the size and the property under study. Hence, narrower size distribution yields a more attractive synthetic procedure. The best synthetic schemes today produce nanocrystals with diameter distribution of around 5%. The other important issues are the choice of the capping agent and control over the shape. Sols produced by chemical means can either be in aqueous media (hydrosols) or in organic solvents (organosols). Organosols are sterically stabilized, while hydrosols can either be sterically or electrostatically stabilized. Steric stabilization of hydrosols can be brought about by the use of polymers as stabilizing agents.

Natural polymers such as starch and cellulose, synthetic polymers, such as polyvinyl pyrrolidone (PVP), polyvinyl alcohol (PVA), and polymethyl vinyl ether are used as stabilizing agents. Unlike textbook colloids such as India ink and dust in river beds, sterically stabilized sols are redispersible. The nanoparticulate matter in the sols can be precipitated by various means, filtered and dissolved again in a solvent. Redispersibility of the particles is an important characteristic of great utility. Furthermore, metal nanocrystals in a sterically stabilized sol can be dispersed in high concentrations. Generally, organic solvents provide better control over the size of the nanocrystals.

### **Metal nanocrystals by reduction**

Nanocrystal synthesis via chemical reduction is used most extensively in the liquid phase, including aqueous and nonaqueous media. As a rule, metal compounds are represented by their salts, while aluminohydrides, borohydrides, hypophosphites, formaldehyde, and salts of oxalic and tartaric acids serve as the reducers. The wide application of this method stems from its simplicity and availability.

In the general case, the behavior of a metal particle in solution is determined by the potential difference  $\Delta E = E - E_{\text{redox}}$ , where  $E$  is the equilibrium redox potential of particle and  $E_{\text{redox}}$  is the corresponding solution potential. Particles grow when  $\Delta E > 0$  and dissolve when  $\Delta E < 0$ . For  $\Delta E = 0$ , an unstable equilibrium is established. The situation is complicated by the fact that the redox potential of a metal particle depends on the number of atoms. In this respect, the chemical reduction occurs in systems thermodynamically and is kinetically unstable. Chemical reduction is a multifactor process. It depends on the choice of a redox pair and concentrations of its components as well as on the temperature, pH of the medium, and diffusion and sorption characteristics. Recently, the processes in which a reducer simultaneously performs the function of a stabilizer became widely used. Among such compounds are numerous N-S-containing surfactants, thiols, salts of nitrates, and polymers containing functional groups.

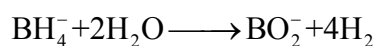
Reagents most frequently used as the reducers of metal ions are tetrahydroborates of alkali metals ( $\text{MBH}_4$ ), which operate in acidic, neutral, and

alkaline aqueous media. Alkali-metal tetraborates can reduce most cations of transition and heavy metals, which is explained by the high redox potential of  $\text{MBH}_4$  (1.24V in alkaline medium) as compared with the standard potentials of many metal ions, which lie in the interval  $-0.5 \leq -E \leq -1.0$  V. Reduction of metal ions was shown to involve the formation of complexes with bridge bonds  $\text{M}\dots\text{H}\dots\text{B}$ , which favors the subsequent hydrogen-atom transfer with the break of the bridge bond, followed by a redox process with the breakage of a B–H bond to give  $\text{BH}_3$ . The obtained borane undergoes hydrolysis and catalytic decomposition on the surface of metal particles.

Organic solvents are preferred for the preparation of nanocrystals. They perform stabilizing functions. Such solvents or surfactants play a key role in the synthesis of nanocrystals. They are bound to the surface of growing nanocrystals via polar groups, form complexes with species in solutions, and control their chemical reactivity and diffusion to the surface of a growing particle. All the mentioned processes depend on the temperature, the surface energy of a nanocrystal, concentration of free particles in solution and their sizes, and the surface-to-volume ratio of a particle. A variety of reducing agents are used to reduce soluble metal salts to obtain the corresponding metals. By terminating the growth with appropriate surfactants or ions, metal nanocrystals are produced.

### **Borohydride Reduction**

Borohydride reduction, known since the 1950s, was one of the subjects of investigation under the Manhattan project [27, 28]. The basic reaction involves the hydrolysis of the borohydride accompanied by the evolution of hydrogen.



Nanocrystals of a variety of metals have been made by borohydride reduction [29]. Thus, Pt nanocrystals with mean diameter 2.8 nm were prepared by the reduction of chloroplatinic acid with sodium borohydride [30]. Hirai and coworkers [31] made Cu sols by the borohydride reduction of Cu salts.

Schiffirin and coworkers [25] developed a two-phase method to reduce noble metals. This method, popularly known as the Brust method, has been widely used



to prepare organosols. In this method, aqueous metal ions are transferred to a toluene layer by the use of tetraoctylammonium bromide, a phase transfer catalyst which is also capable of acting as a stabilizing agent (see Figure 1.4). The Au complex transferred to toluene is reacted with alkanethiols to form polymeric thiolates. Aqueous borohydride is added to this mixture to bring about the reduction that is modulated by the interface of toluene and water. The thiol molecules also serve as capping agents. The capping action of the thiols is related to the formation of a crystalline monolayer on the metal particle surface Figure 1.5. When alkanethiols are used, the formation of Au nanocrystals and the appearance of a protective layer proceed in two stages.

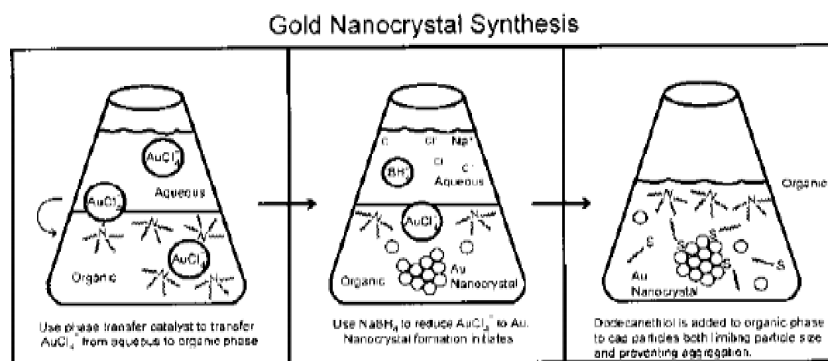


Figure 1.4 Schematic for Au nanocrystal synthesis using the two-phase reduction technique developed by Brust et al. [25].

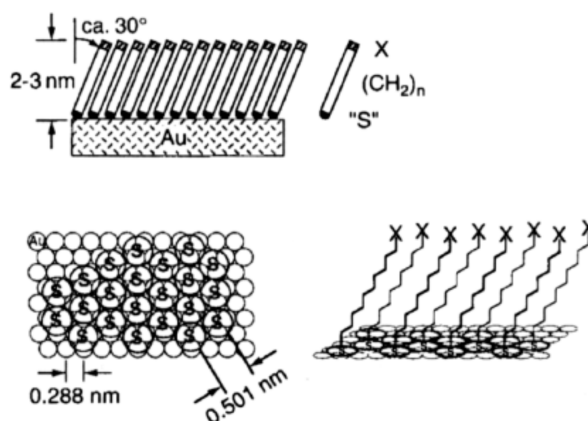
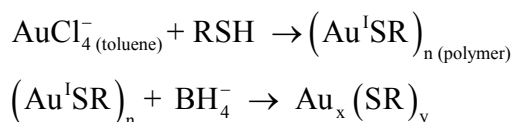


Figure 1.5 Crystallographic details of the thiol adsorption on the Au(111) surface [32].



These reactions combined the processes of nucleation and passivation. On average, an increase in the RSH–Au molar ratio and the acceleration of the reducing agent addition favored the formation of particles with smaller metal cores. A brief interruption of the reaction caused the formation of thicker coatings and very small cores (2 nm).

Since the formation of alkane thiol monolayers on Au was discovered by Nuzzo and Allara [32, 33], the interaction of thiols with Au has been exploited widely in nanoscience. The powerful capping action of alkanethiols at metal particle surfaces prompted Murray [34] to name these particles monolayer protected clusters (MPC). The length of the alkane chain and the concentration of borohydride affect the size of the nanocrystals obtained by the Brust method. This method has been successfully extended to prepare monolayer protected clusters of Ag and Pd as well [35-37].

### Citrate Reduction

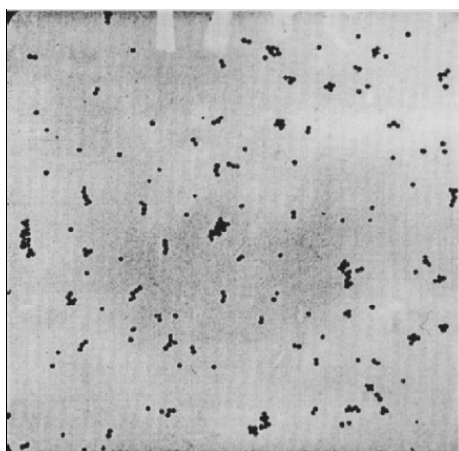


Figure 1.6 TEM image of Au nanocrystals synthesized by citrate reduction. The magnification is 50,000 [29].

The citrate route to colloidal Au, first described by Hauser and Lynn [38], is a popular method to prepare Au hydrosols. Synthesis by the citrate method involves the addition of chloroauric acid to a boiling solution of sodium citrate [29]. A wine red color indicates the onset of reduction. The average diameter of the nanocrystals can be varied over a range of 10–100 nm by varying the concentration ratio between chloroauric acid and sodium citrate (see Figure 1.6). Turkevich [39] proposed that the reaction involved the formation of acetone dicarboxylate.

Subsequent reduction occurs by the dicarboxylate species. The citrate method has been extended to synthesize Pt and Ag nanocrystals [40, 41]. Turkevich and coworkers [42] prepared Au–Pt bimetallic nanocrystals by reducing a mixture of chloroauric acid and chloroplatinic acid by citrate. By a similar procedure, Pd–Pt nanocrystals could also be prepared.

### **Alcohol Reduction**

The ability of small metal particles in catalyzing the oxidation of alcohols to aldehydes or acids has long been known in organic chemistry. The fine metal particles that catalyse these reactions get reduced during the course of the reaction and are deposited as spongy precipitates. This reaction is further catalyzed by a base and requires the presence of  $\alpha$ -hydrogen in the alcohol. The growth of metal particles can be arrested on using polymeric capping agents such as PVP [43-45]. The mechanism of the reaction involves the formation of an alkoxide, with an oxonium ion as the intermediate, followed by the formation of a carbonyl compound by hydride elimination. The base aids the deprotonation of the oxonium intermediate. A counter ion, such as the acetate, serves as an effective base. Otherwise, water is added, especially in the case of lower alcohols. Palladium acetate refluxed with ethanol in the presence of PVP yields Pd nanocrystals of 6.0 nm diameter [46, 47]. Organosols of Pd are formed by the reduction of Pd salts in 1-decanol. In this case, the alcohol also acts as the stabilizing agent [48]. In an elegant demonstration of size control, Teranishi and Miyake [49] have prepared monodisperse PVP covered Pd nanocrystals of various sizes in the 2–5nm range, by employing ethanol as the reducing agent and varying its power by diluting with water. Larger Pd nanocrystals have been prepared by employing the small nanocrystals as seeds in the reaction mixture. Nanocrystals of Ag, Au, Pd, and Cu have been prepared by ethyl alcohol reduction of metal salts under refluxing conditions in the presence of PVP [49, 50]. Other metal sols prepared by alcohol reduction include Pt, Au, and Rh [51]. Toshima and coworkers [52] have prepared PVP-capped Pd–Pt alloy nanocrystals by reducing a mixture of palladium chloride and chloroplatinic acid in a alcohol-water mixture. Ag-Pd and Cu-Pd alloy nanocrystals of a wide range of composition have been prepared by the alcohol reduction method [53].

### **Photochemical Synthesis**

Photochemical synthesis of nanocrystals is carried out by the light-induced decomposition of a metal complex or the reduction of a metal salt by photogenerated reducing agents such as solvated electrons. The former is called photolysis and the latter radiolysis. The formation of photographic images on a AgBr film is a familiar photolysis reaction. Henglein, Belloni, and their coworkers have pioneered the use of photolysis and radiolysis for the preparation of nanoscale metals [54]. Metals such as Cd and Tl have been obtained by photolysis. PVP-covered Au nanocrystals are produced by the reduction of H<sub>Au</sub>Cl<sub>4</sub> in formamide by UV-irradiation [55]. The reaction is free radical mediated, with the radicals being generated by photodegradation of formamide. This provides a route to ion-free reduction of H<sub>Au</sub>Cl<sub>4</sub>. Radiolysis of Ag salts in the presence of polyphosphates produces extremely small clusters that are stable in solution for several hours. Effective control can be exercised over the reduction process by controlling the radiation dosage.

### **Laser Synthesis**

The plume generated by a laser upon impacting a metal surface is known to consist of small atomic condensates. Cotton and coworkers [56] carried out early work in dispersing plumes in the form of nanocrystals in solution. In recent times, Kondow and coworkers [57-60] have developed this method to synthesize Au, Ag, and Pt nanocrystals. To prepare Au nanocrystals, an Au plate dipped in water containing sodium dodecyl sulfate (SDS) was irradiated with laser light of wavelength 1,064 nm. The size of the nanocrystals obtained depends on the laser fluence and surfactant concentration. Further modification of the initial distribution is possible by continued laser irradiation that causes fragmentation of the nanocrystals.

#### **1.2.2 Properties of individual nanocrystals**

The most striking optical property of a metal nanocrystal is its color. Metals such as Au and Ag exhibit characteristic absorption bands at 540 and 420 nm respectively, when the size of the nanocrystals is typically a few nanometers. The position of the band crucially depends on the size of nanocrystals [61], the

refractive index [62, 63] of ligand protecting nanocrystals, and the refractive index of the solvating medium [62], temperature [64, 65]. Unlike, optical properties, electrical properties of a nanocrystal are studied in isolation, by placing it between two electrodes either in a tunnel junction [66-68] or in break junction [69]. The factors that influence electrical measurements are a) the size of a nanocrystal [70], b) the nature of the ligand, c) electrode coupling, and d) temperature [71]. The electrical properties of a nanocrystal are related to its charging energy.

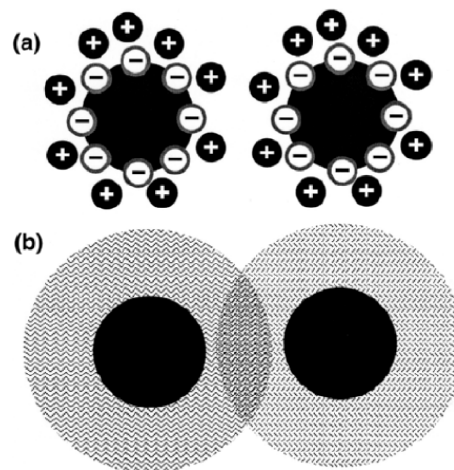


Figure 1.7 Schematic illustration of the factors lending stability to a colloidal dispersion: (a) an electric double layer and (b) loss of conformational freedom of chain-like ligands [2].

Nanocrystals of materials are generally obtainable as sols. Sols containing nanocrystals behave like classical colloids. For example, the stability of dispersion depends on the ionic strength of the medium. Nanocrystalline sols possess exceptional optical clarity. A key factor that lends stability to nanocrystal sols is the presence of a ligand shell, a layer of molecular species adsorbed on the surface of the particles. Without the ligand shell, the particles tend to aggregate to form bulk species that flocculate or settle down in the medium. Depending on the dispersion medium, the ligands lend stability to particles in two different ways. Thus, in an aqueous medium, coulomb interactions between charged ligand species provide a repulsive force to counter the attractive van der Waals force between the tiny grains, by forming an electrical double layer. In an organic medium, the loss of conformational freedom of the ligands and the apparent increase in solute concentration provide the necessary repulsive force (as illustrated in Figure 1.7). Nanocrystals dispersed in liquids are either charge-stabilized or sterically

stabilized. Nanocrystals devoid of ligands are generally studied in vacuum. Such particles deposited on a substrate are readily examined by photoelectron spectroscopy and other techniques. Beams of uniformly sized clusters traversing a vacuum chamber (cluster beams) with some fixed velocity provide opportunities for studies of the intrinsic physical properties of nanoparticulate matter.

### **Structural properties**

The dimensions of nanocrystals are so close to atomic dimensions that an unusually high fraction of the total atoms would be present on their surfaces. For example, a particle consisting of 13 atoms would have 12 atoms on the surface, regardless of the packing scheme followed. Such a particle has a surface more populated than the bulk. It is possible to estimate the fraction of atoms on the surface of the particle ( $P_s$ , percentage) using the simple relation,

$$P_s = 4N^{-1/3} \times 100, (1.2)$$

where  $N$  is the total number of atoms in the particle [72]. The variation of the surface fraction of atoms with the number of atoms is shown in Figure 1.8. We see that the fraction of surface atoms becomes less than 1% only when the total number of atoms is of the order of  $10^7$ , which for a typical metal would correspond to a particle diameter of 150 nm.

Nanocrystals are generally assumed spherical. However, an interesting interplay exists between the morphology and the packing arrangement, especially in small nanocrystals. If one were to assume that the nanocrystals strictly follow the bulk crystalline order, the most stable structure is arrived at by simply constraining the number of surface atoms. It is reasonable to assume that the overall polyhedral shape has some of the symmetry elements of the constituent lattice. Polyhedra such as the tetrahedron, the octahedron, and the cuboctahedron can be constructed following the packing scheme of a fcc lattice [73]. Figure 1.8 shows how a cuboctahedral cluster of 146 constituent atoms follows from a fcc type abcabc layer stacking. In contrast to the above, small clusters frequently adopt non-close packed icosahedral or dodecahedral shapes. The clusters adopting such schemes suffer a loss in packing efficiency. The icosahedron has five-fold symmetry, inconsistent with the packing requirements of a regular crystalline

lattice with long-range order. While employing close packing schemes, a stacking fault becomes necessary to arrive at an icosahedral arrangement. Such a scheme is outlined in Figure 1.9.

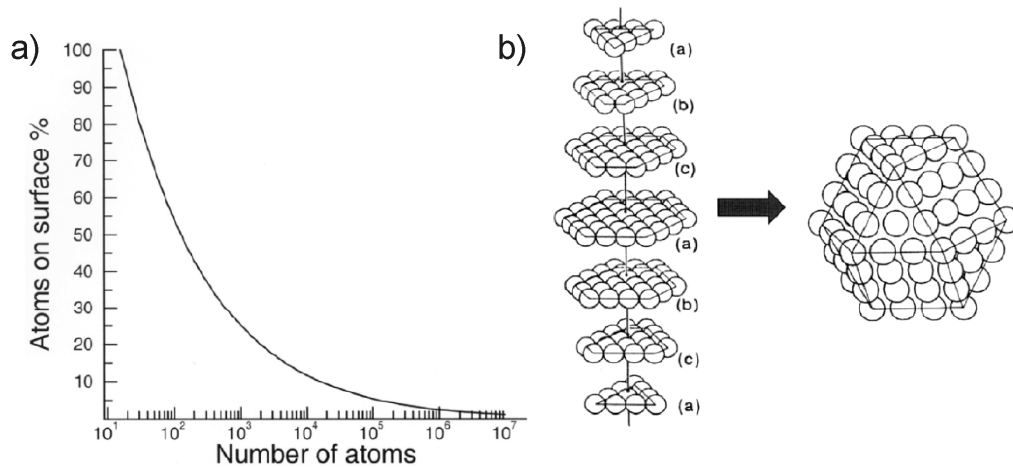


Figure 1.8 (a) Plot of the number of atoms vs. the percentage of atoms located on the surface of a particle. (b) Schematic illustration of how a cuboctahedral 147 atom-cluster, composed of seven close-packed layers can be made out of a stacking sequence reminiscent of a fcc lattice [16].

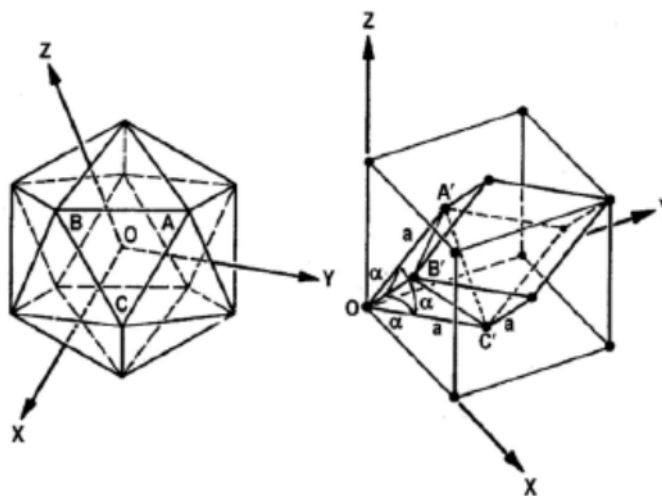


Figure 1.9 The regular icosahedron is made up of twenty irregular tetrahedra like OABX. The rhombohedral cell in a fcc lattice ( $OA'B'C'$ ) has  $\alpha = 60^\circ$ . When  $\alpha$  is distorted to  $63.43^\circ$ ,  $A'B'C'$  and OABC become similar. Small nanocrystals distort in a similar manner from regular fcc lattice to adopt the icosahedral shape [2].

The icosahedron that has twenty triangular faces and twelve vertices consists of a fcc-like close packing. Each of the twenty triangular faces of an icosahedron can be considered as a base of a tetrahedron, whose apex is at the inversion center

(see Figure 1.9a). A tetrahedron  $OA'B'C'$  in Figure 1.9b joining three face-centered atoms and an atom at the base of a fcc unit cell has the angle,  $\alpha = 60^\circ$ . These angles can be distorted to  $63.43^\circ$ , to obtain the tetrahedron (OABC) that forms the building block of an icosahedron. Such a distortion results in the lowering of the packing fraction from 0.74080 to 0.68818. Several theoretical investigations have sought to explain the unusual stability of icosahedral clusters [74]. Allpress and Sanders [75], based on potential energy calculations, showed that the binding energy per atom is lower than that in a corresponding octahedron containing the same number of atoms. Molecular dynamics simulations have shown that Al clusters with nuclearities upto 147 atoms exhibit distorted icosahedral structures while  $Al_{147}$  has a cuboctahedral shape [76]. Rigorous theories (ab initio, density functional) broadly support this contention. A decahedral shape can be thought of as being made up of four edge-sharing tetrahedra, followed by some relaxation and the consequent loss of packing fraction. Ino [77] has suggested the use of the term “multiply twinned particle” to denote a decahedral particle, and such particles obtained by the twining of tetrahedra.

The properties of nanocrystals are also influenced by the formation of geometric shells which occur at definite nuclearities [78]. Such nuclearities, called magic nuclearities endow a special stability to nanocrystals as can be demonstrated based on purely geometric arguments. A new shell of a particle emerges when the coordination sphere of an inner central atom or shell (forming the previous shell) is completely satisfied. The number of atoms or spheres required to complete successive coordination shells is a problem that mathematicians, starting with Kepler, have grappled with for a long time [79]. The “kissing” problem, as it is known in the mathematical world, was the subject of a famous argument between Newton and Gregory at Cambridge. In retrospect, Newton, who held that 12 atoms are required to complete the second shell was indeed correct. An idea of the mathematical effort involved can be gauged from the fact that the proof of Newton’s argument was provided only in 2002. It is quite apparent that the ultimate shape of the emerging crystallite should play a role in determining the number of atoms that go into forming complete shells. The magic nuclearities would then yield information on the morphology of the cluster. By a strange



coincidence, the number of atoms required to form complete shells in the two most common shapes (icosahedron and cuboctahedron) is the same.

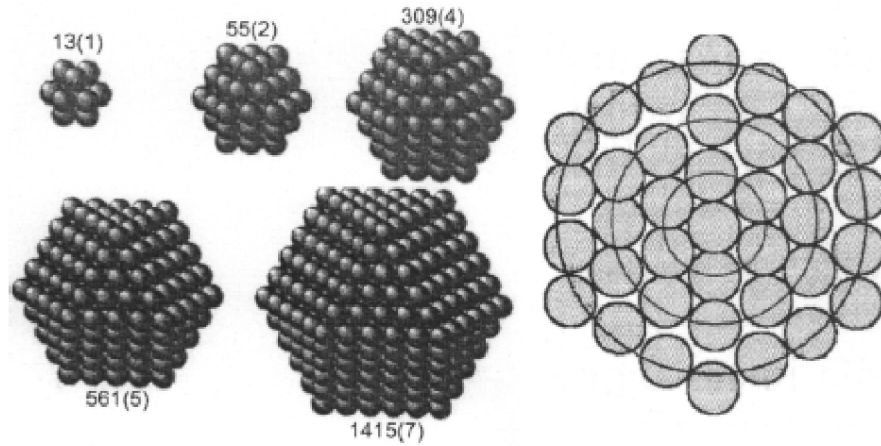


Figure 1.10 Nanocrystals in closed-shell configurations with magic number of atoms. The numbers beside correspond to the nuclearity (N) and the number of shells (L). The figure on the left is a cross-sectional view showing five coordination shells in a 561 atom cluster [2].

The number of atoms, N, required to form a cluster with L geometric shells is given by

$$N = \frac{(10L^3 + 15L^2 + 11L + 3)}{3} \quad (1.3)$$

This represents the solution for the “kissing” problem in three dimensions and is valid for icosahedral and cuboctahedral morphologies. For other shapes, the reader may refer to a paper from the group of Martin [80]. Particles possessing the above number of atoms are said to be in a closed-shell configuration. The number of atoms required to fill up coordination shell completely,  $n_L$  of a particular shell, is given by

$$n_L = (10n_{L-1}^2 + 2) \quad (1.4)$$

where  $n_0=1$ . Thus, 12 atoms are required to complete the first shell, 42 to complete the second shell etc. A schematic illustration of the observed magic nuclearity clusters is provided in Figure 1.10. The notion of the closed-shell configuration can be extended to larger dimensions as well. Closed-shell

configurations lend stability to giant clusters made of clusters and even to a cluster of giant clusters.

Determination of the structures of nanocrystals should ideally follow from X-ray diffraction, but small particles do not diffract well owing to their limited size. The peaks in the diffraction pattern are less intense and are broad. Structural studies are therefore based on high-resolution transmission electron microscopy (HRTEM), extended X-ray absorption fine structure (EXAFS), scanning tunneling microscopy (STM) and atomic force microscopy (AFM). X-ray diffraction patterns provide estimates of the diameters ( $D$ ) of nanocrystals from the width of the diffraction profiles, by the use of the Scherrer formula [81]

$$D = \frac{0.9\lambda}{\beta \cos \theta} \quad (1.5)$$

Here,  $\beta$  is the full-width at half-maximum of the broadened X-ray peak corrected for the instrumental width,

$$\beta = \beta_{observed}^2 - \beta_{instrumental}^2 \quad (1.6)$$

Estimates based on the Scherrer relation are used routinely. It is desirable to carry out a Reitveld analysis of the broad profiles of nanocrystals to obtain estimates of  $D$ .

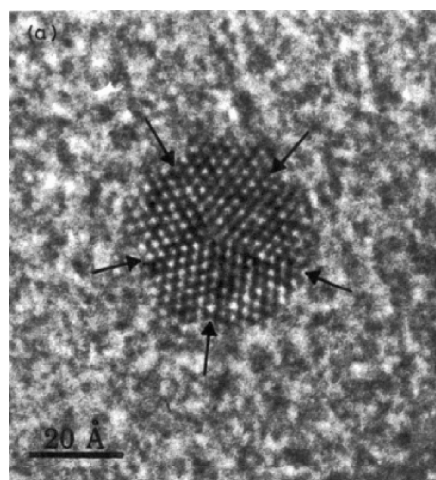


Figure 1.11 A high-resolution TEM image showing the icosahedral shape and the five fold symmetry axis of a Ag nanoparticle [31].

HRTEM with its ability to image atomic distributions in real space, is a popular and powerful method. The icosahedral structure of nanocrystals is directly observed by HRTEM and evidence for twinning (required to transform a crystalline arrangement to an icosahedron) is also obtained by this means (see Figure 1.11) [82]. The images are often compared with the simulated ones [83]. High resolution imaging provides compelling evidence for the presence of multiply twinned crystallites especially in the case of Au and Ag nanocrystals [84]. Characterization by electron microscopy also has certain problems. For example, the ligands are stripped from the clusters under the electron beam; the beam could also induce phase transitions and other dynamic events like quasi-melting and lattice reconstruction [85]. The fact that ligands desorb from clusters has made it impossible to follow the influence of the ligand shell on cluster packing.

STM, with its ability to resolve atoms, provides exciting opportunities to study the size and morphology of individual nanocrystals. In the case of ligated nanocrystals, the diameters obtained by STM include the thickness of the ligand shell [86]. Ultra high vacuum STM facilitates in situ studies of clusters deposited on a substrate. Furthermore, it is possible to manipulate individual nanoscale particles using STM. However, it is not possible to probe the internal structure of a nanocrystal, especially if it is covered with a ligand shell. AFM supplements STM and provides softer ways of imaging nanocrystals. EXAFS has advantages over the other techniques in providing an ensemble average, and is complimentary to HRTEM [87].

### **Optical Properties**

The optical absorption spectrum of nanocrystals of metals is dominated by the surface plasmon band that arises due to the collective coherent excitation of the free electrons within the conduction band [61, 88]. A schematic illustration of the electric field component of an incoming light wave inducing a polarization of the free or itinerant electrons is shown in Figure 1.12. It corresponds to the dipolar excitation mode, which is the most relevant for particles whose diameters are much less than the wavelength of light. However, higher order excitations are possible and come into play for nanocrystals with diameters in the range of tens of nanometers [89]. As mentioned earlier, the theory of optical absorption of small

particles was proposed by Mie in 1908 [11]. Mie's electrodynamic solution to the problem of light interacting with particles involved solving Maxwell's equations with appropriate boundary conditions and leads to a series of multipole oscillations for the extinction ( $C_{ext}$ ) and scattering ( $C_{sca}$ ) cross-sections of the nanocrystals. Thus

$$\begin{aligned}
 C_{ext} &= \frac{2\pi}{k^2} \sum_{n=1}^{\infty} (2n+1) \operatorname{Re}(a_n + b_n), \\
 C_{sca} &= \frac{2\pi}{|k|^2} \sum_{n=1}^{\infty} (2n+1) \operatorname{Re}(|a_n|^2 + |b_n|^2),
 \end{aligned} \tag{1.7}$$

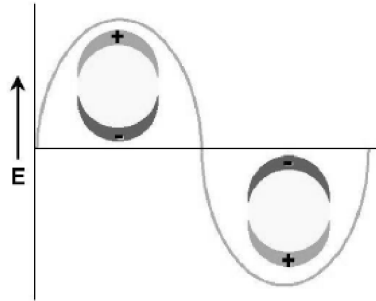


Figure 1.12 A schematic illustration of the excitation of the dipole surface plasmon oscillation by the electric field component of the light wave. The dipolar oscillation of the electrons has the same frequency as that of the incoming light wave.

Where  $\varepsilon_m$  is the dielectric constant of the surrounding medium,  $k = 2\pi\sqrt{\varepsilon_m}/\lambda$ ,  $a_n$  and  $b_n$  are Ricatti-Bessel functions that depend on the wavelength and the nanoparticle radius ( $R$ ). For small particles, the scattering term and the higher order extinction terms are negligible. The extinction coefficient is therefore, given by,

$$C_{ext} = \frac{24\pi^2 R^3 \varepsilon_m^{3/2}}{\lambda} \frac{\varepsilon_2}{(\varepsilon_1 + 2\varepsilon_m)^2 + \varepsilon_2^2} \tag{1.8}$$

where  $\varepsilon_1$  and  $\varepsilon_2$  are the real and imaginary part of the frequency-dependent dielectric constant,  $\varepsilon$ , of the substance. The dielectric constants can be obtained either from the Drude free electron model or from experiments [90]. The Drude model relates the dielectric constant to the bulk plasmon frequency,  $\omega_p$ , and the dampening frequency,  $\omega_d$ , which are given by

$$w_p = \frac{N_e e^2}{m_e^* \epsilon}, \quad (1.9)$$

$$w_d = \frac{V_f}{L}, \quad (1.10)$$

where  $N_e$  is the concentration of the free electrons,  $m_e^*$  the effective mass of the electron,  $V_f$  the velocity of the electrons at the Fermi level and  $L$ , the mean free path. Small particles with diameters comparable to the mean free path exhibit a diameter dependent  $L$ , given by,

$$\frac{1}{L_{\text{effective}}} = \frac{1}{2R} + \frac{1}{L}. \quad (1.11)$$

The origin of color lies in the denominator of (1.8) which predicts an absorbance maximum for a sol, when

$$\epsilon_1 = -2\epsilon_m. \quad (1.12)$$

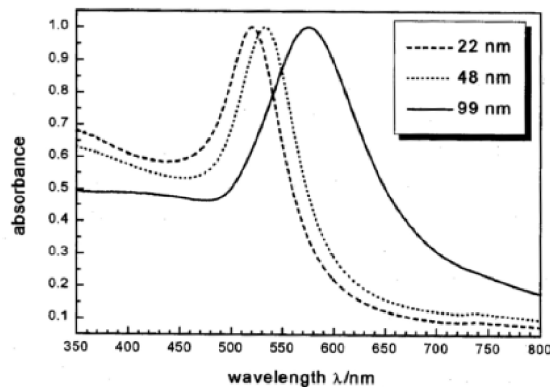


Figure 1.13 Optical absorption spectra of Au nanocrystals with diameters of 22, 48, and 99nm [61].

Thus, metal nanocrystals of various sizes exhibit characteristic colors depending on their diameters and the dielectric constant of the surrounding medium. Typical size-dependent changes in the optical spectra are shown in Figure 1.13. Mathematical methods have been developed to accurately compute the higher order terms in Mie’s theory [91]. Several off-the-shelf programs are available to apply Mie’s theory and its extensions to a variety of nanocrystals. One such code called “BHCOAT,” presented in the book by Bohren and Huffman [92] is very popular. The somewhat complicated nature of surface plasmon excitation and its

dependence on factors such as the distribution in particle diameters have thwarted attempts to derive fundamental physical quantities and to obtain quantitative information on the electronic structure of fine particles based on plasmon resonance spectroscopy. Initial studies such as those by Kreker and Kreibig [93, 94] have been instrumental in verifying the validity of Mie's theory for noble metal particles such as Au and Ag. Qualitative estimates however can be easily made based on the observed plasmon resonance band. Some of the features of plasmon bands and their dependence on the dielectric constant of the medium and the number of free electrons present in the nanocrystals find interesting uses. It is possible to probe events occurring in the vicinity of nanocrystals using the plasmon resonance band. There have been many experiments to demonstrate the high sensitivity of the plasmon band to small changes in the surrounding dielectric. Events that alter the surrounding dielectric such as binding of molecules and the solvent refractive index have been studied using plasmon resonance spectroscopy [62, 95]. Chemisorption of molecules on the surface of the nanocrystals alters the number of free electrons as well as the dielectric constant of the medium, thereby leading to striking changes in the plasmon band [88].

Mie theory is applicable for a system of non-interacting spheres. When nanoparticles are present in close proximity to each other, new collective properties emerge due to strong interaction among them. The optical absorption of such non-interacting nanoparticles can be very different from that of the interacting nanocrystals. More details on this subject are presented in the section on collective properties.

In the case of semiconductor and other particles, the number of free electrons is much smaller and the plasmon absorption band is shifted to the infrared region. The absorption of visible radiation by semiconductor nanocrystals is due to excitonic transitions. Much of our understanding of the absorption processes in semiconductor nanocrystals in the visible region stems from the work of Efros and Brus and coworker [96-98]. They propose a theory based on effective mass approximation to explain the size dependent changes in the absorption spectra of semiconducting nanocrystals. The absorption spectra can be understood by following the changes in the size of the nanocrystals in comparison to the exciton

diameter. It may be recalled that excitons are imaginary quasiparticles produced by pairing of an electron (from the conduction band) and a hole (from the valence band), due to Coulomb interaction. Excitons in semiconductors form hydrogen atom like states with diameters significantly larger than the unit cell length. The exciton diameter is,  $\alpha_b$ , given by,

$$\alpha_b = \frac{\hbar^2 \epsilon}{e^2} \left[ \frac{1}{m_e^*} + \frac{1}{m_h^*} \right], \quad (1.13)$$

where  $m_h^*$  is the effective mass of a hole. When the diameter of a nanocrystal,  $D$ , is much larger than  $\alpha_b$ , the absorption spectrum is similar to that of the bulk. However, when  $\alpha_b$  and  $D$  become closer, a sharp, size-dependent rise in the absorption onset accompanied by a blue-shift of the absorption maximum is seen. Thus, CdS, a yellow solid, exhibits an excitonic absorption around 600 nm, which gradually shifts into the UV region as the nanocrystal is decreased till a value below 10 nm. In contrast to metal nanocrystals, the absorption band can be varied over a wide range by changing the dimensions of semiconductor nanocrystals. The excitonic nature of the absorption band permits a direct correlation of the bandgap of the semiconductor nanocrystal with the absorption edge. It is possible to model key effects such as the surface structure and coupling of the electronic states and reproduce experimental observations [99, 100]. However, our understanding of optical properties is far from being complete. In addition to properties associated with optical absorption, semiconductor nanocrystals exhibit interesting luminescent behavior. The luminescence is generally dependent on the size of the nanocrystal and the surface structure [101]. Wide ranges of applications have been envisaged for luminescent nanocrystals.

### **Electronic properties**

Bulk metals possess a partially filled electronic band and their ability to conduct electrons is due to the availability of a continuum of energy levels above  $E_F$ , the fermi level. These levels can easily be populated by applying an electric field and the electrons now behave as delocalized Bloch waves ( $\lambda \sim 5\text{--}10 \text{ \AA}$ ) [72]. When a metal is divided finely, the continuum of the electronic states breaks down and the sample ultimately becomes insulating. The discreteness of energy levels

does not physically manifest itself as long as the gap is less than  $k_bT$ , the thermal energy at temperature  $T$ . The discreteness of the levels can be measured in terms of average spacing between the successive quantum levels,  $\delta$ , which is known as the Kubo gap [102]. Here,  $n_e$  is the number of valence electrons in the cluster (a contribution of one valence electron per constituent atom is assumed). In the case of semiconductors, a reduction in the size of the system causes the energy levels at the band edge to become discrete, with interlevel spacings similar to metals. This effectively increases the bandgap of the semiconductor [103]. The issues at hand are sketched schematically in Figure 1.14. Additional complications are introduced by the strong directional covalent bonds present in a semiconductor. Accompanying the appearance of the discrete levels are other consequences such as the change from metallic to van der Waals type of bonding, lowering of the melting point, odd–even effects, and perhaps most significantly, a metal–insulator transition. The whole gamut of such changes is generally referred to quantum size effect [104].

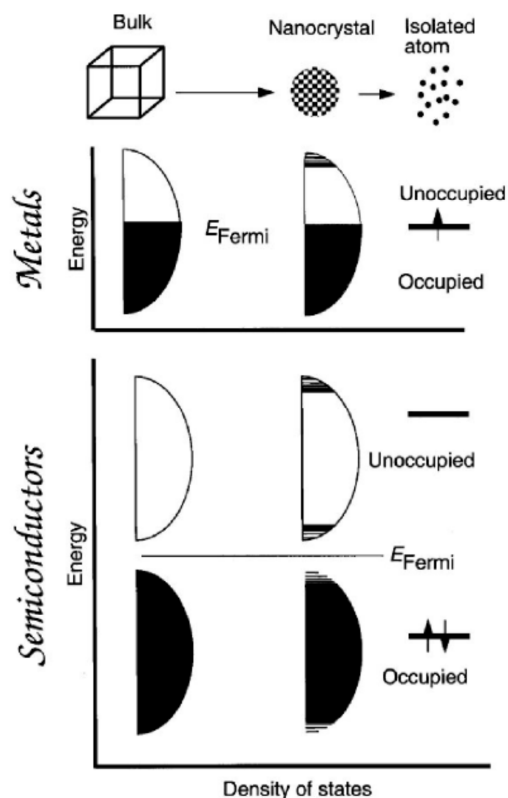


Figure 1.14 Schematic illustration of the changes in the electronic structure accompanying a reduction in size, in metals and semiconductors.



Another consideration required to describe the electronic structure of metal clusters is the emergence of electronic shells. The closure of electronic shells, similar to the closure of geometric shells, bequeath special stability to specific nuclearities and is manifest best in the variation of ionization energies with cluster nuclearity [80, 105]. The total number of electrons required to arrive at successive closed-shell configuration is 2, 10, 28, 60. . . The closed shell configuration is based on a hydrogen atom-like potential and hence the familiar 2, 8, 18, 32 pattern for the outer electron configuration to fill the electronic shells in the clusters. Other theoretical models predict different sets of closed-shell configurations. A unified picture of both geometric and electronic shells can be obtained by considering a characteristic length in closed-shell configurations [73, 80]. Unit increase in the characteristic length scale results in the closure of a shell. For geometric clusters, the characteristic length is the interatomic distance, while the characteristic length for electronic shells is related to the electron wavelength in the highest occupied level. In the case of alkali metal clusters, this wavelength is around twice the interatomic distance.

Electronic shell effects dominate the properties of alkali metal clusters. They are also broadly applicable to p-block metals. The properties of transition and noble metal nanocrystals, however, are influenced more by the formation of geometric shells. In fact, a transition from shells of electrons to shells of atoms is seen in the case of Al [80, 106]. It appears that the abundance of available oxidation states and the directional nature of the d- and f-orbitals (and to a limited extent, of the p-orbital) play a role in determining the shell, which governs the property of a particular cluster.

A host of physical techniques has been used to follow phenomena such as the closure of the bandgap and the emergence of the metallic state from the cluster regime. Photoelectron spectroscopy methods are among the most popular methods to study nanocrystals. Core level X-ray photoelectron spectroscopy (XPS) provides information on the oxidation state of the atoms. Changes in the electronic structure are manifested as binding energy shifts and through the broadening of photoemission bands. XPS is ideally suited to study changes in the electronic structure of clusters, accompanying the adsorption of gases. The density of states

around the fermi level can be probed by means of ultraviolet photoelectron spectroscopy (UPS), while Bremsstrahlung isochromat spectroscopy (BIS) provides information on the unoccupied levels. Direct information on the gap states in nanocrystals of metals and semiconductors is obtained by scanning tunneling spectroscopy (STS). This technique provides the desired sensitivity and spatial resolution making it possible to carry out tunneling spectroscopic measurements on individual particles. The various techniques and the region of the band structure probed by them are schematically illustrated in Figure 1.15.

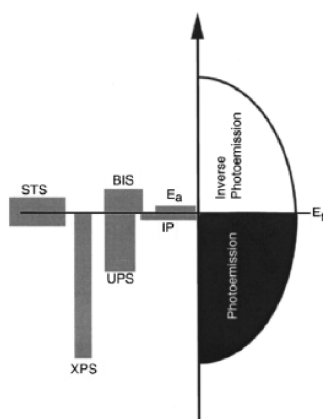


Figure 1.15 A schematic illustration of the spectroscopic techniques and the portion of the band structure that they probe. The techniques illustrated are ionization potential (IP) measurements, electron affinity measurements ( $E_a$ ), Bremsstrahlung isochromat spectroscopy (BIS), Ultraviolet photoelectron spectroscopy (UPS), X-ray photoelectron spectroscopy (XPS), Scanning tunneling spectroscopy (STS) [2].

### Nanocrystals (theoretical overview)

Nanoscale particles of metals and semiconductors have been subject to numerous theoretical investigations [107]. Theories have evolved in sophistication and rigor since the beginnings made by Kubo and Frölich. The electronic and geometric structure of noble metal clusters containing up to a few hundred atoms are studied using ab initio calculations. A few surprises have resulted from such investigations. For example, detailed calculations on anionic coinage metal clusters with seven atoms have indicated that while  $\text{Cu}_7^-$  and  $\text{Ag}_7^-$  have three-dimensional structures,  $\text{Au}_7^-$  is planar [108]. Planar structures are energetically favored for other Au nuclearities as well [109]. Ab initio molecular dynamics simulations have been carried out on clusters containing up to a few tens of atoms. For example,

Landman and coworkers [110] have carried out extensive computer simulations, on the structure and dynamics of alkanethiol-capped Au nanocrystals of different sizes. Numerous methods have been devised to study the properties of larger clusters often borrowing from theories used to model the bulk. Self-consistent Jellium model and local density approximation (a DFT based method) are popular for the study of metal clusters. The latter is also useful to investigate semiconductor nanocrystals. Tight-binding approximation based methods are used to study tetrahedrally coordinated semiconductors. Currently, experiments and theories go hand in hand in the study of small particles (~1 nm) and as the methods develop, it is not difficult to visualize a time in the near future, where the same can be said for investigations on larger nanocrystals.

In a bulk metal, the energies required to add or remove an electron are equivalent and are called the work function (W). In contrast, in the case of a molecule, the corresponding energies, electron affinity ( $E_a$ ) and ionization potential (IP) are nonequivalent [111]. The two energies differ to a smaller extent in a nanoparticle and are size-dependent.  $E_a$  and IP are given by

$$\begin{aligned} IP &= W + \frac{\alpha e^2}{R} \\ E_a &= W + \frac{\beta e^2}{R} \end{aligned} \quad (1.14)$$

with the constraint,  $\alpha + \beta = 1$

Here, R is the radius of the particle and  $\alpha$  and  $\beta$  are constants. The physical significance and the values of  $\alpha$  and  $\beta$  have been a subject of much debate. It appears that the value  $\alpha = 3/8$  is appropriate for alkali metal clusters while  $\alpha = 1/2$  agrees with the experimental results on noble metal particles [105, 112]. The difference in the two energies,  $E_a$  and IP, is the charging energy, U, given by,

$$U = IP - E_a = \frac{(\alpha - \beta) e^2}{R} \quad (1.15)$$

Typical values of U are of the order of a few hundred meV. It is to be noted that U is manifest as a Coulombic gap and is different from the electronic energy gap. It is possible to define differences between successive IPs and  $E_a$ s and arrive

at various states called the Coulombic states, defined by successive  $U_s$ . The Coulombic states are presumed to be similar for both semiconductor and metallic nanocrystals unlike the electronic states [113]. A quantity closely related to  $U$  that aids in a better understanding is the capacitance ( $C$ ) of a particle, which is given by

$$C = \frac{U}{2e} \quad (1.16)$$

The classical expression for the capacitance of a metal sphere embedded in a dielectric with a dielectric constant,  $\epsilon_m$  is

$$C = 4\pi\epsilon\epsilon_m R \quad (1.17)$$

Equations (1.16) and (1.17), agree with each other and yield capacitances of the order of  $10^{-18}$  F (or 1 aF) for nanocrystals. In this regime of finite charging energies and low capacitances, the charging of a capacitor is no longer continuous, but is discrete. For a current to flow through a nanocrystal, an external voltage  $V_{\text{ext}}$  greater than  $e/2C$  is required. This phenomena of current exclusion across zero bias is called Coulomb blockade. When the Coulomb blockade barrier is broken applying sufficient voltage, electrons tunnel into the nanocrystal and tunnel out almost immediately. The electrons may reside long enough to provide a voltage feedback preventing an additional electron from tunneling in simultaneously. A continuous one electron current,  $I$  given by

$$I = \frac{e}{2RC}, \quad (1.18)$$

flows through the circuit. To place an additional electron on the nanocrystal, a full  $e/C$  increase in voltage is required. Thus, steps called a Coulomb staircase become visible in the IV spectra of nanocrystals. A schematic illustration of a Coulomb staircase observed in the IV spectra is given in Figure 1.16. While Coulomb blockade is ordinarily observed, the observation of a Coulomb staircase requires a tuning of the circuit characteristics. The most significant impact of this discovery is in the realization of single electron devices at room temperature [18, 114-116]. Exploratory single electron devices, including single electron transistors, operable at room temperature have been realized by exploiting the low capacitance

of nanocrystals [18, 114, 115]. Single electron devices use the smallest possible charge to store information and hence are among the most efficient of known devices. It is indeed fascinating that the measurement of IP and Ea has led to such possibilities.

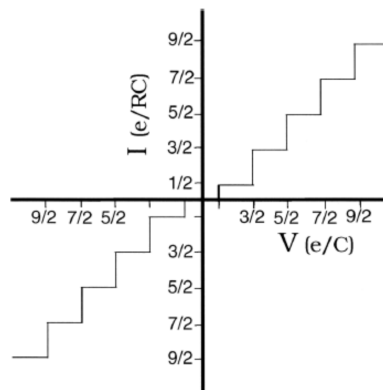


Figure 1.16 Schematic illustration of the Coulomb staircase behavior seen in the I-V spectra.

### Magnetic properties

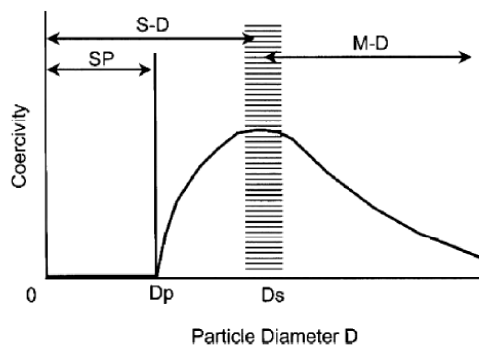


Figure 1.17 Schematic illustration of the change in the coercivity of a ferromagnetic particle with the diameter. SP denotes the superparamagnetic regime, S-D the single-domain regime and M-D the multi-domain regime.

Isolated atoms of most elements possess magnetic moments that can be arrived at on the basis of Hund's rules. In the bulk, however, only a few solids are magnetic. Nanoscale particles provide opportunities to study the evolution of magnetic properties from the atomic scale to the bulk. Even before the explosion of interest in nanoscience, magnetic properties of the so-called fine particles had been examined. In fact, size effects were perhaps first noticed in magnetic measurements on particles with diameters in the 10–100 nm range [117]. In order

to understand size-dependent magnetic properties, it is instructive to follow the changes in a magnetic substance as the particle size is decreased from a few microns to a few nanometers. In a ferromagnetic substance, the  $T_c$  decreases with decrease in size. This is true of all transition temperatures associated with long-range order. For example, ferroelectric transition temperatures also decrease with particle size. With the decrease in the diameter, the coercivity ( $H_c$ ), increases initially till a particular diameter,  $D_s$ , and thereafter decreases as shown in Figure 1.17. The critical diameter,  $D_s$ , marks a region wherein the particle changes from being a multi-domain particle to a single domain particle. The value of  $D_s$  is normally a few tens of nanometers. The single-domain nature of the nanoparticle is its single most attractive magnetic property. Below  $D_s$ ,  $H_c$  tends to decrease due to thermal effects and follows a relation of the form:

$$H_c = g - \frac{h}{D^{3/2}} \quad (1.19)$$

where  $g$  and  $h$  are constants [118]. Below the critical diameter  $D_p$ , coercivity becomes zero as the thermal energy would be sufficient to randomize the magnetic moments in the particle. Nanocrystals below the diameter  $D_p$  (~10 nm), exhibit such a behavior and are said to be superparamagnetic. Superparamagnetic particles do not possess long-range magnetic order, but show characteristic magnetic properties at low temperatures. Particles delineated on the basis of the above critical regimes, follow different paths to the final magnetized state and the magnetization reversal mechanism. These paths and mechanisms are rather complicated [118].

The superparamagnetic behavior was first modeled by Neel in the 1950s [119]. In the case of nanocrystals with uniaxial anisotropy, Neel's theory suggests that the temperature induced relaxation varies exponentially with temperature and scales with the sample volume. Besides the loss of coercivity, another characteristic feature of superparamagnetic behavior is the scaling of magnetization with temperature. A plot of the magnetization ( $M$ ) and the ratio of the magnetic field and the temperature ( $H/T$ ) produces a universal curve for all temperatures above  $T_b$ . Experimentally, superparamagnetism may be probed by techniques such as neutron scattering, Mössbauer spectroscopy and magnetization

measurements. Since superparamagnetic behavior is related to the relaxation rate, it is sensitive to the characteristic time scale of measurement. In the experimental techniques indicated above, the time scales of measurements vary over a wide range ( $10^{-14}$ – $10^{-12}$  for neutron scattering to around 10 s for magnetization measurement).

While reasonable progress has been made in understanding the magnetic properties of isolated particles, ensembles of particles represent a relatively poorly researched area [120]. A typical ensemble consists of particles with distributions in size, shape and easy anisotropy direction. Further, interparticle interactions play a role in determining the magnetic response of the ensemble. Theoretical investigations predict interesting phenomena in such assemblies, including changes in the mechanism of magnetization, depending on interparticle interactions. Experimentally, controlled interactions are brought about by varying parameters such as the volumetric packing density. Experiments have been carried out on ensembles of nanocrystals obtained in various ways such as freezing a sol containing a known fraction of magnetic nanocrystals or dilution in a polymer matrix [120, 121]. Seminal advances have been made in obtaining such ensembles by self-assembly based techniques. Self-assembled nanocrystalline ensembles possess several advantages over those obtained by other means.

### **Melting Point and Heat Capacity**

“Does the melting temperature of a small particle depend on its size?” asked Lord Kelvin as early as in 1871 [122]. The consensus in those days seemed to be that it would not be the case. An initial attempt was made to examine this issue by Pawlow in 1909 [123]. The first demonstration that the melting point was indeed different in small particles is due to Takagi [124], who established by means of electron microscopy that nanoscale particles of Pb, Sn, and Bi with sizes in the range of a few nanometers exhibited lower melting temperatures. Buffat et al. [125] carried out extensive studies on the melting points of Au nanocrystals by means of scanning electron diffraction technique and compared their results with previous findings. The change in the melting point can be quite dramatic, with lowering of as much as 600K in Au nanocrystals. It is supposed that the surface atoms are more susceptible to thermal displacement and initiate the melting

process due to the lower coordination. Such a surface melting process is thought to be the major cause for the lowering of melting points. Shi and others have developed theoretical models predicting a  $1/r$  dependence for the melting behavior of nanocrystals [126]. In the recent past, an entirely different melting behavior has been observed for much smaller particles of nuclearities less than 500. In addition to size-dependent melting points, size-dependent specific heats have been observed [127, 128]. At high temperatures, there is an increase in the specific heat of nanocrystals. For example, an enhancement of 29–53% is seen in the case of Pd nanocrystals of  $\sim 6$  nm diameter in the 150–300K range [129]. Similar but less dramatic enhancements have been seen in other metallic and semiconducting elements. There is no clear explanation for these observations. At temperatures near absolute zero, when the specific heat can be decomposed into lattice and electronic contributions, interesting effects are observed. The early work of Frölich [130] and Kubo [102] showed that the electronic contribution to specific heat is reduced up to two-thirds.

Bai et al. [131] have measured the changes in specific heat of thermally evaporated Fe particles of 40 nm diameter at low temperatures. An increase in specific heat was observed, but such a change was considered to be consistent with an increase in the lattice contribution and a decrease in the electronic contribution as predicted by Frölich. Such a decrease is observed in heat capacity measurements at very low temperatures on magic nuclearity Pd nanocrystals [132].

### **1.3 Array of nanocrystals**

In last decade, a lot of research has been done in synthesis of nanocrystals, improving their qualities in terms of size, shape and structure and in understanding their properties. Interestingly, group or arrays of these nanocrystals are considered to be a truly new class of materials, and the reason for such distinction is the emergence of a new class of properties in arrays of nanocrystals. Most properties of nanocrystals are governed by confinement of electrons in the nanocrystal. If individual particles are brought sufficiently close, electrons can tunnel between the particles and the tunneling strength decreases exponentially with distance. In simple words electron is not confined to just one nanocrystal. Thus the quantum



confinement properties of nanoscale particles crucially depend on the choice of the material, the size of each particle, temperature and the surrounding environment. Besides this, ordered arrays of nanoscale particles are expected to manifest novel electronic, magnetic, and optical properties because of cooperative interactions between the particles. These arrays are nothing but a lattice of nanocrystals, similar to the conventional lattice of atoms, where the basic building blocks are nanocrystals instead of atoms. The properties of nanocrystals not only depend on the chemical elements are used to form the building blocks, but also depend on the number of atoms in a block and the coupling of the blocks. Nanocrystal arrays can also be ordered or disordered, analogous to crystalline and amorphous materials. Ordered nanocrystal arrays are referred as nanocrystal superlattices. In principle, if bulk material is produced using nano material as building block one would expect more control over the structure and its properties and still expect new properties emerging out from these systems.

A typical array has three parameters that decide its stability and structure 1) nanocrystals (also main building material), 2) capping, (ligand and its nature) and 3) size and symmetry of organization

Nanoparticles and capping decide the material aspect of the array, whereas size and symmetry decide the design and structural aspect. Synthesis and properties of individual nanocrystals have already been discussed in the previous section. Though the choice of capping of nanocrystals is normally made at the beginning of the reaction, a few studies, such as that of Sarathy et al. [26] have demonstrated that capping can be modified at a later stage of the reaction as well.

### **1.3.1 1D array**

The mostly common approach to the preparation of one-dimensional assemblies of Nanocrystals is the use of a linear template. This is a versatile method for all kind of linear nanoparticles assemblies. Carbon nanotubes or semiconductor nanowires are probably the most rational structure-directing matrix for the preparation of one-dimensional nanocrystal assemblies. For instance, multiwall carbon nanotubes were used as templates for spontaneous assembly of Au on them, which subsequently merged into complex coaxial (albeit granular)

nanowires [133]. Among other templates, linear pores and channels inside polymers, alumina, and silica templates can be used to make linear agglomerates [134]. In addition to them, one-dimensional assemblies of metallic nanocrystal can be made at the edge of lattice plane terraces by chemical and electrochemical reduction of corresponding metal ions [135]. Hutchinson et al. [136] demonstrated that ditches of the corrugated carbon surface act as nucleation sites for the synthesis of aligned Au nanocrystals. Fort et al. [137] applied the same idea to the preparation of Ag nanocrystal chains in faceted grooves of alumina. Biomolecules, including DNAs, proteins, and sometimes even more complex structures, are rapidly becoming a very frequent template for one-dimensional nanocrystal assemblies. The possibility of self-assembly of very complex structures following the amino acid or peptide code is very attractive to many scientists. Among biotemplates, DNA is probably the most frequently used class of molecules owing to its strong electrostatic and coordination interaction with nanocrystals. Different kinds of nanocrystals, such as Ag [138, 139], Pd [140], Au [141-143], and Pt [144] have been organized by this technique. As such, Braun et al. [138] initially stretched DNA molecules between two Au electrodes with a separation of about 15  $\mu\text{m}$ . After that,  $\text{Ag}^+$  was ion exchanged and complexed with amino groups present on the surface of DNA. Further chemical reduction transformed  $\text{Ag}^+$  to Ag nanocrystals. After several cycles of ion exchange and reduction of Ag, one-dimensional Ag nanocrystal chains along the DNA molecular template were prepared. Fu et al. [145] obtained double-helical arrays by assembling Au and Pd nanocrystals peptide nanofibrils at different pH values.

Matsui and coworkers [146-149] have assembled Au nanocrystals onto the surface of polypeptide nanotubes, and their assembly position on the biomolecules could be controlled by specific affinity of polypeptide sequences. Munn and coworkers [150-152] have employed biotemplates of higher levels of complexity, such as the tobacco mosaic virus with a shape of a linear tube and assembled various kinds of nanocrystals inside or outside the tubes. Heterodimeric tubulin was used as a template to assemble Pd nanocrystals [153].

There is a growing realization in the research community that the templates may not be necessary for the nanocrystal to form one-dimensional structures at all

because under certain conditions they may self-assemble due to inherent anisotropy of nanocrystal–nanocrystal interactions. This statement refers not only to magnetic particles, for which chain formation and anisotropy was known a long time ago, but also to numerous nonmagnetic colloids in the absence of external fields. In one of the early experiments, Korgel and Fitzmaurice demonstrated that the prolate Ag nanocrystals self-assembled into nanowires during solvent evaporation [154]. Although, the process of formation of chain or nanowire may be driven by other interactions [155, 156]. It needs to be emphasized that a number of basic aspects of the spontaneous chaining of the nanocrystals are not clear. For instance, it is not understood to what extent the stabilizer needs to be removed to see the effect of the dipole moment. The nonuniform distribution of the stabilizer on the nanoscale surfaces can strongly affect any transformation of nanocrystals. There is a growing body of evidence that the conventional models of nanocrystals as spheres with uniformly distributed molecules of layers of organic ligands are not quite accurate [157]. At the same time, there is some evidence that intermolecular interactions of organic stabilizers between each other or with the nanocrystal surface can play a prominent role in the self-assembly process. For instance, the anisotropic interaction of Au nanocrystals and poly(vinyl pyrrolidone) in Langmuir–Blodgett films was suspected to be the reason for chain formation by Reuter et al. [158], which was morphologically exceptionally similar to that observed by Tang et al. [159]. Thus, it is expected that the interplay between the nanocrystal–nanocrystal forces originating in the stabilizer layer, as well as in the nanocrystal core, can be an interesting area of research for the next few years. The understanding of this interplay can yield many unique nanocrystal systems.

### **1.3.2 2D array**

#### **Scanning probe based techniques**

Lot of research work has been done in preparations of nanocrystal with 2-D assemblies and several methods have gain popularity. One methods of is STM/AFM manipulation of individual colloidal particles, as was demonstrated by various research groups [160-163]. Superstructures of a one- and three-dimensional nature can also be made in this way. A simple implementation of this approach is pushing nanocrystals along the surface to create two-dimensional

patterns made from cleared areas [163]. More complex nanomanipulation systems with rotation and translation of a linked two-particle structure from 5- and 15-nm Au nanocrystals, and literal building of nanoscale pyramids resting on the silanized surface of the silicon wafer and on mica, were also reported [164, 165]. SPM also affords in situ synthesis of nanocrystals in a selected area of the surface when particles are made by tip-induced (predominantly electrochemical) reactions [161, 166-168]. Yamashita et al. has employed ferritin molecules for fabrication of 2-D array of nanoparticles [169]. The same family of methods of nanocrystal organization also includes surface probe lithography, which is often realized as area-selective modification of a prospective substrate by tip-induced chemical reactions of the surface [170, 171] or charge injection [172]. Sugimura and Nakagiri [173] demonstrated that an organosilane monolayer on a silicon wafer could be locally degraded through electrochemical decomposition of adsorbed water at the junction of the monolayer and the SPM probe. Then the probe-scanned region reacted with another organosilane, resulting in high-contrast patterns. The latter selectively adsorbed nanocrystals or proteins [173]. A similar approach can be used for the modification of thiol coatings on the substrates [174]. After the tip-induced reaction of thiol replacement with dissolved R-SH compound with specific affinity to Au, noble metal nanocrystals were adsorbed on the new surface-bound functionalities. This method yielded line widths of ca. 10-nm resolution and complex bottom-up nanostructures suitable for SET devices. Nonelectrochemical surface modification of adsorption layers was realized by Blackledge et al. [175] through selective surface modification by a catalytically active SPM tip with a layer of palladium. It induced chemical reactions in a terminal azide and carbamate functional groups of organosiloxane. The minimum measured line widths of 33 nm were reported for Au nanocrystals subsequently adsorbed to the thiolic pattern [175]. Forty-nanometer spacing was observed for a similar SPM tip nanochemistry procedure involving chlorosilanes [176].

One of the recent SPM methods of patterning is dip-pen lithography, initiated by the group of Mirkin and coworkers [177, 178]. In our laboratory, John et al. [179] have used colloidal sol of various inorganic nanoparticles as direct ink for writing. The two-dimensional maps of thiols can be used to assist adsorption of nanocrystals in specific areas. Demers et al. [180] functionalized thiols with

oligonucleotides and observed selective adsorption of Au colloids 13 to 30 nm in diameter bearing complementary DNA strands.

### **Lithographic techniques**

Two-dimensional patterns of nanocrystal can also be created by a large variety of other lithographic techniques. One of the more popular approaches is microcontact printing, which makes possible 50- to 60-nm features. This level of spatial resolution was reproduced by several groups with both metal and semiconductor nanocrystals [181-183]. Qin et al. [184] reported the record small spacing in nanocrystal arrays of 20 nm made by microcontact printing. Typically, the patterned surfaces are exposed to dispersions of nanocolloids, which selectively adsorb on areas with appropriate chemical functionalities. The use of premade nanocrystal solutions affords better size uniformity; however, the in situ synthesis provides additional orientation of the crystal lattice [185].

The traditional lithography with photo- or electron beam-active resists is also widely used to create patterns on which nanocrystals or other nanocolloids are subsequently adsorbed in the form of a monolayer [186]. The feasibility for the bottom-up fabrication and spatial fixation of some of the key components of future nanoscale electronic circuits of metal nanocrystals and metal nanowires connected to addressable contact electrodes was demonstrated [170]. Vossmeier et al. [187] developed a special photoresist based on nitroveratryloxycarbonyl glycine to render the substrate photosensitive. Irradiation with 340 nm of light through a microchip mask yielded a pattern of free and protected amino groups. 12-aminododecanecapped Au particles were found to selectively bind to the surface amino groups. Importantly, the original pattern can be amplified by repeated treatment with 1,8-octanedithiol and Au nanocrystal adsorption, similar to the layer-by-layer technology, to make the pattern readily visible with the naked eye. Amplification of the pattern in the third dimension can also be achieved with a high degree of selectivity by LBL assembly [188]. Among all methods most versatile, easy and simple process of generating array of nanocrystals is self-assembly. Despite the simplicity, some of the best-organized two-dimensional superstructures were produced by this method.

## Self-assembly

The geometry of the two-dimensional patterns may be self-defined rather than predetermined by a stamp or a lithographic mask, i.e., two-dimensional self-assembly. Spontaneous organization of matter into hierarchical ordered structures is ubiquitous in nature [189, 190]. From a single strand of DNA in a biological cell to a colony of king penguins on an Antarctic island, self-assembled structures exist not only on molecular level, but also on a macroscopic length scale. Under a strict definition, self-assembly is a process whereby large quantities of pre-existing components undergo spontaneous organization to form larger structures driven by internal interactions or external constraints. The assembled structures may retain the properties of their constituent building blocks, but more importantly, can demonstrate new collective phenomena due to the interactions between their components. Under this definition, crystallization of atoms driven by the formation of covalent or ionic bonds is a self-assembling process. However, it is the self-assembly process driven by noncovalent interaction that has attracted much more attention lately. This is largely because the energy associated with noncovalent bonds is comparable to thermal energy. Thus, a slight variation of interaction or temperature can drive the same system into vastly different structures. This is partly responsible for the existing complexity of nature. Understanding the mechanism for self-assembly is not only of fundamental interest, but may also lead to many technological applications. A large number of self-assembled structures exist in biological systems.

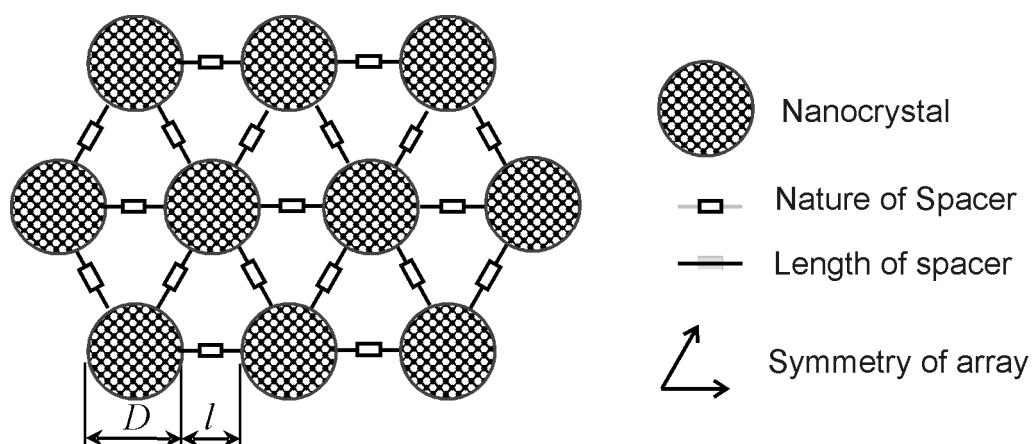


Figure 1.18 Typical 2-D array and its components.

One of the early examples of this technique is the organization of nanocrystals by the forces during solvent evaporation [191] and other interfacial solid–liquid interactions at the nanoscale level. Ordered nanocrystal mono- and multilayers in a closely packed arrangement were produced from a nanocolloid suspension upon the solvent evaporation [192-194] or adsorption of nanocrystals on electrically charged substrates [195, 196] provided that the nanocrystals were highly monodisperse. The ordered domains can cover relatively large areas in the micron scale. For less uniform particles and somewhat lower concentrations of nanocrystal, the drying dispersion can produce circular patterns [197]. Their deliberate modulation of the fluid dynamics can make nanocrystals assemble in surprisingly highly ordered layers [198] and networks [199], even for fairly polydispersed colloids. A complex interplay of wetting dynamics, capillary forces, and interface instabilities, and the spontaneous formation of complex patterns, are involved in their formation [191, 200]. The numerical simulations on the basis of linear stability analysis of the nanoscale liquid dynamics which revealed the dependence of particle distribution on equilibrium film separation distance, initial packing concentration, rate of evaporation, and nanocrystal surface activity [191].

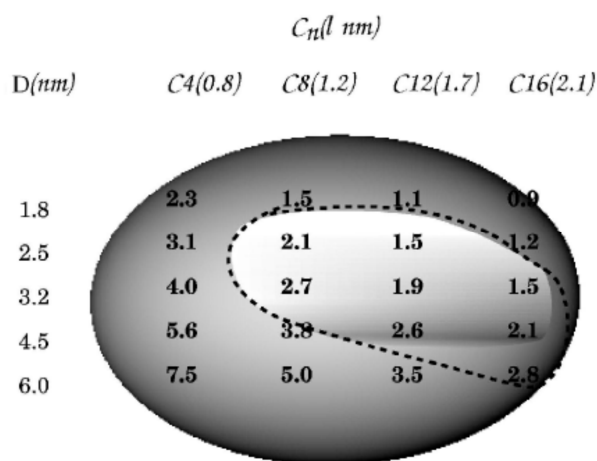


Figure 1.19 The  $D$ – $l$  phase diagram for Pd nanocrystals capped with different alkanethiols. The mean diameter,  $D$ , was obtained from the TEM measurements on as prepared sols. The length of the thiol,  $l$ , is estimated by assuming an all-trans conformation of the alkane chain. The thiol is indicated by the number of carbon atoms,  $C_n$ . The bright area in the middle encompasses systems that form close-packed organizations of nanocrystals. The surrounding darker area includes disordered or low-order arrangements of nanocrystals. The area enclosed by the dashed line is derived from calculations from the soft sphere model [201].

The cooperative assembly of nanocrystals described previously was mainly driven by entropy, the factors playing a key role in deciding the nature of organization being the nanocrystal diameter ( $D$ ) and the ligand chain length ( $l$ ). It is observed that for a given diameter of a nanocrystal, the packing changes swiftly as the length of the thiol ligand is varied. Based on a study of the organization of Pd nanocrystals of diameters in the range of 1.8–6.0nm with alkane thiols of various chain lengths, a phase diagram in terms of  $D$  and  $l$ , shown in Figure 1.19, has been derived [201]. In Figure 1.19, the intensity of grey shade is representative of the disorder in nanocrystalline organization. The light area corresponds to ordered arrays and the dark area to disordered arrangements. Although entropy driven, the organization is treated as being due to soft spheres rather than hard spheres.

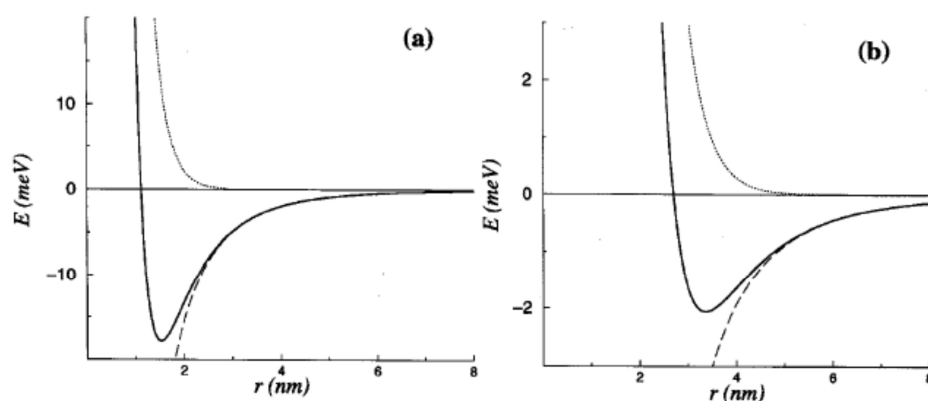


Figure 1.20 Variation of the attractive and repulsive components and the total potential energy with the separation distance between two Pd nanocrystals of 4.5nm diameter coated with (a) octanethiol and (b) dodecanethiol [201].

Korgel et al. [36, 202] observed that changing the nature of the solvent used in the evaporation step results in dramatic changes in the arrays obtained. When toluene was used as the solvent, extended two-dimensional arrays made of a single layer of nanocrystal were obtained. With the addition of increasing amounts of ethanol to toluene, the nanocrystals exhibited an increasing affinity to form multilayered structures with one nanocrystal collapsing on another. To account for these observations, Korgel et al. proposed a soft sphere model considering the interparticle interaction. Accordingly, a ligated nanocrystal allows for penetration of each other's ligand shell up to a certain extent. In this model, the total potential



energy,  $E$ , between a pair of nanocrystals, is considered to be a result of two types of forces between the nanocrystals,

$$E = E_{\text{steric}} + E_{\text{vdW}} \quad (1.20)$$

van der Waals interaction due to the polarization of the metal cores constitutes the attractive term ( $E_{\text{vdW}}$ ) and the steric interaction between the thiol molecules on the two surfaces forms the repulsive term ( $E_{\text{steric}}$ )

$$E_{\text{vdW}} = \frac{A}{12} \left\{ \frac{D^2}{\tau^2 - D^2} + \frac{D^2}{\tau^2} + 2 \ln \left[ \frac{\tau^2 - D^2}{\tau^2} \right] \right\} \quad (1.21)$$

$$E_{\text{steric}} = \frac{50D\ell^2}{(\tau - D)\pi\sigma_a^3} kT e^{-\pi(\tau - D)} \quad (1.22)$$

where,  $\tau$  is the interparticle distance,  $A$  the Hamaker constant,  $\sigma_a$ , the footprint or area occupied by the thiol molecule on the nanocrystal surface. In the case of Pd nanocrystals coated with alkane thiols in toluene, it was found that the total energy is attractive over a range of interparticle distances, the magnitude increasing with fall in distance (see Figure 1.20). The lowest points in the total energy curve refer to the maximum stabilization energy achievable for a given set of  $D$  and  $l$  values. In the case of Pd nanocrystals with  $D = 4.5$  nm, stabilization energies of 17 and 2 meV are obtained for particles coated with octanethiol and dodecanethiol, respectively. When the stabilization energies have moderate values, comparable to the thermal energy, ordered organizations are to be expected. If the stabilization energy is not favorable, collapsed monolayers of nanocrystals or loosely packed structures would be seen. The favorable regime is the area encircled by a dashed line in the phase diagram in Figure 1.19. A reasonable degree of correspondence is seen between the model and the experimental observations. Clearly, the interdigitation of thiol molecules plays a major role in attributing hardness to the ligated nanocrystal, which in turn decides the nature of the two-dimensional organization. This treatment is easily extendable to other metal and semiconductor nanocrystals. The observation of two-dimensional arrays with nanocrystals of different diameters clearly poses a challenge to this notion (see Figure 1.21). The prototypical AB and AB<sub>5</sub> types of lattices found in these arrays are traditionally

associated with the packing of hard spheres.

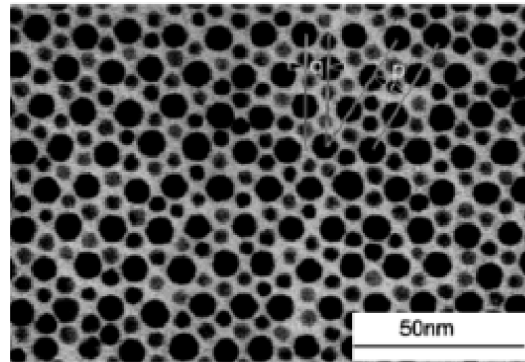


Figure 1.21 TEM images of an array of Au nanocrystals with the AB structure. The radius ratio of the nanocrystals is 0.58 [598].

Bigioni et al. [203] have used video microscopy to study the process of assembly of Au nanocrystals into extended two-dimensional arrays. They suggest that the morphology of the drop-deposited nanocrystal films is controlled by evaporation kinetics and particle interactions with the liquid–air interface. In the presence of an attractive particle–interface interaction, rapid early-stage evaporation dynamically produces a two-dimensional solution of nanocrystals at the liquid–air interface, from which nanocrystal islands nucleate and grow upon further evaporation.

The driving forces for self-assembly of nanocrystals in solution and on surfaces have been extensively studied in a variety of systems [202, 204–208]. The mechanisms are, however, quite complicated, depending on the specific materials, the size and shape of the particles, the charges on their surfaces, and on the physical environment during the self-assembly process. They can be roughly categorized into the following types.

Entropy-driven systems: Colloidal particles with strong repulsive interaction can crystallize when the concentration of particles exceeds a critical limit [204, 205, 208]. This is because the entropy gain associated with local motions around the regular lattice point compared with motion around random sites is sufficient to compensate the entropy loss arising from long-range ordering. In some cases, the structure of colloidal crystals grown from the surface can also be controlled by prefabricated patterns on the surface [207].

Attraction-driven systems: For neutral, uncharged particles of sufficiently large size, van der Waals interaction can be strong enough to induce aggregation. At large distance, the attraction force varies as  $-AR^6/D^6$ , where A is the Hamaker constant, R is the particle radius, and D is the interparticle distance. At small distance, the functional form changes into  $-AR/D$  [202, 206, 209]. If the attraction force is the only force that acts upon the particles or it is significantly stronger than any other interaction that is present, it will cause irreversible, diffusion-limited aggregation. Ligand coating on nanocrystal surfaces can act as a “bumper” or buffer layer to prevent such irreversibility. Diffusion of nanocrystals under the influence of the attractive force can lead to formation of large ordered arrays [210, 211]. Temperature also plays an important role to anneal out some defect sites during the self-assembly process. For a pair of 6-nm Au particles separated by a gap of 1.7 nm (dodecanethiol chain length), a simple calculation shows that the interparticle van der Waals force is roughly 46 meV, which is comparable to the thermal energy at room temperature.

Other physically driven systems: Assembly of micron spheres and nanocrystals can also be accomplished by electrophoretic deposition [212, 213]. The assembly of particles on the electrode surface is a result of electrohydrodynamic fluid flow arising from an ionic current flowing through the solution. By adjusting the electric field strength or frequency, the lateral attraction force between particles can be modulated. This facilitates the reversible formation of two dimensional fluid and crystalline states on the surface.

According to a different point of view, self-assembly is mediated via repulsion force. Self-assembly may be viewed as pushing or cornering of one type of particles through repulsive action.

Water-oil mixture is a part of most self-assembly processes as the mixture of these two immiscible liquids provides a favorable medium for self-assembly. In the case where there is very little water in oil, the oil will push the scattered water molecules and cause them to aggregate. In such a case, repulsion is the driving force for the assembly of particles and not the attraction between those particles. Researchers have introduced surfactant in such systems to study and modify the

type of self-assembly. We also studied a system where oil-water and surfactant coexisted and obtained many interesting nano structures and assemblies.

Also, highly ordered two-dimensional arrays of magnetic particles were obtained by the evaporation of aqueous solutions on octadecyltrichlorosilane-stamped surfaces [214]. The droplets of water containing metal salts prefer the hydrophilic surface of untreated silica and are confined by surface forces. The metal salt residue can be subsequently transformed into ferrites or other compounds. The resolution of 70 to 460 nm in X and Y of these arrays enables addressing each magnetic island as an individual memory cell. A similar result can be achieved by so-called nanosphere lithography, when a mono or multilayer of uniform latex spheres serves as a mask through which a metal can be plated on the surface [215].

A two-dimensional organization method related to fluid dynamics is the assembly of nanocrystal on surfaces of copolymers, which form intricate surface patterns due to nanoscale phase separation of the polymer blocks with hydrophilic/hydrophobic balance. Being cast from organic solution, nanocrystals adsorb preferentially on the low-surface-tension areas and often form aggregates with pronounced fractal dimensionality [216].

### **Langmuir-Blodgett technique or Air water**

Two-dimensional layers of nanocrystals with some degree of short range order can be obtained by using the air–water interface as a template [217]. Application of surface pressure helps to improve the quality of the monolayer as well as facilitates transfer of the film to a substrate. Such studies are typically carried out using a Langmuir–Blodgett trough, which combines the advantages of the self-organization of nanocrystals and operator-controlled pattern organization. It has a very well established reputation for nanoscale organic films and was extended to nanocrystal systems in 1994 by Kotov et al. [218] and Dabbousi et al. [219]. It remains one of the most popular approaches to the preparation of remarkable two-dimensional superstructures with potential practical applications in nanoscale electronics [113, 218, 219]. Additionally, the Langmuir–Blodgett technique also affords the preparation of 1-D [158] and 3-D [220] systems. Unlike many of the

techniques, it provides the ability to control the distance between individual nanocrystals in two-dimensional monolayers [221]. Collier et al. [222] demonstrated the transition from insulator to metal state as the distance between Ag nanocrystals decreases. Surface pressure–volume isotherms have been obtained with metal [223, 224] nanocrystals coated with hydrophobic ligands. Thiol-capped Au nanocrystals are reported to organize in the form of polydisperse opals at the air–water interface [223]. Two dimensional assemblies of Au nanocrystals have been obtained using tetrapyridylporphine molecules [225], Free-standing films of Au has been obtained using polymers containing amine functionalities such as polyethyleneimine or poly-L-lysine [226]. However, insufficient mechanical strength and susceptibility to environmental effects resulted in a significant decrease of interest in Langmuir–Blodgett two-dimensional assemblies of nanocrystals after initial enthusiasm. Although in many cases this concern is justified, there are a number of ways to make fairly robust Langmuir–Blodgett films [227, 228] that can be further improved with inclusion of nanocolloids [229]. Nevertheless, a number of interesting prototype devices have been demonstrated on their basis, such as memory structures [230, 231], SET electronics [220, 232], nonlinear optical elements and sensors [220]. The spectrum of applications is identical to other thin films from nanocolloids because the charge transfer in Langmuir–Blodgett films of nanocrystals, as well as other properties, follow the same regularities as for other nanocrystal assemblies.

Somewhat similar self-organization of 90-nm triangular prisms from Ag in two dimensional sheets was also observed by Chang et al. [233]. The crystal lattices in the Ag platelets in the superstructure were aligned, producing an intricately interconnected network.

### **Biological techniques**

Self-assembly of nanocrystals in organized two-dimensional systems can also be facilitated by proteins and other biomolecules. Considering the popularity of other combinations of biotechnology and nanotechnology (discussed above), the recent appearance of multiple studies in this area becomes quite logical. Willner and Willner consider the nanocrystal–biomolecule systems as one of the most promising techniques for programmed assemblies of nanostructures [234]. This

notion is substantiated by the record performance of nanocrystal-based detection and imaging procedures, which can significantly advance the life science experimental methods [235]. Neat Au nanocrystals as well as other nanocrystals of various sizes have been organized into two-dimensional lattices using a protein (chaperonin) template [236].

The biological support can be patterned by one of the lithographic methods, such as traditional photolithography [237], dip-pen lithography [238], or microcontact printing [239]. After that, the nanocrystal dispersions can be used as ink with specific adhesion to biomolecular surfaces. Several groups utilized the ability of proteins to self-organize in two-dimensional lattices.

One of the best examples of such superstructures is proteins from bacterial surface layers, i.e., S-layers, recrystallizing *in vitro* into sheets and tube-shaped protein crystals with typical dimensions in the micrometer range [240]. The periodic solvent-exposed thiols within chaperonin templates were used to size selectively bind and organize either Au (1.4, 5, or 10 nm) or CdSe-ZnS semiconductor (4.5 nm) quantum dots into arrays. The lattices with pronounced alignment motifs in nanocrystal can be made from viral proteins [241].

### **1.3.3 3D array**

Three-dimensional assemblies of nanocrystals are less common and widespread than two-dimensional superstructures. Additionally, the level of their three-dimensional organization is not as sophisticated as for the planar arrangements. Moreover, some of them can be considered derivatives of the two-dimensional systems. For instance, electron beam and photolithography can be used to create some three-dimensional nanocrystal elements with limited complexity, inducing growth of nanocrystal islands in certain areas [242, 243]. Other two-dimensional lithographic patterns transcending into three dimensional include selective decoration of one hemisphere of colloidal particles with Au nanocrystals and nanowires [244, 245]. SPM manipulation can also be expanded in another dimension: pyramidal structures were built up by pushing an nanocrystal on top of two others [165]. Overall, the current three-dimensional nanocrystal assemblies can be classified into structures that are organized by three-dimensional

supports, self-assembled systems, and stratified layers. All of them have limitations of three-dimensional organization imposed by the particular method, and none of them can be used to create a freehand three-dimensional nanostructure by design.

### **Templeted 3D structures**

Similar to one-dimensional and two-dimensional systems, the three-dimensional nanocrystal superstructures can be formed by adsorption on solid surfaces exhibiting three-dimensional organization. Much work in this area has been done for nanocrystal adsorption on colloidal crystals (synthetic opals). They display so-called photonic band gaps formed due to the periodic structure of the crystal. Light cannot propagate through the photonic crystal at these wavelengths, and optical effects analogous to the electronic effects in semiconductors can be observed.

Three-dimensional structures from metallic nanocrystals such as Ag or Au templeted by colloidal crystals are produced [246, 247]. The possibility of highly efficient surface enhanced Raman scattering in these three-dimensional systems often serves as motivation for this work [248]. The mesoporous films from Pt/Pd nanocrystals are considered for highly efficient catalysts [249]. Uniform mesoporous thin films were also employed as templates for the nucleation and growth of unidirectional nanowire arrays with almost perpendicular orientation to a substrate surface.

### **Self-assembled 3D structures**

One of the most typical examples of the self-assembly of nanocrystals in three-dimensional is also related to colloidal crystals. Now, they are made directly from the monodispersed nanocrystals rather than serving as a micron- or submicron-scale template. Murray et al. [192] opened this field of research by making crystalline superlattices from CdSe quantum dots. As is the case with many self-assembly processes, the preparation of this type of three-dimensional assemblies is rather simple, although the synthesis of the corresponding species and substrates may not be. Most often, an aqueous or organic dispersion of uniformly sized nanocrystals is evaporated on a solid surface [250]. In particular, much work has been done for Au nanoclusters [193, 251-254].

Importantly, the nanocrystals in the supercrystals are typically arranged in the closely packed face-centered-cubic (fcc) structure. If the interactions between the nanoclusters exhibit some anisotropy, then they assemble in different lattices, such as double diamond in the case of  $\text{Cd}_{17}\text{S}_4(\text{SCH}_2\text{CH}_2\text{OH})_{26}$  clusters [248], cubic structure for nanocrystals of Prussian Blue [255], or polyhedral lattices for  $\text{SnS}_2/\text{SnS}$  spheres [256]. Superlattices from magnetic particles can also change their packing under the influence of the magnetic field.

The tendency to self-assemble in the crystalline arrays is so strong for nanocrystals that polydispersed nanocolloids may spontaneously phase segregate according to their size. Depending on mixture composition and crystallization conditions, three types of organization can be observed: (1) different-sized particles intimately mixed, forming an ordered bimodal array; (2) size-segregated regions, with continuous hexagonal close-packed monodisperse particles; and (3) a structure in which particles of several different sizes occupy random positions in a pseudohexagonal lattice [193]. Three-dimensional binary superlattices of nanocrystal compositions are also obtained [257, 258]. By selecting the sizes and ratios, different nanocrystals, such as semiconductor and magnetic nanocrystals, can co-crystallize into binary three-dimensional arrays with varying crystalline structures, for example, AB, AB<sub>2</sub>, AB<sub>5</sub>, and AB<sub>13</sub> types [257]. In addition to nanocrystals, the three-dimensional self-assembly of Au nanorods (12 nm in diameter and 50 to 60 nm in length) has also been reported [259].

### **Layered system**

All of the layered systems allow the researchers to organize the nanocrystal or other nanocolloids along the normal to the surface of substrates. The control over the distribution of nanocrystals in plane remains difficult. Thus, all of the nanocrystal multilayers (sandwiches) should be characterized as pseudo-three-dimensional systems, because they have an axis of symmetry coinciding with the direction of organization. This actually is convenient for the description of, say, charge transfer phenomena, which can be treated as essentially a one-dimensional system.

Interesting properties, one of them can be seen in the dependence of the



multilayer capacitance on voltage. It is affected by the scan direction and exhibits strong hysteresis. This effect arises from the electron storage in the layer of nanocrystals [230] combined with relatively high resistivity of the nanocrystal assemblies [260]. Note that this should be a rather common property in nanomaterials with an exceptionally high area of interfaces, where the charges accumulate. Samokhvalov et al. [261] made Langmuir–Blodgett films with gradual changing of the nanocrystal diameter from the first layers to the last. Energy transfer from one layer to another should be observed in such multilayers. It is ideologically similar to the light waveguiding in semiconductor and metal nanocrystal chains [262-264].

### **Layer-By-Layer (LBL)**

Deficiency of Langmuir–Blodgett films' stability can be efficiently overcome with the LBL assembly technique. The process of LBL assembly was first described for polyelectrolytes by Decher [265]. In 1995, the LBL technique was adopted for nanocrystals by Kotov et al. [266]. The principle of the LBL assembly is quite simple. It consists of repeating cycles with sequential dipping of the substrate in oppositely charged nanocolloids and polymers. This results in sequential adsorption of layers of nanocolloids and polyelectrolytes. As one builds up the film, the nature of the absorbing species may be changed periodically and thus organized system of multiple layers were produced. Commercially available deposition systems can do this in automatic regimes and produce multilayer systems made of different nanocrystals or other nanoscale materials, such as nanowires, proteins, clay platelets, or functional polymers, with any desirable sequence of strata. Most often, the negatively charged nanocrystals and positively charged polymers with strong electrostatic attraction to each other are used. However, other intermolecular forces can also lead to sequential layering, such as coordination, Van der Waals forces, or hydrogen bonding.

Complexation of metal ions by polyelectrolytes can be utilized for selective synthesis of metal and semiconductor nanocrystals with controlled size and position inside the LBL films [267]. The accuracy of the positioning of the nanocrystal stratum made in this way approaches the interpenetration thickness of polyelectrolyte LBL films, which is two to three bilayers, i.e., equal to 5 to 7 nm.

There also exist modifications of the multilayer technology when nanocrystals are combined with bifunctional surfactants strongly binding to the surface of nanocrystals. The range of organizational accuracy for them is still similar to classical LBL, because it is determined essentially by the diameter of nanocrystals and interfacial roughness. Musick et al. [268] utilized alkane dithiol to link the layers of Au nanocrystals and observed optical transition from semiconductor to conductor with the increase of numbers of Au nanocrystals. Muller et al. [70] proposed a model of electron conduction in such films of Au nanocrystals.

Numerous optical and electronic prototype devices have been demonstrated on the basis of LBL materials from LEDs [269, 270] to dopamine sensors [271] and single electron charging. For instance, negatively charged Au nanocrystals were built up on mercapto-ethylamine hydrochloride-treated gold [272]. The electrical characteristics of these multilayer systems were identical to a double-insulator tunnel junction device with nanometer thickness. Due to the presence of Au nanocrystals at a controllable distance from the electrodes, current–voltage curves displayed tunable Coulomb gaps [272].

The distinct properties of the resulting nanometer-scale building blocks can be harnessed in assemblies with new collective properties, which can be further engineered by controlling interparticle spacing, packing material and by material processing.

#### **1.3.4 Structural properties of 1D, 2D and 3D array**

One should also briefly mention interesting mechanical properties of one-dimensional assemblies of nanocrystals and related structures [273]. Organic particles in a blend with linear polystyrene macromolecules have revealed a rather unusual behavior. The blend viscosity was found to decrease and scale with the change in free volume introduced by the nanocrystals and not with the decrease in entanglement. The entanglements did not seem to be affected at all, suggesting unusual polymer dynamics [274]. Remarkable viscoelastic properties of nanocrystal composites can also be predicted on the basis of molecular dynamic simulations, as demonstrated in the pioneering works of Starr et al. [275, 276], followed by Smith et al. [277].

### 1.3.5 Electrical properties of an array

Charge transfer through nanocrystal arrays is of great importance not only because of the fundamental new physics involved in such highly correlated system, but also because the modern electronic components are approaching the size limit of standard photolithography techniques [278]. Self-assembled structures based on chemically synthesized nanocrystals have the potential to circumvent such limitations and thus be used as alternative future electronic components [279].

The transport through individual nanocrystals has been well-studied both theoretically and experimentally (by both scanning tunneling microscopy [280, 281] and two-terminal measurements [282]). For metal nanocrystal, its main feature is the Coulomb blockade effect, in which transfer of a single electron on or off a nanocrystal is strongly affected by electrostatic interaction with the nanocrystal's charge. Because of the large number of free electrons in metal nanocrystals, the discrete level spacing due to quantum confinement effects is small and becomes significant only at very low temperatures, typically  $\sim 1$  K. For semiconductor nanocrystals, the number of free carriers is much smaller and quantum confinement effects, together with the Coulomb blockade, determine transport properties [282].

Many-particle systems, on the other hand, are not as well understood and are more complex because of the intricacies of coupling between constituent nanocrystals, effects of structural order and disorder, and charge transfer between nanocrystal cores and ligands. A variety of phenomena have been reported in different systems, including spin-dependent tunneling in magnetic particle assemblies [283], hopping-type transport in dithiol linked arrays [284], and metal-insulator-like transitions in Ag nanocrystal monolayers [65, 222, 285]. Size-induced metal to semiconductor transition in array of gold cluster [286].

Our own work has focused on weakly coupled metallic nanocrystal system—monolayers of 8 nm diameter 1-hexadecanethiol-ligated Au nanocrystals, self-assembled at liquid-liquid interface. By “weakly coupled” we mean that the Coulomb blockade energy, associated with the transfer of individual electrons between individual nanocrystals, dominates transport—the Coulomb or single

electron charging energies are large compared with  $k_B T$ , and the electron wavefunctions, consequently, are localized on the scale of single nanocrystals. A typical current–voltage ( $I$ – $V$ ) curve at 12 K, from an array of length  $N=50$  particles separating the electrodes and width  $M=270$  particles, is shown in Figure 1.22. There is a significant voltage threshold ( $V_T=4.2$  V) below which no current flows. The voltage threshold is the direct consequence of the Coulomb blockade. For each particle, an energetic cost  $V_0 \sim e/\epsilon r = e/C_0$ , where  $r$  is the particle radius,  $\epsilon$  is the dielectric constant of the medium surrounding the metal core, and  $C_0$  is the self-capacitance of the metal sphere, must be paid to transport a single electron onto the charged nanocrystal. For the particles in Figure 1.22,  $V_0$  is around 100 mV, and voltage threshold arises as the sum of this single electron charging energy over all nanocrystals traversed in crossing from one electrode to the other. Voltage threshold grows linearly with array length:  $V_T = \alpha N(e/C_0)$ , where the parameter  $\alpha$  ( $\alpha < 1$ ) accounts for interparticle capacitive coupling and the randomness of the offset charges in the underlying substrate that give rise to the Coulomb blockade repulsion [287, 288].

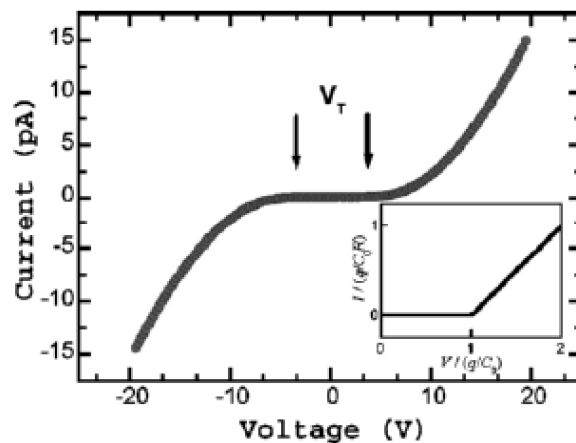


Figure 1.22 Current-voltage curve for a weakly coupled gold nanocrystal superlattice at low temperature (12 K). The distance between the in-plane electrodes was 330 nm and the array width was 2  $\mu$ m. The lower inset shows a schematic  $I$ – $V$  curve for a single nanocrystal [287].

Interparticle coupling can be increased by the use of more complex conjugated or aromatic ligands [284] or by compressing arrays in Langmuir–Blodgett troughs. The latter technique has been used extensively by Heath et al. [222, 285]. Characteristic of transport data from these systems is the lack of a voltage

threshold, i.e., a finite zero-bias conductance, down to the lowest temperatures examined.

The most dramatic feature of compressed nanocrystal monolayers, discovered by Heath's group, is the appearance of shiny, metallic optical reflectivity beyond a certain critical compression [222, 285]. This has been referred to as a metal-insulator transition. At present, simultaneous optical and electronic transport data do not exist. However, a wide range of transport data from these films (transferred from Langmuir troughs onto solid substrates), from compressions at both sides of the optical transition, show resistivity which increases exponentially with decreasing temperature, indicating insulating behavior. Although not technically metallic, the arrays show a rich variety of transport characteristics, with conductivity ( $\sigma$ ) following activated hopping forms [ $\sigma \sim \exp(-U/T)$ ] [289], variable-range hopping of interacting electron forms [ $\sigma \sim \exp(U/T^{1/2})$ ] [290], and other forms depending on variables such as compression and disorder [290]. We will return to some of the issues raised by these experiments in the final section of this article.

Optical and electrical properties of one-dimensional assemblies of nanocrystals can be a good example of collective behavior in nanocrystal assemblies, which were established both theoretically and experimentally [291]. The interactions between the aligned nanocrystals induced strong dichroism in the absorption spectra, i.e., unequal propagation velocity in perpendicular and parallel directions to the chains. The resonance plasmon wavelengths of Ag nanocrystals were shifted to 455 and 550 nm for transverse and longitudinal polarization, respectively [137]. Far-field polarization spectroscopy on chains of Au nanocrystals confirmed the existence of longitudinal and transverse plasmon polariton modes [292]. Moreover, waveguiding of light in the chain of coupled metal nanocrystals, initially proposed by Quinten et al. [293], can also be observed experimentally. This process occurs because the oscillations of the conduction electrons are coupled to the optical excitation to form surface plasmon polaritons bound to the nanocrystals, which are propagating from particle to particle in the chain. The actual measurements of plasmon transfer along a Ag nanocrystal chain were realized by Maier et al. [294] with the help of the near-field microscope. The

characteristic propagation length of light in the chains was only several hundred nanometers. This is a rather short distance for a waveguide. Nevertheless, these data substantiate the theoretical predictions concerning the extremely strong damping of the plasmon propagation in nanocrystal assemblies [262, 263, 295]. According to theoretical calculations by Zhao et al. [291], similar effects should be expected in two-dimensional superstructures as well.

### 1.3.6 Optical properties of an array

Optical properties of metallic nanocrystals are dominated by surface plasmon phenomena, where spatially confined electrons oscillated in resonance with incident electromagnetic waves. For specific metals, such as Ag and Au, the plasmon absorption occurs in the visible wavelength range, giving rise to the visible colors for these colloids. For example, 5-nm Au nanocrystals are deep maroon in color. The frequency-dependent polarizability of a single nanocrystal is given by the Clausius–Mossotti equation: [296]

$$\alpha_A(\omega) = R^3 \frac{\varepsilon(\omega) - \varepsilon_m}{\varepsilon(\omega) + 2\varepsilon_m} \quad (1.23)$$

where  $R$  is the radius of the particle,  $\varepsilon(\omega)$  is the dielectric function of the particle, and  $\varepsilon_m$  is the dielectric function of the medium. Using the dielectric function of metals, the polarizability of a single nanocrystal is

$$\alpha_A(\omega) = \frac{R^3}{1 - \omega(\omega + i/\tau)/\Omega^2} \quad (1.24)$$

where  $\Omega = \omega_p/\sqrt{3}$  and  $\omega_p$  is bulk plasmon frequency. The single particle therefore behaves like a harmonic oscillator of frequency  $\Omega$  and damping constant  $\tau$ . The dipolar oscillation produces a strong electrical field near the surface, which is responsible for the surface-enhanced Raman scattering (SERS) of small molecules adsorbed on surfaces. When nanocrystals are brought into close vicinity, interparticle coupling can lead to additional resonances [94, 297]. Figure 1.23 shows, in a schematic diagram, how light at normal incidence can induce a coupled mode where neighboring particles are oscillating in phase. This coupling causes additional absorption peaks in the long wavelength region. This coupling resonance

depends not only on the particle size and interparticle spacing, but also on the polarization of the incident light and the structure of the nanocrystals lattices [298]. Persson and Liebsch [299] performed a theoretical calculation of a p-polarized light incident on a two-dimensional square lattice (Figure 1.23c). Two resonant peaks in the imaginary part of the polarizability correspond to coupled plasmon oscillations, either parallel or perpendicular to the array. The frequencies of these resonances are given by:

$$\begin{aligned}\Omega_{\parallel} &= \Omega^2 \left( 1 - \frac{1}{2} R^3 U_o \right) \\ \Omega_{\perp} &= \Omega^2 \left( 1 + R^3 U_o \right)\end{aligned}\quad (1.25)$$

where  $U_0$  is a geometric factor that depends on the structure of the array. In the case of disordered particle arrangements, the same calculation based on a coherent potential approximation shows that both of these absorption peaks are broadened. Experiments on disordered nanocrystal arrays confirmed that prediction [300].

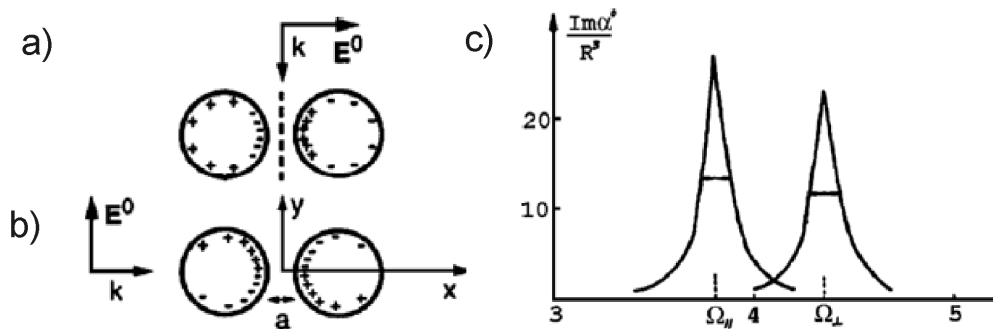


Figure 1.23 Schematic diagram of surface plasmons induced by a polarized plane wave incident upon two adjacent nanocrystals from different directions. (a) The external electric field is parallel to the line joining the nanocrystals. (b) The external field is perpendicular to the line joining the nanocrystals. (c) Calculated imaginary part of the polarizability of nanocrystals arranged on a square lattice. Resonance frequencies  $\Omega_{\perp}$  and  $\Omega_{\parallel}$  correspond to surface plasmon oscillations perpendicular and parallel to the plane of nanocrystals.

A promising scheme of utilizing surface plasmons of coupled nanocrystals for optical applications was proposed by Quinten et al. [293] in their model, a linear chain of metal nanocrystals was used to transmit electromagnetic waves through interparticle dipolar coupling. The field intensity of the transmitted electromagnetic wave depends strongly on the polarization of the incident light.

Traditional dielectric optical waveguides have a fundamental wavelength limitation. In comparison, small particle arrays have the potential to become functional units for guiding, modulation, and amplification of light signals on a length scale that is much smaller than the wavelength of light.

In the case of strongly coupled nanocrystal arrays, such as Ag nanocrystal arrays compressed on the Langmuir trough, the optical properties also undergo dramatic changes when metal-insulator-like transitions occur [222, 285]. The real part of the dielectric constant turns negative, indicating features that are more metallic. However, the derived value of the dielectric constant is about 10 times larger than typical values for an ordinary Ag film. This indicates that the “metallic” state caused by the strong coupling of neighboring nanocrystals is still quite different from the bulk metallic states that we are familiar with. Schatz group has studied the influence of structure of arrays on the extinction spectra [291] and importance of radiative dipole coupling in 2D arrays [301].

An ensemble of individual Au nanocrystals near each other (separations of the order of angstroms) in an ordered array is referred to as a superlattice, whereas an ensemble of individual Au nanocrystals near each other with no ordered arrangement is referred to as an aggregate. Superlattices and aggregates can consist of tens to thousands of Au nanocrystals arranged in a variety of different structures. It is this structural arrangement that has a profound influence on the plasmon resonance of these Au nanocrystal systems. However, analogies can be drawn between the behavior of the plasmon resonance of superlattices and aggregates and that of discrete Au nanocrystals to achieve a qualitative understanding of the plasmon resonance in these structures. For example, Au superlattices display a red-shifted plasma resonance, which can be viewed as a consequence of interparticle interaction [35]. The collective plasma oscillations of the individual Au nanocrystals in the lattice determine  $\epsilon_m$ , and it is this  $\epsilon_m$  that is responsible for the red shift in the plasmon resonance. The plasmon resonance in Au nanocrystal aggregates displays a similar behavior. Generally, aggregates of Au nanocrystals can be divided into two groups: weakly interacting aggregates and strongly interacting aggregates. These two types of structures display different optical characteristics.



Typically in weakly interacting aggregate structures, the Au nanoparticles are linked to each other by a spacer molecule such as DNA [302, 303] or a dithiol [304]. Both the density of Au nanocrystals in the weakly interacting aggregates and the number of particles in the weakly interacting aggregates affect the position and width of the plasmon resonance. A broader and redder plasmon resonance occurs in weakly interacting aggregate structures, with a greater number and higher density of Au nanoparticles. As in superlattices, the collective plasma oscillations of the Au nanocrystals determine  $\epsilon_m$ . The broadening can be viewed because of dampening of the plasma oscillations, which leads to changes in  $\epsilon_1$  and  $\epsilon_2$ . In large Au nanocrystals, inhomogeneous polarization by wavelengths of light of the order of the particle size can cause changes in the dielectric constants, which leads to broadening of the plasmon resonance. As a consequence of the coupling of the plasmon resonance from the individual particles in the aggregate, weakly interacting aggregate structures can be viewed as a giant Au nanocrystal. Therefore, the broadening seen in larger and denser aggregates can be viewed as the effect of inhomogeneous polarization of the weakly interacting aggregates by light, whose wavelengths are of the same order of magnitude as the weakly interacting aggregate size.

The characteristic feature in the absorption spectrum of strongly interacting aggregate structures is a distinct transverse plasmon resonance and longitudinal plasmon resonance or extended plasmon resonance band. An example of a strongly interacting aggregate system is that produced by the reduction of  $\text{HAuCl}_4$  by  $\text{Na}_2\text{S}$  [305]. During this reaction, a broad extended plasmon resonance band emerges in the near infrared that subsequently shifts to bluer wavelengths as the reaction progresses. Most strongly interacting aggregate systems studied, however, are prepared by first producing Au nanocrystals and then introducing an agent to partially remove the stabilizing agent [306, 307]. In these cases, the extended resonance band red shifts from the transverse plasmon resonance as the strongly interacting aggregate structures form. The factors affecting the position of the extended band in strongly interacting aggregate structures are not fully understood. However, experiments have shown that aggregate size, shape, density, and method of preparation play a key role in determining the nature of such band [306].

A small-angle X-ray-scattering (SAXS) experiment suggests that the shift observed in the extended plasmon resonance of the  $\text{HAuCl}_4\text{-Na}_2\text{S}$  system is the consequence of a change from a globular to a stringy strongly interacting aggregate structure [308]. A structural feature of many strongly interacting aggregate systems that distinguishes them from weakly interacting aggregate structures is a physical connection between some of the particles in the aggregate. This would imply that the individual particles in the aggregates cannot be treated as spherical particles, but as spheroidal or rod-shaped particles.

## 1.4 Concluding remarks

The controlled assembly of nanocrystals into large arrays and superlattices opens the door to a new class of artificial materials whose properties can be tuned by choosing different core materials, by varying the core sizes and shapes, and by tuning the interparticle coupling strength. In particular, the ability to vary independently the properties of the individual nanocrystal building blocks and the type and strength of the interactions between them allows for new and unprecedented control. As a result, materials with electronic or optical properties not obtainable from bulk can be designed “bottom up” by nanocrystal assembly [309]. At present, the main challenge still lies in ability to tune all of the crucial physical parameters of a nanocrystal array at will. In general, effect of single electron Coulomb blockade dominates the electronic transport properties of weakly coupled arrays. Strongly coupled arrays, on the other hand, are considerably different. Understanding the strongly coupled state and the transitions between strong and weak coupling are two pressing issues in this field. Experimentally, it is difficult to regulate interparticle coupling. Compression in Langmuir troughs has yielded the fascinating properties as mentioned, but it suffers from the disadvantage of simultaneously altering both the voltage and current scales of transport. As nanocrystals are brought closer together, their capacitive coupling increases, lowering the Coulomb blockade cost for electron transport [288]. In addition, the tunneling barrier separating the metal cores narrows, increasing the interparticle tunneling amplitudes. Techniques to independently control one of these two effects would do much to further our understanding. One possible route is a better grasp of the role of ligands in nanocrystal systems, perhaps designing

metal core/ligand particles with specific tunneling rates. Such feats have been accomplished in the context of electron tunneling through proteins [310].

Theoretical studies of Coulomb blockade-dominated array transport have been limited. Even for weakly coupled arrays, open questions remain, such as the discrepancy between the predicted and observed values of the exponents for the current–voltage scaling relations. For strongly coupled arrays, the paucity of studies is even more pronounced. It is not yet clear to what extent such well-known concepts such as variable-range hopping, metal-insulator transitions, localization, etc. developed for microscopic disorder in semiconductors or disordered thin metal films carry over directly to nanocrystal arrays. For example, it is not obvious that anything besides fixed range, nearest-neighbor hopping should even occur in metal nanocrystal arrays because of the large, mesoscopic distances involved and because, in contrast to hopping between sharp impurity levels in semiconductors, in metals, at any finite temperatures, the spectrum of available states is broad. Furthermore, the interplay of several types of disorder (random offset charges and variations in the particle size modulating the local charging energy and variations in the particle spacings giving rise to coupling strength disorder) as well as the potentially complex roles played by any electronic states inside the ligands make application of these established, but more microscopic concepts nontrivial.

Controlling the optical response on a nanometer scale is another emerging direction of much promise. With strong coupling between nanocrystals, theoretical models have predicted that coherent transfer of electromagnetic energy along nanocrystal arrays should be possible, despite significant radiative loss. Experiments have not unambiguously demonstrated this phenomenon so far largely because of the difficulty of creating the desired array structures on a very small length scale and also because of current limitations with near-field optical detection schemes.

Few of the recently developed approaches discussed in this chapter provide new pieces to the expanding toolkit for nanocrystal array assembly. The digestive ripening method can produce size dispersions significantly below 5% and fully ligand-saturated Au nanocrystals can assemble into extended monolayer superlattices with exceptional degree of long-range order [311]. Nanocrystal arrays

can be patterned into arbitrary 2-D shapes by electron beam exposure or can be interfaced with lithographically defined electrodes; and the use of membrane substrates allows for transport measurements and, with the same samples, for characterization of the local structural order by transmission electron microscopy.

## 2 Ultra-Thin Nanocrystalline Films of Metals Generated at the Liquid-Liquid Interface

### 2.1 Summary

The air-water interface has been traditionally employed to prepare particle assemblies and films of metals and semiconductors. The liquid-liquid interface between water and an organic liquid, however, has not been investigated sufficiently for possible use in preparing nanocrystals and thin-films of materials. We prepared nanocrystalline films of Au, Ag and Cu at the toluene-water interface by the interaction of metal-triphenylphosphine complexes in the organic layer with partially hydrolysed tetrakis(hydroxymethyl)phosphonium chloride (THPC) in the aqueous layer. The nanocrystals have been characterized by a host of microscopic and spectroscopic techniques. The free-standing films can be transferred from the interface onto solid supports. The films may be dissolved to yield either a hydrosol or an organosol with the help of appropriate surfactants. The films are smooth and continuous over relatively large length scales and are generally ~ 100 nm thick. Further, nanocrystalline films of Au formed at different temperatures at the organic-aqueous interface have been prepared and examined for their electrical conduction and optical properties. The studies have revealed that variation in the concentration of organometallic precursor affects the size of the nanocrystals only slightly, while a change in the interface temperature or the contact time has a marked effect on the properties of the films. The size of the nanocrystals is found to depend on the reaction temperature as also the film properties; higher the reaction temperature, bigger are the nanocrystals. The surface plasmon band of Au is highly red-shifted in these films. Adsorption of alkanethiols and conjugated thiols alters the properties of the films significantly, the effect depending on the alkane chain length or the effective conjugation in the molecule.

By the reaction of the appropriate organometallic precursors and THPC at the toluene-water interface, films of Au-Ag and Au-Cu with a range of compositions have been prepared and characterized. The particle size of the nanocrystals in the films

varied with the composition, (0:1, 1:3, 1:1, 3:1 and 1:0). The surface plasmon band of the alloy films as well as of the organosols obtained by the disintegration of films by the addition of an alkanethiol show the expected composition-dependence. Nanocrystalline films of a ternary system, Au-Ag-Cu have also been prepared.

Rheological properties of a nanocrystalline Ag films prepared at liquid-liquid interface have been examined. We studied the interfacial properties of monolayers of Ag nanocrystals (10-50 nm in diameter) formed at the toluene-water interface under steady as well as oscillatory shear. Strain amplitude sweep measurements carried out on the film have revealed a shear thickening peak in the loss moduli ( $G''$ ) at large amplitudes followed by a power law decay of the storage ( $G'$ ) and loss moduli with exponents in the ratio 2:1. In the frequency sweep measurements at low frequencies, the storage modulus remains nearly independent of the angular frequency, whereas  $G''$  reveals power law dependence with a negative slope, a behavior reminiscent of soft glassy systems. Under steady shear, a finite yield stress is observed in the limit of shear rate  $\dot{\gamma}$  going to zero. However, for  $\dot{\gamma} > 1 \text{ s}^{-1}$ , the shear stress increases gradually. In addition, a significant deviation from the Cox-Merz rule confirms that the monolayer of Ag nanocrystals at the toluene-water interface forms a soft two-dimensional colloidal glass.

The growth and formation of Au nanocrystals at the interface have been investigated by employing X-ray scattering from an as-formed film with a synchrotron X-ray source. The X-ray reflectivity and diffuse scattering measurements show that Au nanocrystals form multiple layers above water-toluene interface. We could probe three layers of nanocrystals separated by about 30 Å and an in-plane peak at 0.046 Å<sup>-1</sup>. The in-plane and out-of-plane data obtained from these measurements could be explained with a model that assumes a hexagonal lattice of 1.3 nm particles separated from each other by 15.8 nm.

We have studied the dependence of the optical and the electronic properties of nanocrystalline Au films with the mesoscopic structure, in particular the interparticle separation. This was investigated by examining the interaction of alkane thiols of varying chain length on nanocrystalline Au films prepared at the organic-aqueous interface. Adsorption of alkane thiols causes blue-shift of the surface plasmon absorption band of the films, the magnitude of shift being proportional to the chain

length. The disordered nanocrystals thus created ( $\lambda_{\max}$ , 530 nm) are in equilibrium with the ordered nanocrystals in the film ( $\lambda_{\max}$ , 700 nm) as indicated by an isosbestic point around 600 nm. The rate of interaction of thiols with the film decreases with decreasing chain length. The long chain thiols disintegrate or disorder the Au film more effectively, as evidenced by the increased population of the thiol-capped Au nanocrystals in solution. The effect of an alkanethiol on the spectrum of the Au film is specific, in that the effects with long and short chains are reversible. The changes in the Au plasmon band due to interparticle separation can be satisfactorily modeled using the Maxwell-Garnett formalism. Adsorption of alkanethiols seems to perturb the structure of the films, the magnitude of the effect depending on the chain-length of alkanethiol. Accordingly, the electrical resistance of the films is affected on interaction with alkanethiols, while the plasmon band occurs at wavelengths close to that of isolated nanocrystals in the presence of long-chain thiols.

The effect of surfactants such as tetraoctylammoniumbromide (TOAB) and cetyltrimethylammoniumbromide (CTAB) on the type of nanostructures formed when Au ions present in the organic phase are reduced at the interface by hydrazine in the aqueous phase has been investigated. Extended fractal structures are formed at the liquid-liquid interface, the fractal structures themselves comprising cauliflower type units formed by Au nanorods. Accordingly, the nanostructures exhibit transverse and longitudinal plasmon adsorption bands in the 550 and 800 nm regions respectively. Dendritic structures of Ag are formed at the interface when Ag ions are reduced similarly in the presence of surfactants. Many of the nanostructures consisted of nanocrystals or nanorods with five-fold symmetry.

## 2.2 Introduction

Mesoscale assemblies of metal nanocrystals are of considerable interest since both short and long range interactions coexist in these systems and compete giving rise to a host of interesting structural [312], optical [94, 313], electrical [314-316], magnetic [317] and other properties [3, 317]. A number of studies have aimed to explore their potential in technological applications. A nanocrystal assembly, analogous to an atomic lattice, derives its properties from the nature of the nanocrystal (also called a superatom) [318], its geometric arrangement as well as from the nature of the material in the intervening space. Nanocrystals are anchored to surfaces in the

form of a film. Such films constitute a novel class of materials with a combination of notionally zero and two dimensionalities. There has been much interest in the self-organization of monodisperse nanocrystals in two-dimensional arrays, with the thiolized metal nanocrystals readily forming crystalline 2D arrays depending on the particle diameter and the chain length of the alkane thiol. Whetten et al. [319] subjected a thiol-protected Au organosol to centrifugation to separate out fractions containing nanocrystals of different mean sizes, thereby obtaining well-ordered two-dimensional arrays of size-selected nanocrystals. Continuous films of thiolized Ag nanocrystals covering micron-sized areas have been reported [36]. Colloidal dispersions of Co nanocrystals capped with fatty acids self-assemble to yield hexagonally ordered arrays. Schmid et al. [320] obtained an ordered 2D array of Au55 nanocrystals on a polymer film. Arrays consisting of Au and Ag nanocrystals of different sizes [193], of Au-Ag [321] and Fe-Pt [194] alloy nanocrystals as well as of core-shell nanoparticles [322] are also reported. There are a number of reports on the synthesis of well-defined two dimensional arrays by suitably derivatising the nanocrystals [113, 323], assembling at the air-water interface [35, 324] or by growing nanocrystals in predefined locations [301, 325].

There have been various reports of Au nanocrystal assemblies using the LB method as discussed in first chapter. It has been shown that capped metal nanocrystals possess size-dependent charging energies [326], and therefore, a layer of such nanocrystals in the form of a film can be visualized as a network of discrete charging units connected by tunnel junctions, with characteristics depending on both the particle size and the interparticle separation [327]. Bourgoïn et al. [328] have carried out electrical measurements on strongly interconnected Au nanocrystals at the air-water interface and found Coulomb blockade behavior. Diode-like characteristics have been observed using CAFM measurements on a Au nanoparticle film supported on a self-assembled gadolinium stearate monolayer [329]. Furthermore, transport measurements carried out on layer-by-layer assemblies, wherein nanocrystalline films interspersed with bifunctional molecules built sequentially [330] have revealed that transport through such films can be influenced by altering either the nanocrystal diameter or the spacer length [331]. Similar results have been obtained from a study of the conductivity of a two-dimensional array of nanocrystals with patterned electrodes [65, 287]. A Mott-Hubbard type metal-insulator transition has been



observed at room temperature by compressing a LB film of Ag nanocrystals capped with dodecanethiol [71]. By tuning the properties of the nanoclusters and the spacers, nanocrystalline devices capable of lasing and rectification have been obtained [332]. Opals of polydisperse Au nanocrystals functionalized by alkanethiols and floating at the air-water interface have been prepared [333]. Alkylthiol-capped Ag nanocrystals deposited at the air-water interface form spontaneous assemblies as circles and stripes [334].

A careful examination has shown that the material formed at the interface is an ultrathin nanocrystalline film consisting of closely packed metal nanocrystals coated with the organic species present at the interface. The film at the interface is essentially free-standing and can be deposited onto a substrate for further investigations or could be converted to either an organosol or a hydrosol by using appropriate capping agents. This novel method of obtaining ultrathin metal nanocrystalline films offers a fair degree of control on the properties of the films. We have explored how the various reaction parameters can influence the properties of the films. The parameters that we have studied are the concentration of the precursors, temperature and contact time at the interface. We have investigated the electrical properties of the Au films formed at the interface using the four-probe method. We have subjected the films to chemical modification by adsorbing alkanethiols and monitored the changes in the optical and electrical properties.

Alloy nanocrystals are known to exhibit unique electronic, optical and catalytic properties, different from those of monometallic nanocrystals [335]. Alloy nanocrystals are generally prepared by the coreduction of the constituent metal ions and there are several reports in the literature, on the synthesis and assembly of nanocrystals of alloys such as Pd-Pt [52], Pt-Ru [336], Pd-Rh [337], and Ag-Pt [338]. Henglein [339] used  $\gamma$  radiolysis to produce bimetallic particles of noble metals. A similar procedure was employed by Harriman et al. [340] to prepare Au-Pt nanocrystals. Nanocrystals of Fe-Pt [194] and Co-Pt [341] alloys have been prepared in the form of 2D assemblies for possible use in magnetic recording. Au-Ag alloy particles possessing interesting optical properties [342, 343], have been produced by the reduction of the corresponding salts using sodium borohydride [344-347] or citrate [348], or hydrazine [349] as well as by laser irradiation of monometallic sols

[350, 351], or by the irradiation of an alloy target [352]. Au-Ag nanocrystals have also been prepared by the reduction with biological means [353]. The alloy nanocrystals mentioned in these studies are to be distinguished from bimetallic core-shell nanocrystals, although in some cases, the distinction gets somewhat blurred.

Studies on Langmuir monolayers of micron-sized colloidal particles at the interface have shown that the structure of the film at the interface is sensitive to the nature of the interface, the concentration of the particles at the interface, the particle size, surface charge and wettability, as well as the electrolyte concentration of the subphase. However, very few studies exist on the dynamics of such systems. This is because the instrumentation to probe the interfacial viscoelastic properties of such 2D systems is less well established. Interfacial viscoelastic measurements carried out recently on colloid monolayers [354] formed by micron-sized polystyrene spheres at the liquid/liquid interface, indicate that the behavior of such systems is close to that of a soft glassy state analogous to that of many three-dimensional (3D) systems. Further, the 2D hexagonal array of such particles transforms to a partially ordered structure stretched along the flow direction under steady extensional as well as shear flows, with the flow behavior being sensitive to the particle concentration at the interface [355, 356]. 2D arrays of metal nanocrystals are known for their unique optical and electronic properties that find many novel applications [357].

Understanding chemical reactivity at the liquid-liquid interface is of fundamental importance in several important research areas including drug delivery and diffusion through biological membranes, as the effect of this inhomogeneous environment can alter the behavior of the reacting molecules [358-361]. Molecular ordering accompanying chemical reactions at the buried liquid-liquid interface can be studied effectively by making use of a high-energy synchrotron x-ray beam which allows one to go through the upper liquid phase [362]. We have performed high-energy X-ray scattering measurements at the ID10B beam line of the European Synchrotron Radiation Facility (ESRF) to investigate the formation of ultra thin films of Au nanocrystals at the toluene-water interface.

Capillary wave fluctuations induce long-range logarithmic correlation [363, 364] at liquid-liquid interfaces though bulk liquids do not have such long-range correlation, and can alter hydrogen-bonds of the aqueous surface due to the presence of

microscopic roughness. The characteristic of capillary wave fluctuations, which determine this interfacial roughness, is readily investigated by measuring the X-ray diffuse scattering intensity [363] as a function of the inplane wave-vector transfer ( $q_y$ ). Although liquid surfaces have been studied by diffuse scattering measurements [363-366], it is only recently that the liquid-liquid interface is receiving attention [366-368].

Optical properties of metal nanocrystal arrays find immense applications ranging from bioanalysis to glass industry. The nature of the ligating molecule or that of the medium and the proximity of particles within an array can influence the localized optical excitations and cause measurable shifts in the optical spectra. For example, Mulvaney and coworkers [369] have monitored the localized surface plasmon band from an array of Au nanocrystals coated with SiO<sub>2</sub> that caused red shifts with decreasing shell thickness. The near-field coupling interaction between surface plasmon modes of neighboring metal nanocrystals have been investigated by Sih and Wolf [370] in the case of a thin film of oligothiophene-linked Au nanocrystals. They find that the higher dielectric constant of the medium leads to weaker coupling between the particles. Surface plasmon resonance band of Au nanocrystals arrays embedded in glass and quartz matrices has been exploited to obtain a range of transmitting colors [371, 372]. A nanoscale optical biosensor based on localized surface plasmon resonance properties of noble metal nanocrystals has been realized [373]. Metal nanocrystal arrays have been employed as solid substrates for surface enhanced Raman scattering (SERS) of adsorbed molecules [374, 375] and importantly, there are studies relating SERS activity to the surface plasmon resonance behavior [297].

Besides synthesis, control of the shape of nanocrystals has also received considerable attention [2, 376, 377]. Another aspect of vital interest is the assembly or self-organization of nanocrystals into different types of networks and other forms of aggregates. Thus, a few workers have been interested in the formation of fractal and dendritic nanostructures employing metal nanocrystals. The formation of fractals and dendrites is generally described in terms of the diffusion limited aggregates (DLA) model [378], or the cluster-cluster aggregation model [379]. Dendrites seem to be

generally formed in the presence of a polymer such as polyvinylpyrrolidone (PVP) or in the presence of a template.

## **2.3 Scope of the Present Investigations**

### **2.3.1 Nanocrystalline films of Au and other metals and their characterizations\***

No generalized approach has been found in literature for synthesizing nanocrystals of metals and semiconductors of definite size in the form of an array. We considered it important and interesting to develop a new method that is simple and can be easily adopted for a large variety of nanocrystal systems. This strategy would appear similar to that for air-water interface at first, but existence of liquid phase on either side enhances the prospects for us to generate several types of nanocrystals and to play with their chemistry.

Although the water-organic liquid mixtures have been employed in the presence of phase-transferring reagents to prepare metal nanocrystals, by the reduction of the metal salts, the liquid-liquid interface itself has not been fully exploited to form nanocrystals and their assemblies. It occurred to us that it should be possible to exploit a liquid-liquid interface to synthesize and cast metal nanocrystals into a film in-situ. For this purpose, we have made use of two immiscible liquids toluene and water, with the metal precursor in the organic layer and the reducing agent in the aqueous layer.

The liquid-liquid interface provides a general method of producing a variety of nanomaterials in the form of two-dimensional films. Employing the liquid-liquid interface for the synthesis of nanocrystalline films is a simple, novel, effective, and direct method to obtain meso-assemblies of nanocrystals. This has now evolved as the most generalized method for synthesis of ultrathin nanocrystalline films of various metals, semiconductors, chalcogenides and oxides. This method is to be distinguished from others where the metal nanocrystals, synthesized ex-situ, are obtained in the form of films at the air-liquid or liquid-liquid interfaces. Furthermore, the free-

---

\* Papers based on this work have been appeared in J. Phys. Chem. B (2003), Current Science (2003), J. Colloid Inter. Sci. (2005) and J. Phys. Chem. B (2005).

standing films obtained by the present method could be converted either to an organosol or to a hydrosol by using appropriate capping agents.

### **2.3.2 Nanocrystalline films of Au-Ag, Au-Cu and Au-Ag-Cu alloys<sup>Ω</sup>**

Au and Ag nanocrystals have characteristic plasmon absorption band at 540 and 420 nm respectively, however using alloy nanocrystals of Au and Ag, it is possible to tune the plasmon absorption band from anywhere between 420 nm to 540 nm. We have explored the possibility of uniform alloying of nanocrystals at the interface. This strategy allows us to integrate the properties of two or more elements.

We have reported a novel and simple technique for the synthesis of alloy nanocrystalline films employing liquid-liquid interface, of several compositions of the alloys of Au with Ag and Cu, as well as the ternary Au-Ag-Cu alloy. The nanocrystalline alloy films were transferred onto solid substrates and their morphology was studied.

### **2.3.3 Rheological study of nanocrystalline Ag film<sup>π</sup>**

The study of the structure and dynamics of two-dimensional films of particles at the liquid-gas and liquid-liquid interfaces is currently an active area of research, not only from the point of view of understanding the physics of complex fluids in two dimensions, but also due to their practical applications that range from consumer products to drug delivery [380, 381]. Very few studies exist on the dynamics of an assembly or a film of nanocrystals. Thus, we have investigated the interfacial properties of an ultrathin film of ~50 nm thickness formed by Ag nanocrystals of 10-50nm diameter at the toluene-water interface, under both steady and oscillatory shear using a biconical bob interfacial rheometer [382].

### **2.3.4 Evolution of Au nanocrystalline film studied using SAXS<sup>ψ</sup>**

Microscopic measurements that provide direct information in nanometer length scales are essential to obtain a proper understanding of the interfacial reactions that

---

<sup>Ω</sup> A paper based on this work has appeared in Langmuir (2006).

<sup>π</sup> A paper based on this work has appeared in Langmuir (2007).

<sup>ψ</sup> A paper based on this work has appeared in J. Phys. Chem. C (2008).

form nanostructured materials, besides measurements of macroscopic properties that are generally employed. Understanding chemical reactivity at the liquid-liquid interface is of fundamental importance in several important research areas including drug delivery and diffusion through biological membranes, as the effect of this inhomogeneous environment can alter the behavior of the reacting molecules [358-361]. Molecular ordering accompanying chemical reactions at the buried liquid-liquid interface can be studied effectively by making use of a high-energy synchrotron x-ray beam which allows one to go through the upper liquid phase [362]. However, the process of such ordering of nanocrystals cannot be probed with usual microscopic techniques. Thus, we have performed high-energy X-ray scattering measurements to investigate the formation of ultra thin films of Au nanocrystals at the toluene-water interface.

### **2.3.5 Nanocrystalline films adsorbed with alkanethiols of varying chain lengths<sup>o</sup>**

Individual nanocrystals behave like units that have properties different from their respective bulk. Detailed studies have been done to show, how properties change when the size and dimension of a system is lowered. However, when the bulk system is designed via assembling these nanocrystals, the new structure that emerges possesses properties that are different from that of bulk as well as from nanocrystals. Such collective properties of nanocrystal arrays have not been well understood. In this work, we intend to understand the electrical and optical properties of mesoscale organization of nanocrystals. We assembled nanocrystals using liquid-liquid interface and thereafter we modified the coupling between the nanocrystals by various means, and studied the after effect.

We were interested in investigating changes in the optical absorption spectra of the metal nanocrystal arrays caused by a variation of the interparticle distance. We have therefore investigated how the optical absorption spectrum responds to the changing interparticle separation, as the Au nanocrystals in the array are made to interact with alkanethiols of different chain lengths. The surface plasmon band of Au serves as a good diagnostic tool to monitor changes as a nanocrystalline Au film

---

<sup>o</sup> A paper based on this work is set to appear in Langmuir (2008).

interacts with alkanethiols. We also studied the effect of adsorbing conjugated molecules on the optical spectrum of the nanocrystal array.

### **2.3.6 Effect of surfactants on interfacial reaction<sup>α</sup>**

The interface of aqueous and organic phase has always been a preferential site for surfactants. We studied the effect of surfactant, with the intention of achieving greater control over the synthesis of nanomaterials at the liquid-liquid interface, and exploiting their possible application as building blocks for nanoarchitects. It is known that surfactant reduces the surface tension between the organic-aqueous interfaces, and exists in various shapes depending on their concentration in given phase. Systems where aqueous and organic phases coexist are greatly affected by the presence of even the smallest amount of surfactant. Knowing this, we introduced various types of surfactant and phase transferring agents to the well-understood system of liquid-liquid interface. We have investigated the effect of a surfactant such as tetraoctylammoniumbromide (TOAB) and cetyltrimethylammoniumbromide (CTAB) present in the organic and aqueous phase respectively, on the formation of nanostructures of Au and Ag at the liquid-liquid interface. In addition, we have examined the effect of adding PVP on the nanostructure formed at the interface. By doing so, we also explored the formation of fractal and dendritic nanostructures of Au and Ag at the liquid-liquid interface.

We also studied how and why diffusion limited aggregates are observed in such structures. There is a dendritic growth of Ag and alloys of Au-Ag due to the geometry of the liquid-liquid interface. Such percolating networks are subject of interest for various problems.

## **2.4 Experimental**

### **2.4.1 Materials and synthesis**

Tetrakis(hydroxymethyl)phosphonium chloride (THPC), dodecane thiol, octylamine were obtained from Fluka and used without further purification. Mercaptoundecanoic acid (MUA) was obtained from Aldrich. All Metal precursors such as Au(PPh<sub>3</sub>)Cl (Ph – Phenyl), Cu(PPh<sub>3</sub>)Cl and Ag<sub>2</sub>(PPh<sub>3</sub>)<sub>4</sub>Cl<sub>2</sub> were prepared by

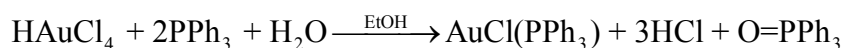
---

<sup>α</sup> A paper based on this work has appeared in J. Colloid Inter. Sci. (2008)

the known procedure [383, 384] as described in the next section. Water used in the experiments was double distilled using a quartz apparatus.

#### 2.4.1.1 Preparation of metal precursors

##### Preparation of Au(PPh<sub>3</sub>)Cl



This synthesis is performed under an atmosphere of argon and is derived from the original preparation. The solvents are degassed prior to use by bubbling argon for 2 min. Hydrogen tetrachloroaurate  $\text{HAuCl}_4 \cdot x\text{H}_2\text{O}$ ,  $x \sim 3$ , 1 g, 2.54 mmol of Au is introduced into a 250-mL round bottomed Schlenk flask equipped with a stopcock and backfilled twice with argon. Degassed 95% EtOH (technical grade, 35 mL) is made to dissolve the hydrogen tetrachloroaurate. To this solution is added under argon a solution of PPh<sub>3</sub> (1.364g, 5.20 mmol) in 50 mL of degassed 96% EtOH, using glass pipette. The reaction mixture immediately becomes colorless, and a white precipitate appears after a few seconds. The mixture is stirred for 2 min, and the product is then removed by filtering through a glass frit (medium porosity), washed with Et<sub>2</sub>O (technical grade, three 15 mL portions), and dried in vacuo. The solid on the frit is then directly dissolved in CH<sub>2</sub>Cl<sub>2</sub> (10 ml) in a 250-mL Schlenk flask. Slow addition of pentane (60 mL) and cooling to -25° C results in the formation of white needles of Au(PPh<sub>3</sub>)Cl.

##### Preparation of [Ag(PPh<sub>3</sub>)<sub>4</sub>](NO<sub>3</sub>)

In a typical preparation of [Ag(PPh<sub>3</sub>)<sub>4</sub>](NO<sub>3</sub>), silver (I) nitrate (1.698 g, 10 mmol) was added to a warm ethanol solution (100 ml) of Ph<sub>3</sub>P (10.492 g, 40 mmol). After 2 h the warm clear solution was allowed to cool slowly in the dark to give well formed crystals of [Ag(PPh<sub>3</sub>)<sub>4</sub>](NO<sub>3</sub>) (10.12 g, 83% yield).

#### 2.4.1.2 Preparation of noble metal nanocrystalline film at the interface

In a typical preparation, 10 ml of 1.5 mM solution of Au(PPh<sub>3</sub>)Cl in toluene was allowed to stand in contact with 16 ml of 6.25 mM aqueous alkali in a 100 ml beaker at 300 K. Once the two layers stabilized, 330 μl of 50 mM THPC was injected into the aqueous layer using a syringe with minimal disturbance to the toluene layer. It is



important to note that cross section area offered by a 100 ml beaker is  $\sim 23 \text{ cm}^2$ . The onset of reduction was marked by a faint pink coloration of the liquid-liquid interface. The reduction thus initiated was allowed to proceed without disturbance for several hours. With the passage of time, the color became more vivid, finally resulting in a robust elastic film at the liquid-liquid interface. It is important to note that the aqueous and the organic layers below and above the film were transparent. Films of Ag and Cu were prepared by a similar procedure using  $\text{Ag}_2(\text{PPh}_3)_4\text{Cl}_2$ ,  $\text{Ag}(\text{PPh}_3)_4](\text{NO}_3)$ ,  $\text{Cu}(\text{PPh}_3)\text{Cl}$  and Cu-cupferron [385].

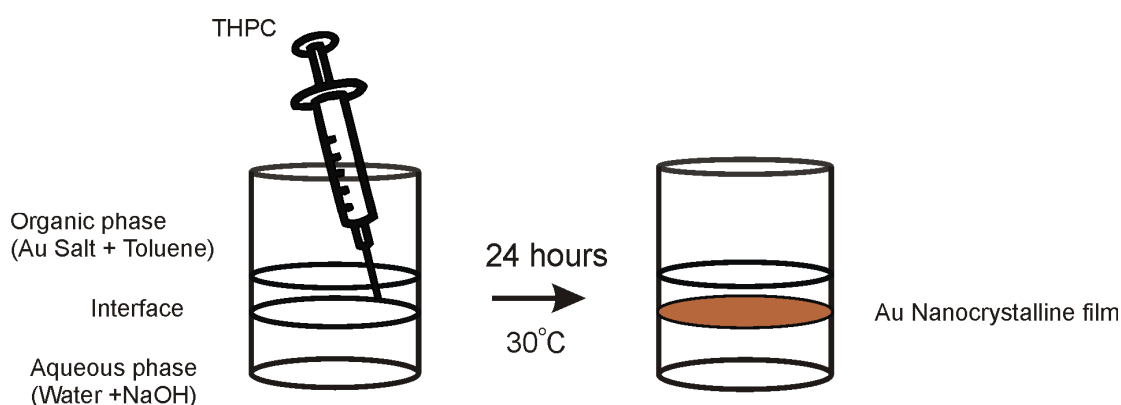


Figure 2.1 Liquid-liquid interface method for preparing Au nanocrystalline film.

#### 2.4.1.3 Preparation of ultrathin film of palladium and platinum nanocrystals

Pd nanocrystals were obtained by reacting a dispersion of palladium acetate (2.4 mg or  $16 \mu\text{mole}$ ) in the toluene layer with hydrazine ( $50 \mu\text{l}$ ) as a reducing agent in the aqueous layer. Palladium acetate was ultrasonicated with toluene for 15 min, as it is poorly soluble in toluene. To obtain Pt nanocrystals,  $\text{H}_2\text{PtCl}_6$  was phase transferred from aqueous phase to toluene using TOAB, and was further reduced with hydrazine ( $50 \mu\text{l}$ ) that was offered through the aqueous phase.

#### 2.4.1.4 Preparation of nanocrystalline film under different physical conditions

We have employed four different temperatures for the film growth,  $30^\circ$ ,  $45^\circ$ ,  $60^\circ$  and  $75^\circ\text{C}$ . The films thus formed were transferred to mica or glass substrates after about 12 hours depending on the temperature, when no further growth of the film was seen. In order to study the effect of contact time at the interface, the growth of the film was arrested after a specific period by simply transferring the film on to the

substrate. Thus, films were collected after 30, 45, 60, 120 and 240 minutes of growth at 45°C. Films were also prepared with different initial concentrations of the metal precursor (2, 8 and 16 mM). In order to study effect of viscosity, glycerol was added to aqueous phase at different volume percentage. We used home built vibrating stage to study effect of vibration on the interfacial reaction.

#### **2.4.1.5 Nanocrystalline films of Au-Ag and Au-Ag-Cu alloy**

Au(PPh<sub>3</sub>)Cl, Ag(PPh<sub>3</sub>)<sub>4</sub>NO<sub>3</sub> and Cu-cupferron were used as the organometallic resources. In a typical preparation, 10 ml of 1.66 mM solution of the metal precursor in toluene formed the top organic layer, with 16 ml of 6.25 mM aqueous NaOH solution forming the bottom aqueous layer. The reducing agent, THPC was gently added to the bottom layer (330 µl of 50 mM) to initiate the reaction at the interface. All reactions were carried out at 75° C for 3 hours. Au-Ag nanocrystalline films were prepared with varying molar ratios of 100:0, 75:25, 50:50, 25:75 and 0:100. Au-Cu films were prepared with molar ratios of 75:25 and 50:50, while a ternary Au-Ag-Cu alloy film was with a ratio, 50:25:25.

#### **2.4.1.6 Organosol of Au-Ag and Au-Ag-Cu alloys**

In order to prepare the organosols, the films were collected onto glass slides and were dipped into a 3 ml solution of 100mM octadecanethiol for 48 hours. At the end of 48 hours, the glass slides were pulled out, the solution was swirled and ultrasonicated prior to absorption studies.

#### **2.4.1.7 Involvement of surfactant and polymer at the interface**

We have employed two methods to investigate the effect of surfactants on the nature of the Au and Ag nanostructures formed at the liquid-liquid interface.

In method 1, the first step involved the phase transfer of AuCl<sub>4</sub><sup>-</sup> (16µ mole) or AgNO<sub>3</sub> (16µ mole) into the organic phase (toluene, 10 ml) by TOAB (3.6µ mole), followed by the addition of triphenylphosphine (PPh<sub>3</sub>, 16µ mole). The addition of PPh<sub>3</sub> changes the color of the organic layer from deep orange to colorless. In the second step, hydrazine (50 µl, 0.5 m mole) was gently added to the aqueous layer (16 ml) to initiate the reduction at the interface. To obtain dendritic structures of Ag, the concentration of AgNO<sub>3</sub> was increased (48µ mole).

In method 2, an organometallic precursor such as  $\text{Au}(\text{PPh}_3)\text{Cl}$  or  $\text{Ag}(\text{PPh}_3)_4\text{NO}_3$  was taken along with TOAB in the toluene phase. In a typical preparation, 16  $\mu$  moles of the metal precursor in toluene (10 ml) formed the top organic layer. Hydrazine (0.5 m mole) was then added to the aqueous phase (16 ml) to carry out the reduction. We have also carried out experiments following method 2 by using an aqueous solution of CTAB (5.5  $\mu$  mole in 16 ml) instead of TOAB in the organic phase. The concentration of the surfactants used by us is below the critical micellar concentration.

In the case of Ag nanostructures, during the phase transfer of  $\text{Ag}^+$  ions from water to toluene, some amount of AgBr formed and got precipitated (first step, method 1). The precipitated AgBr was washed off before proceeding to step 2 for reduction.

We have carried out experiments in the presence of PVP in the organic phase using method 2. The procedure was as follows. 2mg of PVP (M.W. 40,000) was dissolved in 0.5 ml chloroform and the solution was mixed with 10ml of toluene containing 16  $\mu$  mole of  $\text{Au}(\text{PPh}_3)\text{Cl}$ . The whole mixture was ultrasonicated for 2 minutes. The aqueous phase contained 50  $\mu$ l of hydrazine in 16 ml of water.

The concentrations of surfactant used were extremely low. As these surfactants prefer interfacial site to bulk phase, even small quantities of the surfactants were sufficient in number to crowd the interface. Since reactions take place only at the interface, we presume that the surfactants were used to their maximum efficiency.

### **2.4.2 Characterization Techniques and methods**

#### **Transmission electron microscopy (TEM)**

Samples for TEM were obtained by piercing the film with a holey copper-carbon grid from above and gently lifting it along with a tiny portion of the film, following which it was washed with toluene and left to dry overnight. A JEOL 3010 transmission electron microscope operating at 300 kV was employed for TEM studies.

In the case of superposition of crystal lattice plane with period  $l$ , and  $\alpha$  as the angle between lattice plane, a new set of fringes appear with period  $T$  due to

interference. These are known as Moiré fringes. These fringes are often found in TEM images and provide an important means to identify the dislocations in surface lattices, and are generally useful for identifying the relation between various lattice planes [386].

$$T = \frac{l}{2\sin\frac{\alpha}{2}}$$

### UV-visible spectroscopy

Samples for UV-Visible spectroscopy were obtained with a Perkin-Elmer Lambda 900 spectrometer by transferring the film on to a synthetic quartz substrate using the above procedure. Films deposited on quartz were placed perpendicular to the beam in a regular quartz cuvette. Thiol adsorption experiments were carried out by filling the quartz cuvettes with 2.5 ml of the thiol solution (10mM) in toluene. The reference cuvette contained a clean glass slide immersed in the thiol solution.

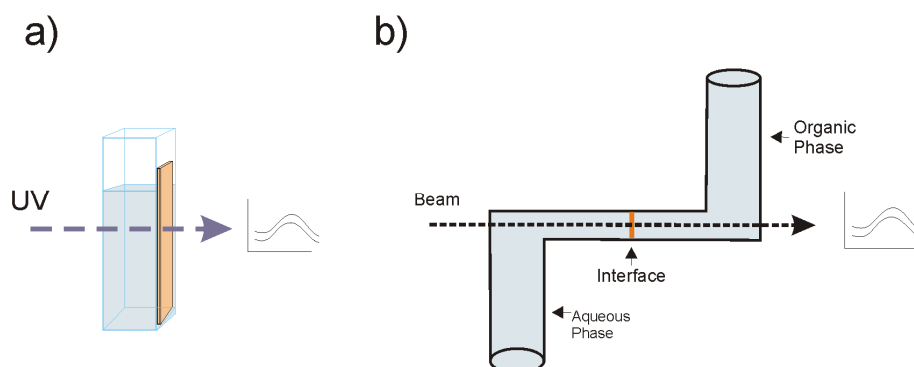


Figure 2.2 (a) The setup used for in-situ measurements of film disintegration using thiols and (b) the setup used to monitor the growth of film.

### Atomic force microscopy (AFM)

Samples for AFM consisted of films transferred by the above procedure on a clean Si(100) surface. Tapping mode AFM images were obtained using a multimode scanner from Digital Instruments operated with a Nanoscope IV controller. Both the amplitude and the phase images were simultaneously acquired. Standard etched Si cantilevers were used for this purpose. Contact mode atomic force microscopy (AFM)

images were obtained for films deposited on glass substrates employing a multimode scanner from Digital Instruments operated with a Nanoscope IV controller.

### **X-ray photoelectron spectroscopy (XPS)**

Samples for XPS were prepared by transferring the films onto graphite substrates. XPS was carried out with a ESCA LAB MK-IV spectrometer equipped with Al  $K\alpha$  (1486.6 eV) source. The binding energies reported here are with reference to the C(1s) level at 284 eV.

$$\varepsilon_{pe} = \hbar\omega - [\varepsilon_B(PE) + e\Phi_{sp}]$$

$e\Phi_{sp}$  is work function with respect to spectrometer is also spectrometer constant which is calibrated with a well known sample such as C or Au. Binding energy of photoelectron  $\varepsilon_B(PE)$ . Kinetic energy of photoelectron  $\varepsilon_{pe}$ .

### **Energy dispersive analysis of X-rays**

The films deposited on a graphite stub were used directly for Energy dispersive X-ray analysis (EDAX) measurements on a Leica S-440i microscope.

### **X-ray diffraction (XRD)**

X-ray diffraction measurements on the films deposited on glass were made with a Seifert 3000 TT diffractometer (Cu- $K\alpha$  radiation). The grain size and strain of the sample can be extracted from the width of the diffraction peak. These factors are signified by the broadening of the diffraction peaks. This is analogous to light diffracting from a grating where the line width is proportional to the number of diffracting grooves in the grating. This broadening effect was quantified by Scherrer [387]:

$$\Delta_{size}(2\theta) = \frac{\lambda}{D \cos(\theta_B)}$$

where  $\Delta_{size}(2\theta)$  is size difference (in radians) between the Full Width Half Maximum (FWHM) value of the Bragg peak for the sample and that of an 'ideal' crystal of finite width due to grain size effects. D is the average size of grain and  $\theta_B$  is the Bragg angle. An introduction of strain within a crystal lattice varies the inter-

atomic spacing, which tends to ‘smear’ the position of the diffraction peak:

$$\Delta_{strain}(2\theta) = 2\varepsilon \tan(\theta_B)$$

where  $\Delta_{strain}(2\theta)$  is the strain component of the angular difference in FWHM and  $\varepsilon$  is the lattice strain. In a sample where both these broadening effects occur, the grain size and strain can be calculated using the Hall-Williamson plot for a series of peaks, which is a linear plot representative of the total broadening effect:

$$\frac{\Delta_{total}(2\theta) \cos \theta_B}{\lambda} = \frac{1}{D} + \frac{2\varepsilon \sin \theta_B}{\lambda}$$

### **Optical Profiler**

Profile thickness measurements (Wyco NT1100 optical profilometer (Veeco, USA)) estimated the average thickness of the film to be 47 nm (Figure 2.48), thus confirming the 2D monolayer of nanocrystals.

### **Field Emission SEM**

Scanning electron microscopy (SEM) measurements (FESEM using Nova nanoSEM 600 (FEI)) were carried out on the film to study the morphology of the film.

### **Four Probe, Transport measurements**

Four-probe electrical resistance measurements were measured in the 40-300 K range on the nanocrystalline films deposited on mica using a home made set up connected to a Keithley multimeter. Rectangular electrical contacts separated from each other by 1 mm were made by Au sputtering using a Al-mask. No noticeable damage was seen following deposition of the electrodes.

### **Nanoindentation**

Nanoindentation on Au films was carried out using Nanoman, Veeco instruments. Calculation of hardness  $H = F/A$ , where  $F$  is indentation force and  $A$  is the area of indent, further for dent made by AFM cantilevers,

$$F = k \cdot x$$

$$F = \text{Spring constant (N/m)} \cdot \text{Trigger threshold (V)} \cdot \text{deflection sensitivity (nm/V)}$$

For indentation measurements carried out on Au films, deflection sensitivity was 218 nm/V and spring constant of cantilever was 192 N/m.

### Rheological measurements

All rheological measurements were carried out using a Physica interfacial rheology system (IRS), which consists of a commercial research rheometer (Physica MCR from Anton Paar) with an interfacial rheology cell based on bicone geometry as shown in Figure 2.3 [382].

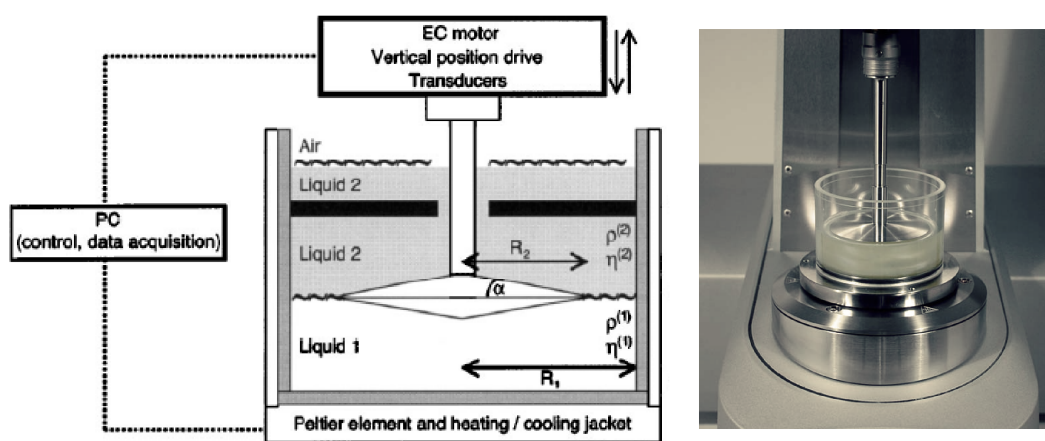


Figure 2.3 Schematic for the interfacial shear rheometer [388].

The 2D film of Ag nanocrystals was prepared in situ in the shear cell as follows: 16 mL of 6.25 mM NaOH in water (deionized, Millipore) and 330  $\mu$ L of 50 mM THPC in water was added to 95 mL of water. The edge of the bicone was positioned at the air-water interface with a precision of 1  $\mu$ m. A 110 mL portion of toluene containing 20 mg of the metal salt  $\text{Ag}_2(\text{PPh}_3)\text{Cl}_2$ , was added carefully along the cone axle without disturbing the liquid/liquid interface. The temperature of the interface was maintained at 22  $^\circ\text{C}$ . The raw data was numerically analyzed after each measurement to determine the interfacial moduli and the interfacial steady shear viscosity and takes into account the correction to the flow field from the bulk phases [382]. To estimate the particle size and the thickness of the film after the rheological measurements, the film was transferred to a Si substrate.

### Small angle x-ray scattering (SAXS)

The energy of the monochromatic beam was set to 21.9 keV (wavelength  $\lambda = 0.057$  nm) to allow the x-ray beam to pass through the upper liquid (toluene here) and x-ray reflectivity and diffuse scattering data was collected from the toluene-water interface. We also collected scattering data in the same geometry from the toluene bulk by moving down the interface 0.2 mm to subtract background arising from bulk scattering. The scattering intensity profile measured as functions of horizontal and vertical components of the wave-vector transfers  $q_y$  and  $q_z$ , being related to the out-of-plane and in-plane angles  $\theta_f$  and  $\phi$  (refer to Figure 2.4), provide information regarding the in-plane and out-of-plane ordering of nanocrystals formed at the liquid-liquid interface. A Langmuir trough was mounted on the liquid spectrometer using an active antivibration system, and two thin silicon wafers of equal heights were used near the entry and exit X-ray windows of the trough to anchor the toluene-water interface. The position of the interface was adjusted to minimize the meniscus by controlled addition and removal of water and monitoring sharpness of reflected beam at small  $\theta_i$ . Reflectivity data were collected using a point detector toluene-water interface by changing the incident and reflected angles and keeping these two angles equal ( $\theta_i = \theta_f$ ). For diffuse scattering measurements, position sensitive detector (PSD) was used to collect the data as a function of the in-plane angle ( $\phi$ ), keeping the incident grazing angle ( $\theta_i$ ) fixed at 80 millidegrees.

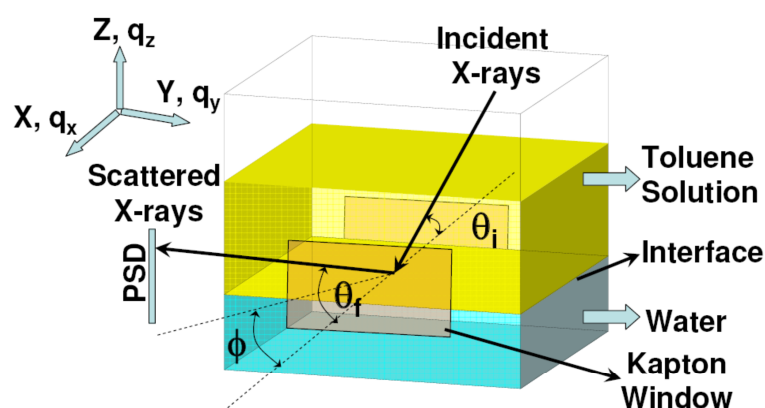


Figure 2.4 Schematics of the experimental geometry for X-rays scattering study of toluene-water interface using a trough.



In order to perform X-ray reflectivity and diffuse scattering measurements during the formation of Au nanocrystals at the toluene-water interface, we carried out the reaction at the interface between a metal-organic compound, Au(PPh<sub>3</sub>)Cl, in the toluene layer and the reducing agent THPC, in the aqueous layer. The process was repeated several times to confirm reproducibility of scattering data. All the measurements were performed at room temperature (23°C) with the incident beam size of 0.017 mm × 1.0 mm (V×H) defined using conventional slits. Details of the experimental arrangement are available in the literature [364, 365, 367].

## **2.5 Results and Discussion**

### **2.5.1 Nanocrystalline films of Au and other metals and their characterizations**

#### **2.5.1.1 Optical Absorption Spectroscopy**

As described in the experimental section, the Au precursor was taken in the organic phase and the aqueous phase was kept as medium for supplying the reducing agent. Within the first 5 minutes after the addition of the reducing agent to the aqueous phase, a thin transparent membrane like structure formed at the interface of the two liquids. It attained a faint pink color, indicating the reduction of Au and the formation of nanocrystals. Since the two phases are stable, interface was the only region where metal ions and its reducing agent existed together and thus reduction process took place only at that thin interfacial region. The nanocrystals were stable at the interface. As a result, the interfacial region got crowded with more number of nanocrystals over a period of time. This change was noticed in the form of brown thick layer of nanocrystals at the interface. This was also marked as the completion of the reaction. At the end, the interface had a thick floating film. This comprises of wrinkles as seen in Figure 2.6. At that instance, we assumed that the reaction was complete. Interestingly, these films can be collected on different types of substrates using lift-off technique. Even after transferring the films onto the substrate, it retains its shape and structure, which lead us to classify it as a film. For the optical and XRD studies, we chose glass substrate and for the electrical studies, we used mica, and for AFM studies, we collected the film on Silicon substrate and for TEM analysis, we collect it on copper grid as mentioned in the experimental section. Please note that, the film can be collected onto any substrate and the choice of substrate may be made

even at the end of synthesis. On analyses with TEM and AFM, we found that, due to constrained reaction volume, nanocrystals came closer to form a closed pack structure. Such closely packed arrangement of nanocrystals gives rise to various interesting optical and electrical properties as discussed in later chapters.

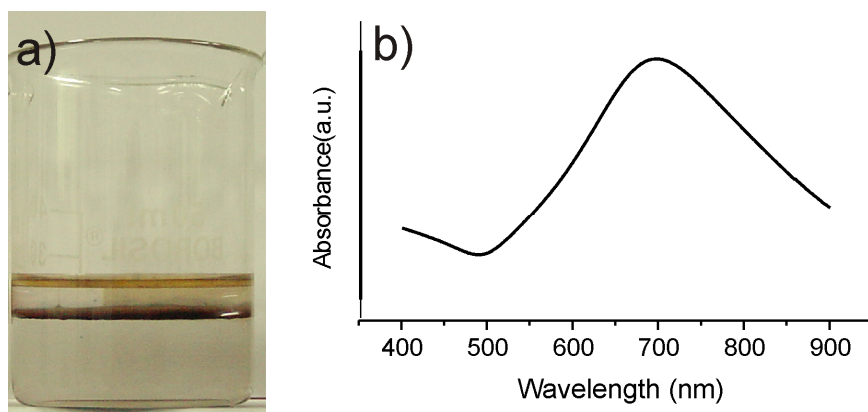


Figure 2.5 (a) Photograph of beaker showing Au film formed at the interface, (b) Typical absorption spectra from Au nanocrystalline film.

Figure 2.5a shows the photograph of beaker, taken after the completion of the reaction carried out at room temperature (30° C). The thick film at the interface is clearly seen. It is noteworthy that organic and aqueous bulk phases are still colorless, suggesting that the reaction has taken place only at the interface and both phases are devoid of nanocrystals. To further check the presence of nanocrystals in either media, we characterized the portion from bulk phases with UV-vis spectroscopy and TEM, and no nanocrystals were found. Figure 2.5b, shows a spectrum of the nanocrystalline film obtained at the liquid-liquid interface at room temperature. The absorption spectrum exhibits a broad band centered at 700 nm, with a very weak shoulder at ~ 540 nm. While the absorption band around 540 nm is characteristic of surface plasmons from uncoupled nanocrystals, the higher wavelength band at 700 nm is a typical response from an assembly of interacting nanocrystals. Such spectroscopic signatures, which are different for individual and assembly of nanocrystals, are discussed in later chapters.

Figure 2.6 shows photographs of the beakers containing fully formed Au film. The film appears different in colour depending on the nature of light source and its position, relative to the interfacial film. Figure 2.6a shows the photograph where light was reflected by the nanocrystalline film present at the interface, while Figure 2.6b

shows the photograph where light was transmitted through the film. The difference in the photographs is due to the angle at which light is scattered by the nanocrystals present in the film. Later in this chapter, we will learn about this phenomenon through extensive studies made using optical spectra. The scattering process is different for different source of light, as seen in Figure 2.6b and c.

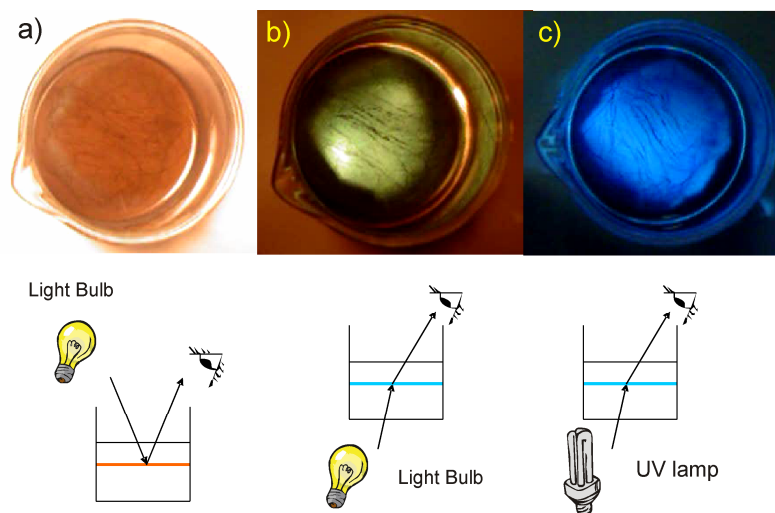


Figure 2.6 Optical view (top view) of fully formed film at the interface, (a) reflection of light, (b) transmission of light, (c) transmission of selected range of light.

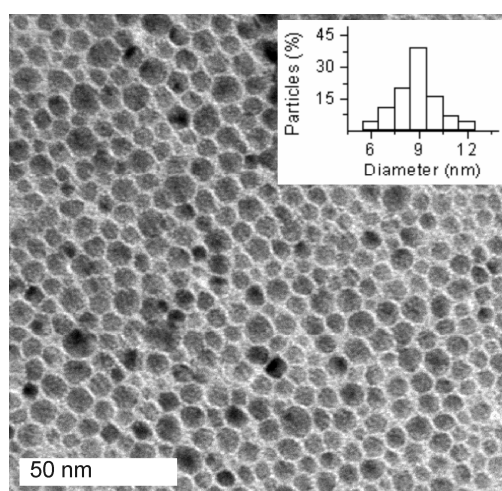


Figure 2.7 TEM micrograph of the as-prepared standard film obtained after 24 h from a liquid-liquid interface containing a 1.5 mM toluene solution of  $\text{Au}(\text{PPh}_3)\text{Cl}$  and 330  $\mu\text{L}$  of 50 mM THPC in 16 mL of a 6.25 mM aqueous NaOH solution. The scale bar corresponds to 50 nm. The inset shows a histogram of the diameter distribution obtained from a few hundred particles.

Figure 2.7 shows a TEM image of an as-prepared film of Au nanocrystals, obtained after maintaining the organic-aqueous interface with the reactants for 24

hours. The as-prepared film consists of nanocrystals with diameters in the range 5.5 to 14 nm with a mean of  $\sim 9$  nm. The nanocrystals are present in a close packed arrangement with typical interparticle distance of 1.5 nm. A lower magnification image revealed that the film essentially consists of a monolayer of nanocrystals with a high coverage ( $> 97\%$ ).

The immediate challenge that we faced after the preparation of such films, was to transfer them onto a solid substrate, which later turned out to be the most advantageous property of these films. Obtained films float at the interface and are very fragile, and thus transfer of the films onto substrate requires extra care. We mostly used lift-off method to collect the films. As a result, we could deposit these films onto any substrate. Which is a great advantage as we collected these films on different substrates like mica, silicon, glass or, NaCl crystal as required for various characterization and studies.

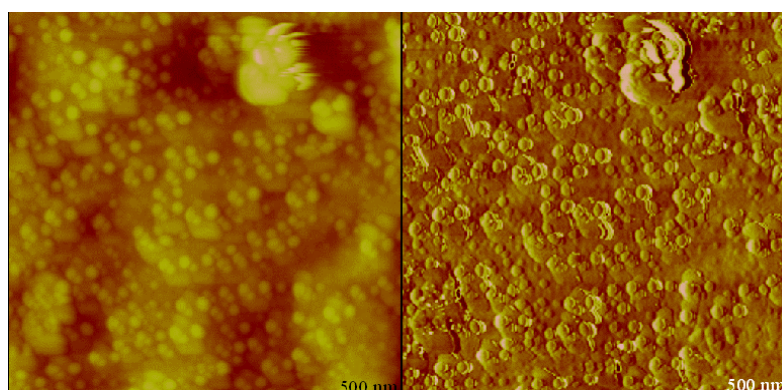


Figure 2.8 AFM images of the as-prepared film in the tapping mode: (left) amplitude and (right) phase imaging.

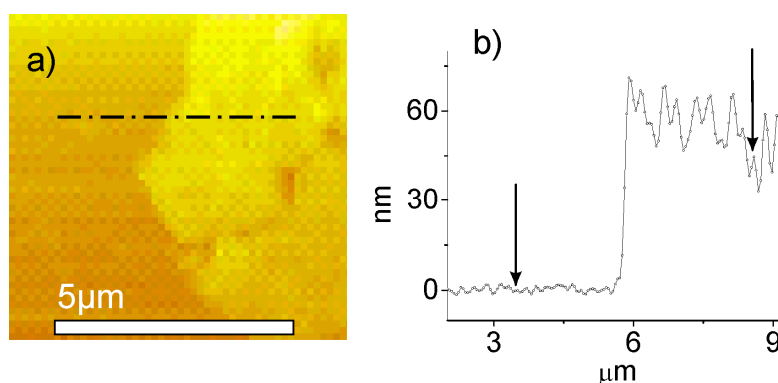


Figure 2.9 (a) Contact mode AFM image showing the boundary of the Au film on a mica substrate, (b) the z-profile of the film boundary.

Tapping mode AFM images of the as prepared Au film reveals several features, which are mostly spherical in nature (Figure 2.8), with diameters between 7 - 16 nm, somewhat higher than those from the TEM measurements. It is therefore possible that the nanocrystals consist of a layer of the organic ligand which are invisible in the TEM measurements [86, 389]. AFM images also reveal regions where the nanocrystals are aggregated. Wider scans covering few microns yielded a r.m.s roughness of  $\sim 35$  nm with the maximum peak to valley distance of 80 nm.

For thickness measurements, images acquired at the broken edges of the films were used. The image in Figure 2.9a shows one such boundary of the 30°C film on mica substrate and the height profile in Figure 2.9b gives an estimate of the thickness to be  $\sim 60$  nm, which corresponds to around 8 monolayers of nanocrystals. The jagged line profile on the right corresponds to the variation in the film thickness with trenches of  $\sim 7$  nm indicating missing particles in the top layer. Several such measurements have shown the thickness of the films to be in the 40-140 nm range. The above observations suggest that the growth of the Au film is essentially limited to the liquid-liquid interface.

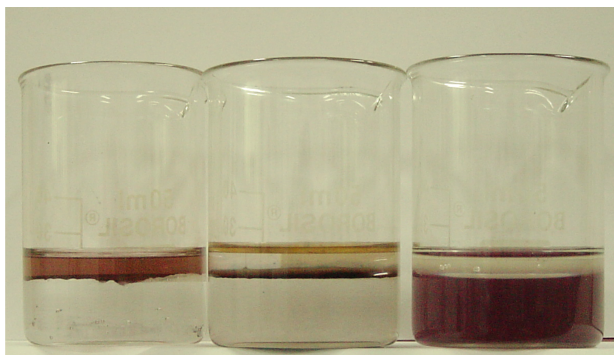


Figure 2.10 Nanocrystalline film of Au formed at the toluene-water interface (middle). Au is introduced as a toluene solution of  $\text{Au}(\text{PPh}_3)\text{Cl}$ , and partially hydrolyzed THPC in water acts as a reducing agent. The film is obtained when the two layers are allowed to stand for several hours. When dodecanethiol is added to the toluene layer, the film breaks up, forming an organosol (left), and mercaptoundecanoic acid added to water produces a hydrosol (right).

With the addition of a few micromoles of capping agents such as dodecanethiol or octylamine to the toluene layer, the Au film at the interface disappeared within minutes accompanying a distinctive pink coloration at the top layer (Figure 2.10), characteristic of an Au organosol. Similarly, addition of a few micromoles of MUA to

the aqueous solution results in complete dissolution of the film after few hours and transfer of its contents to the aqueous layer (Figure 2.10). The sols thus obtained were characterized by TEM and UV-Visible spectroscopy. Samples for TEM were prepared by depositing a few drops of the sols on a holey carbon coated copper grid and allowing it to evaporate overnight in a desiccator.

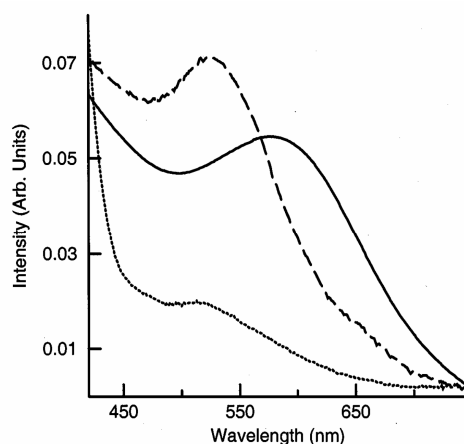


Figure 2.11 UV-vis spectra of the as-prepared standard film on a synthetic quartz substrate (solid line), octylamine-capped nanocrystals in toluene (--), and mercaptoundecanoic acid-capped nanocrystals in water (···).

UV-Visible spectra of the as-prepared Au film as well as of the hydrosol and organosol are shown in Figure 2.11. All the spectra exhibit bands due to the surface plasmon, the position and intensity depending on several factors such as the diameter of the nanocrystals, the nature of the ligand and the refractive index of the surrounding medium [61, 88]. The film on quartz substrate exhibits a broad band centered at 575 nm, while the sols show plasmon bands at  $\sim 530$  nm. The band due to the octylamine-capped nanocrystals (organosol) is more intense compared to that of the MUA capped nanocrystals from the hydrosol, probably due to a dampening of the surface plasmon by the thiol. The higher wavelength of the plasmon band of the film could be due to the relatively higher dielectric constant of the surrounding medium.

The organosol and the hydrosol also consist of nanocrystals with similar average diameters, but with a somewhat wider size distribution as can be seen from Figure 2.12a and b. A number of multiply twinned particles are also present in these cases. The close packing of nanocrystals present in the film is not seen in the images in Figure 2.12a and b.

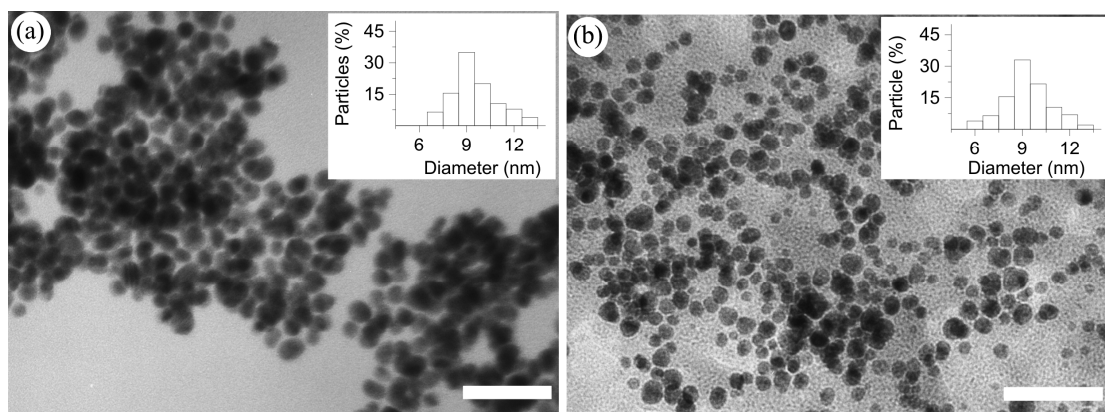


Figure 2.12 TEM micrographs of (a) dodecanethiol-capped nanocrystals in the organosol and (b) mercaptoundecanoic acid-capped nanocrystals in the hydrosol. The scale bar corresponds to 50 nm. The insets show histograms of the diameter distribution obtained from a few hundred particles in each case.

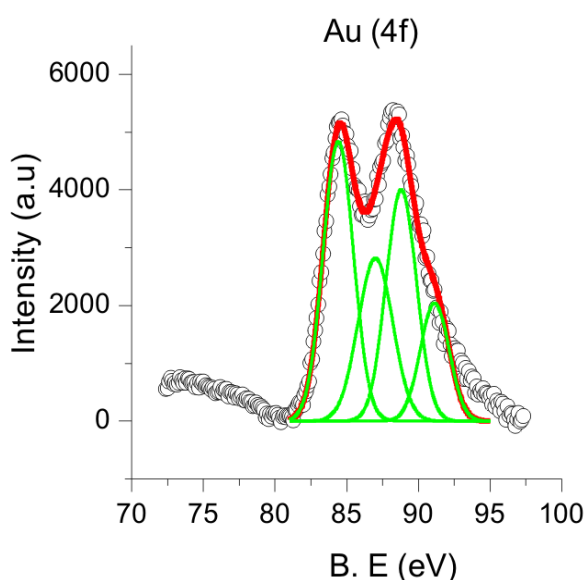


Figure 2.13 XPS spectrum of as-prepared film: signal from Au (4f level).

The surface composition of the film was probed using core-level XPS. The Au(4f) spectra showed a broad doublet, which could be fitted to two Au species with 4f7/2 binding energies of 84 and 85.2 eV as seen in the Figure 2.13. This is consistent with the picture of a metallic core surrounded by a layer of Au atoms bound to the capping agents [390]. The latter may consist of triphenylphosphine ligands and ionic species from THPC. The spectrum revealed the presence of phosphorous and chlorine in the film.

### 2.5.1.2 Effect of time

The nature of the emerging film was examined by systematically varying factors such as contact time at the interface, the relative amounts of reducing agent and the Au precursor. In Figure 2.14, we show the TEM images of the films sampled after a contact times of 3, 6 and 9 hours respectively. These images may be compared with that of the standard film shown in Figure 2.7 corresponding to a contact time of 24 hours. Clearly, an increase in contact time increases the coverage of the film on the substrate, with no observable change in the average diameter of the nanocrystals. Although a more detailed study on the growth of nanocrystals is essential, our observations seem to suggest that the particle growth reaches saturation with time while fresh nucleation sites are constantly being created.

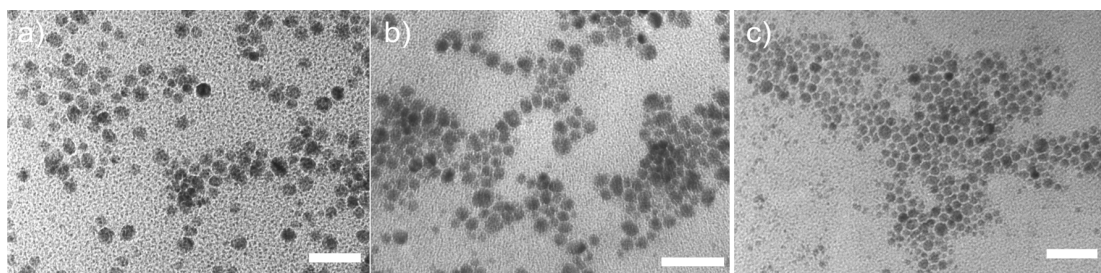


Figure 2.14 TEM micrographs of the films collected from a liquid-liquid interface containing a 1.5 mM toluene solution of Au(PPh<sub>3</sub>)Cl and 330  $\mu$ L of 50 mM THPC in 16 mL of a 6.25 mM aqueous NaOH solution with different contact times: (a) 3, (b) 6, and (c) 9 h. The scale bars in all cases correspond to 50 nm.

### 2.5.1.3 Effect of concentration

Use of high concentrations of the reducing agent results in less uniform films with altered distributions in the particle diameter as can be seen from a comparison of Figure 2.15 with Figure 2.7. When the concentration of THPC was doubled, the distribution was somewhat narrower with the average diameter of  $\sim 9.5$  nm (Figure 2.15a). A further increase in the concentration of the reducing agent results in broader distributions in diameters (Figure 2.15b). We notice that the close packing of the particles seen in Figure 2.7 is lost at higher concentrations of the reducing agent. The films formed at higher concentrations of the reducing agent also exhibit a distinct tendency to form multilayers. On the other hand, when the concentrations of the Au precursor and reducing agent were increased simultaneously, the film consisted of



primarily a monolayer of nanocrystals with a broader size distribution and a higher coverage (Figure 2.15). The broader distribution hinders the formation of the close packed arrangement of nanocrystals.

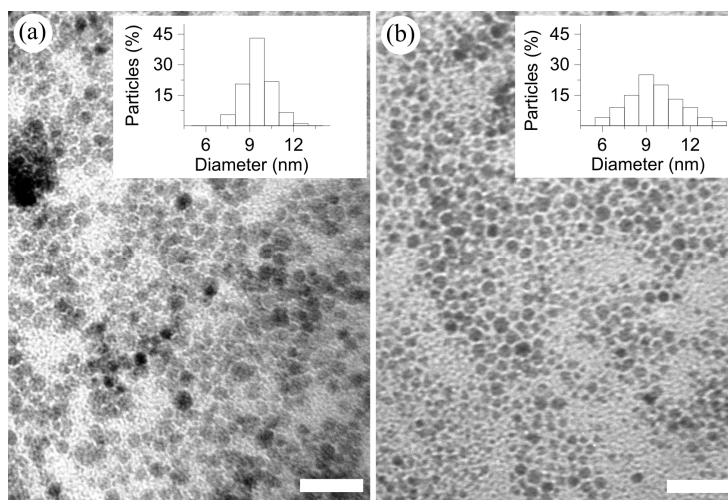


Figure 2.15 TEM micrographs of films collected after 24 h from a liquid-liquid interface containing a 1.5 mM toluene solution of  $\text{Au}(\text{PPh}_3)\text{Cl}$  and 16 mL of a 6.25 mM aqueous NaOH solution with (a) 660 and (b) 1200  $\mu\text{L}$  of 50 mM THPC. The concentrations correspond to metal/reducing agent ratios of 1:2 and 1:4, respectively. The scale bars correspond to 50 nm. The insets show histograms of the diameter distribution obtained from a few hundred particles in each case.

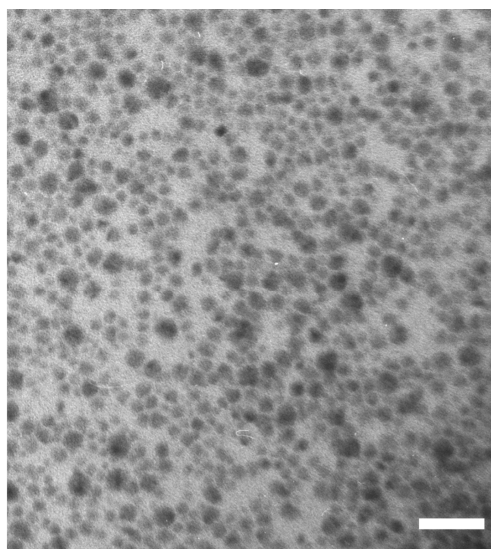


Figure 2.16 TEM micrograph of the film collected after 24 h from a liquid-liquid interface containing a 7.5 mM toluene solution of  $\text{Au}(\text{PPh}_3)\text{Cl}$  and 16 mL of a 31.25 mM aqueous NaOH solution with 1650  $\mu\text{L}$  of 50 mM THPC. The concentrations of the reactants are, therefore, 5 times the usual concentration. The scale bar corresponds to 50 nm.

The choice of the ingredients deserves a mention. It seems important that the right choice of the metal precursor and the reducing agent is employed to obtain stable films at the liquid-liquid interface. For instance,  $\text{Au}^{3+}$  ions complexed with tetraoctylammonium bromide in toluene did not form a film at the interface, but yielded an organosol on reduction with THPC. Similarly, stronger reducing agents such as sodium borohydride fail to produce uniform nanocrystalline films. The choice of the organic solvent also seems important. While we were able to obtain stable films with benzene and dichloromethane, solvents such as octanol were deterrent to film formation.

#### 2.5.1.4 Effect of physical parameters like temperature, vibration and viscosity

Figure 2.17 shows TEM images from the sample obtained from the interface reaction that was under constant externally induced vibrations. We notice the formation of very small size particles at higher vibrations. The amplitude of vibrations was kept similar in all cases. We have not studied the effect of change in amplitude of vibrations. From another study, we have found that when the reaction was carried out on vibration free table, very small nanocrystals of size 1.3 and 2.4 nm were obtained.

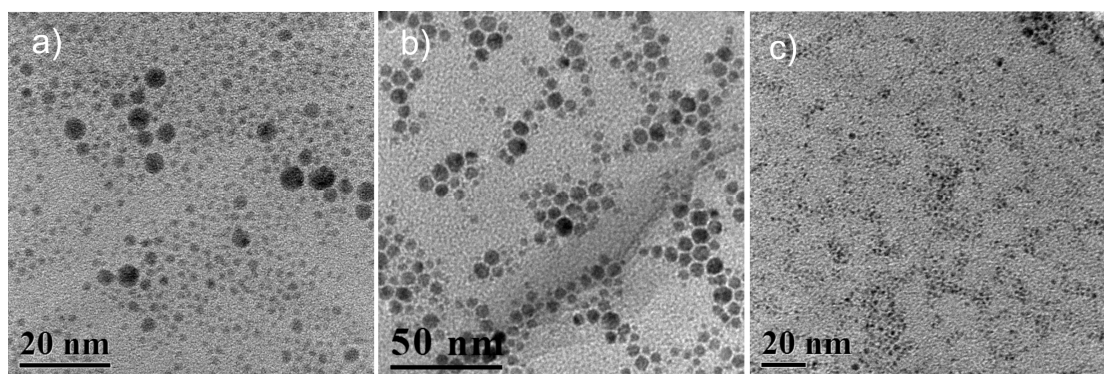


Figure 2.17 TEM micrograph of the film from liquid-liquid interface prepared at (a) 50 Hz, (b) 200 Hz and (c) 600 Hz.

Figure 2.18 shows TEM images of Au nanocrystalline film in which glycerin was added to the water phase. We added glycerin to study the effect of change in viscosity of aqueous phase and thereby changing the surface tension offered by the aqueous phase. As the structure of interface is governed by the difference in surface tension of two liquids, also with change in lateral force one would expect a change in the

packing of nanocrystal or even the chemistry by affecting the diffusion of reducing molecules or Au ions near the interface. We observe a mosaic pattern of nanocrystals. We also find that these nanoparticles have sharp edges, unlike in the usual case.

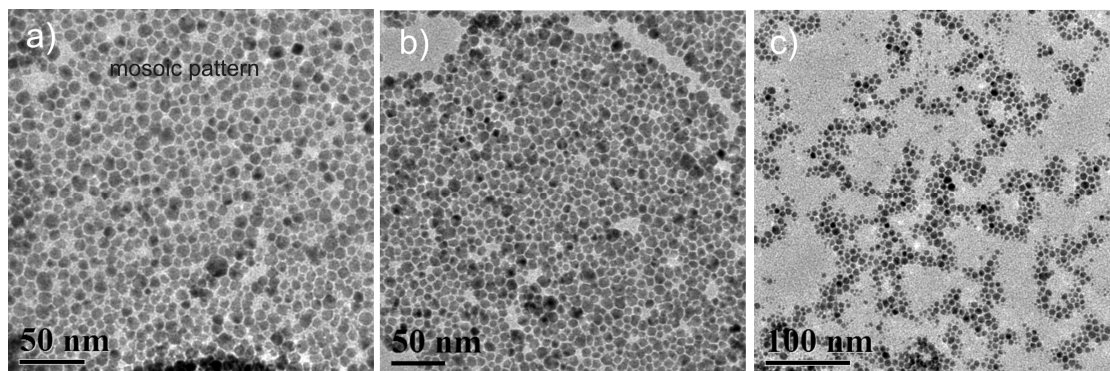


Figure 2.18 Effect of viscosity for different water: glycerin ratios (a) 1:3, (b) 1:1 and (c) 3:1.

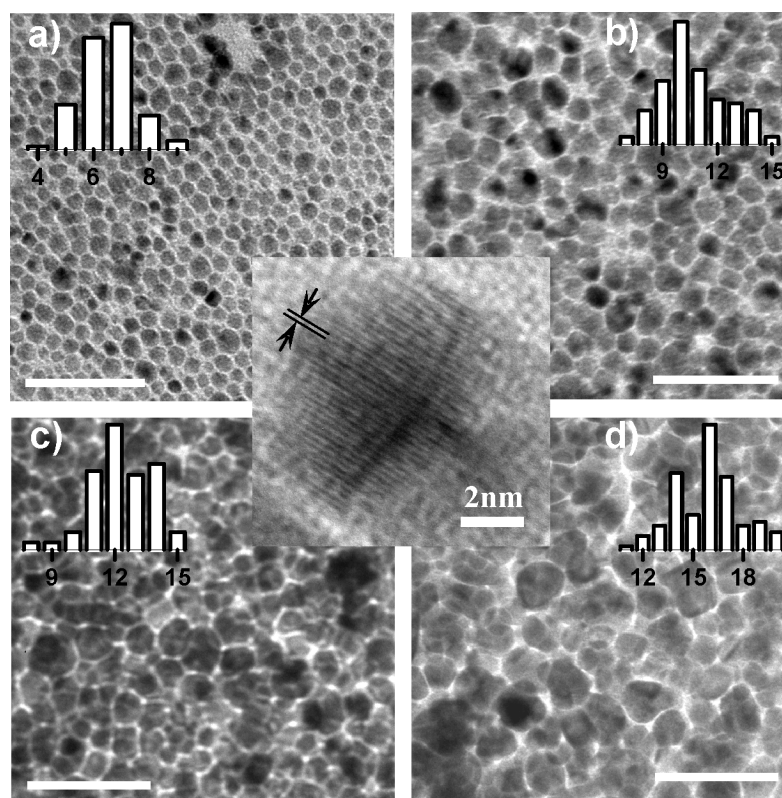


Figure 2.19 Transmission electron micrographs of the ultrathin nanocrystalline Au films prepared at the liquid-liquid interface at (a) 30°C, (b) 45°C, (c) 60°C and (d) 75°C. The histograms of particle size distribution are also shown. The scale bars correspond to 50nm. A high-resolution image of an individual particle is shown at the center.

Figure 2.19 shows TEM images of the nanocrystalline Au films obtained at the liquid-liquid interface held at different temperatures. The films comprise of close-

packed arrays of nanocrystals separated from one another by  $\sim 1$  nm. In the film prepared at  $30^\circ\text{C}$  (Figure 2.19a), the particles appear uniformly spherical with a narrow size-distribution. High-resolution images show that the nanocrystals were mostly single crystalline as shown in the inset at the center of Figure 2.19. The image shows distinct (111) planes with a separation of  $\sim 2.3$  Å. With increase in the interface temperature, however, particles of uneven shapes and sizes tend to form, some of them exhibiting multiply twinned structures (see Figure 2.19 1d). The histograms shown alongside reveal how the size range of the nanocrystals increases progressively with the increase in temperature. The mean diameters of the nanocrystals formed at  $30^\circ$ ,  $45^\circ$ ,  $60^\circ$  and  $75^\circ\text{C}$  are 7, 10, 12 and 15 nm respectively. While hexagonal close-packing, typical of self-assembled nanocrystals [3], is found in films prepared at  $30^\circ\text{C}$ , those prepared at higher temperatures exhibit increased disorder. Thus, the high-temperature films somewhat resemble sputtered nanogranular Au films. Irrespective of the order in the film, the interparticle separation is, however, nearly constant at  $\sim 1$  nm perhaps due to the organic coating present on the particles. It is to be noted that what is shown in TEM micrographs in Figure 2.19, is only a monolayer structure of the film.

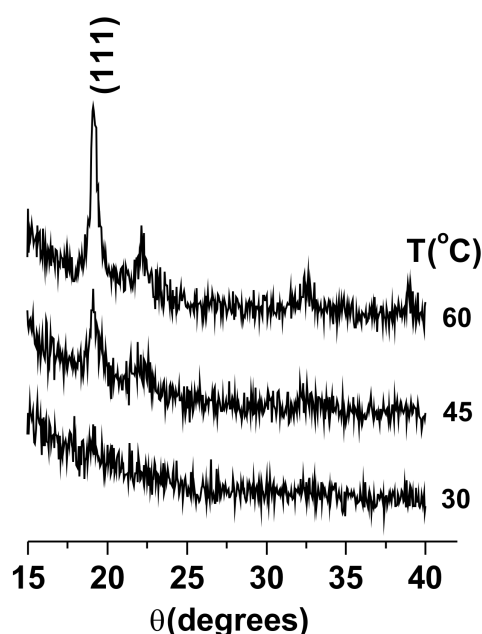


Figure 2.20 X-ray diffraction patterns of the nanocrystalline Au films obtained at different temperatures after transferring to glass substrates (radiation, Cu  $K_\alpha$ ).

The crystallinity of the Au nanocrystals in the films is also revealed by the X-ray diffraction patterns shown in Figure 2.20. While the films obtained at 45° and 60°C exhibit prominent (111) peaks ( $d = 2.33 \text{ \AA}$ ), the film obtained at 30°C shows weak and broad reflections due to the small particle size. The growth of the (111) peak with the increase in the interface temperature reflects the increase in the particle size. The particle sizes estimated from the width of the X-ray reflections are 5 and 6 nm for 45° and 60°C respectively, somewhat lower than the TEM estimates.

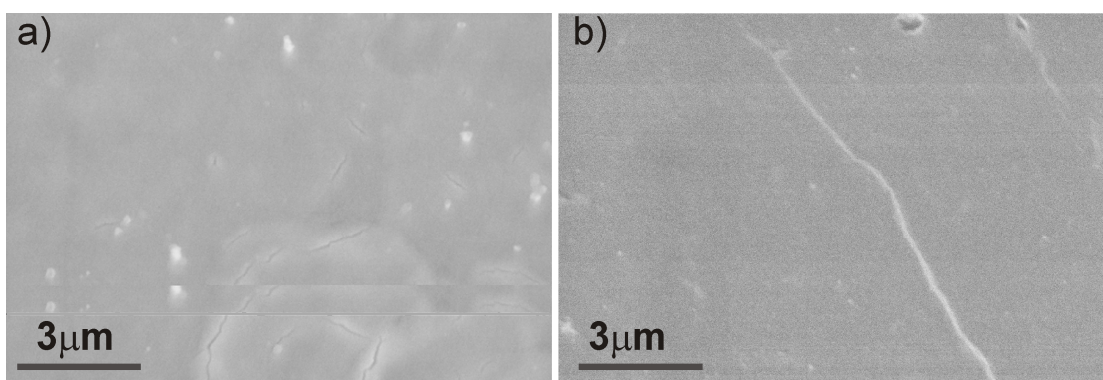


Figure 2.21 Scanning electron micrographs of the nanocrystalline Au films obtained at (a) 30°C and (b) 60°C after transferring to mica substrates. The scale bars correspond to 1 μm.

The morphology of the nanocrystalline films was monitored using SEM. As can be seen in the images in Figure 2.21, the films are fairly smooth and continuous over several tens of microns, although a few micropits and cracks are present. The film prepared at 30°C shows relatively a greater number of pits and cracks and that formed at 60°C exhibits longer cracks with very few pits. The widths of the pits and cracks do not generally exceed 300 nm. The AFM images covering a few micrometers yield a rms roughness in the range 30-35 nm with a maximum peak-to-valley distance of ~ 80-100 nm. However, we did not observe discernible trend in the film thickness with the interface temperature.

Electron transport properties of the films are interesting as demonstrated in Figure 2.22. As seen from the figure, the resistance of the 30°C film is in range of MΩ while that of the 45°C film is in the kΩ range for the given configuration of the electrodes. The resistance of the films formed at higher temperatures (60° and 75°C) is of the order of few ohms. Interestingly, we observe a “metallic type behavior” in the films prepared at higher temperatures (Figure 2.22c and Figure 2.22d) where the size

of the nanocrystals is also higher (Figure 2.19c and Figure 2.19d). Assuming the average thickness of the films to be 100 nm, we estimate the values of the temperature coefficient of resistance to be  $\sim 1.7 \times 10^{-11} \Omega\text{m/K}$  and  $4.7 \times 10^{-11} \Omega\text{m/K}$  respectively for the 60°C and the 75°C films. These values are to be compared with the value of  $8.22 \times 10^{-11} \Omega\text{m/K}$  of bulk Au. However, the estimated resistivity values ( $\sim 10^{-4} \Omega\text{cm}$ ) are higher than that of bulk Au ( $1.3 \times 10^{-6} \Omega\text{cm}$ ). These values are comparable to the reported resistivity of Au monolayer films anchored to polystyrene substrate [391]. The films obtained at 30° and 45°C are essentially activated conductors with small activation energies of 11 and 1 meV respectively as estimated from the Arrhenius plots [392, 393]. The presence of pits in these films may contribute to the high resistance (see Figure 2.21a). The electrical behavior of the films found by us resembles that of the protected Au-monolayer cluster films reported by Murray et al. [394] and of the dithiol- linked nanoparticle network by Brust et al. [395, 396].

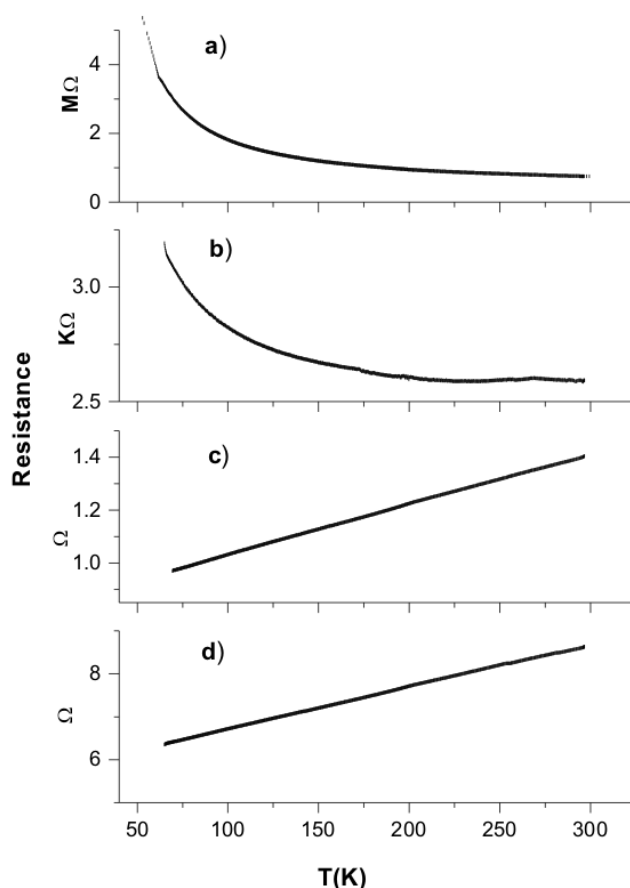


Figure 2.22 Temperature variation of the electrical resistance of the nanocrystalline Au films prepared at (a) 30°C, (b) 45°C, (c) 60°C, and (d) 75°C, (current used, 10 mA).

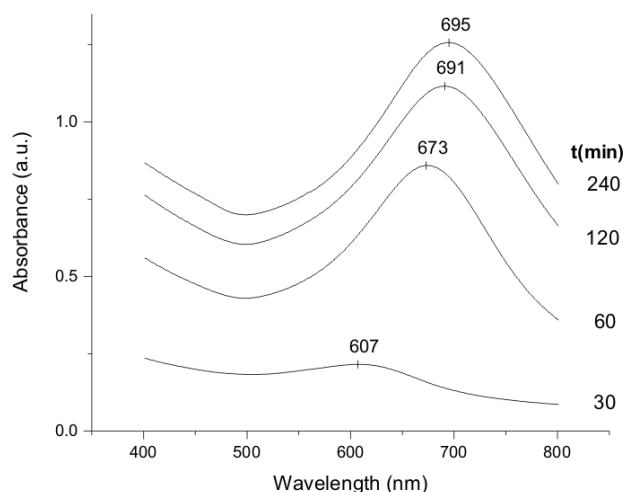


Figure 2.23 Evolution of the optical absorption spectra with the growth of the nanocrystalline Au film at the interface. Interface temperature was 45°C. The spectra were measured ex-situ. Each time, the growth was arrested by transferring the film to a glass substrate.

The Au films formed at all the four temperatures exhibit a strong absorption band around 700nm. This wavelength is rather long compared to the plasmon absorption observed at  $\sim 540$  nm in colloidal Au nanocrystals in solution. The position and the intensity of the plasmon band in such nanocrystal assemblies are truly indicative of the state of aggregation of the nanocrystals [94, 225, 301, 313, 369, 397, 398]. The red shifted band observed here may arise from the proximity of the nanocrystals in the film. This can be seen from Figure 2.23 where we demonstrate how the intensity of the plasmon absorption band grows as a function of the preparation time allotted for the film at the liquid-liquid interface held at 45°C. In the initial stages, the film is very fragile and looks dull red like colloidal Au, and exhibits the plasmon band centered around 600 nm. After an hour of growth at the interface, the film becomes robust with typical golden yellow color and gives rise to a band at 670 nm. After 120 minutes of growth at the interface, we found that the band is shifted to even longer wavelength  $\sim 690$  nm with an accompanying increase in the intensity. Beyond 120 minutes, the absorption band shows negligible changes. At this stage, the film is presumably well packed with fully grown nanocrystals, increasing the electronic coupling. This system is somewhat comparable to the one described by Rechberger et al. [313], and Haynes et al. [301] who monitored optical properties of interacting nanocrystals by varying the interparticle distance. The red shift of the plasmon band with decreasing distance

was interpreted by these workers as due to the increasing dipole-dipole interaction between the particles. Similar observations have been made in the case of evaporated metal films [399, 400]. However, we performed more experiments to trace the evolution of the film in order to avoid any substrate effects [401], as red shift in plasmon has been observed due to substrates contribution. For that purpose, we designed a special cell as described in the experimental section. The objective was to create the interface perpendicular to the UV beam, unlike in the previous experiments, where we get the interface parallel to ground as well as to the UV beam. As seen in Figure 2.24, during very early stages of the reaction, there is no absorption in the visible range, the 540 nm plasmon band develops over a period of time and gradually red shifts due to coupling. In-situ spectra recorded in this geometry confirms that the red shift is not because of substrate effect, and glass or quartz can be used as substrate for future studies.

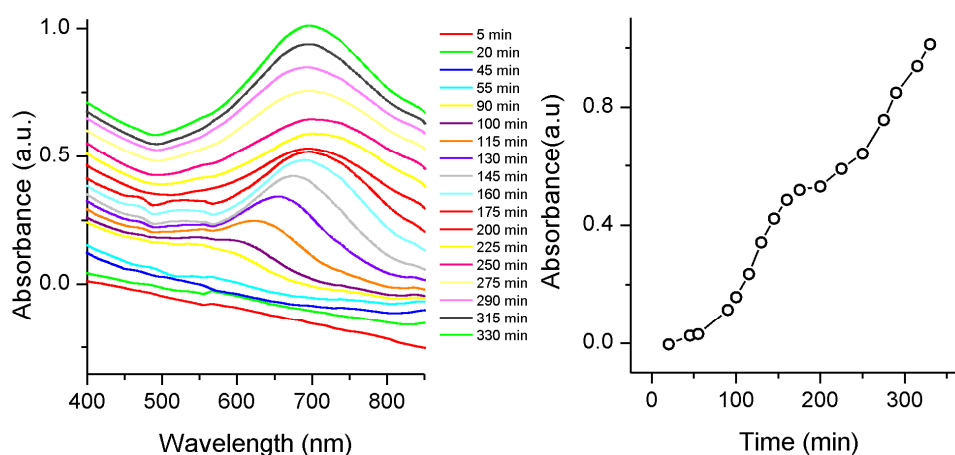


Figure 2.24 Evolution of optical absorption spectra (left). Variation in the absorption intensity of plasmon peak normalized with respect to the final intensity (right).

We have carried out resistance measurements on the films collected at the different stages of growth at the liquid-liquid interface held at 75°C. In Figure 2.25, we show how the film collected after 45 minutes of growth behaves like an activated conductor while that collected after 180 minutes is metallic. The latter is similar to the data shown in Figure 2.22 corresponding to the film that was collected after 12 hours of growth at the interface at 75°C. TEM images shown alongside in Figure 2.25 provide an estimate of the mean particle sizes of 11 and 14 nm respectively. These values may be compared with those obtained from Figure 2.19. Clearly, the contact



time and the temperature have a similar influence on the film properties. The films prepared with different initial concentrations of the AuPPh<sub>3</sub>Cl precursor reveal that with low concentrations of 2 mM or less, the films are extremely thin and unstable in spite of standing for several hours at the interface at room temperature. Furthermore, the aqueous layer developed coloration due to formation of the Au sol. At higher concentrations of the precursor (8 and 16 mM), good quality films were obtained within 24 h. The TEM images, however, revealed no noticeable differences in the size of the nanocrystals (mean, 15 nm).

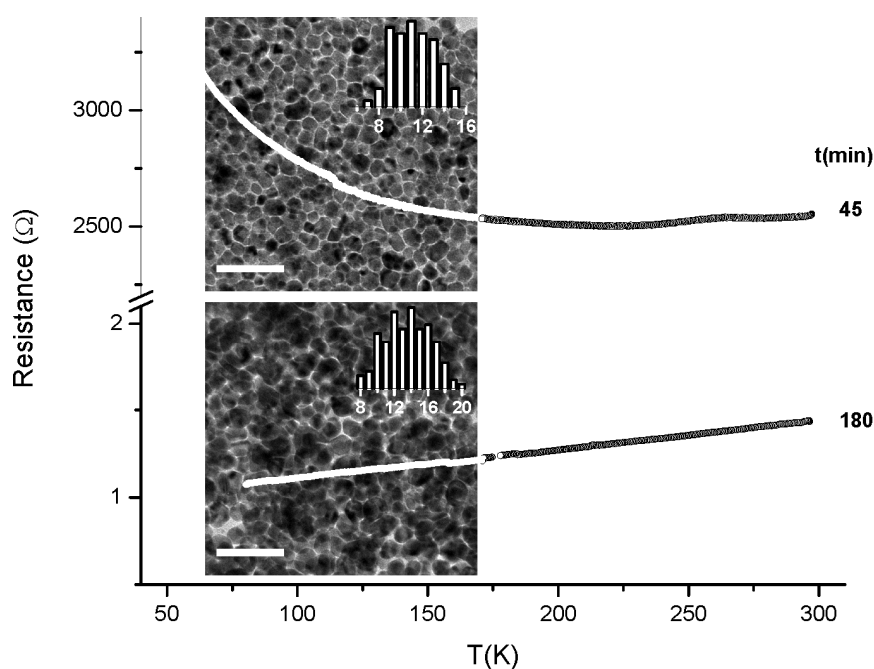


Figure 2.25 Temperature variation of the electrical resistance of the nanocrystalline Au films after 45 and 180 minutes of growth at the liquid-liquid interface at 75°C (current used, 10 mA). The corresponding TEM micrographs of the films are shown along with the histograms.

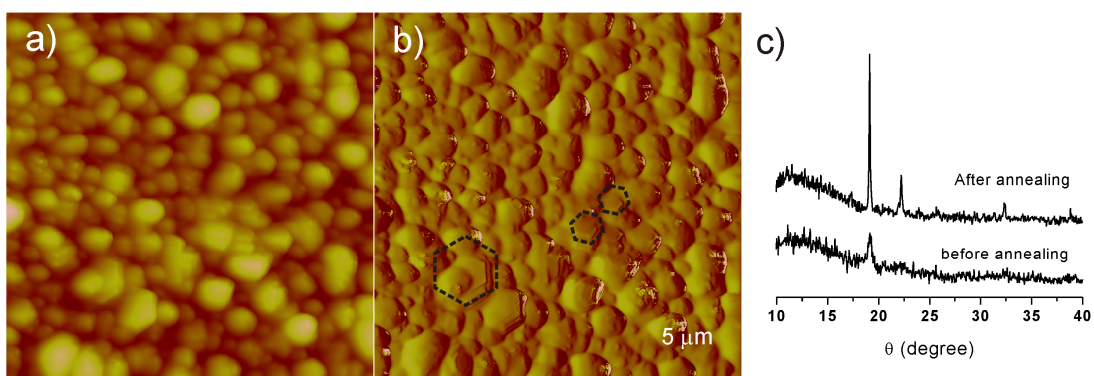


Figure 2.26 (a), (b) AFM image of Au film annealed at 300°C, the film was prepared at 75°C and (c) XRD pattern from the same before and after annealing.

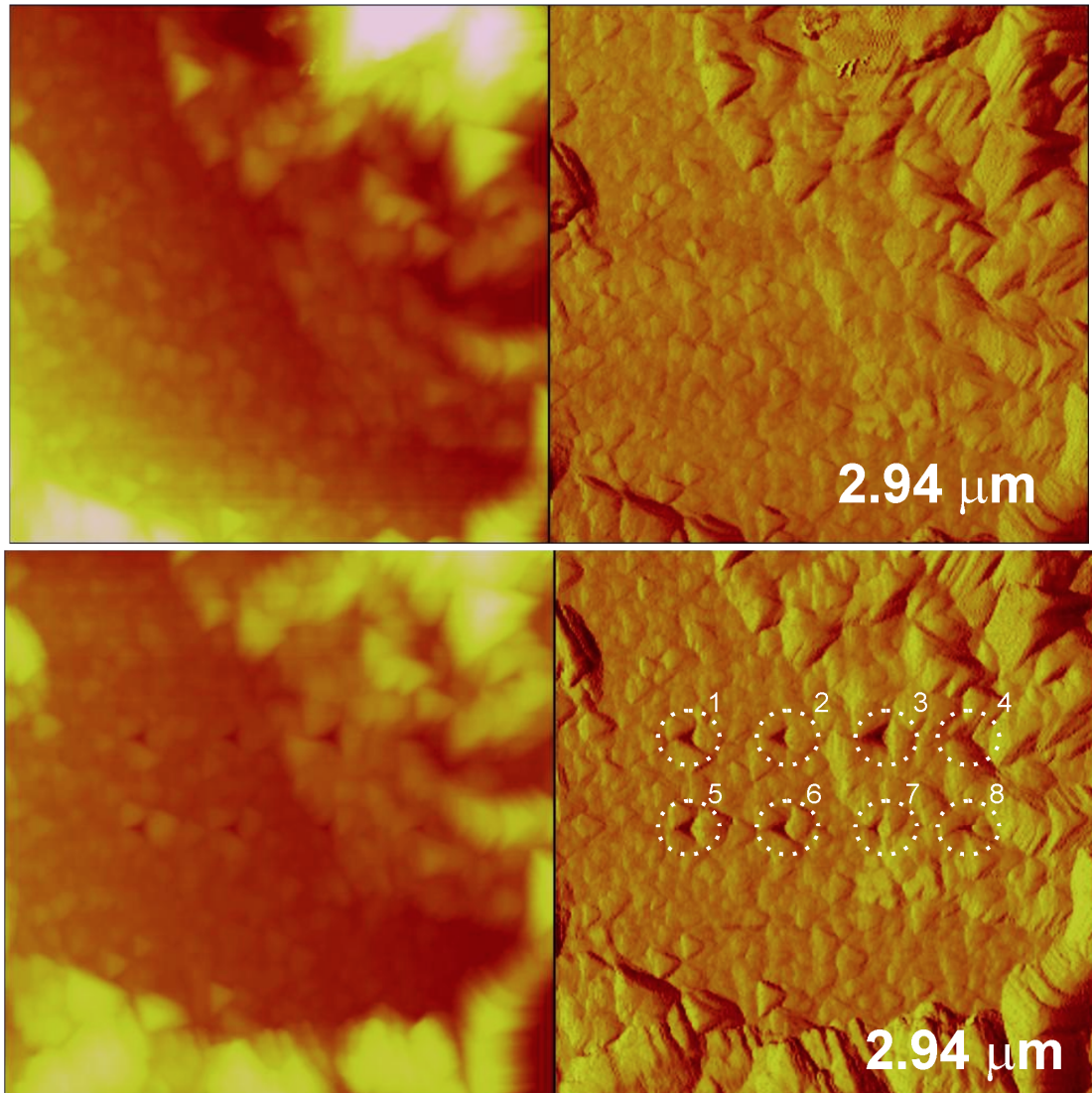


Figure 2.27 Nano indentation on as prepared Au films (top) and after indentation (bottom). Marked circles show various indented regions.

We studied the mechanical properties of Au nanocrystalline film using nanoindentation. Nanoman (veeco, USA) was used for this purpose. Figure 2.27 and Figure 2.28 show AFM images of the film before and after indentation. Indented marks are indicated in the figures. The hardness of nanocrystalline Au film decreased from  $4.1 \pm 0.1$  to  $3.8 \pm 0.1$  GPa after annealing for 2 h at 200 °C. We know that on annealing, the crystallinity of films improves, the number of defects decrease, and it leads to the formation of larger grains. A large grain offers lesser resistance to the external stress.

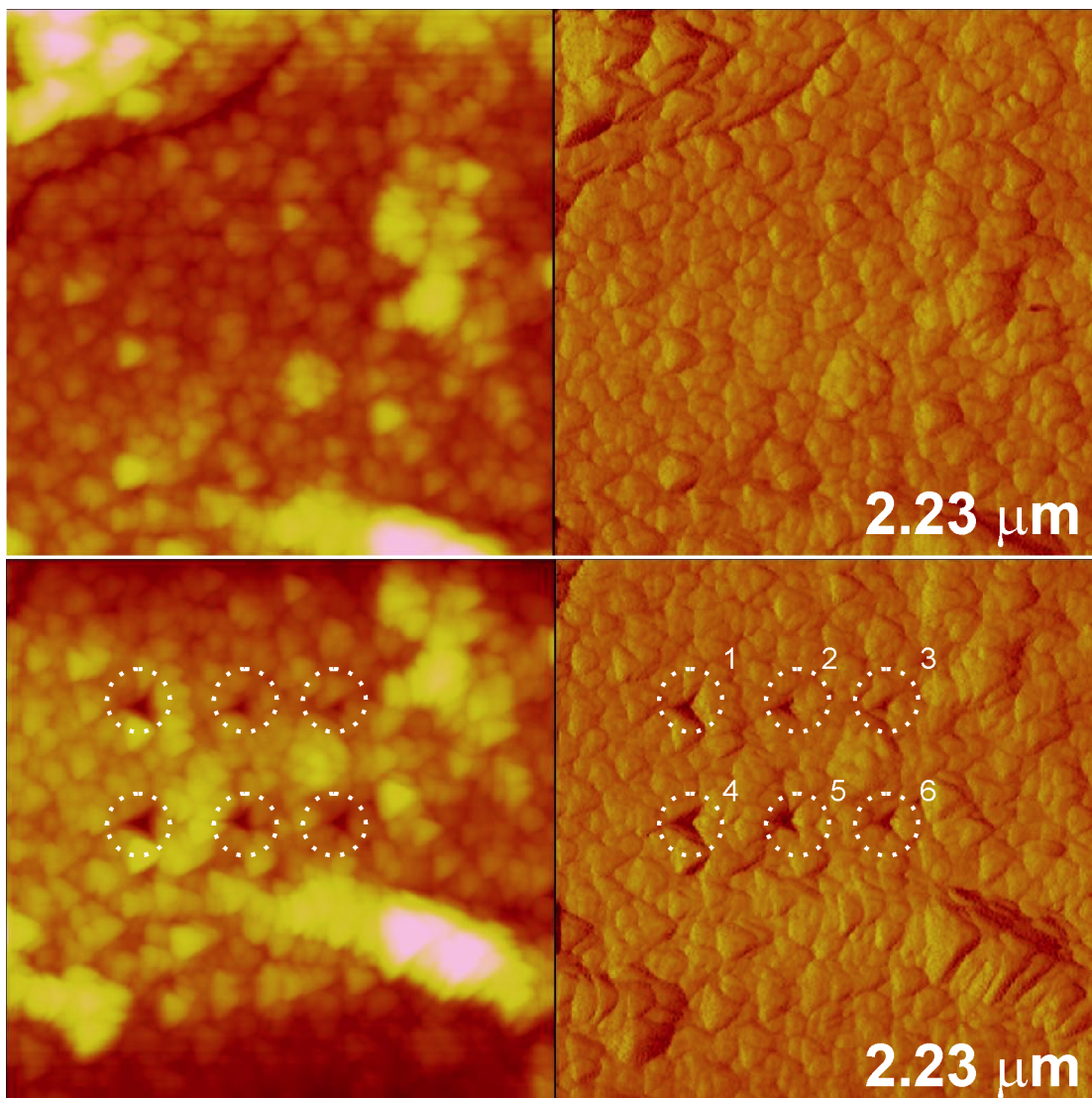


Figure 2.28 Nano indentation on Au films prepared at room temperature and then annealed to 200° C.

### 2.5.1.5 Films of Ag and Cu nanocrystals

By using  $\text{Ag}_2(\text{PPh}_3)_4\text{Cl}_2$  instead of  $\text{Au}(\text{PPh}_3)\text{Cl}$ , films of nanocrystalline Ag were obtained. The Ag films exhibited high metallic luster. TEM and AFM images of the film in Figure 2.29 show nanocrystals of average diameters 10 and 12 nm respectively, the difference mainly arising due to the surface ligands. The film is primarily a nanocrystalline monolayer with a high coverage ( $\sim 70\%$ ).

Films of Ag nanocrystals show the characteristic plasmon band at  $\sim 410$  nm [88]. As seen in Figure 2.30 the initial spectra shows a clear plasmon band while with time, the plasmon band flattens, up to the extent that it is no longer visible. This suggests that due to strong interparticle coupling, new band around 700 nm emerged.

Eventually it dominated the entire visible spectra range, and the TEM images clearly show the presence of nanoparticles.

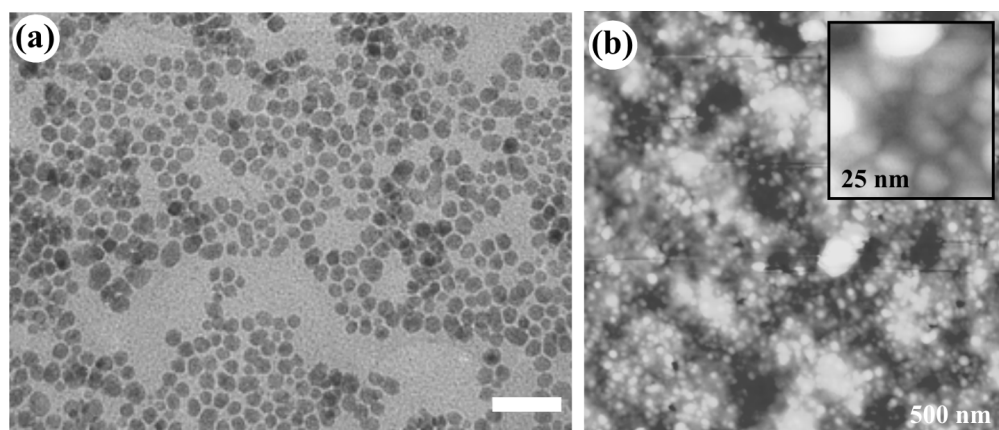


Figure 2.29 (a) TEM micrograph of a Ag nanocrystalline film. The scale bar corresponds to 50 nm. (b) AFM amplitude image of the film in tapping mode. The inset contains a higher-resolution image showing individual nanocrystals.

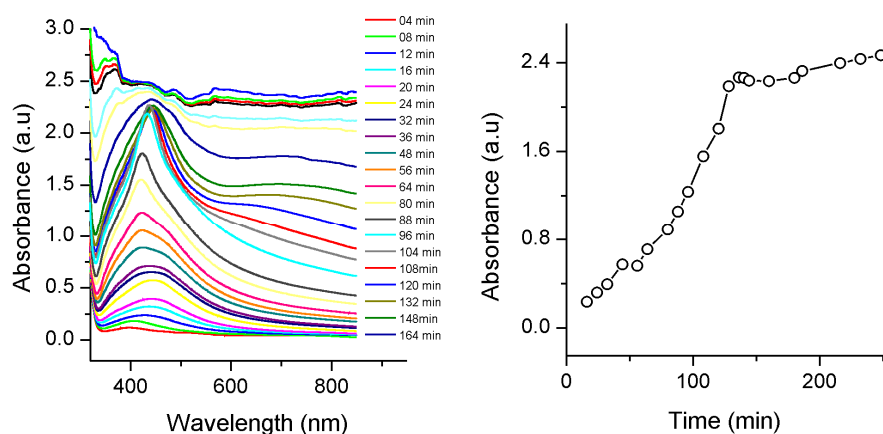


Figure 2.30 Formation of Ag films, evolution of film was captured using optical absorption spectra (left). Variation in the absorption intensity of plasmon peak normalized with respect to the final intensity (right).

XPS measurements revealed the presence of two Ag species as seen from the Figure 2.31, one due to the core of the nanocrystal and the other due Ag bound to the capping agent. Further, no evidence of oxidation of Ag, commonly seen in Ag nanocrystals was apparent [402].

By using  $\text{Cu}(\text{PPh}_3)\text{Cl}$ , and only NaOH in the aqueous layer, we could obtain films of Cu nanocrystals. The film was however not uniform and reveals nanocrystals

with a broad distribution in diameters (Figure 2.32). The film exhibits the red-brown luster characteristic of copper, although one can not be entirely certain that it consisted of only metallic Cu since many Cu-suboxides also show such luster. XPS measurements indicated the presence of metallic Cu with a very small proportion of oxidic species as seen from the Figure 2.33.

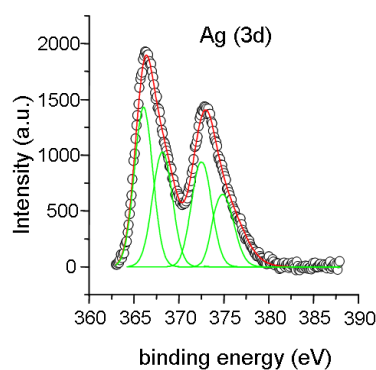


Figure 2.31 XPS from as prepared Ag nanocrystalline film: signal from 3d level of Ag.

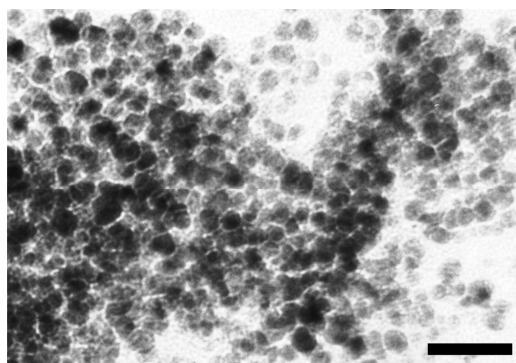


Figure 2.32 TEM micrographs of Cu nanocrystalline films. The scale bar corresponds to 50 nm.

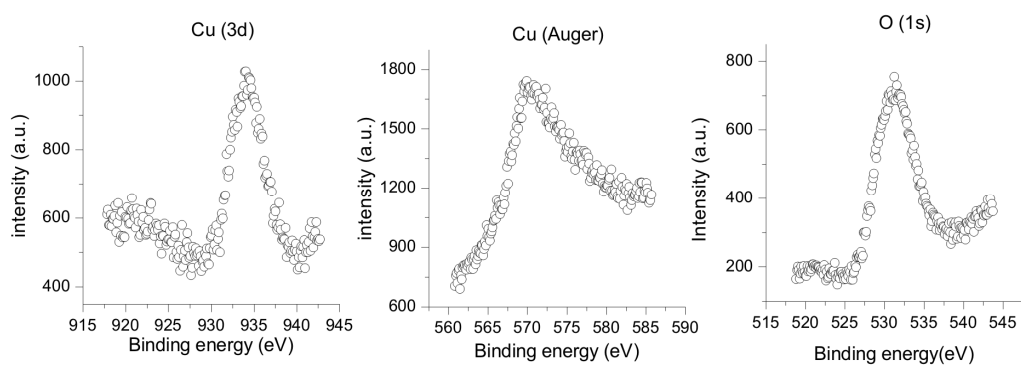


Figure 2.33 XPS spectrum of as prepared copper film: (left) signal from copper (3d), (middle) Cu Auger and (right) signal from Oxygen 1s.

### 2.5.1.6 Films of Pd and Pt nanocrystals

On dissolving Pd Acetate in organic layer and hydrazine in aqueous layer, we obtained Pd nanocrystalline film with average particle size  $\sim 2.5$  nm as shown in Figure 2.34a. The nanocrystals are closely packed. Figure 2.34b shows broadening of (111) peak in X-ray diffraction pattern typical of nanocrystals. Figure 2.35a shows monodisperse Pt nanocrystals of size 2-3 nm obtained when  $\text{H}_2\text{PtCl}_6$  was phase transferred from aqueous phase to toluene using TOAB, and was further reduced with hydrazine in aqueous phase. X-ray diffraction pattern in Figure 2.35b shows broadening of (111) peak due to small size of particles.

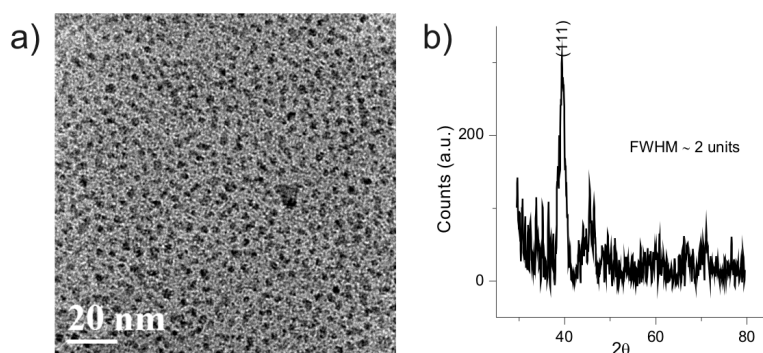


Figure 2.34 (a) TEM image of Pd nanocrystals prepared at the interface and (b) XRD pattern from the same.

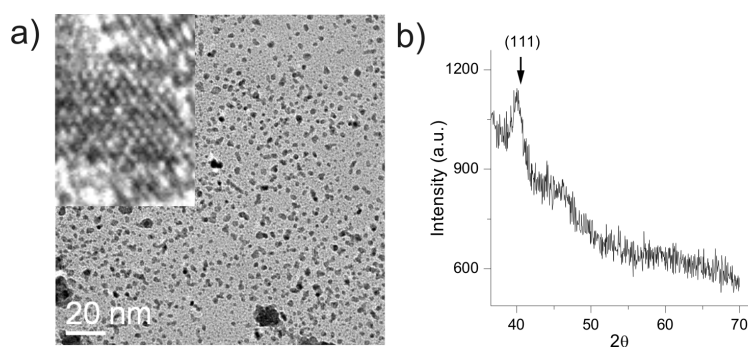


Figure 2.35 (a) TEM image of Pt nanocrystals prepared at the interface and (b) XRD pattern from the same.

The free-standing nanocrystalline films of Au, Ag and Cu can be lent some extra strength with the help of solid supports which may also attribute additional properties. Use of polystyrene support, for example, yields flexible and transparent films. We found that a few drops of a toluene dispersion of the polymer added to the layer atop

the interface yielded the desired film upon evaporation of the solvent. The film thus obtained was continuous and contained a high density of nanocrystals. We envisage several potential applications of such films in color filters and radiation shields. One such film is shown in Figure 2.36.



Figure 2.36 Ag film, blend with polystyrene, free standing film.

### 2.5.2 Nanocrystalline films of Au-Ag, Au-Cu and Au-Ag-Cu alloys

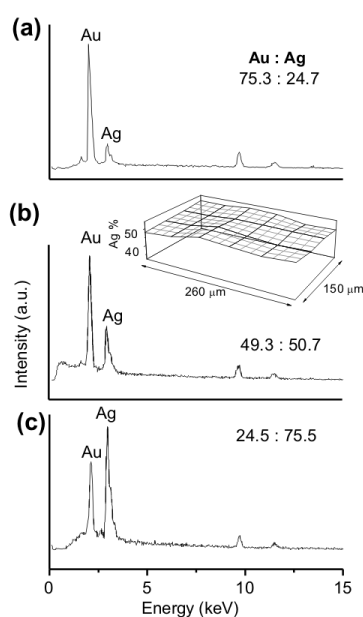


Figure 2.37 EDAX spectra of Au-Ag alloy films with different formal Au:Ag ratios, (a) 75:25, (b) 50:50 and (c) 25:75. The compositions obtained using EDAX analyses are indicated. The inset in b shows an elemental map.

The compositions of the Au-Ag films were estimated based on the intensities of the Au(M) and Ag( $K\alpha$ ) lines in the EDAX spectra (Figure 2.37). The spectral intensity originates entirely from the reduced metallic species as the films were

washed thoroughly to remove any unreduced precursor. The alloy compositions estimated from EDAX analysis closely match the starting molar compositions within 0.5% (Figure 2.37). The liquid-liquid interface method allows the metal precursors to fully get reduced and incorporated in the alloy.

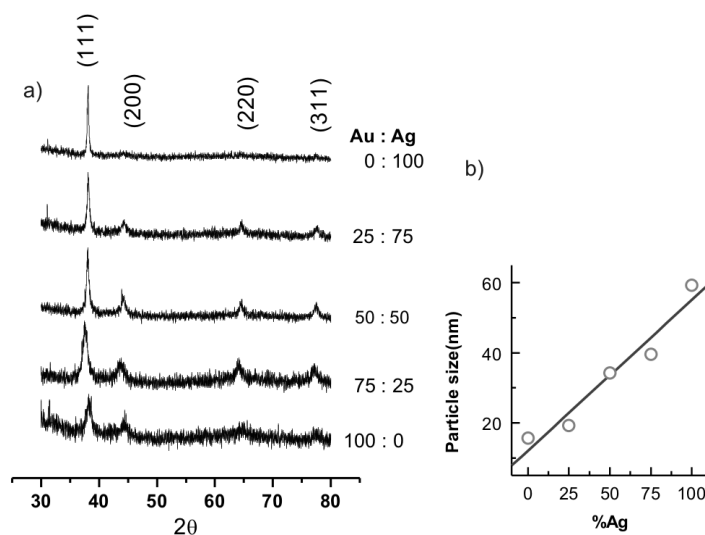


Figure 2.38 (a) X-ray diffraction patterns of nanocrystalline Au-Ag alloy films with different compositions. (b) Particle sizes obtained from X-ray broadening are plotted against Ag content.

In Figure 2.38a, we show the XRD patterns of the nanocrystalline films of Au-Ag alloys of varying compositions along with those of the monometallic Au and Ag films. The Au film as well as the Au-rich Au-Ag alloy films exhibit broad XRD reflections. On increasing the Ag content, the diffraction peaks become sharper, with an increasingly (111) orientation. The particle sizes estimated from the width of the diffraction peaks show a linear variation with the composition as shown in Figure 2.38b. With the increasing Ag content, the mean size of the nanocrystals increases from ~ 16 nm, to ~ 60 nm. A similar observation has been made by Papavassiliou [342].

Nanocrystalline films of Au formed at the liquid-liquid interface exhibit a broad band around 700 nm due to the surface plasmon resonance in the optical absorption spectrum (Figure 2.39). This is typical of a nanocrystalline film with significant electronic coupling among the individual nanocrystals [403]. The absorption spectrum of the nanocrystalline film of Ag is close to that of bulk metal [94]. The plasmon band of the films of Au-Ag alloys becomes progressively prominent and undergoes a



gradual blue shift down to  $\sim 500$  nm when the Ag content reaches 75%. The optical images of the films shown in Figure 2.39, exhibit a clear transformation in the color, from brown-red to silvery-white, as the Ag content increases.

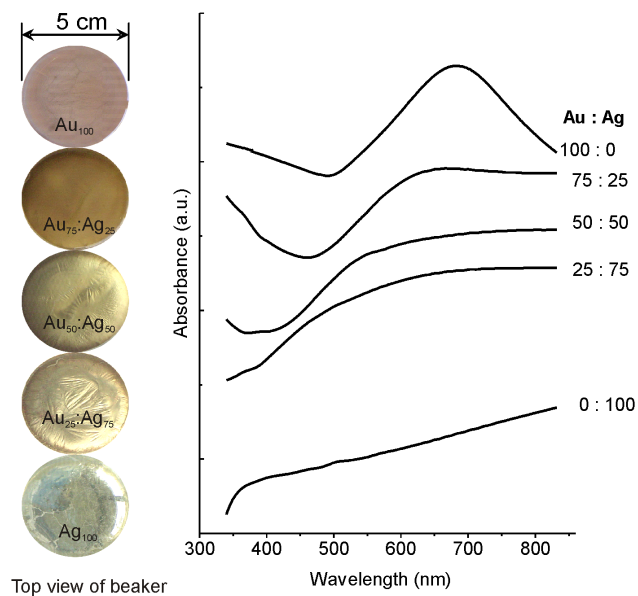


Figure 2.39 Optical absorption spectra of the Au-Ag alloy films of varying compositions. Optical photographs of the films standing at the liquid-liquid interface are shown alongside.

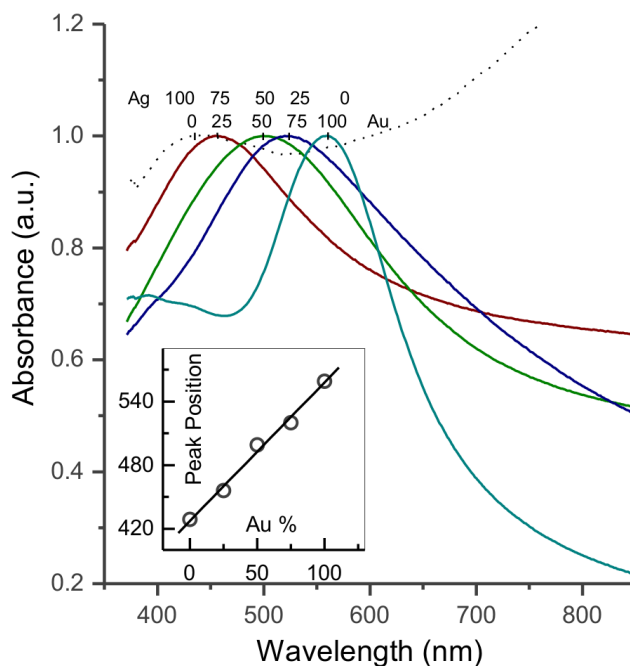


Figure 2.40 Optical absorption spectra of Au-Ag alloy sols with different compositions. Inset shows the plasmon peak position plotted against the Au mole fraction.

The Au-Ag alloy films could be disintegrated to form the organosols in toluene by addition of octadecanethiol. Figure 2.40, shows the optical absorption spectra of the organosols. The Au and Ag organosols exhibit the surface plasmon band at 550 and 420 nm respectively, as expected of these colloids [94]. The plasmon band of the alloy sols appear between those of monometallic sols depending on the composition [348]. The plasmon band position actually varies proportionally with the composition as depicted in the inset of Figure 2.40.

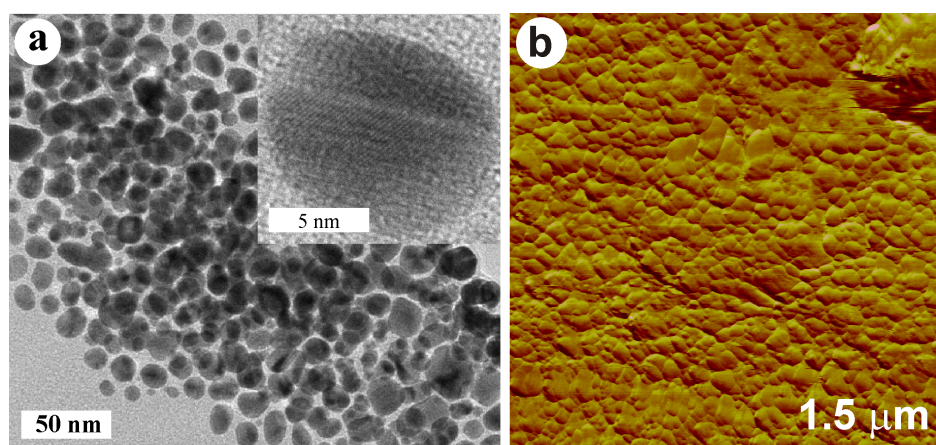


Figure 2.41 (a) TEM micrograph of the alloy nanocrystals (Au:Ag = 50:50) from the organosol obtained by breaking the film. Inset shows a high-resolution image of an individual alloy nanocrystal. (b) LFM image of the as-prepared nanocrystalline Au-Ag alloy film in the contact mode.

Figure 2.41a, shows a TEM micrograph of the nanocrystals from the 50:50 alloy. A high-resolution image of a nanocrystal revealing the (111) planes is shown in the inset of Figure 2.41a. The absence of grain boundaries is indicative of the uniformity in composition of the nanocrystals. The size of the nanocrystals is in a narrow range of 18-26 nm, with a mean value of 23.5 nm. This value is somewhat lower than that estimated from the X-ray diffraction profile (Figure 2.38b). The Friction image of the Au-Ag alloy (50:50) is shown in Figure 2.41b.

As noted from the XRD measurements in Figure 2.38, the monometallic Ag film obtained at the liquid-liquid interface exhibits a preferred (111) orientation. The film was further investigated using AFM and high resolution TEM (Figure 2.42). The height image in Figure 2.42a reveals closely packed flat grains ( $\sim 1 \mu\text{m}$ ) presumably formed from large nanocrystals. TEM imaging shows the nanocrystals of Ag to be generally large (dia.  $\sim 60 - 100 \text{ nm}$ ). One may recall that the size obtained from the X-ray broadening is  $\sim 60 \text{ nm}$ . The z-profile shown in Figure 2.42 indicates that the top

surface of the particles is relatively flat. The rms roughness is estimated to be  $\sim 15$  nm over a micron area. The friction image in Figure 2.42b reveals the curved boundaries of the particles. The single crystalline nature of the sheet-like particles is evident from the HRTEM images in Figure 2.42c. The selected area electron diffraction (SAED) pattern in Figure 2.42c (inset) consists mainly of second and third order (111) reflections, 1.2 and 0.6 Å (the first order reflection was shadowed by the beam stopper). A Moiré pattern obtained at the grain boundary revealed that the two participating particles have their (111) planes oriented at an angle,  $\alpha \sim 20^\circ$  giving rise to a Moiré spacing of 7.2 Å, as shown in the Figure 2.42d. The estimated angle from the Moiré equation [386] is  $18.8^\circ$ .

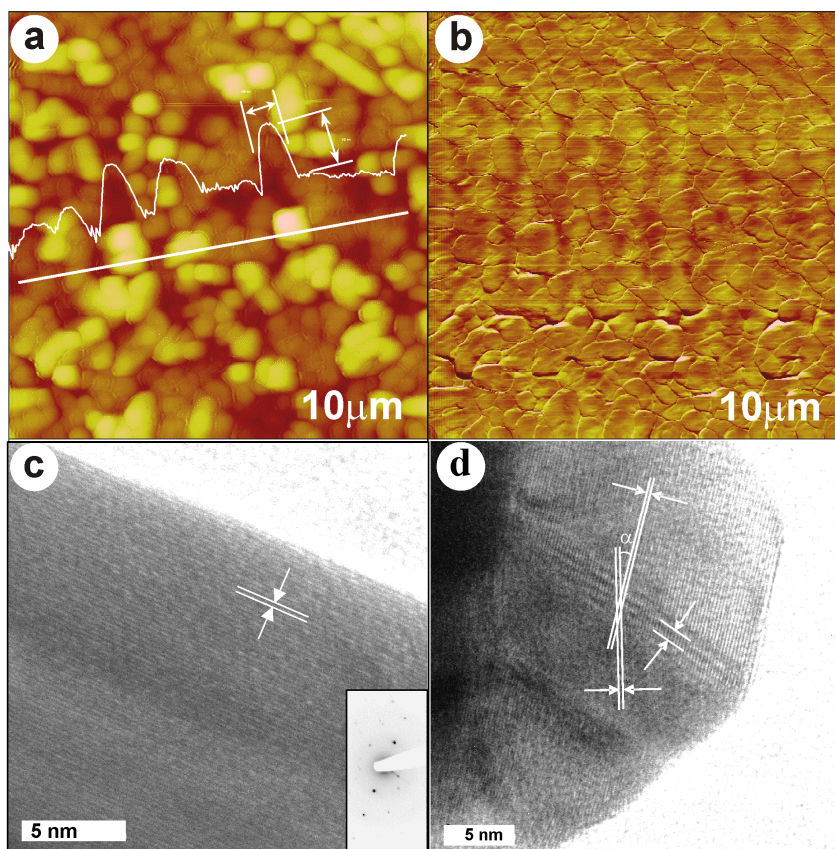


Figure 2.42 AFM images of the as-prepared nanocrystalline Ag(111) film in the contact mode: (a) topography and (b) lateral force micrograph (LFM). (c) High-resolution TEM image of the film, inset shows corresponding SAED pattern, (d) shows a Moiré pattern from another portion of the film.

The results obtained by us with the nanocrystalline Au-Cu alloy films (75:25 and 50:50) are presented in Figure 2.43. The alloy compositions of the films estimated from the EDX spectra shown in Figure 2.43a are close to the starting concentrations of the precursors, the deviation being little higher compared to the Au-Ag films (see

Figure 2.37). The oxidation of Cu is a matter of concern under wet synthetic conditions. The films were therefore subjected to Auger analysis. The Cu(LMM) peak was asymmetric with two features at 918.6 and 916 eV, corresponding to metallic Cu and  $\text{Cu}^{1+}$  oxidic species respectively. The O(1s) core-level spectrum exhibited a low-intensity peak around 531 eV. It appears that a small proportion of Cu is present as  $\text{Cu}_2\text{O}$  in the films, perhaps at the particle boundaries. The XRD patterns in Figure 6b are typical of films containing small particulates. The particle sizes estimated from peak broadening are similar ( $\sim 16$  nm) for the two compositions.

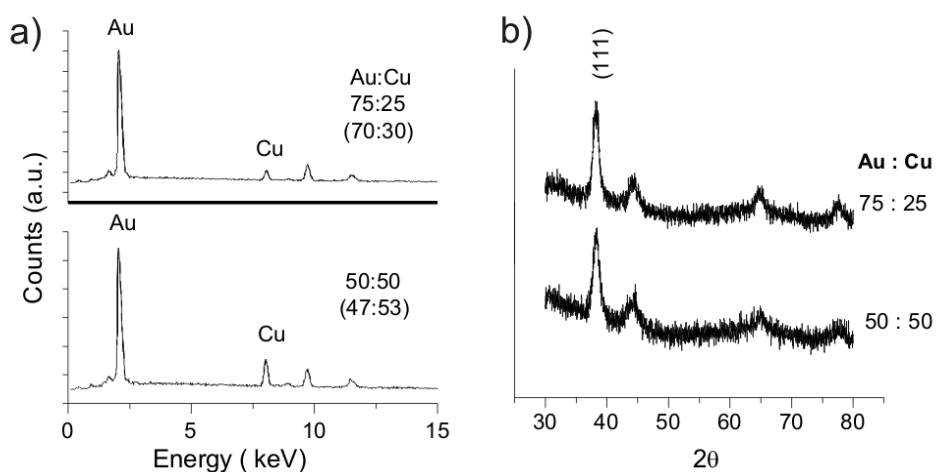


Figure 2.43 EDAX spectra of the Au-Cu alloy films with different formal Au:Cu ratios, (a) 75:25 and 50:50. The compositions obtained EDAX analysis are indicated in parenthesis. (b) XRD patterns of the nanocrystalline Au-Cu alloy films.

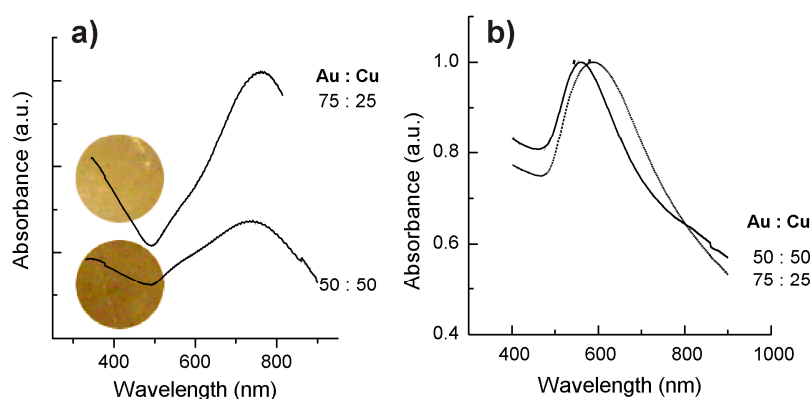


Figure 2.44 (a) Optical absorption spectra of Au-Cu alloy films with different compositions. Optical photographs of the films standing at the liquid-liquid interface are shown alongside, (b) optical absorption spectra of Au-Cu alloy sols with different compositions.

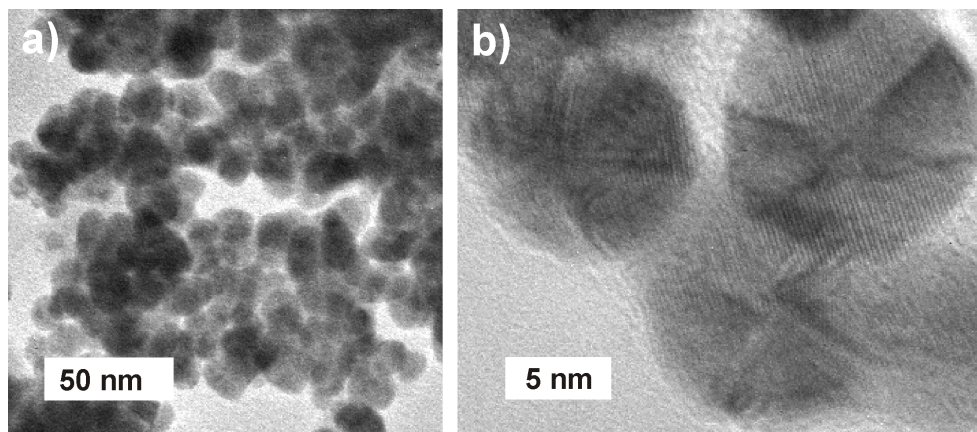


Figure 2.45 (a) TEM micrograph of Au:Cu (50:50) film revealing nanocrystals and (b) a high-resolution image showing four-domain structure of the nanocrystals.

The electronic absorption spectra of the Au-Cu films (Figure 2.44) exhibit broad bands around 700 nm typical of films with considerable coupling. The film with a formal Au:Cu composition of 75:25 appears golden yellow while that with 50:50 composition is relatively dark, as evident from the optical images shown alongside the absorption spectra. We observe a broad shoulder around 580 nm, which may have contributions from surface plasmon excitations from both Au and Cu [94]. Accordingly, toluene sols produced by breaking the films in presence of octadecanethiol, exhibit absorption peaks at 560 and 585 nm respectively for the 50:50 and 75:25 compositions (see Figure 2.44b) [404]. The observed shift in the plasmon band of the nanocrystals therefore appears to be due to alloying. A similar observation has been reported for Au-Cu alloy particles embedded in a silica matrix [372]. The TEM images in Figure 2.45 reveal the particulate nature of the films. The image in Figure 2.45a contains nanocrystals in the 10 - 25 nm range, with a mean size of 18 nm which compares well with the XRD results. Interestingly, the high resolution image in Figure 2.45b shows a four-domain structure of the nanocrystals, similar to the observations reported by Duff et al. [84] in the case of Ag nanocrystals. The resolved planes from the domains are clearly visible (see Figure 2.45b). The domain boundaries would contain some oxidic species of Cu.

We have prepared a nanocrystalline film of the Au-Ag-Cu ternary alloy with a formal composition of 50:25:25. The composition of the alloy obtained from the EDAX analysis (Figure 2.46a) was 37:28:35. The presence of Ag favors the complete reduction of Cu causing a light yellow metallic luster to the film. The absorption

spectrum of sol obtained by the addition of octadecane thiol, exhibits a peak around 550 nm (Figure 2.46b). The long wavelength tail in the spectrum is characteristic of alloy nanocrystals rich in Au.

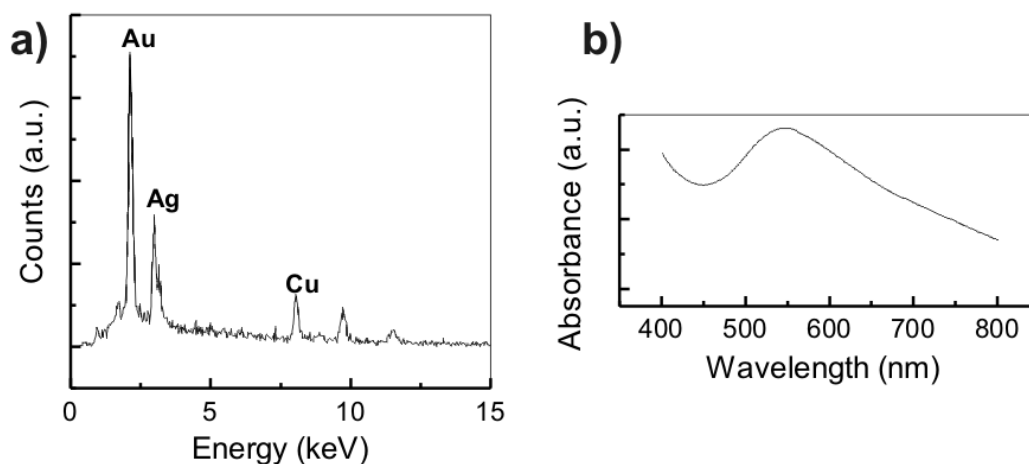


Figure 2.46 (a) EDAX spectrum of the nanocrystalline Au-Ag-Cu (50:25:25) alloy film, (b) optical absorption spectra from the corresponding organosol.

### 2.5.3 Rheological study of nanocrystalline Ag film

#### 2.5.3.1 Monitoring the Formation of the 2D Film of Ag

The formation of the nanocrystals at the toluene-water interface occurs through a diffusion-controlled process at the toluene-water interface. This is facilitated by adding the reducing agent THPC into the water and the organometallic precursor  $\text{Ag}_2(\text{PPh}_3)\text{Cl}_2$  (immiscible in water) to toluene. Care is taken not to destabilize the interface during the formation of the film. Hence, the reduction of the Ag ions into Ag atoms can occur only when the metal ions that diffuse to the toluene-water interface encounter the reducing agents also present at the interface. This is further supported by the fact that the surface coverage of particles at the interface is found to be sensitive to the contact time of the metal ions and the reducing agent, the temperature of the interface, and the concentration of the metal ions and the reducing agent. The nanocrystals thus formed at the interface are stabilized by the triphenylphosphine ligands surrounding the metal core. SEM and TEM images indicate that the spherical nanocrystals synthesized through this method are not strictly monodisperse, and the particle size ranges from 10 to 50 nm (Figure 2.47).

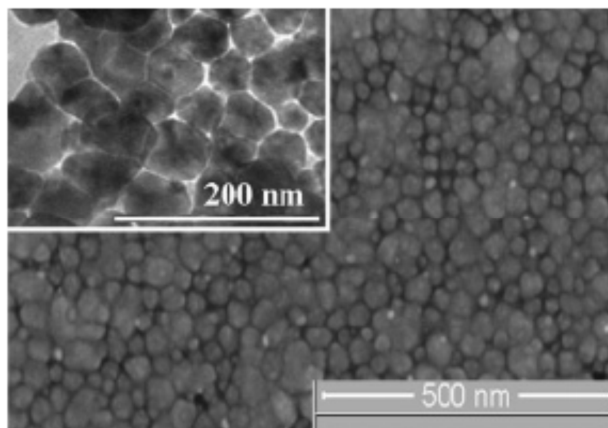


Figure 2.47 SEM and TEM (inset) micrographs of a 2D film of Ag nanocrystals formed at the toluene-water interface obtained by transferring the film onto a suitable substrate after the measurements. The particle size varies between 10 and 50 nm.

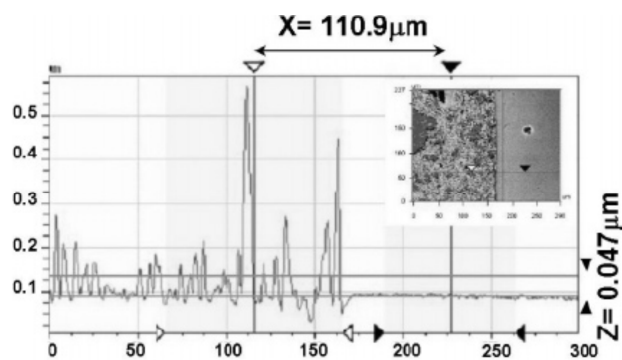


Figure 2.48 Profile thickness measurement of the 2D film of Ag nanocrystals after transferring to a Si substrate. The average film thickness is found to be 47 nm, consistent with a monolayer of the particles.

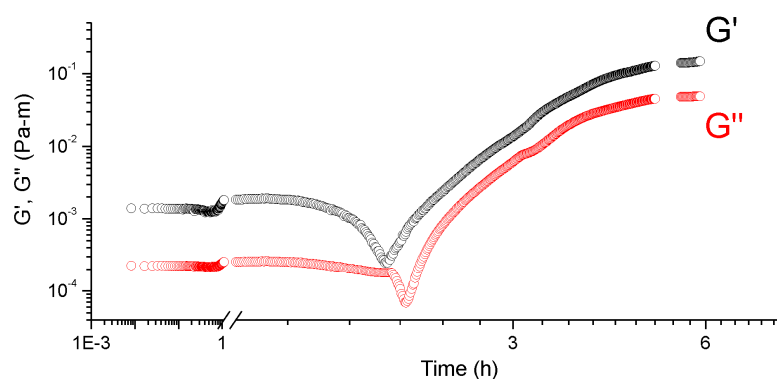


Figure 2.49 Film building of Ag nanocrystals at the toluene-water interface monitored under oscillatory shear. The angular frequency was fixed at 10 rad/s, and the strain amplitude was maintained at 1%. The saturation of the storage and the loss moduli occurs for the film after 5 h. The discontinuity in the curve indicates the time over which data was not recorded.

The film build up at the liquid-liquid interface was monitored by applying an oscillatory shear with strain amplitude of 1% and an angular frequency of 10 rad/s. A pink coloration at the interface indicates the onset of the formation of the film. As the film is built up, a viscoelastic behavior is observed for the monolayer, with the viscous term dominating over the elastic response ( $G' \sim 10^{-4}$  Pa·m and  $G'' \sim 10^{-3}$  Pa·m) up to 2 h, after which a gradual increase in the storage and loss moduli by several orders of magnitude is observed (Figure 2.49). The steady increase observed in the storage and loss moduli with time arises from the increase in the particle concentration of the film (no. of particles per unit area) as more and more particles form at the interface with time. XPS measurements of the nanocrystalline film formed by the present method reveal the presence of two Ag species: one due to the metallic core, and the other due to the Ag bound to a capping agent. The capping agents can consist of the triphenylphosphine ligands as well as the ionic species from THPC, since the core level spectra reveal the presence of phosphorus and chlorine. Moreover, the AFM images of the film indicate a higher diameter for the particles forming the film than that obtained from TEM micrographs. This suggests that the nanocrystals consist of a layer of ligands with a thickness of 1 nm, surrounding the core of the metal nanoparticle, not visible under TEM. It is also consistent with an interparticle separation of 1.5-2 nm obtained from TEM. The presence of the capping agent thus sterically stabilizes the nanocrystals against aggregation. The concentration of the particles (no. of particles per unit area) at the interface increases with the reaction time. The physical cross-linking of the particles can occur at a higher area fraction of particles when the ligands covalently attached to the metal core of the nanocrystals, get entangled. Hence, as the particle concentration in the monolayer increases, the interparticle network, which arises from the physical cross-linking of the ligands, would result in an increase in the strength of the film. The storage and the loss moduli saturate after 5 h. This indicates that the building up of the film is completed, and no more particles can be formed in the monolayer. In these measurements, an estimate of the particle concentration at the interface can be obtained from the SEM images of the film (Figure 2.47), which yields an area fraction of 0.61. The effective area fraction can, however, be higher than the estimated value, due to the contribution from the ligands surrounding the metal core. All the measurements reported here were made after the film reached saturation in  $G'$  and  $G''$  (Figure 2.49).



### 2.5.3.2 Interfacial Oscillatory Measurements.

To probe the structural relaxation of the film, sweep measurements at constant strain frequency were carried out on the film with the strain amplitude fixed at very low values of 0.007%, which corresponds to the linear viscoelastic regime. As shown in Figure 2.50, the storage modulus remains nearly independent of the frequency over the range of frequencies probed, whereas the loss modulus has a power law dependence with  $G'' \sim \omega^{-0.23}$  within the low-frequency range, over 3 orders of magnitude. The loss modulus  $G''$  exhibits minima at 30 rad/s with a nearly linear dependence on angular frequency at higher frequencies.

The low-frequency behavior of the system, with a small negative slope in  $G''(\omega)$ , is similar to that predicted by the soft glassy rheology model just below the glass transition where  $G''(\omega) \sim \omega^{x-1}$  and  $G'$  is nearly constant [405]. Here,  $x=1$  corresponds to the glass transition. In the system under study, the value of the effective temperature  $x$  is 0.77. Such a low-frequency behavior characteristic of a glassy system has not been reported earlier in a 2D system. However, a negative slope for  $G''$  has been seen in 3D colloidal suspensions, emulsions, and gels.

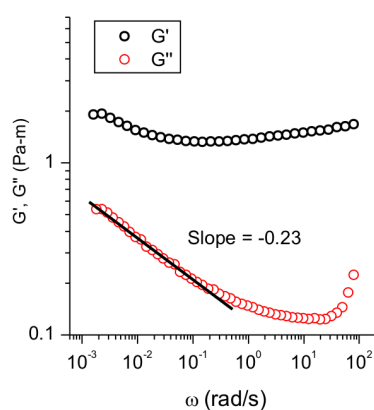


Figure 2.50 Frequency dependence of interfacial storage ( $G'$ ) (black circles) and loss ( $G''$ ) (red circles) moduli of the film. The measurements were carried out by varying the angular frequency ( $\omega$ ) from 0.001 to 100 rad/s, keeping the strain amplitude fixed at 0.007%.

In the present system, the nanocrystals stabilized by the ligands are dispersed at the toluene-water interface, and the viscous contribution of the liquid at high frequencies can lead to the linear dependence of  $G''$  on  $\omega$ . At very low frequencies,  $G''$  should exhibit a maximum, which would correspond to the structural relaxation of the

system. This was not observed in our experiments, since this region is not experimentally accessible. Hence, in the range of frequencies from 0.001 to 100 rad/s, the low-frequency response of the 2D film of metal nanocrystals is that of a soft glassy system with long structural relaxation times.

### 2.5.3.3 Amplitude Sweep

To characterize the strength of the film, amplitude sweep measurements were carried out by varying the strain amplitude  $\gamma$  from 0.01 to 100% and by keeping the angular frequency fixed at 10 rad/s. At low strain amplitudes, both  $G'$  and  $G''$  are found to be independent of  $\gamma$  (Figure 2.51). At higher values of  $\gamma$ , the storage modulus decreases, exhibiting a monotonic shear thinning behavior. The loss modulus, however, begins to increase and reaches a maxima before it shear thins at higher strain amplitudes. As indicated by the amplitude sweep measurements on the nanocrystalline film, a nonlinear regime is observed above strain amplitude of 0.02%. The size of the linear regime is rather low in comparison with monolayers of insoluble surfactants and proteins, where a linear regime is observed for a strain amplitude of <1%. The low range for the linear regime observed in the present system is consistent with the predictions of soft glassy rheology where the size of the linear regime decreases as the glass transition is approached [406]. The peak in  $G''$  has not been reported for 2D systems. However, it has been observed in many 3D soft glassy systems such as colloidal hard sphere suspensions and emulsions.

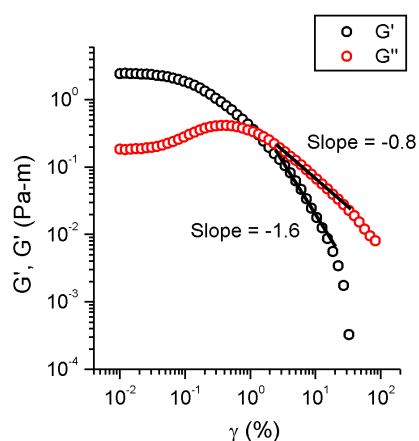


Figure 2.51 Strain amplitude ( $\gamma$ ) sweep experiment on the 2D film of Ag nanocrystals with the angular frequency fixed at 10 rad/s. The storage modulus  $G'$  (black circles) is higher than the loss modulus  $G''$  (red circles) at low strain amplitudes ( $\gamma$ ).

It has been proposed recently that the peak in  $G''$  at high strain amplitudes arises from the dependence of the structural relaxation time  $\tau$  on the strain rate amplitude [407], given by  $1/\tau = 1/\tau_0 + |\dot{\gamma}|^v$ , where  $\tau_0$  is the characteristic relaxation time. Here the strain rate amplitude,  $|\dot{\gamma}| = |\gamma| \omega$ , where  $|\gamma|$  is the strain amplitude, and  $\omega$  is the angular frequency. For a simple Maxwell model for  $G^*(\omega)$ , this would lead to a power law decay of  $G'$  and  $G''$  at high strain amplitudes, with  $G' \sim |\gamma|^{-2v}$  and  $G'' \sim |\gamma|^{-v}$ . This behavior is known to be prominent in systems that exhibit slow dynamics, including glassy systems. The value of the exponent is known to vary with the system. In the present system, the value of the exponent  $v$  is 0.8. Repeated measurements on the same film yield nearly identical curves, indicating that the break down in the structure of the film occurring during shear is reversible.

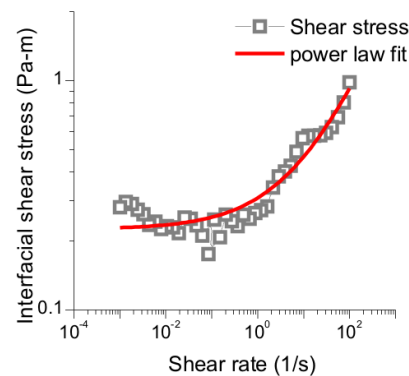


Figure 2.52 Flow curve  $\sigma(\dot{\gamma})$  of a Ag nanocrystalline film (squares) formed at the toluene-water interface. A finite yield stress is observed for the film. The shear stress is fitted (red line) to the model predicted by soft glassy rheology.

The apparent interfacial shear viscosity of the film over a wide range of shear rates was studied. At low shear rates, a finite yield stress (Figure 2.52) is observed for the film. The stress increases gradually at higher shear rates. Such a behavior has been predicted in soft glassy rheology below the glass transition. Here,  $\sigma(\dot{\gamma} \rightarrow 0) = \sigma_y$ , where  $\sigma_y$  is the finite yield stress. The stress exhibits a power law dependence given by  $\sigma_y + A\dot{\gamma}^{(1-x)}$  beyond yield [406]. A fit of the data to this equation, shown by the solid line in Figure 2.52, yields  $\sigma_y = 0.22 \pm 0.01$  Pa·m,  $A = 0.08 \pm 0.01$ , and  $x = 0.54 \pm 0.04$ . This value of  $x$  is different from that obtained from Figure 2.50. However, considering the scaling nature of the soft glassy rheology theory, this difference may not be surprising.

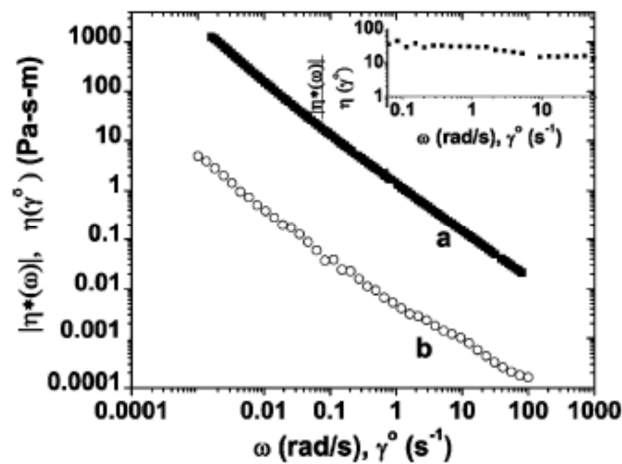


Figure 2.53 Apparent interfacial (a) dynamic and (b) steady shear viscosities measured on the 2D film of Ag nanocrystals. A significant deviation from the empirical Cox-Merz rule is observed, as shown in the inset where the shear rate dependence of the ratio of the interfacial dynamic viscosity to the interfacial steady shear viscosities is plotted.

The empirical Cox-Merz rule suggests that, at high shear rates, the steady shear viscosity  $\eta(\dot{\gamma})$  can be related to the dynamic viscosity  $\eta^*(\omega)$  such that  $\eta(\dot{\gamma}) = |\eta^*(\omega)|$ , with  $\dot{\gamma} = \omega$ . Recall that

$$|\eta^*(\omega)| = \frac{\sqrt{(G')^2 + (G'')^2}}{\omega} \quad (2.1)$$

For soft glassy systems, it has been shown that a significant deviation from the Cox-Merz rule occurs below the glass transition [406]. In the system under study, the Cox-Merz rule is indeed not obeyed (Figure 2.53). This is indicated by the high values ( $\sim 400$ ) of the ratio of the dynamic viscosity to the steady shear viscosity (Figure 2.53) at the strain rates and angular frequencies studied.

The steady shear response of the 2D film of metal nanocrystals observed here is similar to that predicted for soft glassy systems. Furthermore, it is consistent with conclusions of a glassy behavior obtained from the oscillatory shear measurements carried out on the same film. It is known that a crystal-to-glass transition can be observed for a system of hard spheres at high volume fractions upon increasing the polydispersity of the spheres [408]. Hence, it appears likely that the glassy nature of the film arises from the polydispersity of the nanocrystals in the film.

## 2.5.4 Evolution of Au nanocrystalline films studied using SAXS

### 2.5.4.1 Reflectivity curves

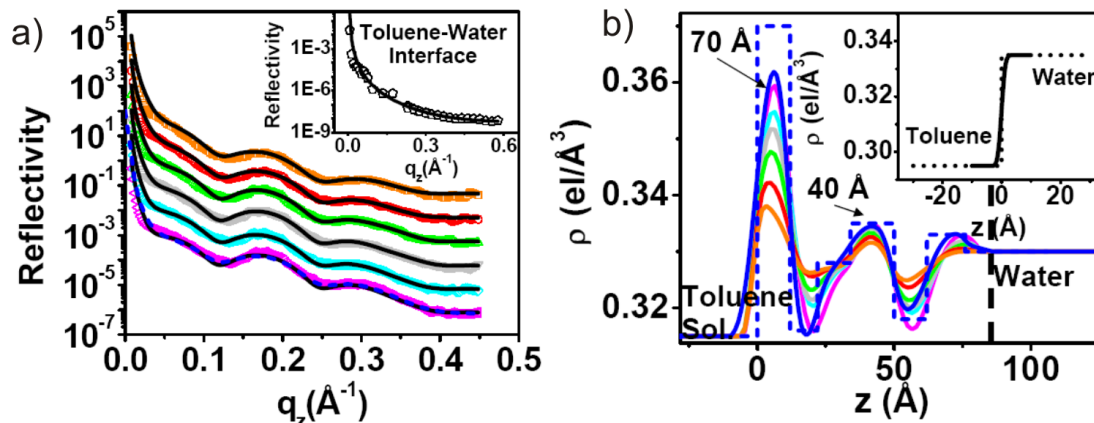


Figure 2.54 (a) Variation of reflectivity and fits as function of  $q_z$  after initiation of the reaction (pink, 194 min; light blue, 224 min; grey, 253 min; green, 283 min; red, 312 min; orange, 364 min) and the fits (solid lines). The reflectivity (dashed line) generated from the simple box model is also shown. Inset: The reflectivity data ( $\Delta$ ) from the toluene-water interface and its fit (solid line). (b) The electron density profiles (EDPs) (colors same as those in a) as function of depth obtained from fitting. Positions of the two upper peaks as measured from the water interface (dashed line) 70  $\text{\AA}$  and 40  $\text{\AA}$  are marked. A simple model without (dashed line) and with roughness convolution (solid line, blue) are also shown.

Figure 2.54a, shows six reflectivity curves collected after the initiation of the reaction and indicated the time of data collection. The insets of Figure 2.54a and b, shows the reflectivity data and electron density profile of the bare toluene-water interface, respectively. We required around 30 min time to collect a reflectivity profile and have not presented the data collected within 194 min of initiation of reaction here because the profiles changed during scans. The oscillations in the curves indicate a presence of thin film at the liquid-liquid interface. These curves were fitted using an iterative inversion technique based on Born approximation [409]. The inversion scheme is based on recursive Fourier Transform (FT) and Inverse Fourier Transform ( $FT^{-1}$ ) of the equation relating the model electron density profile ( $\rho_m(z)$ ) with actual electron density profile ( $\rho_e(z)$ ) as

$$\rho_e(z) = FT^{-1} \left[ \sqrt{\frac{R_e}{R_m}} \int \rho'_m(z) \exp(iq_z z) dz \right] \quad (2.2)$$

where  $\rho_e$ ,  $\rho_m$  are the experimental reflectivity profile and calculated reflectivity from the model  $\rho_m(z)$  by standard slicing technique. In each iteration  $\rho_m(z)$  is replaced by  $\rho_e(z)$  and the process is continued until  $\rho_e$  and  $\rho_m$  becomes indistinguishable.

#### 2.5.4.2 Calculated electron density

We used the water-toluene profile (with a small increase in toluene density due to presence of Au(PPh<sub>3</sub>)Cl to match the critical angle) shown in inset of Figure 2.54b as initial  $\rho_m(z)$  and confirmed the stability of the solutions by setting various total film thicknesses. The extracted final electron density profiles, for these six reflectivity data, which always take the value of water density toward the end of the film, are shown in Figure 2.54b. We also verified the solutions by simple models having a few slices; one such simple model having six slices for 194 min data is also shown with and without roughness convolution, and the corresponding calculated reflectivity data is shown in Figure 2.54a. The dip in reflectivity data around  $0.123 \text{ \AA}^{-1}$  and the subsequent modulation require a strong peak in electron density around  $70 \text{ \AA}$  above the water surface. The width of this peak and the simple model shown in Figure 2.54b suggest the size of the uppermost gold particle to be around  $12 \text{ \AA}$ . There is a broad composite structure around the middle of the film (marked as  $40 \text{ \AA}$ ) and a small hump just before reaching the water density. Interestingly, these three layers have a vertical separation of about  $30 \text{ \AA}$  from each other. The electron density between these layers takes the value ( $\sim 0.32 \text{ electrons/\AA}^3$ ) of a typical organic material. The electron density of the uppermost layers reduces, and the peak electron densities of all of the peaks tend to become equal, as time progresses, but the separation of the layers remain nearly constant.

The profiles obtained in Figure 2.54b with continuous reduction of electron density of the uppermost layer can be explained assuming coexistence of a monolayer of individual nanoparticles having around a  $12 \text{ \AA}$  gold core with an  $11 \text{ \AA}$  organic shell and a layer of a 13-member “magic cluster” of these nanoparticles. With the progress of reaction, the number of individual nanoparticles reduces and only the monolayer of the “magic cluster” remains at the toluene-water interface.

## 2.5.4.3 Diffuse scattering studies

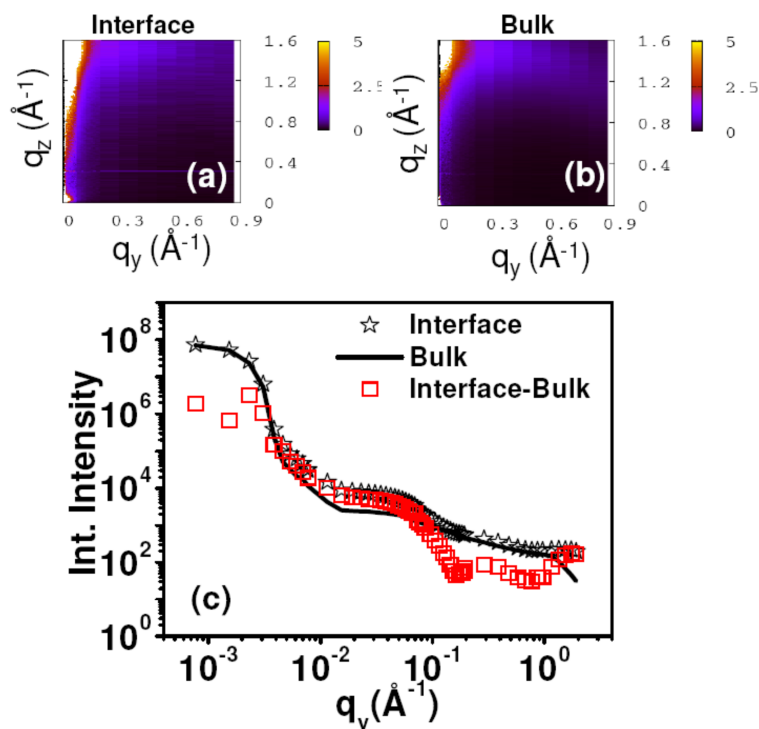


Figure 2.55 (a) The  $(q_y - q_z)$  contour plots of scattered intensity from Au nanocrystals formed at the toluene-water interface. (b) The  $(q_y - q_z)$  contour plots of scattered intensity from bulk Toluene solution 200  $\mu\text{m}$  above the Toluene-Water interface. The colour bar besides the right panel represent the intensity scale. (c) The diffuse scattering intensity from interface and bulk integrated over  $q_z$  are shown as a function of  $q_y$ . Intensity profile of interface scattering is also shown after subtracting bulk contribution from the measured data.

The scattered data collected by the PSD gives the variation of intensity as a function of the reflected angle ( $\theta_f$ ). The collected data were then converted to intensity contours in the  $(q_y - q_z)$  reciprocal space. Figure 2.55a and b shows representative contours taken from water-toluene interface containing the Au nanocrystals and from the bulk toluene (0.2 mm above the interface) respectively. In Figure 2.55c, we have shown the variation of diffuse scattering intensity measured from the interface and the bulk as a function of  $q_y$ , by integrating the PSD data over  $q_z$ . The Au nanocrystals formed at toluene-water interface affect the nature of scattering from interface and the formation of Au nanocrystals is reflected in a peak at  $q_y = 0.046$   $\text{\AA}^{-1}$  in the interface data (see Figure 2.55b). It is noteworthy that diffuse scattering from bulk is different from that obtained from interface and the trace of this peak reduces quickly as the data is collected further above the interface. The bulk scattering data was subtracted

from interfacial data and a small peak around  $0.29 \text{ \AA}^{-1}$  is observed. However, this peak, which may corresponds to the separation between two 1.3nm particles observed in reflectivity, is much weaker than the peak observed at  $0.046 \text{ \AA}^{-1}$ . In the analysis presented below, we shall consider this stronger peak as the only one grazing incidence diffraction (GID) peak.

For determining the effective interfacial tension, we analyzed the diffuse scattering data at small  $q_z$  values. The large diffuse scattering intensity in the low  $q_y$  region as well as the decay of the intensity as  $q_y^{-(2-\eta)}$  (where the  $\eta$  is equal to  $k_B T q_z^2 / (2\pi\gamma)$  and  $\gamma$  is the surface tension) from a liquid surface can be explained using a logarithmic height-height correlation induced by capillary fluctuations without any fitting parameters [363]. The diffuse scattering data was analyzed using the capillary wave model of liquid interfaces as

$$\frac{d\sigma}{d\Omega} = A \times G \times F(q_z) \times \frac{2\pi}{q_z^2} \left[ \frac{e^{-\Gamma_e}}{q_{\max}} \right]^n \frac{\Gamma(1-\eta/2)}{\Gamma(\eta/2)} q_y^{n-2} \quad (2.3)$$

Here A represents area of scattering volume projected on surface, which is fixed here by the incident slits and angle, G is geometric function, which can be approximated by  $G = r_e^2 \rho_w^2 |t_{in}|^2 |t_{sc}|^2 \cos^2 \phi$ . In equation (2.3)  $r_e$  is Thomson's scattering length of electron,  $\Gamma_e (=0.5772)$  is Euler constant, the transmission coefficients  $t_{in}(t_{sc})$  represents scattering intensity as incident (scattered) angle approaches critical angle, the  $\cos^2 \phi$  factor comes from polarization of incident and scattered beam and  $\rho_w$  is electron density of water. The reciprocal of the size of nanocrystals multiplied by  $2\pi$  was taken as the maximum wave-vector  $q_{\max}$  that sustains capillary wave.

Figure 2.56a shows two diffuse scattering data around  $q_z$  values of 0.09 and  $0.13 \text{ \AA}^{-1}$  after subtracting corresponding bulk scattering data. Both these two data could be fitted simultaneously using (2.3) as the slopes of the two straight-lines shown in this log-log plot is determined [363] by the value of the interfacial tension and  $q_z$  value. The value of interfacial tension turned out to be 1.7 mN/m. This value is much lower than the expected value of interfacial tension between toluene and water. The small value of the interfacial tension indicates the enhancement of interfacial roughness. In



Figure 2.56b, we have shown GID peak arising due to scattering of Au nanoclusters by subtracting capillary scattering contribution (Figure 2.56b) from the measured data.

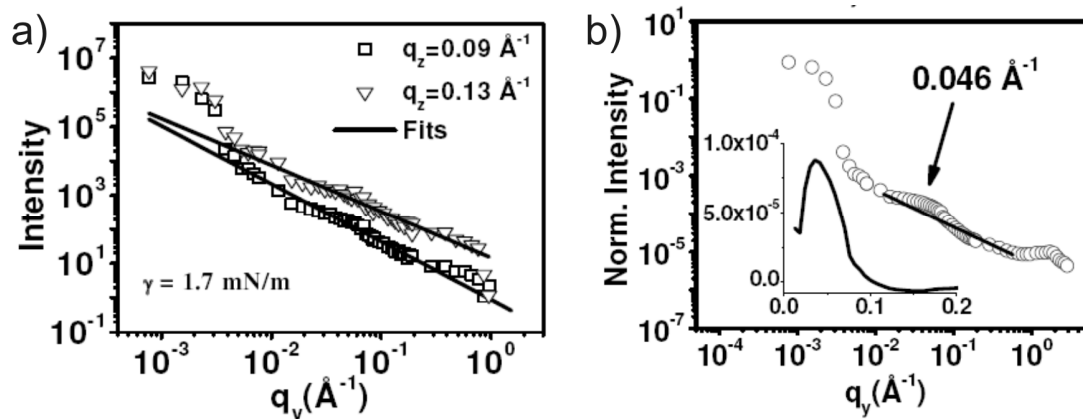


Figure 2.56 (a) The variation of scattered intensity from interface (symbols) at two different  $q_z$  values and the corresponding calculated intensity from capillary wave theory with a fixed surface tension. (b) Grazing Incidence Diffraction (GID) data (symbols) normalized to unity as a function of  $q_y$  from interface. The solid line indicates the contribution of capillary wave at the interface. The intensity of the GID peak obtained after subtracting the capillary contribution from the interface is shown in the inset.

We present a simple model that can explain the electron density profile extracted from reflectivity data and only one GID peak observed in diffuse scattering data. This model assumes a hexagonal lattice of Au nanocrystals of 1.3 nm diameter with a particle-particle separation of 15.8 nm. The electron density of the 70  $\text{\AA}$  peak, which has a width corresponding to Au nanocrystals of 1.3 nm diameter (see Figure 2.54b), takes the value of  $0.36 \text{ \AA}^{-3}$  for this large particle-particle separation. This separation of about 15.8 nm for a hexagonal lattice gives rise to single grazing incidence diffraction (GID) peak at  $q_y = 0.046 \text{ \AA}^{-1}$  (see Figure 2.56b) corresponding to lattice plane distance of 137.7  $\text{\AA}$ . The width of the GID peak indicates an uncertainty of about 1 nm in particle-particle separation. It is interesting that in-plane GID peak is not destroyed due to Brownian motion of the nanocrystals in liquids.

The formation of the hexagonal lattice at the liquid-liquid interface with micron-sized particles has been reported [359] and the cause has been attributed to the interplay between the electrostatic repulsive force and the attractive force generated by modified liquid surface. The nature of the attractive force is still under debate [361,

410] and is unlikely to be important in the present case as the top layer of nanocrystals is about 7 nm above the interface. We propose that the four-orders of magnitude reduction in the in-plane diffusion coefficient in the nanocrystals [411] generates a confinement effect on the charged Au nanocrystals and allows the particles to form the hexagonal lattice with an in-plane particle-particle distance of 15.8 nm due to electrostatic repulsive force. However, the formation of such a lattice with precursor molecules in between can not be ruled out. Further studies are required to understand the nature of the molecular assembly present in between Au nanocrystals. The decrease of electron density of the upper-most peak (refer to Figure 2.54b) from the initial high value shows that the average particle size reduces in the upper layer as time progresses. This observation indicates the movement of smaller nanocrystals away from the liquid-liquid interface. A similar observation has been noted earlier [358]. Larger particles move toward the interface as evident in the broad composite structure observed near the interface (marked as 40 Å in Figure 2.56b).

### 2.5.5 Nanocrystalline films adsorbed with alkanethiols of varying chain lengths

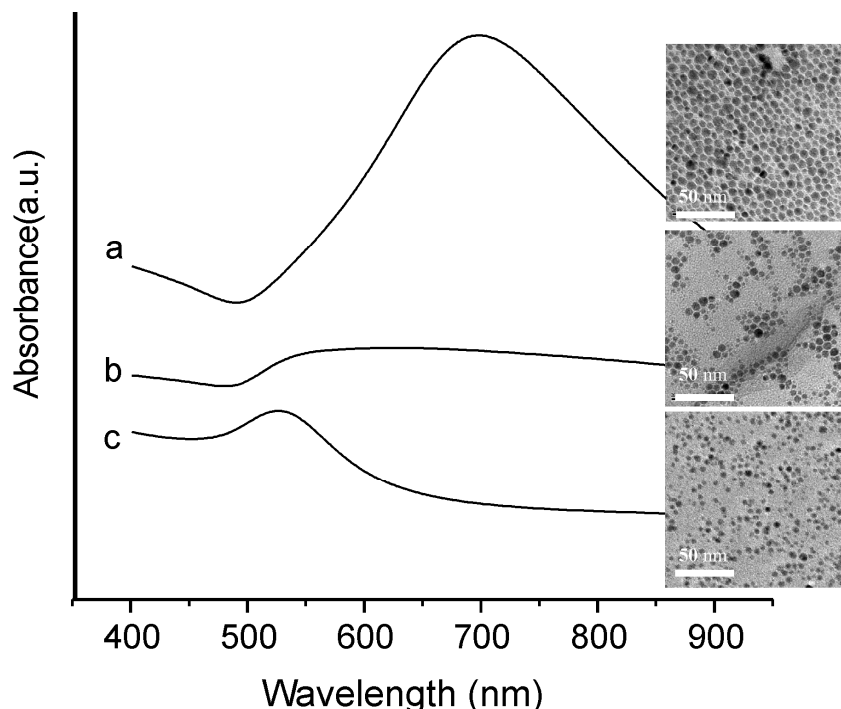


Figure 2.57 Optical absorption spectra of (a) an Au nanocrystalline film prepared at the liquid-liquid interface and deposited on a glass substrate, (b) a sol obtained by sonicating the film in toluene, (c) a sol obtained by derivatising the nanocrystals from the film using hexadecanethiol in toluene. The corresponding TEM images are shown.

Figure 2.57, shows how the optical absorption spectrum of a nanocrystalline Au film changes on perturbation through sonication and interaction with an alkanethiol. Against each spectrum, we have a TEM image to demonstrate the nature of the nanostructure present. The spectrum corresponding to a nanocrystalline film obtained at the liquid-liquid interface at room temperature, Figure 2.57a exhibits a broad band centered at 700 nm, with a very weak shoulder at  $\sim 540$  nm. While the absorption band around 540 nm is characteristic of surface plasmons from uncoupled nanocrystals [412, 413], the higher wavelength band at 700 nm is a typical response from an assembly of interacting nanocrystals [94, 414]. As evident from the corresponding TEM image (Figure 2.57), the nanocrystalline film consists of particles with diameters in the range of 5 - 8 nm in a close-packed array with  $\sim 1$  nm spacing due to the organic shell. At such close distances, one would expect the electronic coupling between the neighboring particles to be significant. Furthermore, the number of interacting nanocrystals may be very large, as the array can extend as in the present case, to several hundred microns. This results in a collective absorption by the nanocrystals, which is red-shifted by as much as 160 nm from the usual surface plasmon band from Au nanocrystals (spectrum 'a' of Figure 2.57). The collective absorption is affected when the nanocrystalline film is subjected to ultrasonication as can be seen in spectrum 'b'. We notice a rise in the absorption at 540 nm followed by an ill-defined broad feature. The TEM image shown alongside depicts fragments of the extended array, comprising smaller assemblies ( $\sim 30$ -50 nm) of few tens of particles, but with similar interparticle spacing (1 nm). The absence of a clear red-shift and the broad nature of the spectrum (b), arises from the reduction in the domain size of the interacting particles. In the limiting case of an organosol formed by derivatising the nanocrystals in the film with hexadecanethiol, we obtain a well-defined peak at 530 nm (spectrum c), typical of uncoupled colloidal Au nanocrystals. Accordingly, the TEM image shows isolated nanocrystals of size (8 nm) expected from a nanocrystalline film prepared at room temperature.

#### **2.5.5.1 Chemical perturbation using alkane thiols**

We have investigated the properties of the nanocrystalline Au films subjected to chemical perturbation brought about by interaction with n-alkanethiols of varying chain lengths (Figure 2.58). For this purpose, a portion of the film ( $75^{\circ}\text{C}$ , 180

minutes) on glass was dipped in a 10 mM toluene solution of a hexadecanethiol for 6 h. The optical absorption spectrum recorded following the interaction with hexadecanethiol (Figure 2.58 left) exhibits a plasmon band, which is blue shifted from 697 to 569 nm. This observation suggests that the electronic coupling between the nanocrystals is considerably reduced following the attachment of the thiol molecules. This interaction with thiol also brings about a change in the morphology of the film as shown in the adjoining AFM images.

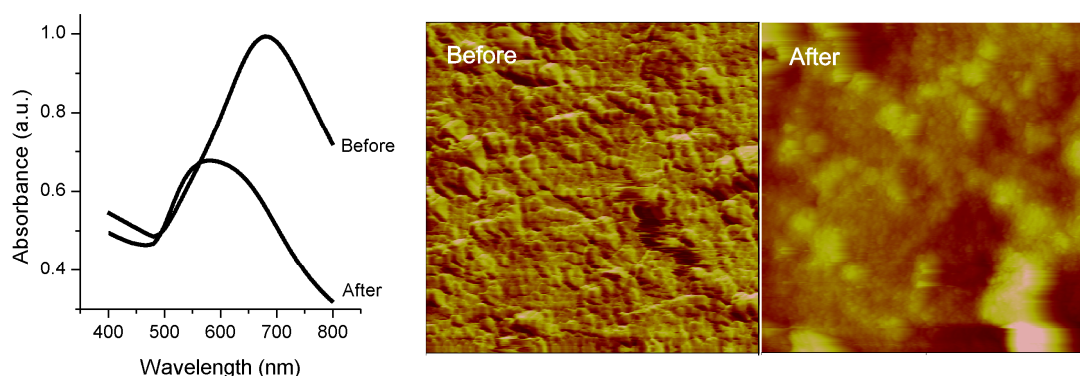


Figure 2.58 Optical absorption spectra of an Au film before and after treatment with hexadecane thiol solution for 6 hours. Tapping mode AFM images are shown alongside (scan area, 500 x 500 nm).

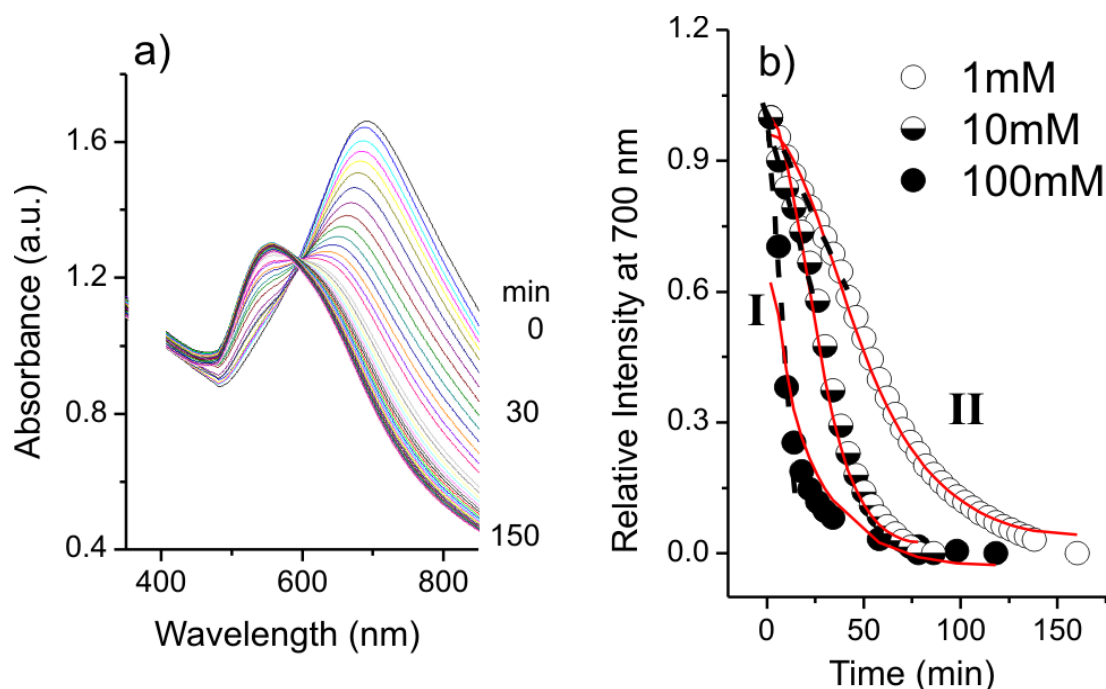


Figure 2.59 (a) Absorption spectra of a Au nanocrystalline film immersed in a toluene solution of hexadecanethiol (100 mM) recorded at intervals of 4 minutes at 15 °C. (b) Variation in the absorption intensity at 700 nm normalized with respect to the initial intensity, for three different concentrations of hexadecanethiol.

the thiol. Initial part (I) shows a linear variation (dashed) while the latter part (II) is fitted to equation (2.4).

The observed contrast between the optical spectra of the nanocrystal film and isolated nanocrystals led us to investigate the effect of thiol adsorption on the nanocrystalline film. For this purpose, we chose the nanocrystalline films prepared at 75 °C with mean diameter of 15 nm. Figure 2.59a, shows the optical absorption spectra from a Au nanocrystalline film following the interaction with hexadecanethiol (100mM in toluene) for increasing time periods. The absorption band of the pristine film undergoes a gradual blue-shift from 697 to 560 nm, with an accompanying decrease in the absorption intensity. The projected length of a hexadecanethiol molecule being 2.2 nm, the average interparticle distance is expected to increase upon thiol adsorption, from ~ 1 nm (see top TEM image in Figure 2.57a) up to 4.4 nm (corresponding to bilayer spacing of hexadecanethiol). The increasing interparticle distance reduces the effective electronic coupling between the nanocrystals, thus causing a blue shift in the optical absorption. We observe an isosbestic point [415, 416] at 600 nm indicating the presence of an equilibrium between two species with characteristic absorption maxima at 690 nm and 560 nm. The equilibrium is clearly between the thiol-covered film and the thiol-capped individual nanocrystals formed by disordering of the film. Figure 2.59b, shows a plot of the relative intensity at 700 nm as a function of time, for three different concentrations of the thiol (1, 10 and 100 mM), to demonstrate how the intensity drops quite rapidly during the first 10 minutes when the nanocrystalline film interact with a 100 mM thiol solution, exhibiting only a negligible decrease in intensity after longer periods. For lower concentrations of the thiol, the initial drop is less steep (particularly for 1 mM), followed by a gradual decrease over 100-150 minutes. It appears that the nanocrystal surface gets covered by the thiol molecules rapidly initially, further adsorption becoming gradual as additional surface sites become difficult to access [417]. This is reminiscent of the two-stage adsorption process well known in the case of self-assembled monolayer of alkanethiols on plane metal surfaces [418]. It is known that the molecules crowd the surface during the initial process, followed by a slow rearrangement to a well ordered monolayer. Figure 2.60 show series of absorption spectra obtained on using thiols of different chain lengths.

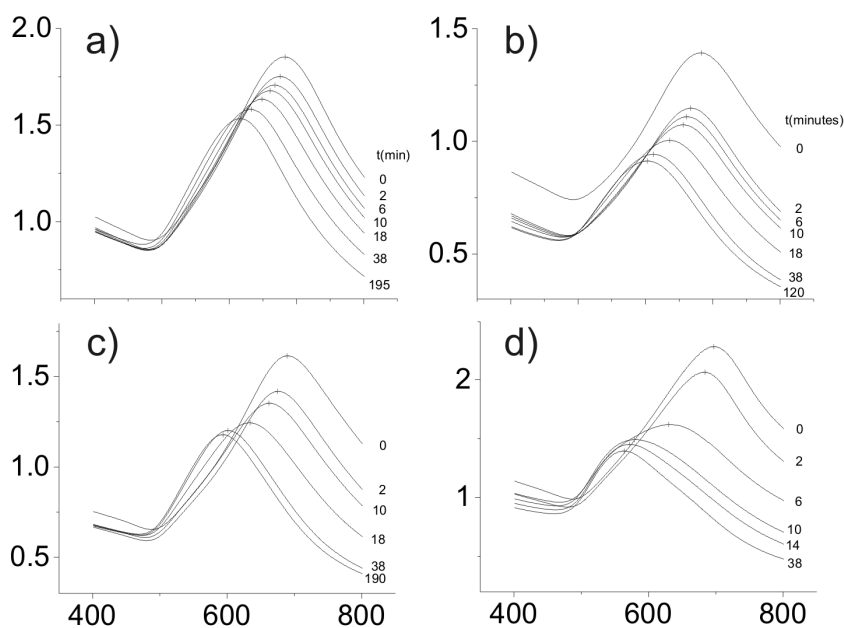


Figure 2.60 Absorption spectra of a Au nanocrystalline film immersed in a toluene solution of (a) Heptanethiol (C7), (b) Nonanethiol (C9), (c) Decanethiol (C10) and (d) Octadecanethiol (C18) alkanethiols.

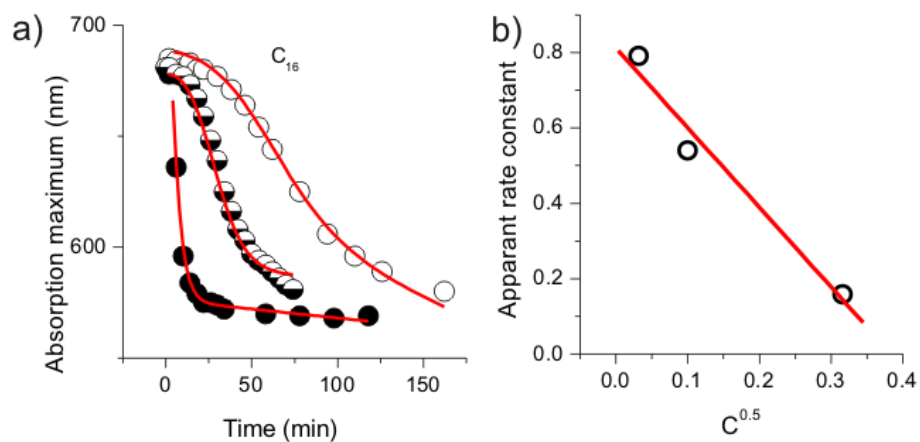


Figure 2.61 (a) Variation of absorption maxima with time, (b) A plot showing variation in apparent rate constant with concentration. This is an alternative approach to plotting absorption intensity vs. time.

### 2.5.5.2 Study of kinetics and mechanism of reaction

Alkane thiol adsorption on metal nanoparticle surfaces has been treated as a modified first order process in earlier studies [419]. Thus, the time variation of the optical absorbance ( $A$ ) is described by,

$$\frac{dA}{dt} = -kC^{\frac{1}{2}}\Delta A_r(1 - \Delta A_r)\exp(-b\Delta A_r) \quad (2.4)$$

$$k = (KC^{\frac{1}{2}} + k_2) \quad (2.5)$$

$$\frac{dA}{dt} = -(KC^{\frac{1}{2}} + k_2)C^{\frac{1}{2}}\Delta A_r(1 - \Delta A_r)\exp(-b\Delta A_r) \quad (2.6)$$

$$\frac{dA}{dt} = -KC\Delta A_r(1 - \Delta A_r)\exp(-b\Delta A_r) - k_2C^{\frac{1}{2}}\Delta A_r(1 - \Delta A_r)\exp(-b\Delta A_r)$$

where  $C$  is the thiol concentration,  $k$  and  $k_2$ , apparent rate constants, the relative absorbance,  $\Delta A_r = (A(t) - A(\infty))/(A(0) - A(\infty))$  and  $b$ , an empirical parameter. This equation is not applicable to the initial part of the curve where the drop in intensity is rapid, but is well suited to deal with the gradual change. The former, when fitted to a linear behavior, yielded zeroth order rate constants of 0.01, 0.02 and 0.06 mol sec<sup>-1</sup> respectively for 1, 10 and 1 mM thiol concentrations. Satisfactory fittings have been obtained for the rest of the data using equation (2.4), with apparent rate constants ( $k$ ) of 0.79, 0.54 and 0.16 dm<sup>3/2</sup> s<sup>-1</sup> mol<sup>-1/2</sup> for 1, 10 and 100 mM, respectively. However, we have also plotted absorption maxima with time, so obtain rate constants as shown in Figure 2.61a. The apparent rate constants are concentration dependent as shown in Figure 2.61b ( $C^{1/2}$  dependence)[420]. The concentration independent rate constant was found to be  $\sim 2$  dm<sup>3</sup>mol<sup>-1</sup>sec<sup>-1</sup>.

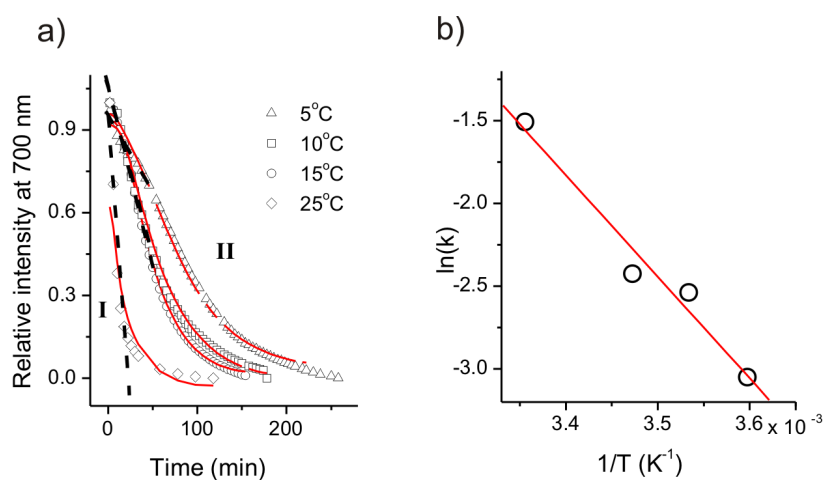


Figure 2.62 (a) Variation in the absorption intensity at 700 nm (normalized with respect to the initial intensity) at 5°, 10°, 15° and 25 °C. Initial part (I) shows a linear variation (dashed) while the latter part

(II) is fitted to equation (2.4). (b) Arrhenius plot where the slope corresponds to an activation energy of 42 kJ/mol.

Figure 2.62 depicts the effect of temperature on the interaction of hexadecane thiol with Au nanocrystals in the film. The thiol adsorption process is much slower at 15 °C, the time taken being ~ 150 mins as against 120 mins at 25 °C. It is even slower at lower temperatures (10 °C and 5 °C) as seen from the plot of the intensity values at 700 nm with time (Figure 2.62a). The data in the figure were fitted with equation (2.4) to determine the values of the apparent rate constant ( $k$ ). Figure 2.62b shows a plot of  $\ln(k)$  vs.  $1/T$ , where the fit to the data is linear, corresponding to an Arrhenius behavior with an activation energy of 40 kJ/mol. Considering the activation energy of 29 kJ/mol for adsorption of alkane thiol on Au and 0.84 kJ/mol per methylene unit of the alkane chain [421]. We estimate the total activation energy for hexadecanethiol adsorption on Au surface to be 42 kJ/mol, which is close to the value obtained in the present experiment.

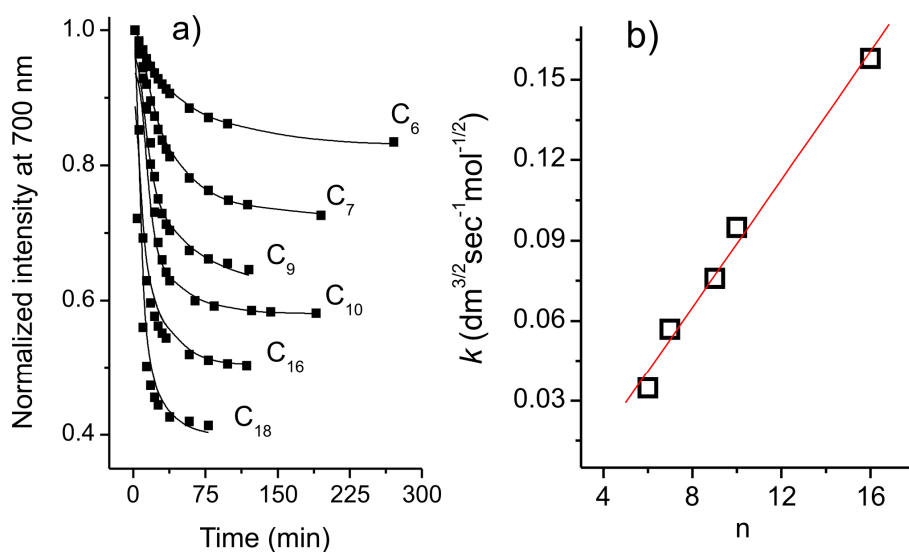


Figure 2.63 (a) Time variation in the absorption intensity at 700 nm normalized with respect to the initial intensity, for alkanethiols of different chain lengths (100 mM, 25 °C). The curves are fitted to equation (2.4). (b) A plot of the apparent rate constant ( $k$ ) versus the number of carbon atoms in the alkanethiol,  $n$ .

The interaction of alkanethiols of different chain lengths with the nanocrystalline Au films has been examined in some detail. Figure 2.63 gives a plot of the absorbance values at 700 nm normalized with respect to the initial value, against the time for which a film is immersed into a thiol solution (100 mM). The relative absorbance



decreases in all the cases, more so for longer chain lengths. Thus, the chain length of the thiol molecule has a remarkable effect on the rate of adsorption, higher the chain length, faster being the thiol adsorption [422]. The data in Figure 2.63a, were fitted with equation (2.4) in order to determine the apparent rate constants for the different alkane thiols. The rate constant increases linearly with the chain length as shown in Figure 2.63b. Thus, the longer chain alkane thiols are more effective in separating out the nanocrystals within the film causing larger blue shifts in the absorption band. The interaction between the Au nanocrystals increases linearly with decrease in chain length, akin to the observation made on alkane thiol adsorption on Au surfaces [423].

Figure 2.63a, suggests that after a sufficient time interval, the absorbance of the nanocrystalline film tapers off, indicating saturation coverage of the thiol molecule. The time interval at which the saturation is reached clearly depends on the rate of thiol adsorption or the length of the thiol molecule, while the relative absorbance at saturation is related to the effective change in the interparticle distance. This is also evident from the position of the absorption maximum at saturation coverage (Figure 2.64). While the band is positioned at  $\sim 700$  nm for the as-prepared film, after thiol adsorption, it is blue-shifted, larger being the shift longer the chain length. Figure 2.64b shows how the position of the absorption band varies with the alkane chain length or interparticle distance. The shift increases rapidly ( $\sim 90$  nm) with chain length at relatively small chain lengths (up to  $C_8$ ) and becomes somewhat gradual for longer chain lengths.

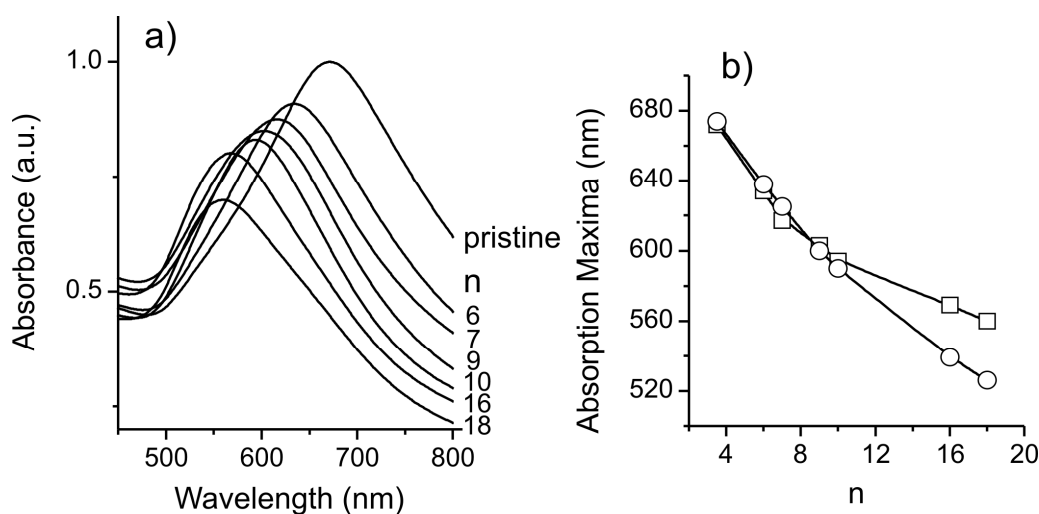


Figure 2.64 (a) Absorption spectra obtained after treating the Au nanocrystalline films with alkanethiols of different chain lengths ( $n$  = number of carbon atoms in the alkane chain). In each case,

the saturation adsorption was marked by no further changes in absorbance with time. (b) Absorption maximum versus the number of carbon atoms in the alkane chain. The values calculated using Maxwell Garnett formalism (circles) is shown along with the experimental values (squares). The latter may be fitted to an exponential behavior with a characteristic decay length of 2 nm.

The spectral changes shown in Figure 2.64 can be explained based on the Maxwell-Garnett formalism [392, 424]. Assuming close packing, the optical absorption by a granular film depends on its packing fraction,

$$f = 0.741 \left( \frac{r}{r+s} \right)^3 \quad (2.7)$$

$r$  being the radius of the grain (nanoparticle) and  $s$ , the interparticle separation. In our nanocrystalline films, the size of the nanocrystals ( $r$ ) is almost constant ( $\sim 15$  nm), as all the films were prepared under similar conditions. The spectral changes take place primarily due to the changes in the value of  $s$  (length of the adsorbed thiol molecule as well as coverage). By inserting suitable values for  $f$ , we have calculated absorption intensities using,

$$\zeta = \frac{4\pi n_{MG} h}{\lambda} \quad (2.8)$$

$$\varepsilon_{MG} = \varepsilon_M \left( 1 + 3f \frac{\varepsilon_D(\omega) - \varepsilon_M}{\varepsilon_D(\omega)(1-f) + \varepsilon_M(f+2)} \right) \quad (2.9)$$

Here  $\zeta$  is the absorption intensity,  $n_{MG}$  is the real part of the effective complex index of refraction  $\lambda$  the wavelength,  $h$  is the film thickness,  $\varepsilon_M$  the dielectric constant of the matrix,  $\varepsilon_D$  Drude dielectric function, and  $\varepsilon_{MG}$  the Maxwell-Garnett dielectric function. The calculated absorption maxima are also plotted against alkane chain length in Figure 2.64b. We see that the calculated values show a monotonic variation and are similar to the experimental values at shorter chain lengths but stand underestimated for hexadecane ( $f$ , 0.51) and octadecanethiol ( $f$ , 0.48). This is understandable since the Maxwell Garnett formalism holds good for films with higher volume fraction of nanocrystals ( $f \sim 0.67$ ) or for shorter lengths of the spacer. We have not taken into account possible interdigitation of molecules, relevant specially for longer thiols [201]. Furthermore, the longer chains tend to curl up.

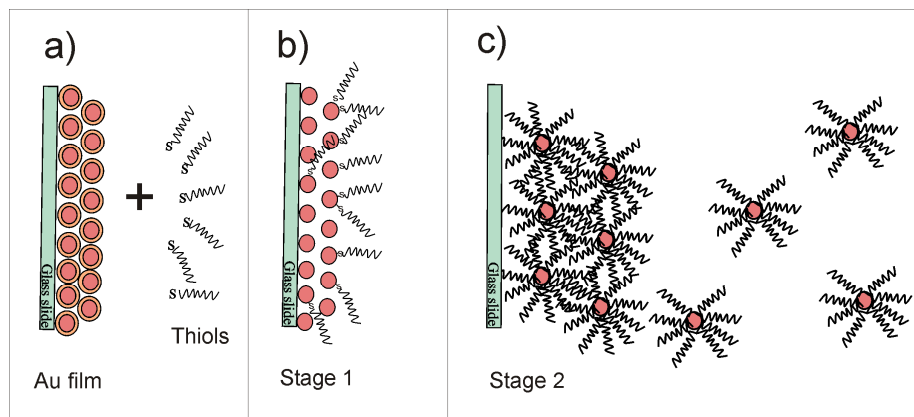


Figure 2.65 A schematic showing the process of thiol adsorption and increasing disorder in the nanocrystalline film.

It is important to understand the processes responsible for the changes in the absorption of the Au nanocrystalline films spectra that we observe on the addition of alkane thiols. The primary process involves the interaction of alkane thiol with the nanocrystalline Au film, causing disorder in the film due to the capping of individual nanocrystals by the thiol molecules (see the Schematic diagram in Figure 2.65). Such a disorder causes an increase in the separation between nanocrystals relative to that obtains in the pristine film. The separation between the particles caused is determined by the length of alkane chain. Thus, the blue shift of surface plasmon band increases with the increasing chain length because of the increased separation between the nanocrystals. In other words, the interaction between the particles decreases with the increase in chain length as revealed by the linear plot in Figure 2.64b. The effect of chain length is also seen in terms of the rate of disordering or disintegration of the nanocrystalline film, where the longer chain thiols are more effective, resulting in the higher rate of film disintegration (Figure 2.63). The extreme case of disordered nanocrystalline film is where the nanocrystals present in the film get fully separated and go into solution, giving rise to as isolated thiol capped nanocrystals. We do indeed see a small concentration of such nanocrystals in solution as evidenced by the pink colored solvent and the surface plasmon band of the organosol with an absorption maximum at 530 nm as shown in Figure 2.66. The concentration of such nanocrystals in the organosol increases with the chain length of thiol, since long chain thiols such as hexadecanethiol are more effective in causing disorder and disintegrating the film. TEM on one such sample confirms the presence of nanocrystals as shown in Figure 2.66.

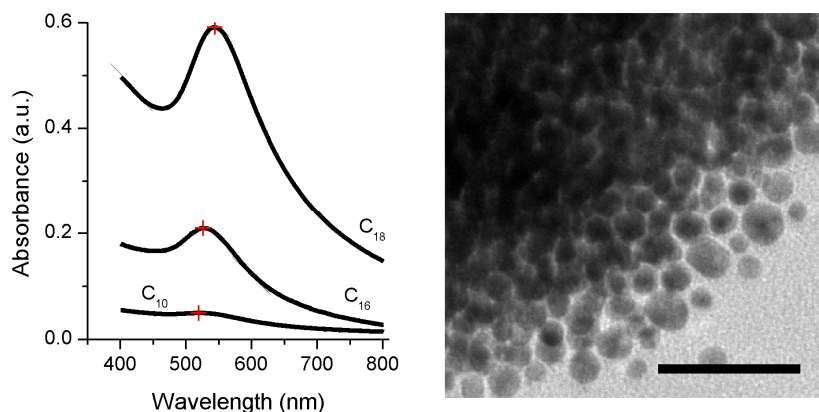


Figure 2.66 Absorption spectra of standing sol (left), TEM image from one such sol (right).

Considering that stage 1 in Figure 2.65 is essentially an exothermic process while stage 2 involves an endothermic disordering process, possibly followed by an exothermic thiol binding process. After the disordering or disintegration of the film, isolated nanocrystals get created which are then capped by the thiol molecules present in the solution. The last step is exothermic.

### 2.5.5.3 Reversibility in controlling interparticle separation

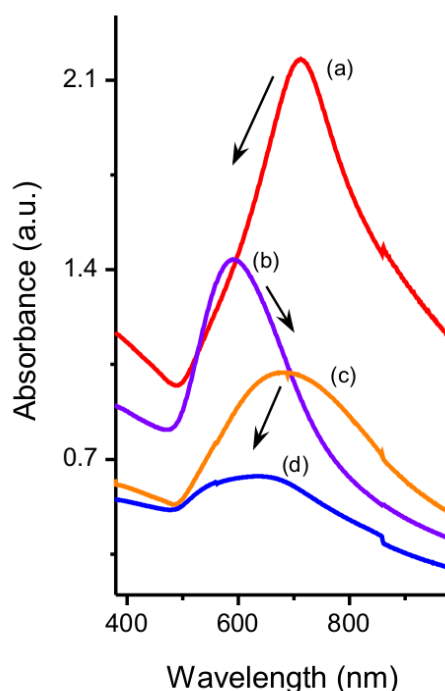


Figure 2.67 Absorption spectra of (a) Au nanocrystalline film obtained after successive dipping, in solution of (b) hexadecanethiol, (c) hexanethiol, and (d) hexadecanethiol.

In order to demonstrate the alkane-thiol (interparticle distance) specific interaction between Au nanocrystals, the absorption spectra have been recorded after interaction with hexane and hexadecane thiol alternatively. In Figure 2.67, we show the absorption spectra from a film that was sequentially treated with 100 mM of hexadecanethiol and hexanethiol, until saturation. The absorption maximum from the as-prepared film is blue shifted by 140 nm after dipping in hexadecanethiol and interestingly, it red-shifts by as much as 120 nm after dipping in hexanethiol. The latter thiol being shorter in length brings the particles closer, causing a red shift. This observation confines the occurrence of interdiffusion and exchange of alkane thiols of different chain lengths, known in the case of self-assembled monolayers [423, 425, 426]. It brings out the versatile nature of the nanocrystalline films. This process cannot, however, be repeated indefinitely as the spectral intensity diminishes with each dip (see Figure 2.67), as the nanocrystals from the film migrate into the solution.

#### 2.5.5.4 Studying effect of conducting thiol

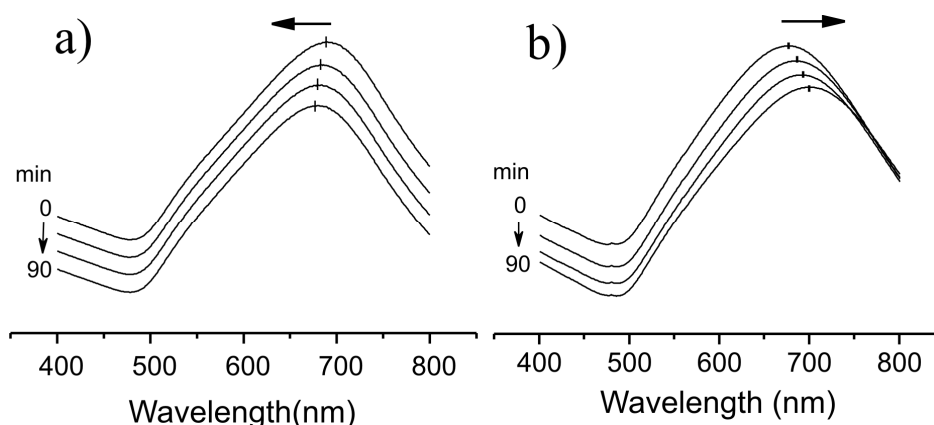


Figure 2.68 Absorption spectra obtained after treating a Au nanocrystalline film with (a) decanedithiol and (b) mercapto 1,2-diphenylacetylene. Arrows indicate the direction of shift of the absorption band.

We have also examined how the nature of the spacer molecule affects the optical absorption spectra of the Au films. We have chosen to compare decanedithiol and mercapto 1,2-diphenylacetylene as both these molecules have similar lengths matching closely with the prevailing gap between nanocrystals ( $\sim 1$  nm) in the film. Figure 2.68a shows the absorption spectra from a decanedithiol derivatized Au film. A blue shift is noticed in the plasmon band. Because of its bifunctionality, decanedithiol does not seem to penetrate the Au film as much as a monothiol of a similar length and concentration. Interestingly, on adsorption of mercapto 1,2-

diphenylacetylene, the plasmon band shifts toward longer wavelengths. The red shift could be due to the enhanced interparticle coupling due to the conjugated nature of the molecule (Figure 2.68b). Since the two molecules have similar lengths, the interparticle distance would be similar in the two cases and we would not expect the position of the adsorption band to change. The observed difference in the band shifts is attributed to the change in the coupling between nanocrystals due to the nature of the spacer molecules.

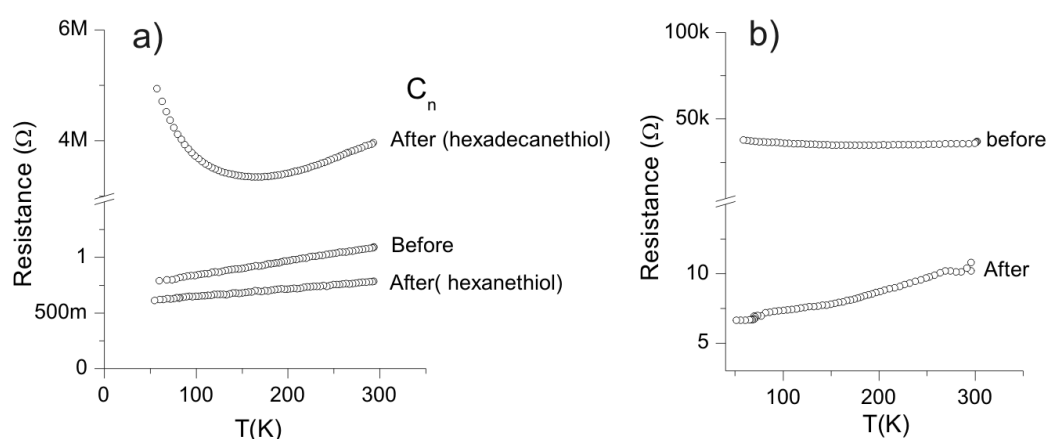


Figure 2.69 (a) Temperature variation of the electrical resistance of Au films (75°C, 180 minutes) before and after treatment with hexadecanethiol and hexanethiol. (b) Temperature variation of the electrical resistance of an Au film (45°C, 60 minutes) before and after treatment with dimercaptodiphenylacetylene.

In Figure 2.69, we show how the electrical property of a film can change depending on the thiol employed to perturb it. Thus, upon interacting with hexadecanethiol, a metallic film (75°C, 180 minutes) behaves like an activated conductor (Figure 2.69a) with a reversal of slope around 150K. Such temperature dependent change in conduction through nanocrystal superlattices has been interpreted as due to a “metal-insulator” transition [71]. On the other hand, hexanethiol with a shorter chain length essentially retains the metallic nature of the pristine film (see Figure 2.69a). This is in accordance with the observation of Shiigi et al. [391], who found that Au nanocrystal films coated with shorter chain length thiol are more conducting. Interestingly, on interaction with dimercaptodiphenylacetylene, a conjugated molecule [427], the resistance of a film (45°C, 60 minutes) decreases, becoming metallic (Figure 2.69b).

### 2.5.6 Effect of surfactants on interfacial reaction

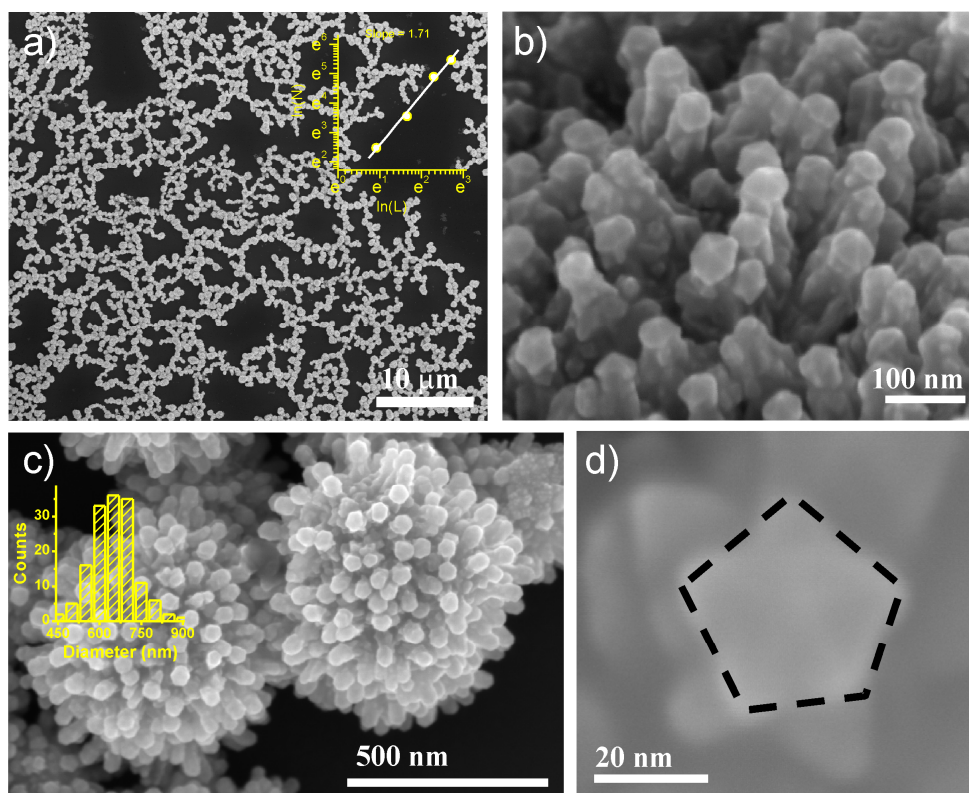


Figure 2.70 (a) SEM image showing the fractal network formed by cauliflower-like Au structures by employing method 1 with TOAB. (b) High resolution SEM image of the nanorods present in the cauliflower-like structures, (c) a high-resolution image of the cauliflower-like structures. The inset shows the histogram of the size distribution of cauliflower-like structures. (d) SEM image shows the end of one such nanorod with a five-fold symmetry.

Figure 2.70a shows a SEM image of the structure obtained at the liquid-liquid interface from the reduction of Au ions by hydrazine employing method 1. At the micron scale, the structure has a fractal type network. We estimate the fractal dimension (Hausdorff dimension) of the structure to be  $\sim 1.7$  [428]. On careful examination at higher resolution, we find that the fractal structures are found to comprise cauliflower-like spherical units (see Figure 2.70c) with a diameter of  $\sim 700$  nm (see inset in Figure 2.70c). Pentagonal nanorods project out of the spherical units (Figure 2.70b), whereas the average density of such nanorods on the surface being typically  $\sim 200$  rods per  $\mu\text{m}^2$ . The average radius of the pentagonal face of the nanorods is 23 nm, the height being 110 nm (Figure 2.71a). The inset in Figure 2.71b shows a high-resolution TEM image of one such nanorod. What we actually obtain are sheets containing networks of cauliflower-like structures with the nanorods

emerging from them. In Figure 2.71c, we show a high-resolution image of the tip of a nanorod in its early stage of growth. The five twin boundaries are clearly discernible. We also obtain similar fractal structures comprising cauliflower-like structure when method 2 involving the reduction of  $\text{Au}(\text{PPh}_3)\text{Cl}$  with hydrazine followed by the addition of TOAB, was employed. Since we obtain similar structures by both methods 1 and 2, we conclude the role of the TOAB surfactant in the organic phase to be crucial.

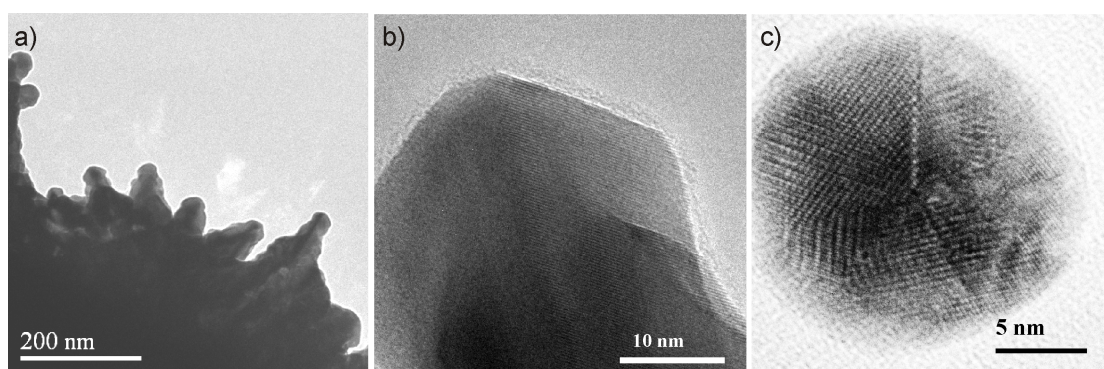


Figure 2.71 (a) TEM image of a cauliflower-like structure showing tips of the nanorods. (b) TEM image shows a high-resolution image from one such rod. (c) High-resolution TEM image of a nanorod in its early stage of growth (formed after 5 min using method 1).

Figure 2.72 shows the optical absorption spectra of the films, which reveal broad features due to plasmon absorption. The long wavelength feature around 860 nm is clearly due to aggregates of the Au nanocrystals. Such bands are characteristic of nanorods [309, 429-432].

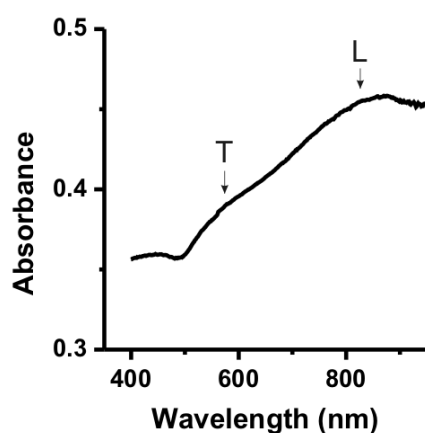


Figure 2.72 Optical absorption spectrum of the cauliflower-like units comprising Au nanorods showing plasmon absorption bands.



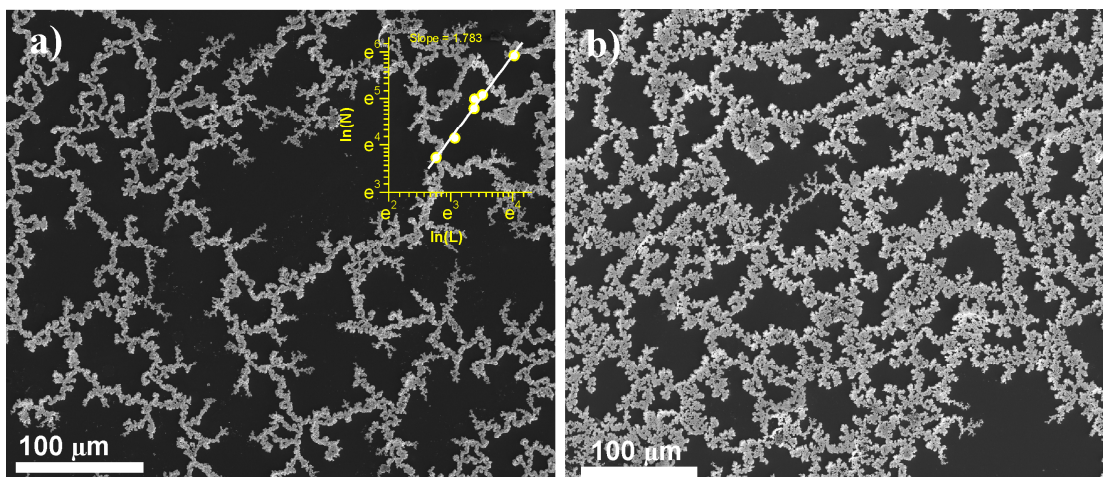


Figure 2.73 (a) SEM image of the network of Au nanostructures obtained by method 1 using TOAB in the absence of  $\text{PPh}_3$  after 2 hours of reaction time. Inset shows calculation for fractal dimension (b) SEM image of the network obtained after 48 hours.

Figure 2.73a shows the structures formed at the liquid–liquid interface using method 1 in the absence of  $\text{PPh}_3$ . In this case, the organic layer had only  $\text{AuCl}_4^-$  ions and TOAB. Yet, we obtain fractal-like structures with a fractal dimension of  $\sim 1.8$ . The fractal structures grow denser over longer time, as shown in Figure 2.73b. These structures are highly reproducible and well-connected (see Figure 2.74 left) and are actually formed by octahedral Au crystals (see Figure 2.74 right) of similar type described by Li et al. [433]. Li et al., however, obtained such crystals by a modified polyol process in a PEG600 solution.

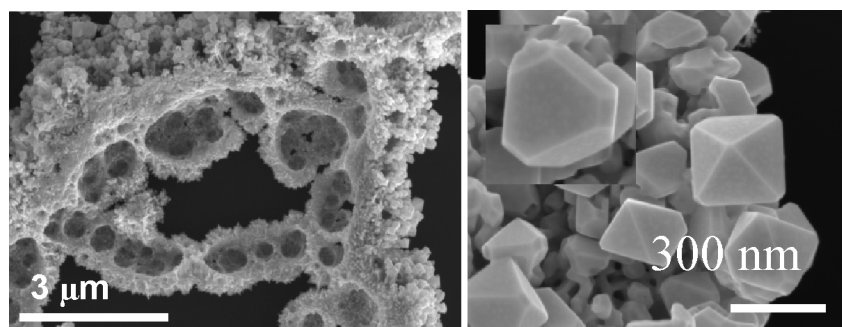


Figure 2.74 The left image shows a high-resolution image of branch of fractal and the right image shows edge of the branch showing octahedral crystals.

Figure 2.75a) shows XRD pattern of the fractal structure formed at the interface. Intense peak at (111) indicate polycrystalline nature of the structure. However, the broadening of the peak can be associated to the presence of strain in the structure. Figure 2.75b shows optical absorption spectra, with poorly resolved peaks around 580

and 800 nm. These peaks are associated with transverse and longitudinal plasmon band arising from the branched structure of fractal [434]. Interestingly, as seen from electrical transport measurement shown in Figure 2.75c that the structure possesses metallic behavior, revealing that the entire structure is electrically connected over the range of few millimeters. Conduction in such a random structure are due to percolation [435, 436].

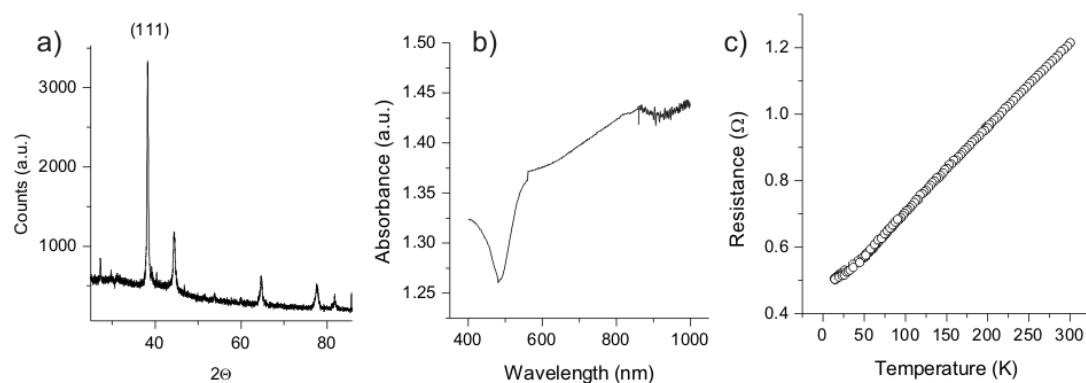


Figure 2.75 (a) XRD pattern from the fractal structure, (b) optical absorption spectra of the same and (c) temperature variation of the electrical resistance of same.

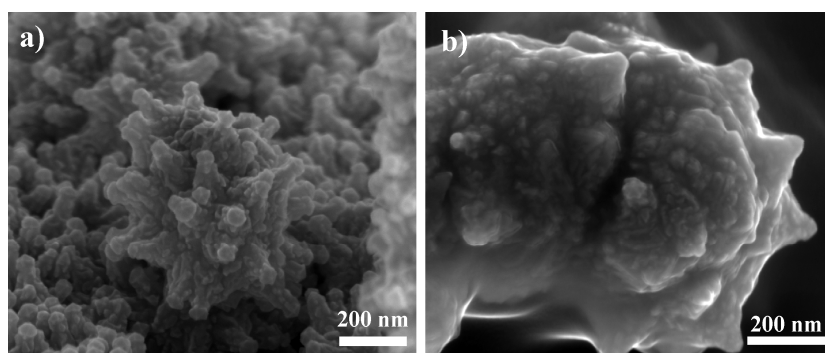


Figure 2.76 SEM images of the Au nanostructures obtained by method 1 using different concentrations of TOAB: (a) 18  $\mu\text{mole}$  and (b) 91  $\mu\text{mole}$ . Other conditions remain similar as in Figure 2.70.

The nanorods emanating from the cauliflower structures (Figure 2.70) owe their presence to the surfactant TOAB, which is known to induce the cylindrical shapes in Au nanostructures [259, 437]. The concentration of TOAB affects the number of nanorods projecting from the cauliflower-like structures. When the concentration was increased to 5 and 25 times, the density of nanorods dropped from 200 per  $\mu\text{m}^2$  to around 70 and 25 respectively. In Figure 2.76, we show the kind of structures we obtained with high concentrations of TOAB (18 and 91  $\mu\text{moles}$ ). On increasing the

surfactant concentration, the surface of the cauliflowers become smoother and less structured. It is noteworthy that unlike the organization of large structures at the air-water interface reported by Jin et al. [438], we obtain cauliflower-like structures at the liquid-liquid interface, which further organize themselves in the form of fractals at the interface. Such an assembly is likely to be due to diffusion-limited aggregation [378]. The interface being two-dimensional (between two liquids), the formation of such structures can be described schematically as in Figure 2.77. It is noteworthy that the nanorods terminate with an icosahedral face (Figure 2.70). Though not common, there are reports of the formation of five-fold structures in the literature. Multiple twinning in Au often occurs in particles larger than 8 nm by coalescence of primary particles with tetrahedral morphology [439]. Molecular dynamics studies on the growth of small Ag nanocrystals show that icosahedral structures are energetically more favorable [440, 441]. The TEM image of a Au nanoparticle (formed after 5 min of the reaction) shown in Figure 2.71c indicates the presence of multiple twin boundaries in five-fold symmetry. The five-fold rotational symmetry probably occurs due to the formation of an early twin boundary in the freshly reduced Au crystals [442].

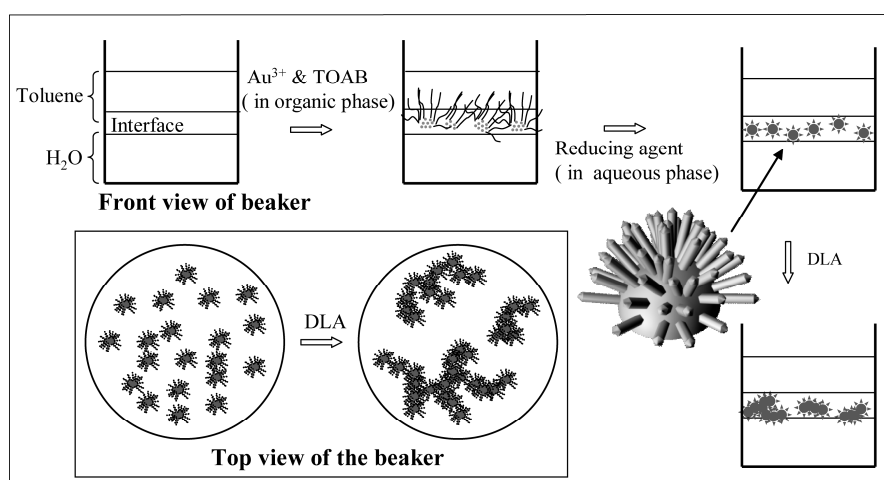


Figure 2.77 Schematic showing the formation of fractal network structures at the interface.

Experiments carried out with CTAB in the aqueous phase (by following method 1) also gave cauliflower-like structures (diameter 400 nm) at the interface. In Figure 2.78a, we show a SEM image of an assembly of cauliflower structures obtained with CTAB. These are densely packed in comparison to those from TOAB Figure 2.70, but the density of nanorods on each cauliflower-like structure is similar in the two cases (see Figure 2.70b and the inset in Figure 2.78a). Interestingly, the growth of the

nanorods is not appreciable on the aqueous side of the interface (Figure 2.78b). The optical absorption spectrum of the film containing these networks show plasmon bands (see Figure 2.78c). The 780 nm band can be considered to be due to the plasmon adsorption of the aggregates as described in the literature.

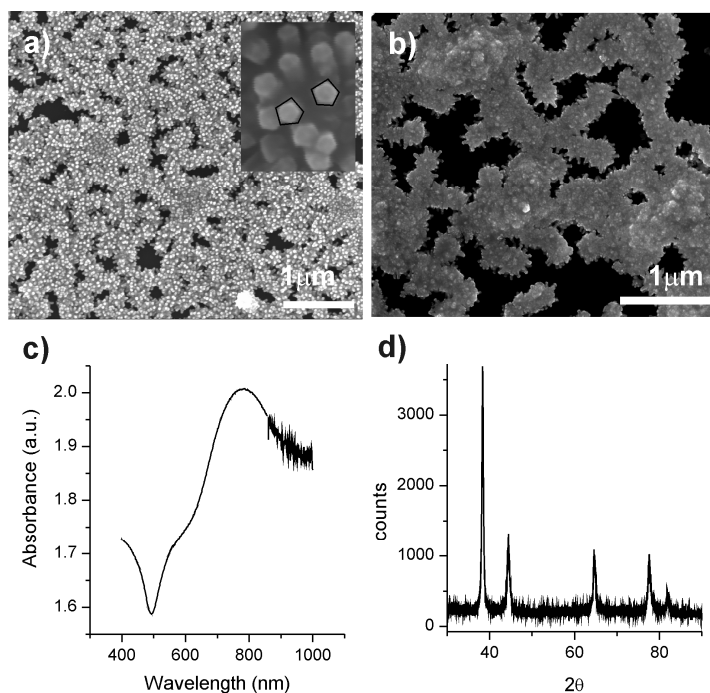


Figure 2.78 (a) SEM image showing a compact network of cauliflower-like structures by method 2 using CTAB. Inset shows a high-resolution SEM image of the end (tip) of nanorods with a five-fold symmetry. (b) SEM image of the network facing aqueous layer, (c) Optical absorption spectrum of the network shows plasmon absorption band and (d) X-ray diffraction pattern of the same.

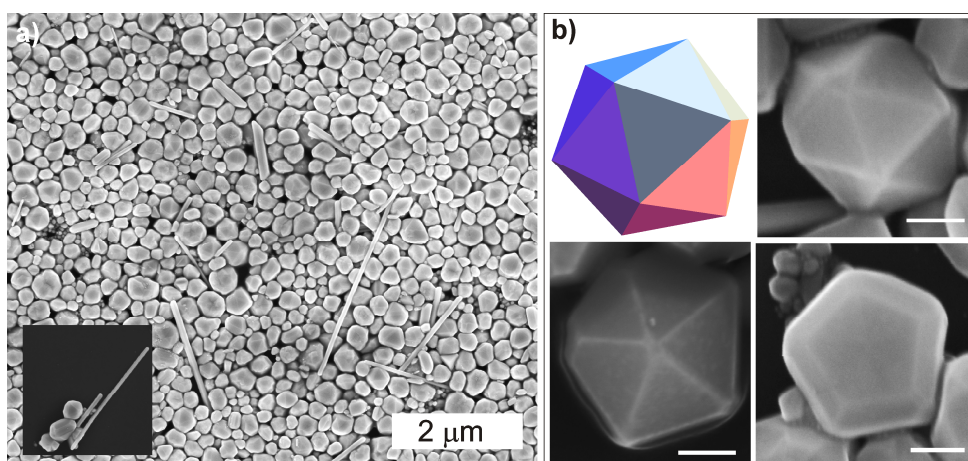


Figure 2.79 (a) SEM image of the Ag network obtained by method 1. The inset shows a nanowire obtained along with nanocrystals. (b) Magnified image of few icosahedral crystals. All scales in (b) correspond to 100 nm.

In the case of Ag, we obtained large nanocrystals and nanowires through method 1 using TOAB as the surfactant (Figure 2.79). Interestingly these nanocrystals possess five-fold symmetry, and are icosahedral in shape. These structures are devoid of pillars and other features observed in the case of Au.

When the concentration of the Ag precursor was increased, large dendritic nanostructures were formed, as shown in Figure 2.80a. We also obtained well-connected network structures by method 1 using TOAB as the surfactant but in the absence of  $\text{PPh}_3$ , as shown in Figure 2.80b. Dendritic nanostructures of Ag have been produced by microwave or ultraviolet irradiation of  $\text{AgNO}_3$  in the presence of PVP. Ag dendrites have been obtained by the interaction of tetrathiafulvalene with  $\text{AgNO}_3$  in the presence of PVP [443]. Dendrite nanostructures are also obtained with the assistance of ultrasonic waves by using Raney nickel as the template as well as the reducing agent [444]. We must also point out that dendrite structures of metal and semiconductor nanocrystals can be produced in the presence of electric fields during the vapor phase synthesis of nanocrystals by laser vaporization [445]. In all these cases, diffusion limited aggregation has been invoked to explain the formation of dendrites [446].

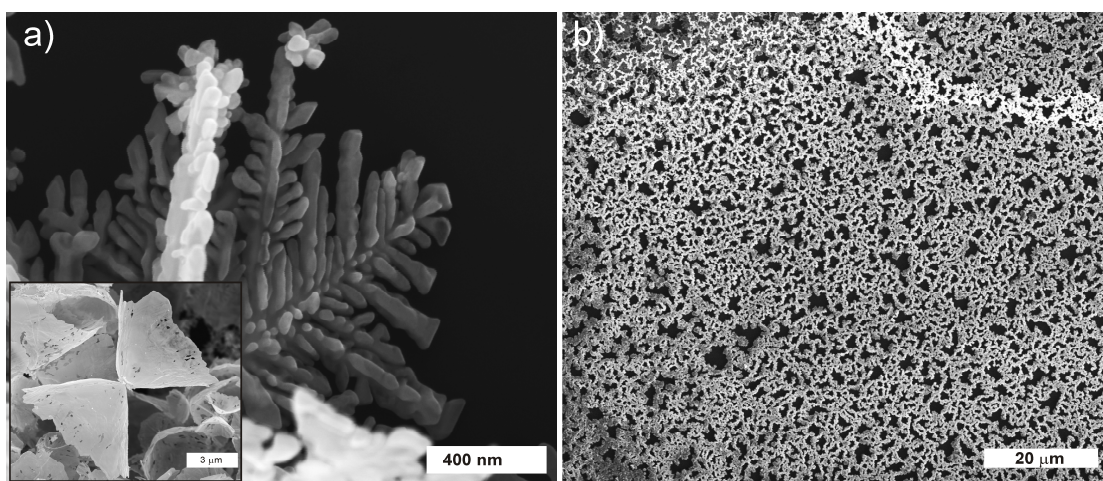


Figure 2.80 (a) SEM image of dendritic nanostructure of Ag obtained on increasing the concentration in method 1. The inset shows an image of cone obtained in same reaction. (b) SEM image of the Ag network obtained by method 2, in the absence of  $\text{PPh}_3$ .

We have been able to obtain dendritic nanostructures of Au-Ag alloys similar to those in Figure 2.80 by taking both Au and Ag ions in the organic phase. We show the results obtained with two different ratios of Au:Ag ratios (15:85 and 75:25) in Figure

2.81. It is remarkable that the observed structures are drastically different, dendrites when Ag-rich, and mesoballs when Au-rich.

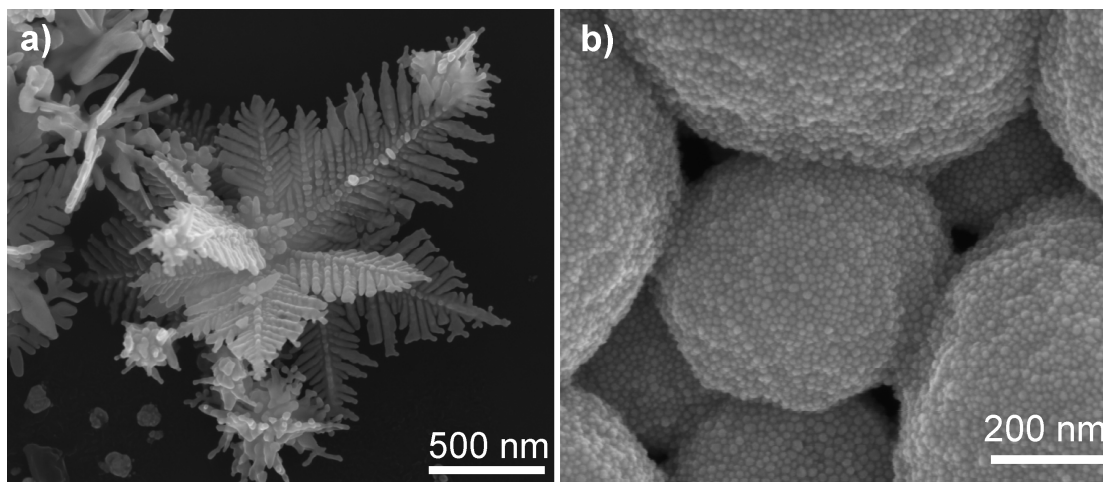


Figure 2.81 SEM images of Au:Ag alloy nanostructures obtained by method 1: (a) 15:85 (b) 75:25.

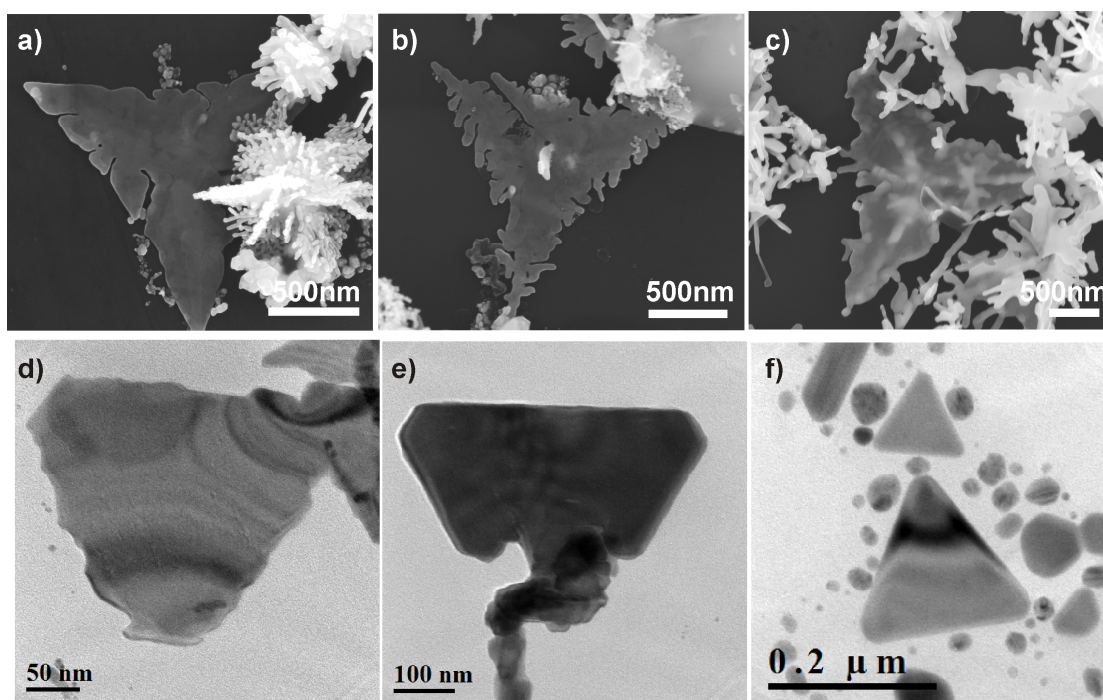


Figure 2.82 Sheets of Ag:Au obtained at the interface, for Ag rich compositions.

Interestingly we obtain triangular sheets with composition dominated by Ag:Au (99:1). As shown in Figure 2.82, such atomically flat structure or sheets can be used as substrates for scanning probe techniques.

Experiments carried out on Au films formed at the interface in the presence of PVP (but in the absence of a surfactant) in the organic phase have also yielded

interesting results. The toluene layer containing chains of Au nanocrystals of 10-20 nm diameter (Figure 2.83a and b) turns blue. The optical absorption spectrum of the organosol shows longitudinal and transverse plasmon bands at 684 and 540 nm respectively due to the presence of the chains (Figure 2.83c). The longitudinal plasmon band occurs at a relatively lower wavelength due to poorer coupling in comparison with well-formed nanorods. We however failed to obtain fractal and dendritic nanostructures in the presence of PVP.

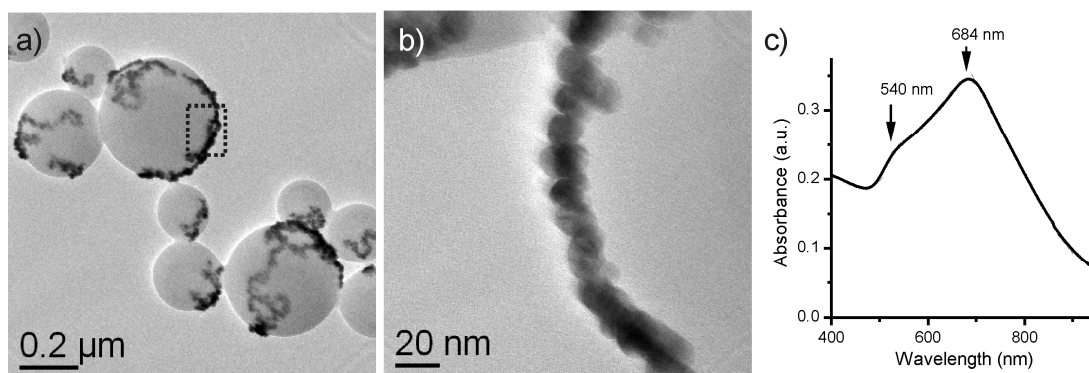


Figure 2.83 (a) PVP balls decorated with a Au nanocrystal chains (b) TEM of one such PVP ball showing chain of nanocrystals (c) Optical absorption spectrum from the same, showing plasmon absorption bands.

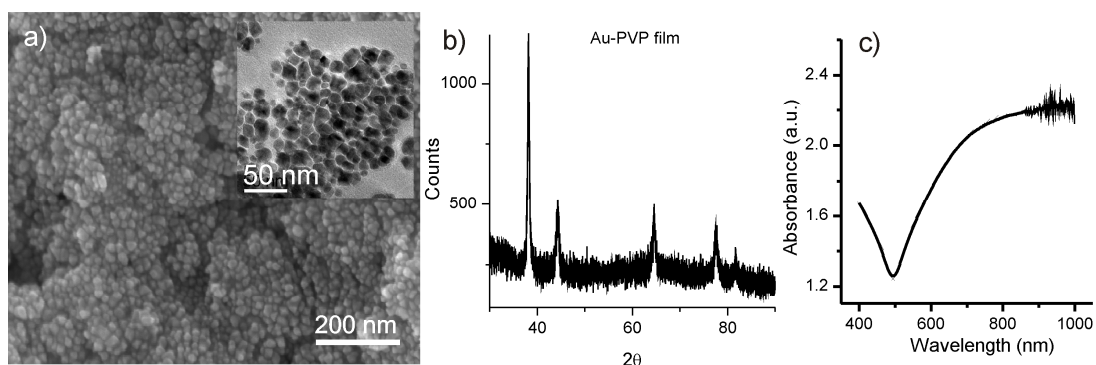


Figure 2.84 (a) SEM image of film obtained using PVP, (b) X-ray diffraction pattern of same, and (c) Absorption spectra of same.

Figure 2.84a shows, film obtained using PVP, it is solid film obtained at the interface with closed network of nanocrystals of irregular shape, but densely packed. Figure 2.84b shows XRD pattern from the film. Figure 2.84c shows UV absorption from the solid film, broad band starting from 500 nm is due to coupled system of nanocrystals.

## 2.6 Conclusions

Preparation of films of nanocrystals of Au, Ag and Cu at the liquid-liquid interface has been accomplished by taking a metallo-organic precursor in organic layer and the appropriate reducing agent in the aqueous layer. The particle diameters and the film coverage are dependent on the contact time and the concentration of the reactants. The films show surface plasmon bands characteristic of metal nanocrystals. The nanocrystals in the films are readily extracted to aqueous or organic layers by adding suitable capping agents. A particularly noteworthy aspect of the study is that the nanocrystalline film at the interface can be easily transferred onto a solid support.

The present study of the properties of ultrathin nanocrystalline Au films prepared at the liquid-liquid interface under different conditions has revealed many interesting features. The size of the nanocrystals constituting the film markedly increases with the temperature employed for preparation, but the concentration of the organometallic precursor has little effect. The nanocrystals are generally separated by  $\sim 1$  nm under the conditions of preparation employed by us. The films are generally smooth and continuous over a length scale of several microns, the overall thickness being in the range of 40-140 nm. Electrical resistance measurements using the four-probe method show that the film prepared at room temperature behaves as an activated conductor with a high resistance ( $\sim$  few m $\Omega$ ). The resistance gradually decreases with increase in preparation temperature, yielding metallic films. UV-vis absorption spectra reveal that the surface plasmon band of Au is red-shifted markedly in the films likely due to electronic coupling between particles. Interaction with alkanethiols perturbs the films considerably, the magnitude of the perturbation depending on the chain length of the thiol. Such perturbation also affects the electrical properties of the films, the long chain thiols increasing the resistance. Interaction with dimercaptodiphenylacetylene, on the other hand, decreases the resistance of the film.

The novelty of the liquid-liquid interface method gets reinforced by the synthesis of the nanocrystalline films of metal alloys. The films exhibit a high level of uniformity in composition and morphology over large length scales. The size of the nanocrystals is well defined for a given composition of the alloy. By the addition of an alkanethiol, the films can be reactively broken down to the corresponding organosols.



The preparation of nanocrystalline alloy films of Au, Ag and Cu at liquid-liquid interface has been accomplished by taking the desired mixtures of metallo-organic precursors in the organic layer and the appropriate reducing agent in the aqueous layer. By this method, films consisting of Au-Ag nanocrystals of nominal compositions of 75:25, 50:50 and 25:75 have been prepared in addition to the monometallic films of Au and Ag. EDAX analysis on the resulting films has revealed that the alloy compositions closely match the initial concentrations of the precursors. The particle size estimated from the XRD patterns increases with increasing Ag content. The Ag-rich films tend to exhibit preferred orientation along the (111) plane. The plasmon band in the electronic absorption spectrum of the films as well as of the sols shows a blue-shift with the increasing Ag content indicative of uniform alloying. The nanocrystalline films of the Au-Cu alloys (50:50 and 75:25) as well as the Au-Ag-Cu (50:25:25) alloy have been prepared at the liquid-liquid interface. The plasmon band of the Au-Cu alloy shows a red shift with increasing Cu content.

In the interfacial rheological measurements of a 2D film of Ag nanocrystals at the interface, the formation of the film at the interface was monitored by applying an oscillatory shear of small amplitude. An increase in the storage modulus by a few orders of magnitude was observed, indicating the formation of the film. Both oscillatory as well as steady shear measurements were carried out on the 2D film. Frequency sweep measurements carried out on the film indicated that the film is elastic at low frequencies, with  $G' > G''$ , and remains nearly frequency independent. The low-frequency behavior of the storage moduli with a negative slope is consistent with the predicted behavior of a soft glassy system. Furthermore, as predicted for soft glassy systems or systems with slow dynamics where the structural relaxation time exhibits strain rate amplitude dependence, strain sweep measurements carried out on the film reveal a shear thickening peak in  $G''$  at large strain amplitudes followed by a power law decay. The shear thinning exponents of  $G'$  and  $G''$  are in the ratio of 2:1 with the value of the exponent 0.8. Experimental studies suggest that such a behavior is universal for 2D as well as 3D systems. Steady shear measurements reveal a finite yield stress as  $\dot{\gamma} \rightarrow 0$ , along with a significant deviation from the Cox-Merz rule, as expected for glassy systems. Thus, the present study clearly indicates that a nanocrystalline film can form a soft colloidal glass. The glassy behavior can be

attributed to the fact that the nanocrystals forming the film are not strictly monodisperse.

The SAXS studies demonstrate that one can monitor chemical reactions at liquid-liquid interfaces, using X-ray scattering techniques. It has been shown that metal-precursor in the upper toluene layer forms molecular layers, and that after the reduction reaction at the toluene-water interface multiple layers of Au nanocrystals are formed. The smaller (1.3 nm) Au nanocrystals move away from the interface and a hexagonal structure with particle-particle separation of 15.8 nm - that is almost 12-times of the particle size. Formation of such lattice, which has been observed earlier in micron-sized particles [359, 447], in charged nanomaterials is of great interest in the physics of strongly interacting charged systems functioning in water [448].

The study of the effect of absorption of alkanethiols of different chain lengths on the optical absorption properties of Au nanocrystalline films prepared at the liquid-liquid interface has yielded interesting results. The as-prepared films consist of Au nanocrystals close-packed in an array with nearly 1 nm spacing. The optical absorption spectrum of the as-prepared films shows a surface plasmon band around 700 nm due to electronic coupling between the nanocrystals. Upon ultrasonication, fragmented arrays are formed as evidenced by TEM, with the absorption spectrum showing a broad band extending from 550 to 700 nm, in contrast to a well-defined band at 540 nm from the organosol of thiol capped nanocrystals. Electronic coupling between the nanocrystals in the array can be varied by interacting the film with alkanethiols of different chain lengths. While thiols with longer chains cause large blue shifts (down to 560 nm in the case of octadecanethiol) indicative of the diminishing coupling, smaller thiols show smaller marginal shifts. For a given alkane thiol, the diminishing absorbance at 700 nm and the increase in intensity at 530 nm give rise to an isosbestic point around 600 nm, which is a clear indication of a chemical equilibrium between the ordered nanocrystalline film and the disordered structure involving nanocrystals separated by alkane thiols. Alkane thiols with longer chains disintegrate or disorder the Au films more effectively and at lower concentrations as evidenced from spectral data as well as calorimetric data. The rate of interaction of the thiols as measured by the time-dependent band shifts also depends on the chain length, the longer chain length rendering the process faster.

Apparent rate constants ( $k$ ) can be estimated considering the thiol adsorption on nanoparticle surface to be a modified first order process. The activation energy of the process (40 kJ/mol for hexadecanethiol) is consistent with the adsorption energy.

The spectral changes due to changing interparticle separation upon thiol interaction have been modeled using the Maxwell-Garnett formalism. The calculated values of absorbance agree well with the experimental trend for shorter chain lengths but are somewhat overestimated for longer chain lengths. The latter is attributed to the curling of the long chains adsorbed on nanocrystals packed in an array. When the separation between the nanocrystals is kept nearly constant, but the alkane chain replaced by a conjugated linker (mercapto 1,2-diphenylacetylene), the absorption band shows a red shift due to increased interparticle coupling. We have also noticed an oscillatory behavior of the plasmon band with time during the alkanethiol adsorption.

The growth study shows that in the presence of a surfactant such as TOAB and CTAB, fractal and dendritic nanostructures of Au and Ag are formed at the liquid-liquid interface. This becomes possible because the surfactant molecules go to the interface and enable these structures to be formed even at low surfactant concentrations. Aggregation of the surfactant molecules appears to give rise to clusters of Au ions at the head of the surfactant molecules. After reduction, they form Au clusters and then cylindrical rods, which then aggregate to form the large cauliflower-like units. These units are involved in the formation of fractal and dendritic structures. It appears that the liquid-liquid interface provides a favorable medium for the self-assembly of nanocrystals [449].



### 3 A Single Molecule Switch Based on Two Pd Nanocrystals Linked by a Conjugated Dithiol\*

#### 3.1 Summary

Tunneling spectroscopy measurements have been carried out on a single molecule device formed by two Pd nanocrystals (dia,  $\sim 5$  nm) electronically coupled by a conducting molecule, dimercaptodiphenylacetylene. The I-V data, obtained by positioning the tip over a nanocrystal electrode, exhibit negative differential resistance (NDR) on a background M-I-M characteristics. The NDR feature occurs at  $\sim 0.67$  V at 300 K and shifts to a higher bias of 1.93 V at 90 K. When the tip is held in the middle region of the device, a coulomb blockade region is observed ( $\sim \pm 0.3$  V).

#### 3.2 Introduction

Molecules were proposed as active electronic devices as early as 1974, by Aviram and Ratner who put forth the concept of unimolecular rectification [450]. Candidates for molecular wires and switches include porphyrins, phenylenes and thiophenes as well as their polymeric derivatives with extended  $\pi$ -conjugation [451, 452]. Organic electronics using conducting polymers has seen a speedy growth in the last three decades but for molecular electronics to come of age, fabrication and measurement techniques would have to reach the nanoscale. With the advent of atomic imaging tools such as scanning tunneling microscopy (STM) and atomic force microscopy (AFM), along with nanolithography and fabrication techniques, it has become possible to carry out reliable measurements on individual molecules in a circuit [453]. There have been several studies of electrical conduction through conjugated oligomers [427, 454-456], typical examples being phenylene ethynylene molecules [457]. An early study based on dc conduction measurements on an Au cluster array cross linked by 1,4-di(4-isocyanophenylethynyl)-2-ethylbenzene showed enhanced conductivity in the nanocrystal film revealing the conducting nature of the molecule [458]. Using STM, Bumm et al [459, 460] reported that 4, 4'-di(phenylene-

---

\* A paper based on this work has appeared in *Pramana* (2005).

ethynylene)benzothioacetate exhibits a relatively high conductivity compared to neighboring alkanethiols in a mixed self-assembled monolayer. A variant of this method has been tried out by anchoring Au nanocrystals on bifunctional molecules and performing I-V measurements by either STM or conducting AFM [461, 462]. Fan et al [463] used a tuning fork tip method and observed features due to negative differential resistance (NDR) in a series of phenylenes. Chen et al [464, 465] using the nanopore method, carried out a systematic study of the NDR effect in molecules containing a nitroamine redox center. In another study on molecules of bisthioterthiophene adsorbed on Au electrodes of a break junction, non-linear I-V curves with step-like features have been observed presumably involving conduction across discrete molecular levels [466]. More recently, Reichert et al [467] performed a study to compare I-V characteristics of symmetric and asymmetric phenylenes using the break junction method [468].

### 3.3 Scope of the present investigations

In spite of the studies cited above, there are certain unsettled issues related to electrical conduction through a metal-molecule-metal device. While issues such as the nature of molecule-electrode coupling [469, 470] and the influence of a non-conducting molecular background in self-assembled monolayer [471] have caused intense debate, ensuring experimentally that only a single molecule actively present between the electrodes remains a problem. As part of continuing interest in electrical transport in molecular nanosystems [326], we have carried out measurements on dimercaptodiphenylacetylene linked to Pd nanocrystals of ~ 5nm diameter on either side (Scheme 1), by employing low temperature STM.

### 3.4 Experimental details

Dimercaptodiphenylacetylene (dmdpa) was prepared by a reported procedure [472] starting with a Sonogashira coupling reaction between 4-iodothioacetate and trimethylsilylacetylene. The resulting derivative was deprotected with tetrabutyl ammonium fluoride and coupled with 4-iodothioacetate followed by treatment with NaOH. Nanocrystals of Pd dispersed in ethanol were prepared following the procedure of Miyake et al. [49]. Briefly, a 15 ml of 2.0 mM aqueous solution of  $H_2PdCl_4$  was refluxed in a mixture of 10 ml of absolute ethanol and 18 ml of water in

the presence of 33.3 mg PVP ( $M_w$ , 40,000  $\text{g mol}^{-1}$ ). In order to prepare dimeric nanocrystal species linked by the conducting molecule (see Figure 3.1), 0.1  $\mu\text{l}$  of 2mM solution of dimercaptodiphenylacetylene in toluene was mixed with 1 ml of the Pd sol resulting in a Pd:dmdpa of 5000:1.

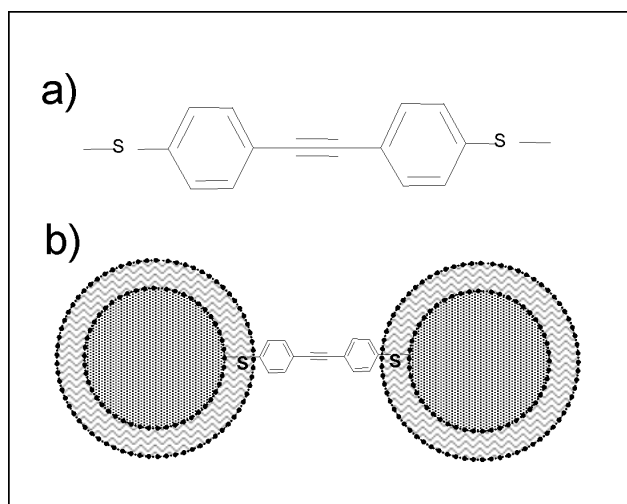


Figure 3.1 (a) Dimercaptodiphenylacetylene (dmdpa) (b) A schematic showing a dimer of Pd nanocrystals linked by a dmdpa molecule.

Transmission electron microscopy (TEM) was carried out using a JEOL 3010 operating at 300 kV. A drop of the sol treated with the conducting molecule was placed on a copper grid coated with thin carbon film and left to dry overnight. Scanning tunneling microscopy was performed using a SPM 32 (RHK technology, USA) attached to a low temperature stage in an ultra high vacuum chamber. In order to prevent tip induced damage and capture of the nanocrystal by the tip, typically a high impedance of 900  $M\Omega$  (bias, 900 mV, set-point current, 1 nA) was used for imaging. The microscope was initially calibrated against the 0001 surface of highly oriented pyrolytic graphite (HOPG) using an Au tip prepared by electrochemical means [473]. The same tip was used throughout the course of the study. After obtaining a stable non-drifting image, I-V data were collected in the spectroscopy mode by placing the tip atop a feature of interest with the feedback loop turned off. A typical voltage sweep was  $\pm 2$  V, with a sweep rate of 10V/s and data interval of 5 mV. Imaging of the area was repeated after the I-V measurement to ensure that the nanocrystals had not drifted away during the I-V measurement. Lower temperatures were achieved by passing liquid nitrogen via a cold stage feed through. Temperature was read out using a thermocouple right below the sample mount.

### 3.5 Results and Discussion

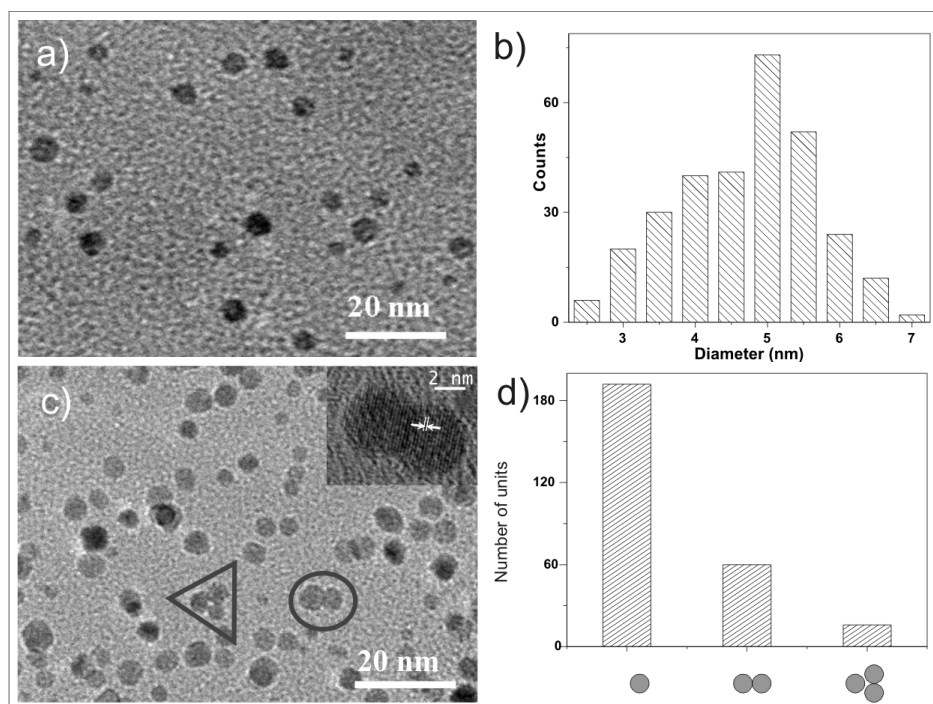


Figure 3.2 (a) TEM micrograph of Pd nanocrystals from the as-prepared sol, (b) Histogram showing size distribution of the nanocrystal in (a), (c) Micrograph taken after adding dmdpa molecules to the Pd sol shows several isolated nanocrystals along with assemblies containing two or three nanocrystals, as marked. Inset shows a high-resolution micrograph of a dimeric species. The distance between Pd(111) lattice planes,  $\sim 2.2$  Å. (d) Histogram showing the populations of monomers, dimers and trimers.

Figure 3.2a, shows a TEM image revealing isolated near-spherical Pd nanocrystals from the as-prepared sol. The diameters of the nanocrystals is in the range of 3-7 nm as shown in the histogram in Figure 3.2b, with a mean particle diameter of  $\sim 5$  nm. The TEM image of Pd nanocrystals treated with dmdpa shown in Figure 3.2c contains some primitive assemblies where two or three nanocrystals. The observed assemblies, dimers and trimers, can only result from the linking of the Pd nanocrystals by the dithiol (dmdpa) molecules. In contrast, the as-prepared sol is completely devoid of such assemblies (Figure 3.2a). Similar observations have been made previously [474] using bifunctional molecules. The inset in Figure 3.2c shows a dimer species with well-resolved 111 planes ( $d \sim 2.2$  Å), although the particle boundaries are not discernible due to line of sight. The populations of the assemblies decrease with the nuclearity (Figure 3.2d). This is rather an expected trend following a simple estimate based on the known Pd:dmdpa ratio and the assumption that one molecule links a pair of nanocrystals to form a dimer and three for a trimer. It would



appear that the probability that a dimer is connected by two dmdpa molecules is negligibly small.

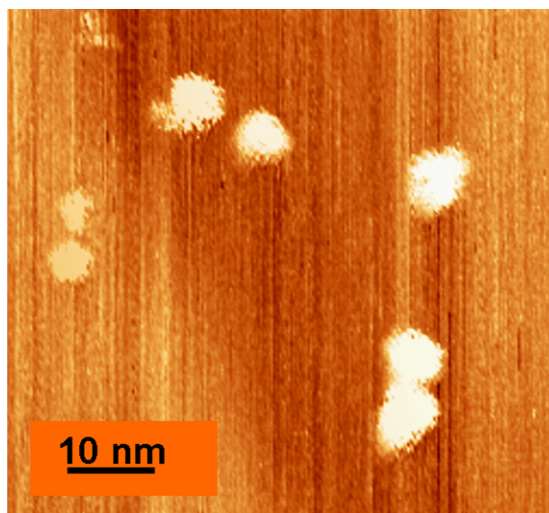


Figure 3.3 STM micrograph of Pd nanocrystals on HOPG substrate.

STM imaging was carried out over large areas ( $\sim 500 \times 500 \text{ nm}^2$ ) initially in order to isolate the monomeric and dimeric species of the nanocrystals. Figure 3.3 shows a typical STM micrograph of a region containing individual nanocrystals along with a dimer. The nanocrystal diameters are somewhat larger (4 - 8 nm) than the diameters observed in TEM, the difference arising due to the PVP ligand shell around the nanocrystals. Tunneling spectroscopy measurements were carried out on monomers as well as on dimers of nanocrystals. Typical I-V data from an individual nanocrystal at 300 K shows coulomb staircase behavior arising from incremental charging of the nanocrystal with the applied bias (Figure 3.4). This observation is in accordance with earlier findings on polymer coated metal nanocrystals [326]. I-V measurements on the dimeric species at 300K obtained with the tip atop either of the nanocrystals reveal M-I-M characteristics but for the presence of a sharp feature (see Figure 3.5). Around 0.6 V, the current increases rapidly with increasing bias to reach its maximum at  $\sim 0.67 \text{ V}$  and falls sharply thereafter. The presence of such a sharp feature in the I-V data is an indicative of a NDR region in the conductance behavior. The on-off ratio (peak-to-valley ratio) of this molecular device is 2.35. At 90 K, the NDR feature appears at much higher bias of 1.93 V consistent with the temperature dependent behavior of NDR in such molecules [464]. The background current is much lesser at the low temperature resulting in a higher on-off ratio of 2.64.

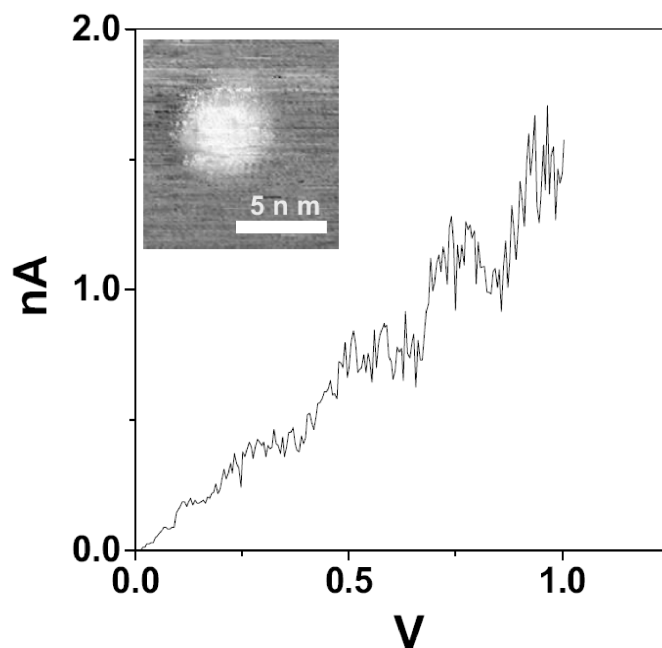


Figure 3.4 I-V data from an isolated Pd nanoparticle showing a coulomb staircase behavior. Inset shows the STM micrograph.

When the tip is brought in the middle region of the nanocrystal dimer possibly right above the conducting molecule, we see an altogether different behavior (Figure 3.5b). In this case, the I-V data is devoid of an NDR feature but exhibits a distinct coulomb blockade region in the range, -0.3 and 0.25 V. We also observe an overall decrease in the current by at least an order of magnitude compared the case in Figure 3.5a. These observations can be understood on the basis of a notional circuit consisting of two RC segments representing the PVP covered nanocrystals, interlinked by a molecular resistance (see right side of Figure 3.5). When the bias is applied on one of the nanocrystals using the STM tip, a voltage drop is expected along the molecular axis that now controls the overlap between the conduction states. An increase in the bias could result in an increased overlap between the conduction states giving rise to a sudden rise in the current till the states flip away at a critical bias (which in this case is, 0.67 V at room temperature) following say, charging or conformational change in the molecule [475]. When the bias is applied to the center of the device (Figure 3.5b), the two molecular ends carry similar potential and no current is expected to flow in the circuit until the intrinsic gap of the molecule is overcome [476]. This gives rise to the observed coulomb blockade behavior as shown in Figure 3.5b.

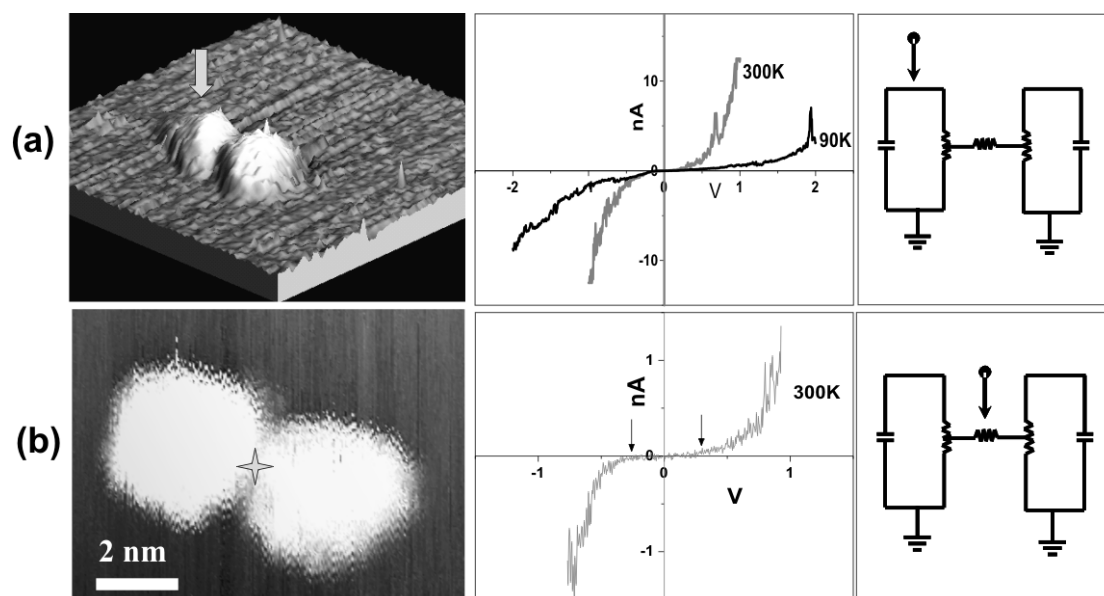


Figure 3.5 Tunneling microscopy and spectroscopy on a dimer of nanocrystals at 300 and 90 K. STM micrographs are shown on the left, I-V data in the middle and schematic circuits on the right side, (a) an isometric view, the tip bias being applied to one of the nanocrystals is shown with an arrow, (b) a top view with tip bias applied to the central region, as marked.

### 3.6 Conclusions

Having demonstrated clearly the switching action of this single molecular device, the merits of the present system deserves some mention. To our knowledge, this is the first study on electrical transport in dimercaptodiphenylacetylene, which is the simplest among the series of phenylene ethynylene oligomers. The molecule is electrically coupled to the Pd metal electrodes (nanocrystals) through Pd-S bonds. It has been suggested that the Pd-S linkage is the best option among many metal-molecule interfaces, the Au-S bond being the worst [469, 470]! The method of making dimeric species of nanocrystals employed by us ensures that the electrical transport measurements indeed pertain to single molecules with a high degree of confidence, thereby avoiding interactions prevalent in a self-assembled monolayer of molecules. Furthermore, we are able to study the electrical behavior along the molecular axis. Thus, a coulomb blockade ( $\sim \pm 0.3$  V) occurs when the tip bias is applied to the central region of the molecule. The switching action of the device is evident in the form of the NDR feature when the bias is applied to one of the nanocrystal electrodes.



## References

- [1] K. Kalantar-zadeh, B. Fry, *Nanotechnology-Enabled Sensors*, Springer, New York, 2008.
- [2] C.N.R. Rao, P.J. Thomas, G.U. Kulkarni, *Nanocrystals: Synthesis, Properties and Applications*, Springer-Verlag, 2007.
- [3] C.N.R. Rao, A. Müller, A.K. Cheetham, *Nanomaterials Chemistry: Recent Developments and New Directions*, Wiley-VCH, 2007.
- [4] J.M. Lehn, *Supramolecular Chemistry: Concepts and Perspectives* Wiley-VCH, Weinheim, 1995.
- [5] J. Jortner, C.N.R. Rao, *Pure Appl. Chem.* **74** 1491 (2002).
- [6] D.J. Barber, I.C. Freestone, *Archaeometry* **32** 33 (1990).
- [7] M. Jose-Yacaman, L. Rendon, J. Arenas, et al., *Science* **273** 223 (1996).
- [8] M. Faraday, *Philosophical Transactions of the Royal Society of London (1776-1886)* **147** 145 (1857).
- [9] Peter P. Edwards, John M. Thomas, *Angew. Chem. Int. Ed.* **46** 5480 (2007).
- [10] A. Einstein, *Annalen der Physik* **322** 549 (1905).
- [11] M. Gustav, *Annalen der Physik* **330** 377 (1908).
- [12] R. Gans, *Annalen der Physik* **342** 881 (1912).
- [13] R. Gans, *Annalen der Physik* **352** 270 (1915).
- [14] Y. Xia, P. Yang, Y. Sun, et al., *Adv. Mater.* **15** 353 (2003).
- [15] J. Wang, H.L. Duan, Z.P. Huang, et al., *Proceedings of the Royal Society A: Mathematical, Physical and Engineering Sciences* **462** 1355 (2006).
- [16] M.T. Swihart, *Current Opinion in Colloid & Interface Science* **8** 127 (2003).
- [17] A.N. Shipway, E. Katz, I. Willner, *ChemPhysChem* **1** 18 (2000).
- [18] J.H. Fendler, *Nanoparticles and Nanostructured Films*, Wiley-VCH: Weinheim, Germany, 1998.
- [19] G. Schmid, *Inorg. Synth.* **27** 214 (1990).
- [20] M.P. Pileni, *J. Phys. Chem.* **97** 6961 (1993).
- [21] D.G. Duff, A. Baiker, P.P. Edwards, *Langmuir* **9** 2301 (1993).
- [22] D.G. Duff, A. Baiker, I. Gameson, et al., *Langmuir* **9** 2310 (1993).
- [23] A.C. Curtis, D.G. Duff, P.P. Edwards, et al., *Angew. Chem. Int. Ed. Eng.* **27** 1530 (1988).
- [24] K. Abe, T. Hanada, Y. Yoshida, et al., *Thin Solid Films* **327-329** 524 (1998).
- [25] M. Brust, M. Walker, D. Bethell, et al., *J. Chem. Soc., Chem. Commun.* 801 (1994).
- [26] K.V. Sarathy, G.U. Kulkarni, C.N.R. Rao, *Chem. Commun.* 537 (1997).
- [27] H.I. Schlesinger, H.C. Brown, A.E. Finholt, et al., *J. Am. Chem. Soc.* **75** 215 (1953).
- [28] H.C. Brown, C.A. Brown, *J. Am. Chem. Soc.* **84** 1493 (1962).
- [29] J. Turkevich, P.C. Stevenson, J. Hillier, *Discuss. Faraday Soc.* **11** 55 (1951).
- [30] P.R.v. Rheenen, M.J. McKelvey, R. Marzke, *Inorg. Synth.* **24** 238 (1983).
- [31] H. Hirai, H. Wakabayashi, M. Komiyama, *Chem. Lett.* **12** 1047 (1983).
- [32] R.G. Nuzzo, D.L. Allara, *J. Am. Chem. Soc.* **105** 4481 (1983).
- [33] Y. Xia, G.M. Whitesides, *Angew. Chem. Int. Ed.* **37** 550 (1998).
- [34] M.J. Hostetler, J.J. Stokes, R.W. Murray, *Langmuir* **12** 3604 (1996).
- [35] J.R. Heath, C.M. Knobler, D.V. Leff, *J. Phys. Chem. B* **101** 189 (1997).
- [36] B.A. Korgel, S. Fullam, S. Connolly, et al., *J. Phys. Chem. B* **102** 8379 (1998).
- [37] S. Chen, K. Huang, J.A. Stearns, *Chem. Mater.* **12** 540 (2000).

- [38] E.A. Hauser, J.E. Lynn, *Experiments in Colloid Chemistry*, McGraw-Hill, New York, 1940.
- [39] J. Turkevich, *gold bull.* **18** 86 (1985).
- [40] D.N. Furlong, A. Launikonis, W.H.F. Sasse, *J. Chem. Soc., Farad. Trans.* **80** 571 (1984).
- [41] A. Harriman, G.R. Millward, P. Neta, et al., *J. Phys. Chem.* **92** 1286 (1988).
- [42] J. Turkevich, R.S. Miner Jr, L. Babenkova, *J. Phys. Chem.* **90** 4765 (1986).
- [43] H. Hirai, Y. Nakao, N. Toshima, *J. Macromol. Sci. Chem.* **A12** 1117 (1978).
- [44] H. Hirai, Y. Nakao, N. Toshima, *J. Macromol. Sci. Chem.* **A13** 727 (1979).
- [45] H. Hirai, *J. Macromol. Sci. Chem.* **A13** 633 (1979).
- [46] J.S. Bradley, J.M. Millar, E.W. Hill, *J. Am. Chem. Soc.* **113** 4016 (1991).
- [47] J.S. Bradley, E.W. Hill, S. Behal, et al., *Chem. Mater.* **4** 1234 (1992).
- [48] D. Mandler, I. Willner, *J. Phys. Chem.* **91** 3600 (1987).
- [49] T. Teranishi, M. Miyake, *Chem. Mater.* **10** 594 (1998).
- [50] T. Teranishi, H. Hori, M. Miyake, *J. Phys. Chem. B* **101** 5774 (1997).
- [51] Y. Wang, N. Toshima, *J. Phys. Chem. B* **101** 5301 (1997).
- [52] N. Toshima, M. Harada, T. Yonezawa, et al., *J. Phys. Chem.* **95** 7448 (1991).
- [53] H.N. Vasan, C.N.R. Rao, *J. Mater. Chem.* **5** 1755 (1995).
- [54] J. Belloni, M. Mostafavi, in: P. Braunstein, L.A. Oro, P.R. Raithby (Eds.), *Metal Clusters in Chemistry Vol 2*, ed, Wiley-VCH, Weinheim, 1999.
- [55] M.Y. Han, L. Zhou, C.H. Quek, et al., *Chem. Phys. Lett.* **287** 47 (1998).
- [56] J. Neddersen, G. Chumanov, T.M. Cotton, *Appl. Spectrosc.* **47** 1959 (1993).
- [57] F. Mafune, J.y. Kohno, Y. Takeda, et al., *J. Phys. Chem. B* **106** 7575 (2002).
- [58] F. Mafune, J.y. Kohno, Y. Takeda, et al., *J. Phys. Chem. B* **107** 4218 (2003).
- [59] F. Mafune, J.y. Kohno, Y. Takeda, et al., *J. Phys. Chem. B* **104** 9111 (2000).
- [60] F. Mafune, J.y. Kohno, Y. Takeda, et al., *J. Phys. Chem. B* **104** 8333 (2000).
- [61] S. Link, M.A. El-Sayed, *Int. Rev. Phys. Chem.* **19** 409 (2000).
- [62] A.C. Templeton, J.J. Pietron, R.W. Murray, et al., *J. Phys. Chem. B* **104** 564 (2000).
- [63] L.M. Liz-Marzan, P. Mulvaney, *J. Phys. Chem. B* **107** 7312 (2003).
- [64] S. Link, M.A. El-Sayed, *J. Phys. Chem. B* **103** 4212 (1999).
- [65] R.C. Doty, H. Yu, C.K. Shih, et al., *J. Phys. Chem. B* **105** 8291 (2001).
- [66] A. Bezryadin, C. Dekker, G. Schmid, *Appl. Phys. Lett.* **71** 1273 (1997).
- [67] A. Bezryadin, C. Dekker, *J. Vac. Sci. Technol. B* **15** 793 (1997).
- [68] O.Y. Kolesnychenko, D. Erts, O.I. Shklyarevskii, et al., *Physica B* **315** 171 (2002).
- [69] H. Ohnishi, Y. Kondo, K. Takayanagi, *Nature* **395** 780 (1998).
- [70] K.H. Müller, J. Herrmann, B. Raguse, et al., *Phys. Rev. B* **66** 075417 (2002).
- [71] G. Mederiros-Ribeiro, D.A.A. Ohlberg, R.S. Williams, et al., *Phys. Rev. B* **59** 1633 (1999).
- [72] P.P. Edwards, R.L. Johnston, C.N.R. Rao, in: P. Braunstein, G. Oro, P.R. Raithby (Eds.), *Metal clusters in Chemistry*, Wiley-VCH Weinheim, 1998.
- [73] T.P. Martin, T. Bergmann, H. Goehlich, et al., *J. Phys. Chem.* **95** 6421 (1991).
- [74] B.G. Bagley, *Nature* **208** 674 (1965).
- [75] J.G. Allpress, J.V. Sanders, *Surf. Sci.* **7** 1 (1967).
- [76] S.H. Yang, D.A. Drabold, J.B. Adams, et al., *Phys. Rev. B* **47** 1567 (1993).
- [77] S. Ino, *J. Phys. Soc. Jpn.* **27** 941 (1969).
- [78] P. Chini, *J. Organomet. Chem.* **200** 37 (1980).
- [79] G.F. Szprie, *Kepler's Conjecture: How Some of the Greatest Minds in History Helped Solve One of the Oldest Math Problems in the World*, Wiley, Hoboken, 2003.
- [80] T.P. Martin, *Physics Reports* **273** 199 (1996).
- [81] H. Klug, L.E. Alexander, *X-ray Diffraction Procedures for Polycrystalline and Amorphous Materials*, Wiley, New York, 1974.
- [82] D.G. Duff, A.C. Curtis, P.P. Edwards, et al., *J. Chem. Soc., Chem. Commun.* 1264 (1987).
- [83] P.A. Buffat, M. Flueli, R. Spycher, et al., *Faraday Discuss.* **92** 173 (1991).

- [84] D.G. Duff, A.C. Curtis, P.P. Edwards, et al., *Ang. Chem. Int. Ed.* **26** 676 (1987).
- [85] J.O. Bovin, J.O. Malm, *Zeitschrift fur Physik D Atoms, Molecules and Clusters* **19** 293 (1991).
- [86] M.T. Reetz, W. Helbig, S.A. Quaiser, et al., *Science* **267** 367 (1995).
- [87] D.G. Duff, P.P. Edwards, J. Evans, et al., *Angew. Chem. Int. Ed. Eng.* **28** 590 (1989).
- [88] P. Mulvaney, *Langmuir* **12** 788 (1996).
- [89] P.K. Sudeep, S.T.S. Joseph, K.G. Thomas, *J. Am. Chem. Soc.* **127** 6516 (2005).
- [90] P.B. Johnson, R.W. Christy, *Phys. Rev. B* **6** 4370 (1972).
- [91] D.C. Look, *J. Colloid Interface Sci.* **56** 386 (1976).
- [92] C.F. Bohren, D.R. Huffman, *Absorption and Scattering of Light by Small Particles*, Wiley, New York, 1983.
- [93] M. Kerker, *The Scattering of Light and Other Electromagnetic Radiation*, Academic, New York, 1969.
- [94] U. Kreibig, M. Vollmer, *Optical Properties Of Metal Clusters*, Springer-Verlag, Berlin Heidelberg, 1995.
- [95] C.A. Mirkin, R.L. Letsinger, R.C. Mucic, et al., *Nature* **382** 607 (1996).
- [96] A.L. Efros, M. Rosen, *Annu. Rev. Mater. Sci.* **30** 475 (2000).
- [97] L.E. Brus, *J. Chem. Phys.* **79** 5566 (1983).
- [98] L.E. Brus, *J. Chem. Phys.* **80** 4403 (1984).
- [99] P.E. Lippens, M. Lannoo, *Phys. Rev. B* **39** 10935 (1989).
- [100] M.V.R. Krishna, R.A. Friesner, *J. Chem. Phys.* **95** 8309 (1991).
- [101] B.O. Dabbousi, J. Rodriguez-Viejo, F.V. Mikulec, et al., *J. Phys. Chem. B* **101** 9463 (1997).
- [102] R. Kubo, *J. Phys. Soc. Jpn.* **17** 975 (1962).
- [103] S.V. Gaponenko, *Optical Properties Of Semiconductor Nanocrystals*, Cambridge University Press, Cambridge, 1998.
- [104] W.P. Halperin, *Reviews of Modern Physics* **58** 533 (1986).
- [105] W.A. De Heer, *Rev. Mod. Phys.* **65** 611 (1993).
- [106] U. Naher, U. Zimmermann, T.P. Martin, *J. Chem. Phys.* **99** 2256 (1993).
- [107] M. Brack, *Reviews of Modern Physics* **65** 677 (1993).
- [108] H. Häkkinen, M. Moseler, U. Landman, *Phys. Rev. Lett.* **89** 033401 (2002).
- [109] H. Häkkinen, B. Yoon, U. Landman, et al., *J. Phys. Chem. A* **107** 6168 (2003).
- [110] W.D. Luedtke, U. Landman, *J. Phys. Chem.* **100** 13323 (1996).
- [111] M. Seidl, J.P. Perdew, M. Brajczewska, et al., *J. Chem. Phys.* **108** 8182 (1998).
- [112] M.M. Kappes, *Chem. Rev.* **88** 369 (1988).
- [113] C.P. Collier, T. Vossmeier, J.R. Heath, *Annu. Rev. Phys. Chem.* **49** 371 (1998).
- [114] H. Grabert, M.H. Devoret (Eds.), *Single Electron Tunneling*, Plenum, New York, 1992.
- [115] D.L. Feldheim, C.D. Keating, *Chem. Soc. Rev.* **27** 1 (1998).
- [116] D.V. Averin, K.K. Likharev, *J. Low Temp. Phys.* **62** 345 (1986).
- [117] J.L. Dormann, D. Fiorani, *Magnetic Properties of Fine Particles North-Holland, Amsterdam* 1992.
- [118] Q.A. Pankhurst, R.J. Pollard, *J. Phys.: Condens. Matter* **8** 8487 (1993).
- [119] L. Neel, *C.R. des s'éances de l'Acad. des Sci.* **237** 1468 (1953).
- [120] E.D. Torre, *Magnetic Hysteresis*, IEEE NJ, 1992.
- [121] S. Chikazumi, S.H. Charap, *Physics of Magnetism* Wiley, New York, 1964.
- [122] W. Thomson, *Philos. Mag.* **42** 448 (1871).
- [123] P. Pawlow, *Z. Phys. Chem.* **65** 545 (1909).
- [124] M. Takagi, *J. Phys. Soc. Jap.* **9** 359 (1954).
- [125] P. Buffat, J.P. Borel, *Phys. Rev. A* **13** 2287 (1976).
- [126] Q. Jiang, S. Zhang, M. Zhao, *Mater. Chem. Phys.* **82** 225 (2003).
- [127] K.N. Shrivastava, *Nano Lett.* **2** 519 (2002).
- [128] K.N. Shrivastava, *Nano Lett.* **2** 21 (2002).
- [129] J. Rupp, R. Birringer, *Phys. Rev. B* **36** 7888 (1987).

- [130] H. Frölich, *Physica* **4** 406 (1937).
- [131] B. Hai Yang, L. Jian Lin, J. Duo, et al., *J. Appl. Phys.* **79** 361 (1996).
- [132] Y. Volokitin, J. Sinzig, L.J. de Jongh, et al., *Nature* **384** 621 (1996).
- [133] S. Fullam, D. Cottell, H. Rensmo, et al., *Adv. Mater.* **12** 1430 (2000).
- [134] C.R. Martin, *Chem. Mater.* **8** 1739 (1996).
- [135] R.M. Penner, *J. Phys. Chem. B* **106** 3339 (2002).
- [136] T.O. Hutchinson, Y.P. Liu, C. Kiely, et al., *Adv. Mater.* **13** 1800 (2001).
- [137] E. Fort, C. Ricolleau, J. Sau-Pueyo, *Nano Lett.* **3** 65 (2003).
- [138] E. Braun, Y. Eichen, U. Sivan, et al., *Nature* **391** 775 (1998).
- [139] K. Keren, M. Krueger, R. Gilad, et al., *Science* **297** 72 (2002).
- [140] J. Richter, R. Seidel, R. Kirsch, et al., *Adv. Mater.* **12** 507 (2000).
- [141] H. Nakao, H. Shiigi, Y. Yamamoto, et al., *Nano Lett.* **3** 1391 (2003).
- [142] A. Kumar, M. Pattarkine, M. Bhadbhade, et al., *Adv. Mater.* **13** 341 (2001).
- [143] O. Harnack, W.E. Ford, A. Yasuda, et al., *Nano Lett.* **2** 919 (2002).
- [144] W.E. Ford, O. Harnack, A. Yasuda, et al., *Adv. Mater.* **13** 1793 (2001).
- [145] X. Fu, Y. Wang, L. Huang, et al., *Adv. Mater.* **15** 902 (2003).
- [146] R. Djalali, Y.f. Chen, H. Matsui, *J. Am. Chem. Soc.* **124** 13660 (2002).
- [147] R. Djalali, Y.f. Chen, H. Matsui, *J. Am. Chem. Soc.* **125** 5873 (2003).
- [148] I.A. Banerjee, L. Yu, H. Matsui, *Nano Lett.* **3** 283 (2003).
- [149] L. Yu, I.A. Banerjee, H. Matsui, *J. Am. Chem. Soc.* **125** 14837 (2003).
- [150] H. Cölfen, S. Mann, *Angew. Chem. Int. Ed.* **42** 2350 (2003).
- [151] E. Dujardin, C. Peet, G. Stubbs, et al., *Nano Lett.* **3** 413 (2003).
- [152] C.E. Fowler, W. Shenton, G. Stubbs, et al., *Adv. Mater.* **13** 1266 (2001).
- [153] S. Behrens, K. Rahn, W. Habicht, et al., *Adv. Mater.* **14** 1621 (2002).
- [154] B.A. Korgel, D. Fitzmaurice, *Adv. Mater.* **10** 661 (1998).
- [155] Y. Deng, C.-W. Nan, G.-D. Wei, et al., *Chem. Phys. Lett.* **374** 410 (2003).
- [156] J. Yang, C. Xue, S.-H. Yu, et al., *Angew. Chem. Int. Ed.* **41** 4697 (2002).
- [157] A.M. Jackson, J.W. Myerson, F. Stellacci, *Nat Mater* **3** 330 (2004).
- [158] T. Reuter, O. Vidoni, V. Torma, et al., *Nano Lett.* **2** 709 (2002).
- [159] Z. Tang, N.A. Kotov, M. Giersig, *Science* **297** 237 (2002).
- [160] J.A. Stroschio, D.M. Eigler, *Science* **254** 1319 (1991).
- [161] P.J. Durston, R.E. Palmer, J.P. Wilcoxon, *Appl. Phys. Lett.* **72** 176 (1998).
- [162] Z. Hens, D.V. Tallapin, H. Weller, et al., *Appl. Phys. Lett.* **81** 4245 (2002).
- [163] C. Baur, B.C. Gazen, B. Koel, et al., The fourth international conference on nanometer-scale science and technology, AVS, Beijing (China), 1997, p. 1577.
- [164] T.R. Ramachandran, C. Baur, A. Bugacov, et al., *Nanotechnology* 237 (1998).
- [165] R. Resch, C. Baur, A. Bugacov, et al., *Langmuir* **14** 6613 (1998).
- [166] W. Li, G.S. Hsiao, D. Harris, et al., *J. Phys. Chem.* **100** 20103 (1996).
- [167] D.M. Kolb, R. Ullmann, T. Will, *Science* **275** 1097 (1997).
- [168] F.P. Zamborini, R.M. Crooks, *J. Am. Chem. Soc.* **120** 9700 (1998).
- [169] I. Yamashita, *Thin Solid Films* **393** 12 (2001).
- [170] S. Hoepfener, R. Maoz, S.R. Cohen, et al., *Adv. Mater.* **14** 1036 (2002).
- [171] W. Yang, M. Chen, W. Knoll, et al., *Langmuir* **18** 4124 (2002).
- [172] P. Mesquida, A. Stemmer, *Adv. Mater.* **13** 1395 (2001).
- [173] H. Sugimura, N. Nakagiri, *J. Am. Chem. Soc.* **119** 9226 (1997).
- [174] S. Kramer, R.R. Fuieler, C.B. Gorman, *Chem. Rev.* **103** 4367 (2003).
- [175] C. Blackledge, D.A. Engebretson, J.D. McDonald, *Langmuir* **16** 8317 (2000).
- [176] D. Wouters, U.S. Schubert, *Langmuir* **19** 9033 (2003).
- [177] R.D. Piner, J. Zhu, F. Xu, et al., *Science* **283** 661 (1999).
- [178] S. Hong, J. Zhu, C.A. Mirkin, *Science* **286** 523 (1999).
- [179] P. John Thomas, G.U. Kulkarni, C.N.R. Rao, *J. Mater. Chem.* **14** 625 (2004).
- [180] L.M. Demers, S.-J. Park, T.A. Taton, et al., *Angew. Chem. Int. Ed.* **40** 3071 (2001).
- [181] X.M. Li, V. Paraschiv, J. Huskens, et al., *J. Am. Chem. Soc.* **125** 4279 (2003).
- [182] H.W. Li, B.V.O. Muir, G. Fichet, et al., *Langmuir* **19** 1963 (2003).



- [183] Q. Guo, X. Teng, S. Rahman, et al., *J. Am. Chem. Soc.* **125** 630 (2003).
- [184] D. Qin, Y. Xia, B. Xu, et al., *Adv. Mater.* **11** 1433 (1999).
- [185] C.-C. Chen, J.J. Lin, *Adv. Mater.* **13** 136 (2001).
- [186] M.H.V. Werts, M. Lambert, J.P. Bourgoïn, et al., *Nano Lett.* **2** 43 (2002).
- [187] T. Vossmeier, E. Delonno, J.R. Heath, *Angew. Chem. Int. Ed. Eng.* **36** 1080 (1997).
- [188] F. Hua, J. Shi, Y. Lvov, et al., *Nano Lett.* **2** 1219 (2002).
- [189] D. Philp, J.F. Stoddart, *Angew. Chem. Int. Ed.* **35** 1154 (1996).
- [190] P. Ball, *Self-Made Tapestry: Pattern Formation in Nature*, Oxford Press, Oxford, 1998.
- [191] M.R.E. Warner, R.V. Craster, O.K. Matar, *J. Colloid Interface Sci.* **267** 92 (2003).
- [192] C.B. Murray, C.R. Kagan, M.G. Bawendi, *Science* **270** 1335 (1995).
- [193] C.J. Kiely, J. Fink, M. Brust, et al., *Nature* **396** 444 (1998).
- [194] S. Sun, C.B. Murray, D. Weller, et al., *Science* **287** 1989 (2000).
- [195] V.L. Colvin, A.N. Goldstein, A.P. Alivisatos, *J. Am. Chem. Soc.* **114** 5221 (1992).
- [196] Z. Tang, Y. Wang, N.A. Kotov, *Langmuir* **18** 7035 (2002).
- [197] Z. Zhang, B.Q. Wei, P.M. Ajayan, *Appl. Phys. Lett.* **79** 4207 (2001).
- [198] O. Giraldo, J.P. Durand, H. Ramanan, et al., *Angew. Chem. Int. Ed.* **42** 2905 (2003).
- [199] H. Haidara, K. Mougïn, J. Schultz, *Langmuir* **17** 1432 (2001).
- [200] H. Haidara, K. Mougïn, J. Schultz, *Langmuir* **17** 659 (2001).
- [201] P.J. Thomas, G.U. Kulkarni, C.N.R. Rao, *J. Phys. Chem. B* **104** 8138 (2000).
- [202] B.A. Korgel, D. Fitzmaurice, *Phys. Rev. Lett.* **80** 3531 (1998).
- [203] T.P. Bigioni, X.-M. Lin, T.T. Nguyen, et al., *Nat Mater* **5** 265 (2006).
- [204] B.J. Alder, T.E. Wainwright, *J. Chem. Phys.* **27** 1208 (1957).
- [205] W. van Meegen, S.M. Underwood, *Phys. Rev. Lett.* **70** 2766 (1993).
- [206] D. Bargeman, F. Van Voorst Vader, *J. Electroanal. Chem.* **37** 45 (1972).
- [207] A. van Blaaderen, R. Ruel, P. Wiltzius, *Nature* **385** 321 (1997).
- [208] G.H. William, H.R. Francis, *J. Chem. Phys.* **49** 3609 (1968).
- [209] P.C. Ohara, D.V. Leff, J.R. Heath, et al., *Phys. Rev. Lett.* **75** 3466 (1995).
- [210] A.M. Kalsin, M. Fialkowski, M. Paszewski, et al., *Science* **312** 420 (2006).
- [211] X.M. Lin, H.M. Jaeger, C.M. Sorensen, et al., *J. Phys. Chem. B* **105** 3353 (2001).
- [212] M. Trau, D.A. Saville, I.A. Aksay, *Science* **272** 706 (1996).
- [213] M. Giersig, P. Mulvaney, *J. Phys. Chem.* **97** 6334 (1993).
- [214] Z. Zhong, B. Gates, Y. Xia, et al., *Langmuir* **16** 10369 (2000).
- [215] S.P. Li, W.S. Lew, Y.B. Xu, et al., *Appl. Phys. Lett.* **76** 748 (2000).
- [216] L.S. Li, J. Jin, S. Yu, et al., *J. Phys. Chem. B* **102** 5648 (1998).
- [217] R.P. Sear, S.-W. Chung, G. Markovich, et al., *Phys. Rev. E* **59** R6255 (1999).
- [218] N.A. Kotov, F.C. Meldrum, C. Wu, et al., *J. Phys. Chem.* **98** 2735 (1994).
- [219] B.O. Dabbousi, C.B. Murray, M.F. Rubner, et al., *Chem. Mater.* **6** 216 (1994).
- [220] G. Schmid, *Adv. Eng. Mater.* **3** 737 (2001).
- [221] N.A. Kotov, F.C. Meldrum, J.H. Fendler, *J. Phys. Chem.* **98** 8827 (1994).
- [222] C.P. Collier, R.J. Saykally, J.J. Shiang, et al., *Science* **277** 1978 (1997).
- [223] M. Sastry, A. Gole, V. Patil, *Thin Solid Films* **384** 125 (2001).
- [224] L.F. Chi, S. Rakers, M. Hartig, et al., *Thin Solid Films* **327-329** 520 (1998).
- [225] I. Sloufova-Srnova, B. Vlckova, *Nano Lett.* **2** 121 (2002).
- [226] L. Maya, G. Muralidharan, T.G. Thundat, et al., *Langmuir* **16** 9151 (2000).
- [227] S. Chen, *Langmuir* **17** 2878 (2001).
- [228] F. Mallwitz, W.A. Goedel, *Angew. Chem. Int. Ed.* **40** 2645 (2001).
- [229] M. Sastry, K.S. Mayya, V. Patil, *Langmuir* **14** 5921 (1998).
- [230] S. Paul, C. Pearson, A. Molloy, et al., *Nano Lett.* **3** 533 (2003).
- [231] P. Poddar, T. Telem-Shafir, T. Fried, et al., *Phys. Rev. B* **66** 060403 (2002).
- [232] V. Erokhin, P. Facci, S. Carrara, et al., *Biosens. Bioelectron.* **12** 601 (1997).
- [233] J.-Y. Chang, J.-J. Chang, B. Lo, et al., *Chem. Phys. Lett.* **379** 261 (2003).
- [234] I. Willner, B. Willner, *Pure Appl. Chem.* **73** 535 (2001).
- [235] J.-M. Nam, C.S. Thaxton, C.A. Mirkin, *Science* **301** 1884 (2003).

- [236] R.A. McMillan, C.D. Paavola, J. Howard, et al., *Nat Mater* **1** 247 (2002).
- [237] H. Feng, L. Yuri, C. Tianhong, J. Nanosci. Nanotech. **2** 357 (2002).
- [238] K.B. Lee, J.H. Lim, C.A. Mirkin, *J. Am. Chem. Soc.* **125** 5588 (2003).
- [239] P.S. Doyle, J. Bibette, A. Bancaud, et al., *Science* **295** 2237 (2002).
- [240] W. Shenton, D. Pum, U.B. Sleytr, et al., *Nature* **389** 585 (1997).
- [241] S.-W. Lee, S.K. Lee, A.M. Belcher, *Adv. Mater.* **15** 689 (2003).
- [242] F. Stellacci, C.A. Bauer, T. Meyer-Friedrichsen, et al., *Adv. Mater.* **14** 194 (2002).
- [243] J. Zhang, X. Li, K. Liu, et al., *J. Colloid Interface Sci.* **255** 115 (2002).
- [244] L. Nagle, D. Ryan, S. Cobbe, et al., *Nano Lett.* **3** 51 (2003).
- [245] L. Nagle, D. Fitzmaurice, *Adv. Mater.* **15** 933 (2003).
- [246] D. Wang, V. Salgueiriño-Maceira, L.M. Liz-Marzán, et al., *Adv. Mater.* **14** 908 (2002).
- [247] O.D. Velev, P.M. Tessier, A.M. Lenhoff, et al., *Nature* **401** 548 (1999).
- [248] W. Wang, S.A. Asher, *J. Am. Chem. Soc.* **123** 12528 (2001).
- [249] H. Kang, Y.w. Jun, J.I. Park, et al., *Chem. Mater.* **12** 3530 (2000).
- [250] M.P. Pileni, *J. Phys. Chem. B* **105** 3358 (2001).
- [251] S. Wang, S. Sato, K. Kimura, *Chem. Mater.* **15** 2445 (2003).
- [252] S.I. Stoeva, B.L.V. Prasad, S. Uma, et al., *J. Phys. Chem. B* **107** 7441 (2003).
- [253] L.O. Brown, J.E. Hutchison, *J. Phys. Chem. B* **105** 8911 (2001).
- [254] J.E. Martin, J.P. Wilcoxon, J. Odinek, et al., *J. Phys. Chem. B* **104** 9475 (2000).
- [255] S. Vaucher, M. Li, S. Mann, *Angew. Chem. Int. Ed.* **39** 1793 (2000).
- [256] S.Y. Hong, R. Popovitz-Biro, Y. Prior, et al., *J. Am. Chem. Soc.* **125** 10470 (2003).
- [257] F.X. Redl, K.S. Cho, C.B. Murray, et al., *Nature* **423** 968 (2003).
- [258] E.V. Shevchenko, D.V. Talapin, A.L. Rogach, et al., *J. Am. Chem. Soc.* **124** 11480 (2002).
- [259] B. Nikoobakht, Z.L. Wang, M.A. El-Sayed, *J. Phys. Chem. B* **104** 8635 (2000).
- [260] N.Y. Morgan, C.A. Leatherdale, M. Drndić, et al., *Phys. Rev. B* **66** 075339 (2002).
- [261] A. Samokhvalov, R.W. Gurney, M. Lahav, et al., *J. Phys. Chem. B* **106** 9070 (2002).
- [262] S.A. Maier, P.G. Kik, H.A. Atwater, et al., *Nat Mater* **2** 229 (2003).
- [263] S.A. Maier, P.G. Kik, H.A. Atwater, *Appl. Phys. Lett.* **81** 1714 (2002).
- [264] Z. Tang, B. Ozturk, Y. Wang, et al., *J. Phys. Chem. B* **108** 6927 (2004).
- [265] G. Decher, *Science* **277** 1232 (1997).
- [266] N.A. Kotov, I. Dekany, J.H. Fendler, *J. Phys. Chem.* **99** 13065 (1995).
- [267] S. Joly, R. Kane, L. Radzilowski, et al., *Langmuir* **16** 1354 (2000).
- [268] M.D. Musick, C.D. Keating, M.H. Keefe, et al., *Chem. Mater.* **9** 1499 (1997).
- [269] H. Mattoussi, M.F. Rubner, F. Zhou, et al., *Appl. Phys. Lett.* **77** 1540 (2000).
- [270] M. Gao, B. Richter, S. Kirstein, et al., *J. Phys. Chem. B* **102** 4096 (1998).
- [271] D.S. Koktysh, X. Liang, B.G. Yun, et al., *Adv. Funct. Mater.* **12** 255 (2002).
- [272] D.L. Feldheim, K.C. Grabar, M.J. Natan, et al., *J. Am. Chem. Soc.* **118** 7640 (1996).
- [273] S.C. Glotzer, *Nat Mater* **2** 713 (2003).
- [274] M.E. Mackay, T.T. Dao, A. Tuteja, et al., *Nat Mater* **2** 762 (2003).
- [275] F.W. Starr, J.F. Douglas, S.C. Glotzer, *J. Chem. Phys.* **119** 1777 (2003).
- [276] F.W. Starr, T.B. Schröder, S.C. Glotzer, *Phys. Rev. E* **64** 021802 (2001).
- [277] G.D. Smith, D. Bedrov, L. Li, et al., *J. Chem. Phys.* **117** 9478 (2002).
- [278] R.F. Service, *Science* **293** 785 (2001).
- [279] U. Simon, *Adv. Materials* **10** 1487 (1998).
- [280] M. Dorogi, J. Gomez, R. Osifchin, et al., *Phys. Rev. B* **52** 9071 (1995).
- [281] B. Wang, H. Wang, H. Li, et al., *Phys. Rev. B* **63** 035403 (2000).
- [282] D.L. Klein, R. Roth, A.K.L. Lim, et al., *Nature* **389** 699 (1997).
- [283] C.T. Black, C.B. Murray, R.L. Sandstrom, et al., *Science* **290** 1131 (2000).
- [284] R.P. Andres, J.D. Bielefeld, J.I. Henderson, et al., *Science* **273** 1690 (1996).
- [285] G. Markovich, C.P. Collier, J.R. Heath, *Phys. Rev. Lett.* **80** 3807 (1998).
- [286] A.W. Snow, H. Wohltjen, *Chem. Mater.* **10** 947 (1998).
- [287] R. Parthasarathy, X.-M. Lin, H.M. Jaeger, *Phys. Rev. Lett.* **87** 186807 (2001).

- [288] A.A. Middleton, N.S. Wingreen, *Phys. Rev. Lett.* **71** 3198 (1993).
- [289] J.F. Sampaio, K.C. Beverly, J.R. Heath, *J. Phys. Chem. B* **105** 8797 (2001).
- [290] K.C. Beverly, J.F. Sampaio, J.R. Heath, *J. Phys. Chem. B* **106** 2131 (2002).
- [291] L. Zhao, K.L. Kelly, G.C. Schatz, *J. Phys. Chem. B* **107** 7343 (2003).
- [292] S.A. Maier, M.L. Brongersma, P.G. Kik, et al., *Phys. Rev. B* **65** 193408 (2002).
- [293] M. Quinten, A. Leitner, J.R. Krenn, et al., *Opt. Lett.* **23** 1331 (1998).
- [294] S.A. Maier, P.G. Kik, H.A. Atwater, *Phys. Rev. B* **67** 205402 (2003).
- [295] J.R. Krenn, *Nat Mater* **2** 210 (2003).
- [296] J.D. Jackson, *Classical Electrodynamics*, 2nd Ed, John Wiley & Sons, New York, 1975.
- [297] R. Alvarez-Puebla, B. Cui, J.P. Bravo-Vasquez, et al., *J. Phys. Chem. C* **111** 6720 (2007).
- [298] J.P. Kottmann, O.J.F. Martin, *Opt. Lett.* **26** 1096 (2001).
- [299] B.N.J. Persson, A. Liebsch, *Phys. Rev. B* **28** 4247 (1983).
- [300] T. Yamaguchi, S. Yoshida, A. Kinbara, *Thin Solid Films* **21** 173 (1974).
- [301] C.L. Haynes, A.D. McFarland, L. Zhao, et al., *J. Phys. Chem. B* **107** 7337 (2003).
- [302] A.A. Lazarides, G.C. Schatz, *J. Phys. Chem. B* **104** 460 (2000).
- [303] J.J. Storhoff, A.A. Lazarides, R. Mucic, et al., *J. Am. Chem. Soc.* **122** 4640 (2000).
- [304] K.S. Mayya, V. Patil, M. Sastry, *Bull. Chem. Soc. Jpn.* **73** 1757 (2000).
- [305] T.J. Norman, C.D. Grant, D. Magana, et al., *J. Phys. Chem. B* **106** 7005 (2002).
- [306] A.N. Shipway, M. Lahav, R. Gabai, et al., *Langmuir* **16** 8789 (2000).
- [307] C.G. Blatchford, J.R. Campbell, J.A. Creighton, *Surf. Sci.* **120** 435 (1982).
- [308] J. Thaddeus J. Norman, C. Grant, D. Magana, et al., *Physical Chemistry of Interfaces and Nanomaterials* **4807** 51 (2002).
- [309] C.J. Murphy, T.K. Sau, A.M. Gole, et al., *J. Phys. Chem. B* **109** 13857 (2005).
- [310] J.R. Winkler, A.J. Di Bilio, N.A. Farrow, et al., *Pure Appl. Chem.* **71** 1753 (1999).
- [311] B.L.V. Prasad, S.I. Stoeva, C.M. Sorensen, et al., *Langmuir* **18** 7515 (2002).
- [312] Z. Lin, Wang, *Adv. Mater.* **10** 13 (1998).
- [313] W. Rechberger, A. Hohenau, A. Leitner, et al., *Opt. Comm.* **220** 137 (2003).
- [314] J.B. Pelka, M. Brust, P. Gierlowski, et al., *Appl. Phys. Lett.* **89** 063110 (2006).
- [315] R.H. Terrill, T.A. Postlethwaite, C.-h. Chen, et al., *J. Am. Chem. Soc.* **117** 12537 (1995).
- [316] W.P. Wuelfing, S.J. Green, J.J. Pietron, et al., *J. Am. Chem. Soc.* **122** 11465 (2000).
- [317] M. P. Pileni, Y. Lalatonne, D. Ingerter, et al., *Faraday Discuss* **125** 251 (2004).
- [318] E. Roduner, *Chem. Soc. Rev.* **35** 583 (2006).
- [319] Robert L. Whetten, J.T. Khoury, M.M. Alvarez, et al., *Adv. Mater.* **8** 428 (1996).
- [320] G. Schmid, M. Bäuml, N. Beyer, *Angew. Chem. Int. Ed.* **39** 181 (2000).
- [321] S.T. He, S.S. Xie, J.N. Yao, et al., *Appl. Phys. Lett.* **81** 150 (2002).
- [322] T. Teranishi, M. Miyake, *Chem. Mater.* **11** 3414 (1999).
- [323] S.Y. Zhao, S. Wang, K. Kimura, *Langmuir* **20** 1977 (2004).
- [324] B. Kim, S.L. Tripp, A. Wei, *J. Am. Chem. Soc.* **123** 7955 (2001).
- [325] N. Chandrasekharan, P.V. Kamat, *Nano Lett.* **1** 67 (2001).
- [326] P.J. Thomas, G.U. Kulkarni, C.N.R. Rao, *Chem. Phys. Lett.* **321** 163 (2000).
- [327] F. Remacle, R.D. Levine, *ChemPhysChem* **2** 20 (2001).
- [328] J.-P. Bourgoin, C. Kergueris, E. Lefevre, et al., *Thin Solid Films* **327-329** 515 (1998).
- [329] S. Pal, N.S. John, P.J. Thomas, et al., *J. Phys. Chem. B* **108** 10770 (2004).
- [330] K.V. Sarathy, P.J. Thomas, G.U. Kulkarni, et al., *J. Phys. Chem. B* **103** 399 (1999).
- [331] Y. Liu, Y. Wang, R.O. Claus, *Chem. Phys. Lett.* **298** 315 (1998).
- [332] V.C. Sundar, H.J. Eisler, M.G. Bawendi, *Adv. Mater.* **14** 739 (2002).
- [333] A. Swami, M. Kasture, R. Pasricha, et al., *J. Mater. Chem.* **14** 709 (2004).
- [334] Y.S. Seo, K.S. Kim, K. Shin, et al., *Langmuir* **18** 5927 (2002).
- [335] N. Toshima, T. Yonezawa, *New J. Chem.* **22** 1179 (1998).
- [336] D. Richard, J.W. Couves, J.M. Thomas, *Faraday Discuss. Chem. Soc.* **92** 109 (1991).
- [337] B. Zhao, N. Toshima, *Chem. Express* **5** 721 (1990).

- [338] K. Torigoe, Y. Nakajima, K. Esumi, *J. Phys. Chem.* **97** 8304 (1993).
- [339] A. Henglein, *J. Phys. Chem.* **97** 5457 (1993).
- [340] A. Harriman, *J. Chem. Soc., Chem. Commun.* **24** (1990).
- [341] X. Sun, Z.Y. Jia, Y.H. Huang, et al., *J. Appl. Phys.* **95** 6747 (2004).
- [342] G.C. Papavassiliou, *J. Phys. F: Met. Phys.* **6** (1976).
- [343] B.K. Teo, K. Keating, Y.H. Kao, *J. Am. Chem. Soc.* **109** 3494 (1987).
- [344] L.M. Liz-Marzan, A.P. Philipse, *J. Phys. Chem.* **99** 15120 (1995).
- [345] N. Kometani, M. Tsubonishi, T. Fujita, et al., *Langmuir* **17** 578 (2001).
- [346] N. Sandhyarani, T. Pradeep, *Chem. Mater.* **12** 1755 (2000).
- [347] M.P. Mallin, C.J. Murphy, *Nano Lett.* **2** 1235 (2002).
- [348] S. Link, Z.L. Wang, M.A. El-Sayed, *J. Phys. Chem. B* **103** 3529 (1999).
- [349] D.H. Chen, C.J. Chen, *J. Mater. Chem.* **12** 1557 (2002).
- [350] Y.H. Chen, C.S. Yeh, *Chem. Commun.* **371** (2001).
- [351] J. Zhang, J. Worley, S. Denomme, et al., *J. Phys. Chem. B* **107** 6920 (2003).
- [352] I. Lee, S.W. Han, K. Kim, *Chem. Commun.* 1782 (2001).
- [353] S. Senapati, A. Ahmad, M.I. Khan, et al., *Small* **1** 517 (2005).
- [354] P. Cicuta, E.J. Stancik, G.G. Fuller, *Phys. Rev. Lett.* **90** 236101 (2003).
- [355] E.J. Stancik, M.J.O. Widenbrant, A.T. Laschitsch, et al., *Langmuir* **18** 4372 (2002).
- [356] E.J. Stancik, G.T. Gavranovic, M.J.O. Widenbrant, et al., *Faraday Discuss.* **123** 145 (2003).
- [357] G. Schmid, *Nanoparticles: From Theory to Application* (2004).
- [358] Y. Lin, H. Skaff, T. Emrick, et al., *Science* **299** 226 (2003).
- [359] M.G. Nikolaidis, A.R. Bausch, M.F. Hsu, et al., *Nature* **420** 299 (2002).
- [360] I. Benjamin, *Chem. Rev.* **96** 1449 (1996).
- [361] R.A.W. Dryfe, *Phys. Chem. Chem. Phys.* **8** (2006).
- [362] G. Luo, S. Malkova, J. Yoon, et al., *Science* **311** 216 (2006).
- [363] M.K. Sanyal, S.K. Sinha, K.G. Huang, et al., *Phys. Rev. Lett.* **66** 628 (1991).
- [364] C. Fradin, A. Braslau, D. Luzet, et al., *Nature* **403** 871 (2000).
- [365] A. Datta, S. Kundu, M.K. Sanyal, et al., *Phys. Rev. E* **71** 041604 (2005).
- [366] M. Fukuto, O. Gang, K.J. Alvine, et al., *Phys. Rev. E* **74** 031607 (2006).
- [367] E. Saint Martin, O. Konovalov, J. Daillant, *Thin Solid Films* **515** 5687 (2007).
- [368] M. Mezger, H. Reichert, S. Schoder, et al., *Proceedings of the National Academy of Sciences* **103** 18401 (2006).
- [369] T. Ung, L.M. Liz-Marzan, P. Mulvaney, *J. Phys. Chem. B* **105** 3441 (2001).
- [370] B.C. Sih, M.O. Wolf, *J. Phys. Chem. B* **110** 22298 (2006).
- [371] M.V. Meli, R.B. Lennox, *J. Phys. Chem. C* **111** 3658 (2007).
- [372] G. De, C.N.R. Rao, *J. Phys. Chem. B* **107** 13597 (2003).
- [373] A.J. Haes, S. Zou, G.C. Schatz, et al., *J. Phys. Chem. B* **108** 109 (2004).
- [374] L. Baia, M. Baia, J. Popp, et al., *J. Phys. Chem. B* **110** 23982 (2006).
- [375] G.A. Baker, D.S. Moore, *Analytical and Bioanalytical Chemistry* **382** 1751 (2005).
- [376] M. Zhou, S. Chen, S. Zhao, *J. Phys. Chem. B* **110** 4510 (2006).
- [377] C. Burda, X. Chen, R. Narayanan, et al., *Chem. Rev.* **105** 1025 (2005).
- [378] T.A. Witten, L.M. Sander, *Phys. Rev. B* **27** 5686 (1983).
- [379] P. Meakin, *Phys. Rev. Lett.* **51** 1119 (1983).
- [380] D.A. Edwards, H. Brenner, D.T. Wasan, *Interfacial Transport Processes and Rheology* (1991).
- [381] M.A. Bos, T.V. Vliet, *Adv. Colloid Interface Sci* **91** 237 (2001).
- [382] E. Philipp, F. Peter, J.W. Erich, et al., *Rev. Sci. Instrum.* **74** 4916 (2003).
- [383] P. Braunstein, H. Lehner, D. Matt, *Inorg. Synth.* **27** 218 (1990).
- [384] M. Khan, C. Oldham, D.G. Tuck, *Can. J. Chem.* **59** 2714 (1981).
- [385] N.H. Furman, W.B. Mason, J.S. Pekola, *Anal. Chem.* **21** 1325 (1949).
- [386] J. Bartl, R. Fira, M. Hain, *Measurement Science and Review* **1** 29 (2001).
- [387] A.L. Patterson, *Phys. Rev.* **56** 978 (1939).
- [388] O.H. Soo-Gun, J.C. Slattery, *J. Colloid Interface Sci.* **67** 516 (1978).

- [389] G. Schmid, S. Peschel, *New J. Chem.* **22** 669 (1998).
- [390] M. Quinten, I. Sander, P. Steiner, et al., *Zeitschrift für Physik D Atoms, Molecules and Clusters* **20** 377 (1991).
- [391] H. Shiigi, Y. Yamamoto, H. Yakabe, et al., *Chem. Commun.* 1038 (2003).
- [392] B. Abeles, P. Sheng, M.D. Coutts, et al., *Advances in Physics* **24** 407 (1975).
- [393] J.E. Morris, T.J. Coutts, *Thin Solid Films* **47** 3 (1977).
- [394] W.P. Wuelfing, R.W. Murray, *J. Phys. Chem. B* **106** 3139 (2002).
- [395] M. Brust, D. Bethell, C.J. Kiely, et al., *Langmuir* **14** 5425 (1998).
- [396] M. Brust, D.J. Schiffrin, D. Bethell, et al., *Adv. Mater.* **7** 795 (1995).
- [397] M.L. Sandrock, C.A. Foss, *J. Phys. Chem. B* **103** 11398 (1999).
- [398] M. Gluodenis, C.A. Foss, *J. Phys. Chem. B* **106** 9484 (2002).
- [399] S. Norrman, T. Andersson, C.G. Granqvist, et al., *Phys. Rev. B* **18** 674 (1978).
- [400] I. Rubinstein, *Chem. Eur. J.* **8** 3850 (2002).
- [401] P. Royer, J.P. Goudonnet, R.J. Warmack, et al., *Phys. Rev. B* **35** 3753 (1987).
- [402] F. Strelow, A. Henglein, *J. Phys. Chem.* **99** 11834 (1995).
- [403] E. Hutter, J.H. Fendler, *Adv. Mater.* **16** 1685 (2004).
- [404] J.F. Sánchez-Ramírez, C. Vazquez-Lopez, U. Pal, *Superficies Vacio.* **15** 16 (2002).
- [405] P. Sollich, F. Lequeux, P. Hébraud, et al., *Phys. Rev. Lett.* **78** 2020 (1997).
- [406] P. Sollich, *Physical Review E* **58** 738 (1998).
- [407] K. Miyazaki, H.M. Wyss, D.A. Weitz, et al., *EPL (Europhysics Letters)* 915 (2006).
- [408] C. Pinaki, K. Smarajit, D. Chandan, et al., *Phys. Rev. Lett.* **95** 248301 (2005).
- [409] M.K. Sanyal, S. Hazra, J.K. Basu, et al., *Phys. Rev. B* **58** R4258 (1998).
- [410] M.G. Nikolaidis, A.R. Bausch, M.F. Hsu, et al., *Nature* **424** 1014 (2003).
- [411] Y. Lin, A. Boker, H. Skaff, et al., *Langmuir* **21** 191 (2005).
- [412] J.A. Creighton, D.G. Eadon, *J. Chem Soc. Faraday Trans.* **87** 3881 (1991).
- [413] C.G. Granqvist, O. Hunderi, *Phys. Rev. B* **16** 3513 (1977).
- [414] L. Gunnarsson, T. Rindzevicius, J. Prikulis, et al., *J. Phys. Chem. B* **109** 1079 (2005).
- [415] E. Fischer, *J. Phys. Chem.* **71** 3704 (1967).
- [416] I.I.S. Lim, M.M. Maye, J. Luo, et al., *J. Phys. Chem. B* **109** 2578 (2005).
- [417] S. Liao, Y. Shnidman, A. Ulman, *J. Am. Chem. Soc.* **122** 3688 (2000).
- [418] F. Schreiber, A. Eberhardt, T.Y.B. Leung, et al., *Phys. Rev. B* **57** 12476 (1998).
- [419] M.G. Bellino, E.J. Calvo, G. Gordillo, *Phys. Chem. Chem. Phys.* **6** 424 (2004).
- [420] H.M. Schessler, D.S. Karpovich, G.J. Blanchard, *J. Am. Chem. Soc.* **118** 9645 (1996).
- [421] C.D. Bain, E.B. Troughton, Y.T. Tao, et al., *J. Am. Chem. Soc.* **111** 321 (1989).
- [422] A. Ulman, *Chem. Rev.* **96** 1533 (1996).
- [423] F. Schreiber, *Prog. Surf. Sci.* **65** 151 (2000).
- [424] J.C.M. Garnett, *Philosophical transaction of the royal society of london, series A* **203** 385 (1904).
- [425] J.P. Folkers, P.E. Laibinis, G.M. Whitesides, et al., *J. Phys. Chem.* **98** 563 (1994).
- [426] J.B. Schlenoff, M. Li, H. Ly, *J. Am. Chem. Soc.* **117** 12528 (1995).
- [427] A. Salomon, D. Cahen, S. Lindsay, et al., *Adv. Mater.* **15** 1881 (2003).
- [428] D.A. Weitz, M. Oliveria, *Phys. Rev. Lett.* **52** 1433 (1984).
- [429] W.P. Stuart, M. Paul, *J. Appl. Phys.* **99** 123504 (2006).
- [430] J. Perez-Juste, I. Pastoriza-Santos, L.M. Liz-Marzan, et al., *Coord. Chem. Rev.* **249** 1870 (2005).
- [431] B.M.I. van der Zande, M.R. Bohmer, L.G.J. Fokkink, et al., *Langmuir* **16** 451 (2000).
- [432] S. Link, M.B. Mohamed, M.A. El-Sayed, *J. Phys. Chem. B* **103** 3073 (1999).
- [433] C. Li, Kevin L. Shuford, Q.H. Park, et al., *Angew. Chem. Int. Ed.* **46** 3264 (2007).
- [434] B.K. Pong, H.I. Elim, J.X. Chong, et al., *J. Phys. Chem. C* **111** 6281 (2007).
- [435] M.B. Isichenko, *Reviews of Modern Physics* **64** 961 (1992).
- [436] J. Schmelzer, S.A. Brown, A. Wurl, et al., *Phys. Rev. Lett.* **88** 226802 (2002).
- [437] B. Nikoobakht, M.A. El-Sayed, *Langmuir* **17** 6368 (2001).
- [438] Y. Jin, S. Dong, *Angew. Chem. Int. Ed.* **41** 1040 (2002).

- [439] K. Yagi, K. Takayanagi, K. Kobayashi, et al., *J. Cryst. Growth* **28** 117 (1975).
- [440] F. Baletto, C. Mottet, R. Ferrando, *Phys. Rev. Lett.* **84** 5544 (2000).
- [441] F. Baletto, C. Mottet, R. Ferrando, *Phys. Rev. B* **63** 155408 (2001).
- [442] M.Z. Liu, P. Guyot-Sionnest, *J. Phys. Chem. B* **109** 22192 (2005).
- [443] X. Wang, H. Itoh, K. Naka, et al., *Langmuir* **19** 6242 (2003).
- [444] J.P. Xiao, Y. Xie, R. Tang, et al., *Adv. Mater.* **13** 1887 (2001).
- [445] M.S. El-Shall, V. Abdelsayed, Y.B. Pithawalla, et al., *J. Phys. Chem. B* **107** 2882 (2003).
- [446] M. Tsuji, M. Hashimoto, Y. Nishizawa, et al., *Chem. Eur. J.* **11** 440 (2005).
- [447] P. Pieranski, *Phys. Rev. Lett.* **45** 569 (1980).
- [448] A.Y. Grosberg, T.T. Nguyen, B.I. Shklovskii, *Rev. Mod. Phys.* **74** 329 (2002).
- [449] W.H. Binder, *Angew. Chem. Int. Ed.* **44** 2 (2005).
- [450] A. Aviram, M.A. Ratner, *Chem. Phys. Lett.* **29** 277 (1974).
- [451] J. Jortner, M. Ratner, *Molecular Electronics* (1997).
- [452] D.L. Pearson, L. Jones Iii, J.S. Schumm, et al., *Synth. Met.* **84** 303 (1997).
- [453] D.M. Adams, L. Brus, C.E.D. Chidsey, et al., *J. Phys. Chem. B* **107** 6668 (2003).
- [454] S.T. Purcell, N. Garcia, V.T. Binh, et al., *J. Am. Chem. Soc.* **116** 11985 (1994).
- [455] R.M. Metzger, *Chem. Rev.* **103** 3803 (2003).
- [456] M.T. Cygan, T.D. Dunbar, J.J. Arnold, et al., *J. Am. Chem. Soc.* **120** 2721 (1998).
- [457] J.M. Tour, L. Jones Ii, D.L. Pearson, et al., *J. Am. Chem. Soc.* **117** 9529 (1995).
- [458] D.B. Janes, V.R. Kolagunta, R.G. Osifchin, et al., *Superlattices Microstruct.* **18** 275 (1995).
- [459] L.A. Bumm, J.J. Arnold, M.T. Cygan, et al., *Science* **271** 1705 (1996).
- [460] L.A. Bumm, J.J. Arnold, L.F. Charles, et al., *J. Am. Chem. Soc.* **121** 8017 (1999).
- [461] G. Leatherman, E.N. Durantini, D. Gust, et al., *J. Phys. Chem. B* **103** 4006 (1999).
- [462] A.M. Rawlett, T.J. Hopson, L.A. Nagahara, et al., *Appl. Phys. Lett.* **81** 3043 (2002).
- [463] F.R.F. Fan, J. Yang, S.M. Dirk, et al., *J. Am. Chem. Soc.* **123** 2454 (2001).
- [464] J. Chen, M.A. Reed, A.M. Rawlett, et al., *Science* **286** 1550 (1999).
- [465] J. Chen, W. Wang, M.A. Reed, et al., *Appl. Phys. Lett.* **77** 1224 (2000).
- [466] C. Kergueris, J.P. Bourgoin, S. Palacin, et al., *Phys. Rev. B* **59** 12505 (1999).
- [467] J. Reichert, R. Ochs, D. Beckmann, et al., *Phys. Rev. Lett.* **88** 1768041 (2002).
- [468] M.A. Reed, C. Zhou, C.J. Muller, et al., *Science* **278** 252 (1997).
- [469] J.M. Seminario, C.E. De La Cruz, P.A. Derosa, *J. Am. Chem. Soc.* **123** 5616 (2001).
- [470] J.G. Kushmerick, D.B. Holt, J.C. Yang, et al., *Phys. Rev. Lett.* **89** (2002).
- [471] G.K. Ramachandran, A.M. Rawlett, T.J. Hopson, et al., *Mat. Res. Soc. Symp. Proc.* **728** (2002).
- [472] D.L. Pearson, J.M. Tour, *J. Org. Chem.* **62** 1376 (1997).
- [473] A.J. Nam, A. Teren, J.A. Lusby, et al., *J. Vac. Sci. Technol. B* **115** 2046 (1996).
- [474] L.C. Brousseau Iii, J.P. Novak, S.M. Marinakos, et al., *Adv. Mater.* **11** 447 (1999).
- [475] S. Lakshmi, S.K. Pati, *J. Chem. Phys.* **121** 11998 (2004).
- [476] H. Ishii, K. Sugiyama, E. Ito, et al., *Adv. Mater.* **11** 605 (1999).

## Index

- activated conductor, 98
- activated hopping, 55
- activation energy, 130
- Ag
  - nanowires, 143
  - synthesis of
    - dendritic nanostructures, 76, 143
    - nanocrystalline film, 75
    - nanocrystals, 12, 14
- Ag-Au. *See* Au-Ag
- air–water interface, 46
- alcohol reduction, 13
- Arrhenius plot, 96, 130
- assembly
  - attraction driven, 45
  - entropy driven, 42, 44
  - self assembly, 40
- Au
  - nanocrystal chains, 145
  - nanocrystalline film
    - electrical properties, 95
    - mechanical properties, 100
    - optical properties, 84
    - thickness, 87
  - nanorods, 137
  - synthesis of
    - fractal assembly, 76
    - nanocrystalline film, 74
    - nanocrystals, 14
- Au-Ag
  - alloys, 143
  - mesoballs, 143
  - nanocrystalline film, 71, 106
  - triangular nano sheets, 143
- Au-Ag-Cu
  - nanocrystalline film, 71, 105
- Au-Cu
  - nanocrystalline film, 71, 105
- Au–Pt
  - synthesis of, 13
- BHCOAT, 23
- binding energy, 79
- Bloch waves, 25
- Born approximation, 119
- borohydride reduction, 10
- Brownian motion, 5
- Brust method, 10, 12
- charging energy, 6, 15, 29, 54, 61
- citrate method, 12
- Clausius–Mossotti equation, 56
- Coulomb blockade, 30, 53, 54, 60, 61, 66, 156, 157
- Cox-Merz rule, 64, 118, 147
- Cu
  - synthesis of
    - nanocrystalline film, 75
    - nanocrystals, 10
  - cupferron, 75, 76
  - diffusion limited aggregation, 45, 69, 73, 143
  - Drude dielectric function, 132
  - electron affinity, 29
  - electrophoretic deposition, 45
  - five fold symmetry, 16, 137, 141, 143
  - fractal dimension, 137, 139
  - Hamaker constant, 43, 45
  - Hausdorff dimension. *See* fractal dimension
  - Hund's rules, 31
  - hydrazine, 75, 76
  - icosahedral, 141, 143
  - icosahedron, 16, 19
  - interfacial rheology, 71
  - interparticle coupling, 136
  - ionization energy, 6
  - ionization potential, 29
  - I-V spectra, 153, 156
  - Jellium model, 29
  - Kubo gap, 26, 34
  - Langmuir–Blodgett, 37, 46, 47, 51, 54, 66
  - laser synthesis, 14
  - layer by layer, 51, 52
  - lithography
    - dip-pen, 38
    - microcontact printing, 39
    - nanosphere, 46
  - local density approximation, 29
  - Lycurgus cup, 4
  - magic nuclearity, 19, 34, 120

- Maxwell-Garnett formalism, 132
- metal-insulator transition, 136
- Mie theory, 22, 23, 24
- Moiré pattern, 78, 109
- monolayer protected clusters, 12
- Mott-Hubbard transition, 66
- multiply twinned particle, 18
- nanindentation, 80, 100
- Neel's theory, 32
- negative differential resistance, 152, 155, 157
- neutron scattering, 32
- Ostwald ripening, 8
- Pd
  - dimeric nanocrystal, 152
  - synthesis of
    - nanocrystalline film, 75
    - nanocrystals, 12, 13, 152
- Pd–Pt
  - synthesis of, 13
- photochemical synthesis, 14
- photolithography, 53
- photonic band gap, 49
- photonic crystal, 49
- plasmon frequency, 22, 56
- plasmon resonance. *See* surface plasmon
- Polyhedra, 16
- Pt
  - synthesis of
    - nanocrystals, 10, 14, 75
  - quantum confinement, 2, 35
  - Scherrer formula, 20, 79
  - size dependent
    - magnetic properties, 32
  - Sonogashira coupling reaction, 152
  - specific heat, 34
  - steric interaction, 43
  - structural relaxation, 115
  - superparamagnetic, 32
  - suprastructure, 2
  - surface enhanced Raman scattering, 49, 69
  - surface plasmon, 56, 84, 106, 138
    - longitudinal, 59, 145
    - transverse, 59, 145
  - Thomson's scattering length, 122
  - triphenylphosphine, 76
  - Turkevich method, 12
  - van der Waals force, 43, 45
  - variable-range hopping, 55
  - viscoelastic, 114
  - X-ray scattering, 68
    - diffuse, 69, 121
    - reflectivity, 82, 119